Multispecies Reactor Design for Fluorination Reduction of Lunar Regolith

Riddhi Anubhav Maharaj

Dissertation in Partial Fulfilment of the Master of Philosophy in Space Studies
Department of Electrical Engineering
University of Cape Town
June 2024

SL.24.02

Plagiarism Declaration

I, Riddhi Maharaj, know the meaning of plagiarism and declare that all the work in the document, save for that which is properly acknowledged, is my own. It has not been previously submitted, in part or whole, to any university or institution for any degree, diploma, or other qualification. This thesis/dissertation has been submitted to the Turnitin module (or equivalent similarity and originality checking software) and I confirm that my supervisor has seen my report and any concerns revealed by such have been resolved with my supervisor.

This thesis/dissertation has been submitted to the Turnitin module (or equivalent similarity and originality checking software) and I confirm that my supervisor has seen my report and any concerns revealed by such have been resolved with my supervisor.

Signed Signed by candidate

Date: 10 February 2025

Abstract

Humans last landed on the Moon in December 1972, the last of six brief visits to the lunar surface that lasted from one to three days. After an absence of more than 50 years, several countries are planning for humanity's return to the Moon, this time to establish a permanent human presence on the lunar surface. A sustained human presence on the Moon will require the construction of a permanent lunar base. This requires a large amount of structural and functional materials, which can be obtained in two ways. The first is to transport all the materials required from the Earth to the Moon, and the second is to realize in-situ resource utilization (ISRU) of lunar resources, which will allow humans to "live off the land".

The effective utilisation of locally available materials can reduce the required launch mass and cost for a given mission and eventually reduce the reliance of lunar settlements on Earth for supply of critical resources to sustain human life.

Lunar regolith is the top layer of soil on the surface of the Moon. It is a mixture of tightly bound metal oxides. This can provide valuable materials for a sustained human presence on the Moon. In a seminal paper in 1989, Landis and Perino (1989) first proposed using fluorine to reduce the regolith to produce oxygen, which is critical for life support and return propellant. The process reduces regolith to its base elements, silicon, iron, magnesium, calcium, aluminium, and a trace amount of titanium, whilst liberating oxygen. These are needed to build and maintain critical systems required to support a long-term sustained human presence on the Moon.

The focus of this work was to derive a robust heterogenous reaction system (from first principles) that models the regolith furnace in the process proposed by Landis and Perino (1989). The model can describe how a regolith particle, which consists of a mix of metal oxides, is reduced by fluorine gas to produce metal fluorides and oxygen. The model incorporates the varying porosity of the particle, and the concentration profiles of the reactants in a multiple reaction system with diffusion limitations. The model also allows for a parameter sensitivity study to be conducted to determine the optimum operating regimes (reaction-controlled, diffusion-controlled or feed-controlled) and the production rate of oxygen and the metal fluorides ($SiF_4, TiF_4, FeF_3, AlF_3, CaF_2, MgF_2$). This will provide the basis for a full reactor design to be conducted in the future. The principal limitation to this study is that there is no experimental reaction rate or diffusion data available to validate the model.

The system was modelled as a gas-solid system that consists of six reactions that occur simultaneously. The six reactions occur as the particle reacts with fluorine. The gas products leave in the exit stream of the semi-batch reactor, and the converted metal fluoride solids remain as an inert ash layer.

The changing porosity of the particle as the reaction occurs is accounted for, as this changes the available reaction sites in the particle. Knudsen diffusion was assumed and the reaction rate for each reaction was

assumed and was used to calculate the overall reaction rate in the reactor. The reaction rate was derived and modelled to react with fluorine until the solid reactants where depleted. The particles react in a semi-batch reactor and the surface concentration of the particle is assumed to be the same as the exit stream of the reactor. The model predicts and plots the concentration variation of each species and the porosity over the reaction time and through the particle. It also calculates and plots the conversion over time, the solids contact time and the Thiele modulus, which is used to determine the operating regimes of the system.

The base case was chosen as to have a feed flowrate of $Q_0 = 1000\frac{m^3}{s}$, the particle size of $R_p = 35\mu m$ and a reaction rate of $, k_j = 1$. The results showed that the reaction happens within 2.5 seconds and reaches 100% conversion of all solid reactants. It shows a flat concentration profile of oxygen being produced, both through the particle and over time, which implies very few diffusion limitations in the system. This is a desired operating regime, as it implies minimal contamination of the product reactor exit stream with fluorine, which is difficult to separate further downstream. The conversion of the regolith particle was calculated for each solid reactant, and they all follow the same pattern because each reaction has the same reaction rate and only minor deviation due to differences in diffusion of species. The reaction is very fast and therefore requires a low residence time and solids contact time, which is the amount of time that the particles spend in the reactor and in contact with the fluorine gas.

A parametric sensitivity study was conducted on the effect that flowrate Q_o, particle size R_p and reaction rate k_j have on the system. The values were varied and compared against the base case. The analysis showed that the optimum operating regime is when maximum oxygen is being produced consistently through the particle, shown by a flat oxygen concentration profile through the particle and over time, indicating few diffusion limitations. This means that the fluorine can diffuse through and react in the whole particle and produce oxygen and other products evenly throughout the particle. It also showed that the system is very sensitive to changes in the reaction rate.

The system needs to be balanced with the production volume of the exit products' production rate and the purity of the exit product stream which produces the oxygen, silicon tetrafluoride and titanium fluoride. The optimum operating regime occurred when the volumetric flowrate was set to 100 m^3/s, or when the particle was very small and below $R_p = 3.5\mu m$.

The Theile modulus was calculated and used as an indicator of the starting point of the reaction. The calculated values, across the varying parameters, showed that the system does not follow the expected catalytic limits and definitions. The calculated Theile modulus of less than 1 for each reaction gave rise to maximum oxygen conversion profiles, showing very few diffusion effects in the system. This occurred when $Q = 100\ m^3/s$ and $R_p = 3.5\ \mu m$.

Acknowledgements

Thank you to my supervisors, Prof. K. Moller and Prof. P. Martinez, for there endless patience, kindness and support with this thesis. It would not have been possible without your expertise and guidance. Thank you to my family, I was blessed to have your support and patience through this work.

Acronyms

CRS	Carbothermal Reduction of silicates
CNSA	China National Space Agency
CSTR	Continuous Stirred Tank Reactor
DAE	Differential Algebra Equations
DASRT	DAE solver with zero crossing
ESA	European Space Agency
FBR	Fluidized Bed Reactor
FCR	Fixed Conversion Reactor
HRI	Hydrogen reduction of Ilmenite
ISRU	In-situ Resource Utilisation
LEO	Low Earth Orbit
LUNOX	Lunar Oxygen
MRE	Molten Regolith Electrolysis
NASA	National Aeronautics and Space Administration
ODE	Ordinary Differential Equation
RT	Residence Time
SCM	Shrinking Core Model
SEM	Scanning Electron Microscope

Contents

List of Tables

List of Figures

List of Symbols

$torr$	Torr – unit of pressure
MW	Mega Watt
ton	Mass measurement
kg	Mass measurement
$W.hr/kg$	Unit of specific energy (SI is J/kg)
J	Joule
F_2	Fluorine
O_2	Oxygen
FeF_3	Iron Fluoride
SiF_4	Silicon tetrafluoride
TiF_4	Titanium tetrafluoride
AlF_3	Aluminium Fluoride
MgF_2	Magnesium Fluoride
CaF_2	Calcium Fluoride
KF	Potassium Fluoride
$°C$	Degree Celsius
atm	atmosphere
HF	Hydrogen Fluoride
m	meter
μm	micrometre
V_R	Volume of reactor
V_s	Volume of solid
ε	Porosity
$C_{g,i}$	concentration of the gas species (mol/m^3)
r	Radius (m)
$D_{e,i}$	diffusion coefficients
$\overline{R_g}$	Overall gas reaction rate
x	normalised particle length
R_p	Particle radius (m)
D_k	Knudsen diffusivities
d_p	Pore diameter (cm)
M_{wt}	Molecular weights (g/mol)
T	Temperature

$C_{s,i}$	concentration of the solid species (mol/m^3)
$\overline{R_s}$	Overall solid reaction rate
$i = 1{:}4$	Gas species
$i = 1{:}10$	Solid species
SiO_2	Silicon dioxide
TiO_2	Titanium dioxide
FeO	Iron oxide
MgO	Magnesium oxide
CaO	Calcium oxide
Al_2O_3	Aluminium oxide
r_j	Reaction rate
N_p	Number of particles
$C_{i,1}$	Concentration of fluorine (mol/m^3)
V_p	Volume of particle
ν_g	Stoichiometric coefficients of gas species
ν_s	Stoichiometric coefficients of solid species
M_0	Initial mass of regolith (kg)
ρ_i	Initial density $\left(\frac{kg}{m^3}\right)$
$x_{i,0}$	Initial mass fractions of regolith particle
$V_{s,0}$	Initial volume of solid
ε_0	Initial porosity
M	Total mass
x_i	Mass fractions
A	Porosity constant
$F_{i,0}$	Initial molar concentration (mol/s)
F_i	Exit molar flowrate (mol/s)
$\bar{R}_i$	overall average reaction rate
Q	Volumetric flowrate (m^3/min)
C_t	Total concentration (mol/m^3)
$Q(t)$	Exit volumetric flowrate (m^3/min)
$C_{R,i}$	Reactor exit concentrations (mol/m^3)
t	Time (s)
$C_{i,0}$	Initial concentrations of all species
P	Total pressure
R	Ideal gas constant

ε_k	Porosity at collocation point
x_k	Collocation position
w_j	Weights from collocation analysis
$f\|_{x,t}$	Final solution vector
$X_{s,i}$	Conversion of solid reactants
τ_R	Residence time of the reactor gas
Q_0	Initial volumetric flowrate
τ_S	Residence time of solids
ϕ_i	Calculated psuedo-Thiele modulus
k_j	Reaction rate constant for each reaction

1. Lunar Settlement

1.1 Introduction

Humans first set foot on the Moon on 20 July 1969, as part of the United States' Apollo Programme. All told, a total of twelve humans walked on the Moon between 1969 and 1972 (Bennett, Ellender and Dempster, 2020). These early lunar visits added up to just under 12.5 days that humans spent on the surface of the Moon. They had to bring with them everything needed to sustain their presence on the Moon, which is why those early visits were so short.

After a fifty-year hiatus, human exploration of the Moon and a permanent human presence on the lunar surface is on the space exploration agenda of several countries (Bennett, Ellender and Dempster, 2020; Meurisse & Carpenter, 2020; Granier et al., 2025). In 2017, the National Aeronautics and Space Administration (NASA) launched plans to resume human-crewed exploration missions and to establish a permanent human presence (manned lunar bases) on the Moon by 2040 to promote feasible and sustainable space exploration (Zhou et al., 2021). This is known as the Artemis Program, and it will be led by the United States and conducted in partnership with a number of countries (Zhou et al., 2021, Angelopoulos, 2011; Chi et al., 2024). China's Chang'E-5 spacecraft successfully collected 1.731 kg of samples from Oceanus Procellarum on the Moon's nearside in December 2020. It was the first lunar sample return mission since Luna 24 in 1976 (Jia et al., 2021; Chi et al., 2024). Most recently, India's Chandrayaan-3 successfully landed on the Moon's surface (Wattles, 2023; (Chi et al., 2024)). Many other conceptual designs have already been prepared by, NASA (Artemis Program) (Chi et al., 2024), Chinese Space Agency (Chang'e project), Indian Space Agency (Chandrayaan Program), European (Luna Resurs) (Chi et al., 2024), and Japanese Space Agency (Japanese Lunar Exploration Program) (Pekkanen, Aoki and Takatori, 2023; Chi et al., 2024).

A sustained human presence on the Moon will require the construction of a permanent lunar base (Meurisse & Carpenter, 2020). This requires a large amount of structural and functional materials, which can be obtained in two ways. The first is to transport all the materials required from the Earth to the Moon, and the second is to realize in-situ resource utilization (ISRU) of lunar resources (Just et al., 2020; Zhou et al., 2021; Meurisse & Carpenter, 2020; Schlüter & Cowley, 2020; Šeško et al., 2024), which will allow humans to "live off the land".

A permanently crewed lunar base and lunar settlement will require the development of critical systems such as power, propellants, life support, and construction of support systems and habitats (Rice & Gustafson, 2000; Landis, 2005; Landis, 2007; Meurisse & Carpenter, 2020; Schlüter & Cowley, 2020; Šeško et al., 2024). The complexity of the lunar base will be driven by the availability of electric power on the Moon's surface. Both nuclear and solar photovoltaic systems have been proposed to generate power on the Moon (Landis et al., 1990, Freundlich' et al., 2005).

Transporting materials to the Moon from Earth is very expensive, due to the high cost of launch to lift these materials out of the Earth's gravitational well (Keaton, 1985; Landis et al., 1990; Taylor & Martel, 2003; Schreiner et al., 2015; Schreiner & Hoffman, 2015; Bennett, Ellender and Dempster, 2020; Meurisse & Carpenter, 2020). According to some estimates, it costs up to 10,000 dollars to send 0.45 kg materials into lunar orbit (Zhou et al., 2021). In contrast, utilising ISRU technology in the construction of lunar bases can fundamentally solve the high material transportation cost problem (Taylor & Carrier, 1992; Hepp et al., 1994; Rice & Gustafson, 2000; Taylor & Martel, 2003; Sen, Ray & Reddy, 2005; Schwandt et al., 2012; Zhou et al., 2021; Bennett, Ellender and Dempster, 2020; Meurisse & Carpenter, 2020).

1.2 What is Lunar ISRU?

ISRU refers to the effective utilisation of local indigenous materials. As mentioned above, it can significantly reduce the required launch mass and cost for a given mission and eventually reduce the reliance of lunar settlements on Earth (Landis & Perino, 1989; Landis et al., 1990; Taylor & Martel, 2003; Schreiner et al., 2015; Schreiner & Hoffman, 2015; Lu et al., 2016; Rasera et al., 2020; Guerrero-Gonzalez & Zabel, 2023).

The immediate ISRU goal is to reduce the direct cost of humans going to and returning from the Moon and Mars, and then to build toward self-sufficiency of lunar settlements to expand our exploration of the solar system and possibly return energy or other valuable resources to Earth (Rice & Gustafson, 2000; Rasera et al., 2020; Schlüter & Cowley, 2020; Guerrero-Gonzalez & Zabel, 2023; Granier et al., 2025).

The regolith (soil) on the surface of the Moon contains approximately 40-45% oxygen by mass, with most of the oxygen captive in strong oxide bonds within silicate minerals containing iron, titanium, aluminium, magnesium, calcium and other trace materials (Hepp et al., 1994; Landis, 2005; Landis, 2007; Landis, 2011; Landis, 2014; Schreiner et al., 2015, Sacksteder & Sanders, 2007; Lim & Anand, 2019; Guerrero-Gonzalez & Zabel, 2023). The oxygen and metals are important materials that can be obtained from the available lunar resources (Hepp et al., 1994).

Oxygen is the first and most useful product that can be produced from lunar regolith (Taylor & Carrier, 1992, Šeško et al., 2024). It is essential for life-support and the major mass component of rocket fuel and water (Landis, 2005; Landis, 2007; Schwandt et al., 2012; Schlüter & Cowley, 2020; Šeško et al., 2024). In a 2012 study, Schwandt et al. (2012) projected an initial annual production target of around 5 tons of oxygen to support a human presence on the Moon.

For a long-term sustainable lunar presence and industry, it will become desirable to produce materials for infrastructure and industrial applications from locally available lunar resources (Landis & Perino, 1989; Landis, 2005; Landis, 2007; Schwandt et al., 2012). Silicon will be useful for manufacturing semi-conductors and solar panels; metals such as aluminium, iron, and titanium will be useful as structural materials; aluminium can be further used for manufacturing electrical conductors; and remaining oxides can be used in glassmaking. It may also be valuable to produce metals or silane for use as rocket fuel (Landis & Perino, 1989; Landis, 2005; Landis, 2007). A process that can initially focus on oxygen production, but could later be expanded to produce and refine other raw materials is most desirable (Hepp et al., 1994;Landis, 2005; Landis, 2007; Schwandt et al., 2012, Šeško et al., 2024).

1.3 What are the Benefits of Lunar ISRU?

A number of NASA-supported studies of the need for space resources showed that near-Earth resources are essential to any long-term space activities and can foster growth of human space activities (Mckay et al., 1991; Taylor & Carrier, 1992; Schwandt et al., 2012; Rasera et al., 2020; Guerrero-Gonzalez & Zabel, 2023; Granier et al., 2025).

As stated above, mass launch costs are at a premium in space missions (Keaton, 1985; Landis et al., 1990; Taylor & Martel, 2003; Schreiner et al., 2015; Schreiner & Hoffman, 2015, Sacksteder & Sanders, 2007). There are many benefits to be realised by making use of lunar resources. Chief among them, is the reduction in launch mass to Low Earth Orbit (LEO), which translates directly into a cost savings (Hepp et al., 1994; Sen, Ray & Reddy, 2005; Curreri et al., 2006, Rasera et al., 2020; Sargeant et al., 2020; Guerrero-Gonzalez & Zabel, 2023).

Producing return-trip propellants on the Moon eliminates the need for return propellant mass and the additional outbound propellant mass used to carry return propellant, which reduces the launch cost substantially (Hepp et al., 1994; Rice & Gustafson, 2000; Schlüter & Cowley, 2020). It also means that more mass is available for cargo use for the outbound journey to the Moon. In 1994, NASA's Johnson Space Centre conducted a "LUNOX" study that investigated the possible benefits of producing oxygen on the Moon for early lunar exploration missions. "This study found an associated reduction in launch vehicle mass and a 50% reduction in the program cost" (Schreiner et al., 2015; Schreiner & Hoffman, 2015). Furthermore, other non-fuel ISRU resources obtained from the Moon itself will not need to be hauled up from the Earth, which ultimately will lead to more substantial cost savings (Sacksteder & Sanders, 2007; Crawford, 2015; Schreiner et al., 2015; Schreiner & Hoffman, 2015, Sargeant et al., 2020).

Reducing the mass budget by producing raw materials in-situ will have a cascading effect. It will allow mission designers more mass which can be allocated to the mission payload (Hepp et al., 1994). Various mission analyses have predicted a 40-60 % reduction if oxygen is produced on the Moon to operate with Earth-supplied hydrogen for all near-lunar and Earth return propulsive manoeuvres (Hepp et al., 1994).

"Lunar oxygen production could potentially double or triple the net lunar base mass (and capability) for a given Earth-to-LEO mass throughput." (Landis, 2005; Landis, 2007). It can also provide an inexpensive gas for several uses in lunar exploration. Lunar oxygen may even serve as a possible commercial product be exported to LEO for use in other space systems and to expand settlements to other locations (Landis, 2005; Landis, 2007).

It will be economically beneficial to manufacture electrical power sources from local resources for an expanded lunar facility. The only viable solar power material becomes silicon, as silicon is abundant on the Moon (Sen, Ray & Reddy, 2005). There have been many processes that have been proposed to produce oxygen on the Moon, with many of them producing silicon and other metals as a waste or by-products (Landis & Perino, 1989). Lunar-derived metals, aluminium, iron, silicon and titanium are a potential fuel source (Hepp et al., 1994). Furthermore, the necessary solar array electrically isolating and array structural materials such as aluminium, titanium, steel and glass can be refined from lunar regolith (Landis & Perino, 1989; Landis et al., 1990; Freundlich' et al., 2005; Sen, Ray & Reddy, 2005).

The Moon's surface is covered in regolith which also has, on average a 44% silicon oxide content, furthermore it has an ultra-high vacuum environment (on the order of 10 torr) (Schlüter & Cowley, 2020). This natural vacuum environment can aid in the manufacture of thin-film solar cells by direct evaporation (Freundlich' et al., 2005; Sen, Ray & Reddy, 2005; Meurisse & Carpenter, 2020). This was demonstrated by a preliminary study of the vacuum evaporation of silicon extracted from the lunar regolith using a conventional electron gun evaporation technique, conducted by Freundlich et al. (1998) (Freundlich' et al., 2005; Sen, Ray & Reddy, 2005). Their preliminary results showed that vacuum-fabricated solar cells are adequate for the fabrication of thin film solar cells, thereby showing the viability of the producing in-situ solar panels (Freundlich' et al., 2005; Sen, Ray & Reddy, 2005).

Landis and Perino (1989) predicted that the power requirements for a permanent lunar base to sustain a permanent human presence could be as much as 1 MW/year. If one assumes 17.5% efficient crystalline silicon panels (assuming 65-micron thickness, and 65% utilisation of the silicon refined) are used, one will require approximately 1000 kg/year of refined silicon to be produced (Landis & Perino, 1989). Hence, the Landis and Perino study concludes that it is indeed reasonable to expect that large-scale photovoltaic manufacturing will require regolith extraction facilities in addition to those that would be required to construct a lunar base (Landis & Perino, 1989).

Lunar-derived steel and fiberglass could be used to manufacture tanks for (non-cryogenic) storage (Freundlich' et al., 2005). Alternatively, flywheels could be manufactured from lunar-manufactured glass fibre, with specific energy of perhaps 20 W.hr/kg (SI J/kg) for power storage. This is somewhat lower than is possible with advanced composites on Earth (e.g. Kevlar™) but will require little non-local material usage. The lunar vacuum, low gravity, and plentiful availability of regolith for failure protection make flywheel energy storage a viable alternative for the long lunar of almost 15 Earth days duration experienced in the low and intermediate latitudes. (Landis et al., 1990; Freundlich' et al., 2005; Landis, 2005; Landis, 2007).

Many researchers around the world have discussed the feasibility of using lunar regolith as a building material to construct lunar bases. The primary technical means for the lunar soil's consolidation and hardening are sintering, lunar sulphur concrete, and lunar soil geopolymers (Zhou et al., 2021; Granier et al., 2025).

Successful experimental studies on microwave sintering of lunar soil that was brought back by Apollo-17, were conducted by (Taylor & Meek, 2005). The experiment produced effective sintered lunar soil (Taylor & Meek, 2005; Zhou et al., 2021). Song et al. (2019) experimentally investigated using vacuum sintering technology to process lunar simulant in a simulated lunar space environment to produce thermal insulation material (Song et al., 2019; Zhou et al., 2021). The results showed that, due to the complex composition of lunar soil, the sintered material is usually prone to warping and cracking, and requires more research to achieve the desired insulating properties (Zhou et al., 2021).

Lunar sulphur concrete and cement using lunar simulants was investigated by (Toutanji, Evans & Grugel, 2012; Davis, Montes & Eklund, 2017; Zhou et al., 2021; Schlüter & Cowley, 2020). These processes were proposed based on the premise that sulphur could be extracted from lunar pyrite (Zhou et al., 2021). The experiments have shown the apparent shortcomings of lunar soil sintering and sulphur concrete, more and more studies have begun to focus on lunar soil used to prepare geopolymers (Toutanji, Evans & Grugel, 2012; Davis, Montes & Eklund, 2017; Zhou et al., 2021).

Small quantities of some gaseous volatile materials absorbed onto the surface and implanted into grains of regolith can be released by heating the regolith. These materials are assumed to originate from the solar wind. These can be used to replenish life-support consumables (Landis et al., 1990; Landis, 2005; Landis, 2007), and can be used to pressurize the reactor vessels during the process start-up.

Studies of costs and benefits of ISRU approaches for exploration of the Moon and other celestial bodies, such as asteroids and Mars are plentiful, but little sustained support for the development of the technologies needed to realise their potential has been made available, either by governmental or commercial organisations (Schreiner et al., 2015; Schreiner & Hoffman, 2015).

It is imperative to accurately model the mass and performance of ISRU systems to determine their economic feasibility. Furthermore, ISRU system models can provide guidance for both the hardware development and mission applications of such systems (Schreiner et al., 2015; Schreiner & Hoffman, 2015).

1.4 State Of Work

The aim of this work was to derive a robust gas-solid reaction system that describes the regolith furnace which is the reduction of lunar regolith proposed by Landis and Perino (1989) and Landis (2005 The model can describe how a regolith particle, which consists of a mix of metal oxides, is reduced by fluorine gas to produce metal fluorides. The model incorporates the varying porosity of the particle, and the concentration profiles of the reactants in a multiple reaction system with diffusion limitations. The model also allows for a parameter sensitivity study to be conducted determine to determining the optimum operating regimes. The limitation to this study is there is no experimental data to corollate to the model. This work is structured as follows: Chapter 2 explores lunar in-situ resource utilisation in more detail and discusses the current state of affairs regarding in-situ production methods. Chapter 3 touches on the lunar ISRU properties that are critical parameters required to effectively model the reaction process. Chapter 4 covers the basics required to understand gas-solid reaction systems and contains the detailed derivation of the regolith fluorine reactor system (methodology). Chapter 5 presents the discussion of the baseline system results and explains how the model works and what the results mean. This is followed by a detailed parametric sensitivity study in Chapters 6. Chapter 7 present the conclusions drawn from the study and recommendations for future work.

2. Lunar In-Situ Resource Utilisation

The long-term ISRU goals of sustained habitation and industrialisation of the Moon will need oxygen and other raw materials to be produced from local lunar resources. Therefore, a reaction process that can produce highly-reduced by-products that can refined to useful materials further downstream is more beneficial than a process that produces just oxygen and a slag mixed oxide material (Landis et al., 1990; Landis, 2005).

When designing a complex processing plant on the lunar surface, the following needs to be considered (Hepp et al., 1994):

- No air or water to provide heat sinks for the process.
- Energy to power the process must be locally produced.
- Basic processing chemicals and utilities are absent.
- Processing plant needs to be largely autonomous.

A desirable regolith reduction process should have these characteristics (Landis, 2005, Landis, 2007):

1. It should work on the average lunar regolith composition, and therefor reduce the need for prior beneficiation of the raw materials.
2. It should reduce the majority of the mineral constituents of the regolith, thereby producing large amounts of oxygen.
3. It should mainly use local reagents and/or allow for reagent recycling to minimise the need to bring in replenishments from Earth. In other words, the reduction process must be carefully chosen to avoid irrecoverable losses of reactants.
4. It should occur at a reasonable temperature, to avoid the need for exotic materials for reaction vessels, and reduce the energy requirements of the process.
5. It should produce a reduced by-product, either in easily separable elemental form, or in a state that may be refined downstream for further use.
6. The reduction process must be specifically suited for the conditions of the lunar surface, such as, low gravity and high vacuum.

2.1 Oxygen Extraction Processes

In general, oxygen extraction requires oxidation of oxygen from an oxide (e.g., ilmenite) or from silicates (e.g., mare basalt) (Haskin, 1985; Mendell, 1985, Sargeant et al., 2020).

Most of the proposed lunar oxygen recovery processes involve solid/gas interactions, silicate melts, pyrolysis and aqueous solutions (Mendell, 1985; McKay et al., 1991; Taylor & Carrier, 1992; Hepp et al., 1994; Taylor & Martel, 2003; Schwandt et al., 2012; Schreiner et al., 2015; Schreiner & Hoffman, 2015). ISRU efforts have focused on producing oxygen for fuel, and were not geared towards recovering silicon or any other useful metalloids (Sanders, 2005; Sacksteder & Sanders, 2007; Sanders et al., 2007; Simon & Sacksteder, 2007; Meurisse & Carpenter, 2020; Rasera et al., 2020; Schlüter & Cowley, 2020; Guerrero-Gonzalez & Zabel, 2023; Šeško et al., 2024;).

In the past decade, three proposed methods have undergone dramatic technology maturation (Sacksteder & Sanders, 2007):

1) Hydrogen Reduction of Ilmenite (HRI)
2) Carbothermal reduction of silicates (CRS)
3) Molten Regolith Electrolysis (MRE)

Table 2-1 provides an overview of these three processes. In-depth reviews of the various processes can be found elsewhere (Haskin, 1985; Mendell, 1985; McKay et al., 1991; Taylor & Carrier, 1992; Allen, Morris & McKay, 1994; Hepp et al., 1994; Taylor & Martel, 2003; Sanders, 2005; Sanders et al., 2007; Simon & Sacksteder, 2007; Landis, 2011; Schwandt et al., 2012; Schreiner et al., 2015; Schreiner & Hoffman, 2015; Just et al., 2020, Bennett, Ellender and Dempster, 2020, Meurisse & Carpenter, 2020; Rasera et al., 2020; Sargeant et al., 2020; Guerrero-Gonzalez & Zabel, 2023; Šeško et al., 2024).

Table 2-1: Details of three proposed oxygen extraction processes.

Process	**Process Description**	**Advantages**	**Disadvantages**
Hydrogen Reduction of Ilmenite (HRI)	Hydrogen reduction extracts oxygen by reducing ilmenite, which is a constituent of lunar regolith. Hydrogen reduces ilmenite by only a single oxygen atom per molecule, with a by-product of FeTiO2 (Landis, 2011; Sargeant et al., 2020; Guerrero-Gonzalez & Zabel, 2023). The residue would be an intimate mixture of iron metal and unreduced iron oxide, titanium oxides and some silicate (depending on the purity of the ilmenite) (Landis, 2011; Schwandt et al., 2012; Sargeant et al., 2020; Guerrero-Gonzalez & Zabel, 2023).	• Produces water as a by-product (Landis, 2011). • Moderate temperatures (Landis, 2011).	• Low yield 1-2% of the total regolith mass depending on the iron abundance in the regolith feedstock (Sacksteder & Sanders, 2007). • Requires feedstock beneficiation (Landis, 2011). • Based on expected yields, it has the largest throughput of regolith feedstock (Landis, 2011). • 900-1100 °C (some authors reported temperatures as high as 1200°C (Sacksteder & Sanders, 2007).
Carbothermal reduction of silicates (CRS)	The carbothermal process extracts oxygen from lunar minerals and yields steel as a by-product. The process combines chemistry from steel-making and from coal synthesis gas reforming with electrolysis or	• Produces water as a by-product (Cutler & Krag, 1985; Landis, 2011). • Carbon is a more efficient reduction agent on a per mass basis than hydrogen in the competing ilmenite reduction process. (Cutler & Krag, 1985; Landis, 2011).	• Low yield (Cutler & Krag, 1985; Landis, 2011). • Requires feedstock beneficiation (Cutler & Krag, 1985; Landis, 2011). • A viable plant design awaits further research (Cutler & Krag, 1985).

	thermolysis of water (Cutler & Krag, 1985; Landis, 2011).	• Moderate yield of 15% may be achieved by reducing additional metallic oxides but requires and reagent recycling to reform a hydrocarbon gas and water. separation (Sacksteder & Sanders, 2007).	• High temperatures of 1625 °C for methane reduction of olivine and pyroxene, up to 1800 °C or above for anorthite, and only partially reduces oxides (Landis, 2011).
Molten Regolith Electrolysis (MRE)	MRE is an electrochemical processing technique that performs direct electrolysis on molten lunar regolith to produce gaseous oxygen at the anode and liquid metals at the cathode (Sacksteder & Sanders, 2007; Sirk, Sadoway & Sibille, 2010; Schreiner, 2015; Schreiner et al., 2015; Schreiner & Hoffman, 2015; Guerrero-Gonzalez & Zabel, 2023).	• MRE may result in considerable mass savings compared to HRI and CRS as it can theoretically extract all the oxygen from the lunar regolith. • It does not require any recycling of reagents or a water electrolyser, which may also reduce system mass. • Allows co-production of materials such as iron, silicon, aluminium and glassy materials which can be used to construct spare parts, buildings and solar arrays on the lunar surface. • Potentially can liberate all the available oxygen in the regolith feedstock.	• MRE requires more power due to high operating temperatures compared to HRI and CRS (Sacksteder & Sanders, 2007; Schreiner, 2015; Schreiner et al., 2015; Schreiner & Hoffman, 2015). • It is at a lower technology development level than the other techniques (Sacksteder & Sanders, 2007; Schreiner, 2015; Schreiner et al., 2015; Schreiner & Hoffman, 2015). • Molten regolith is extremely corrosive and cannot be contained for an extended period by traditional crucible materials. This complicates the reactor design and requires a lot of maintenance (Sacksteder & Sanders, 2007; Schreiner, 2015; Schreiner et al., 2015; Schreiner & Hoffman, 2015). • Very high operating temperatures approaching 2700°C. This poses a materials problem.

			• The higher the operating temperature, the more oxygen per kilogram of regolith is extracted. This leads to an increased heat loss and higher regolith heating power requirement per kilogram of regolith. (Sacksteder & Sanders, 2007; Schreiner, 2015; Schreiner et al., 2015; Schreiner & Hoffman, 2015). • Degradation of the electrolysis electrodes (Sacksteder & Sanders, 2007).

2.2 Fluorination reduction of Lunar Regolith

Fluorine reduction of regolith (fluorination) has been proposed as a method for oxygen extraction (Stancati et al., 1991; Taylor & Carrier, 1992; Sebolt et al., 1993; Landis, 2005; Turan et al., 2020; Meurisse & Carpenter, 2020; Schlüter & Cowley, 2020).

Fluorination is favoured due to its potential to produce silicon and other reduced metals, in addition to oxygen. These co-products can be used in the production of solar panels and other vital lunar base materials, as mentioned in Section 1.3 (Landis & Perino, 1989). This would be a useful technology to develop to meet the long-term ISRU goals. The advantages and disadvantages of this technology are discussed in Section 2.2.1.

The fluorination processing sequence was proposed by Landis & Perino (1989), and further developed by Landis (2005). Figure 2-1 is a redrawn process flow diagram of the proposed fluorination process of Landis and Perino (1989).

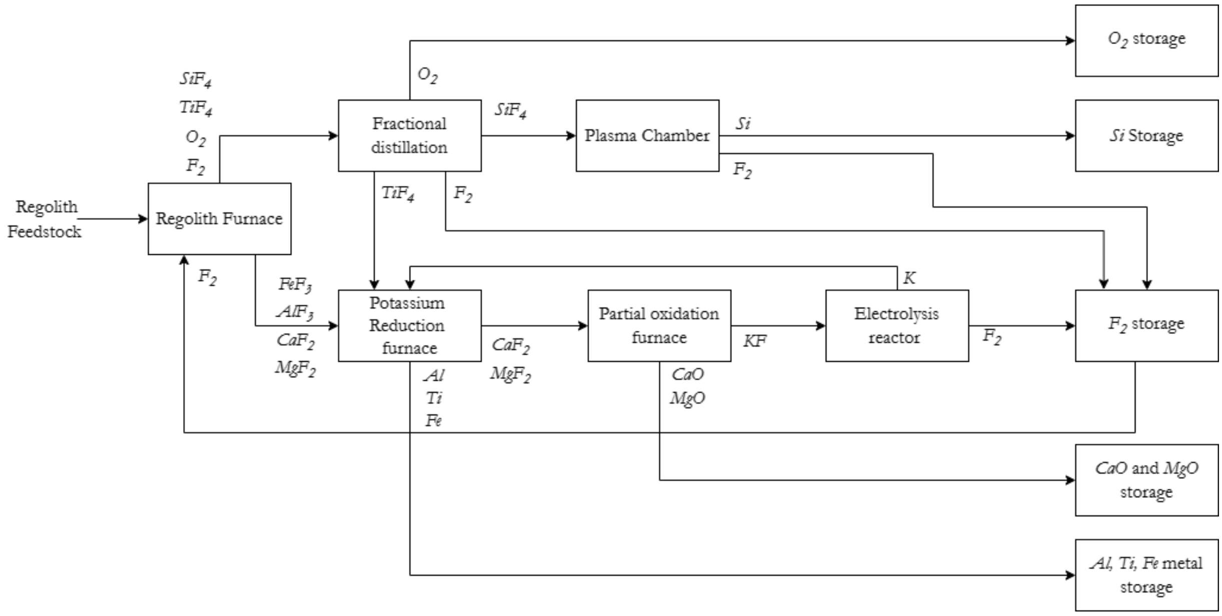

Figure 2-1: Regolith fluorination process flow diagram. (Adapted and redrawn from Landis (2005).

The fluorination process encompasses a reaction between fluorine and regolith particles, to produce and refine high value metals, oxygen and some heavy metal oxides. The process starts in the "Regolith Furnace" (a reactor). Fluorine (F_2) is fed into the regolith furnace where it reacts with the regolith and displaces the oxygen (O_2) to form various solid metal fluoride salts $(FeF_3, AlF_3, CaF_2, MgF_2)$ while producing silicon tetrafluoride (SiF_4), titanium tetrafluoride (TiF_4) and oxygen gases (Landis & Perino, 1989; Landis et al., 1990; Landis, 2005; Turan et al., 2020).

The gaseous products can be purified by fractional distillation and the silicon tetrafluoride can undergo plasma reduction to produce semiconductor grade silicon. The remaining metal fluoride salts are reduced to metals and potassium fluoride (KF) via potassium reduction, in the "potassium reduction furnace" and "partial oxidation furnace". The details for these reactors can be found in Landis & Perino (1989); Landis et al. (1990); Landis (2005). The potassium fluoride is then electrolyzed to produce the required elemental fluorine and potassium for the processing reactor units, closing the recycle loop (Landis & Perino, 1989; Landis et al., 1990; Landis, 2005).

The fluorine can be brought to the Moon in the form of potassium fluoride and is liberated from the salt by electrolysis in a eutectic salt melt (Landis & Perino, 1989; Landis et al., 1990; Landis, 2005; Turan et al., 2020).

Fluorination reduction "proof of concept" demonstrations have been carried out. The solar dynamic ground-test demonstration, based on a power system originally designed for the Space Station Freedom, demonstrated the technology for melting fluoride eutectic under simulated space conditions (Shaltens & Boyle, 1995; Landis, 2005).

Turan et al. (2020) have further developed the Landis (2005) fluorination process by investigating the energy requirements of the entire process. Details of this can be found in the paper by Turan et al., (2020). They have shown the feasibility of the process as a long-term materials processing plant and detail the energy requirements for this process.

This work focuses on developing a model of the fluorination process proposed by Landis and Perino (1989). The model derivation is discussed in more detail, in Section 0. Details on the other processing reactor units can be found in (Landis & Perino, 1989; Landis et al., 1990; Landis, 2005; Turan et al., 2020).

2.2.1 Advantages and disadvantages of the fluorination process

The advantages of the fluorination of regolith process may be summarized as follows:

1) This process is insensitive to the composition of the regolith feedstock/raw material.
2) Does not require extensive feedstock beneficiation processing to produce the raw material, ultimately leading to an easier and better production process that will operate at any site.
3) Produces many reduced materials in a relatively refined form.
4) Fluorine is a very strong reducing agent therefore it has a higher yield than HRI and CRS.
5) It has moderate operating conditions of 500°C and 1 atm, which will be easy to achieve and maintain in the lunar environment.
6) It can be easily adapted to process Martian regolith.

The disadvantages of the fluorination of regolith process have been discussed in several papers (Landis & Perino, 1989; Landis et al., 1990; Landis, 2005; Landis, 2007; Landis, 2014) and can be summarized as follows:

1) It will require recycling of the reagents (*KF*), which is a complicated process.
2) It is not suited for the short-term ISRU goals.

3) Fluorine gas is corrosive, and this poses a reactor materials problem. However, fluorine is used industrially on Earth, and it is not very dangerous at relatively low pressures. It can be easily utilised with just a few precautions. As examples: nickel and Monel crucibles, using copper gaskets, are compatible with fluorine gas and Teflon is appropriate for gaskets and tubing at lower temperatures.

2.2.2 Details of the "Regolith Furnace"

The present work focuses on developing a general gas-solid model that can be used to represent and analyse the fluorination process. This section delves into the proposed reaction system, which forms the basis of the model development.

The basic reduction process is to heat the regolith in the presence of fluorine. Fluorine displaces the oxygen, which is collected as a co-product. Silicon and titanium produce gaseous fluorides. The remaining metals are produced in the form of metal fluoride salts, which must be further purified and reduced to the metals (Landis & Perino, 1989; Landis, 2005, Landis, 2007; Turan et al., 2020). The primary reactions in the regolith particle are:

$$SiO_2(s) + F_2(g) \rightarrow SiF_4(g) + O_2(g) \quad \text{...(Eq 2-1)}$$

$$TiO_2(s) + F_2(g) \rightarrow TiF_4(g) + O_2(g) \quad \text{...(Eq 2-2)}$$

$$FeO\ (s) + \frac{3}{2}F_2(g) \rightarrow FeF_3(s) + \frac{1}{2}O_2(g) \quad \text{...(Eq 2-3)}$$

$$MgO\ (s) + F_2(g) \rightarrow MgF_2(s) + \frac{1}{2}O_2(g) \quad \text{...(Eq 2-4)}$$

$$CaO\ (s) + F_2(g) \rightarrow CaF_2(s) + \frac{1}{2}O_2(g) \quad \text{...(Eq 2-5)}$$

$$Al_2O_3(s) + 3F_2(g) \rightarrow 2AlF_3(s) + \frac{3}{2}O_2(g) \quad \text{...(Eq 2-6)}$$

The reactor operating conditions are considered moderate, and will require a temperature of 500°C and 1 atm (Landis & Perino, 1989; Landis, 2005; Landis, 2007). The initial regolith heating step will also outgas volatiles, primarily materials implanted from the solar wind, out of the regolith. These will include hydrogen, oxygen, carbon monoxide, nitrogen, fluorine, sulphur, helium, and trace amounts of other volatiles. These can be captured after the heating but before the fluorine reaction is initiated by the use of a condenser, or a series of condensers. The evolved fluorine (which will be released as hydrogen fluoride (HF) may be useful for replacement of process losses (Landis, 2005). These volatiles can also be used to create and maintain the pressure in the reactor vessel during the start-up process of the plant.

The regolith furnace design was not discussed or developed prior to the work done by Pavlou et al. (2017) and Turan et al. (2020). Pavlou et al. (2017) investigated the conversion of the silicon. They assumed just the silicon dioxide reaction and investigated the ideal batch reactor and Continuous Stirred Tank Reactor (CSTR) cases. Turan et al. (2020) investigated a Fixed Conversion Reactor (FCR) type for the "regolith furnace" to determine the overall process energy requirements, assuming just the silicon dioxide reaction is occurring. A batch reactor, CSTR and FCR are different reactor types with fixed flow configurations and design equations. More on these reactor types can be found elsewhere (Levenspiel, 1999; Davis & Davis, 2003; Fogler, 2004)

The focus of this work is to build on the previous work done by Pavlou and Pavlou (2017) and develop a more complex and realistic model of the regolith furnace. This will be done by extending the system to incorporate the six oxide reactions present in the particle, and the porosity of the particle as the reaction proceeds in a semi-batch Fluidized Bed Reactor (FBR). The detailed derivation is discussed in Section 4.2.

3. Lunar ISRU resources

The surface of the Moon is characterised by highlands and maria, which are the visible dark and light areas (Freedman, 2008). The darker areas are the lunar maria and the lighter areas are called lunar highlands (also called terrae) (Freeman, 2008). The highlands and maria have soils with different chemical compositions, physical appearance, and age (Papike, Simon & Laul, 1982; Mckay et al., 1991 and Jones, n.d.). Figure 3-1 is a picture showing the maria and highland regions on the near and far side of the Moon (Hanmer, n.d.).

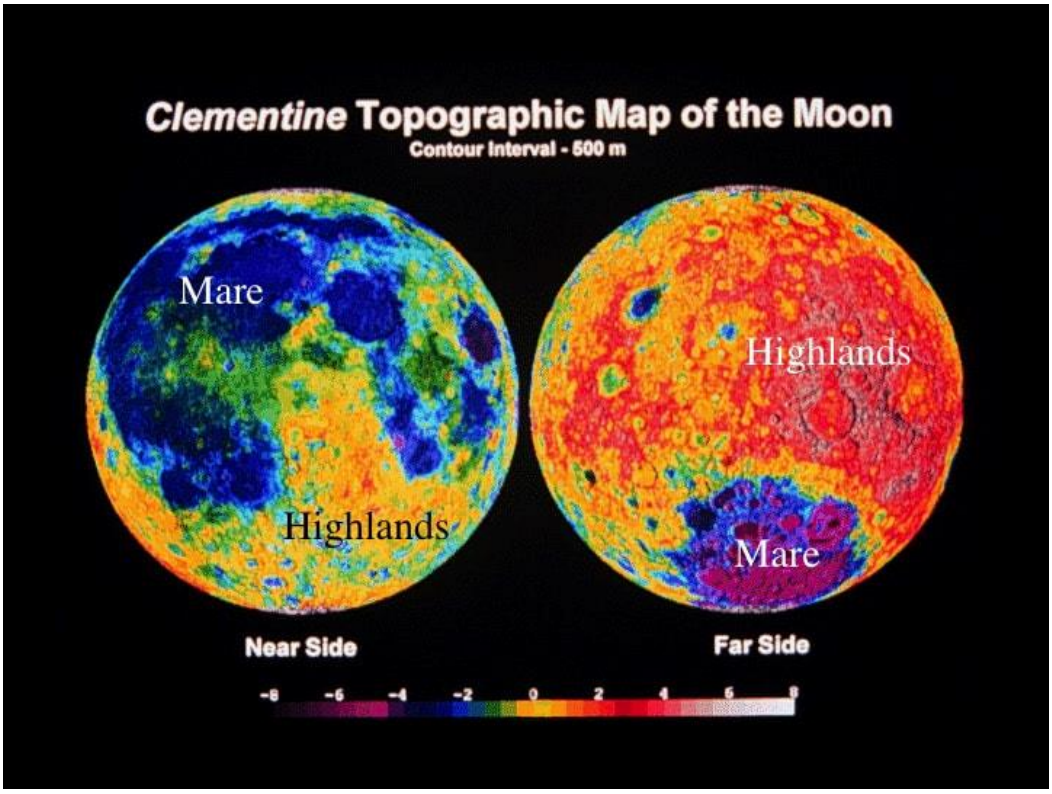

Figure 3-1: A picture showing the maria and highland regions on the near and far side of the Moon (Hanmer, n.d.).

A wealth of information on lunar soils was obtained during the era of intensive American and Soviet lunar exploration by the Ranger, Lunar Orbiter, Surveyor and Apollo (U.S.) and Luna and Zond (U.S.S.R.) missions (1959 – 1976), Chang'e missions (China) and Chandrayaan missions (India) (Hepp et al., 1994; Crawford, 2004; Crawford, 2015; Anand et al., 2012; Crawford et al., 2012; Schwandt et al., 2012a; Jia et al., 2021; Lim & Anand, 2019). Figure 3-2 shows all the lunar landing locations, from the first Soviet Luna mission in 1959, to China's Chang'e-5, which returned regolith samples in 2020 (The Planetary Society [TPS], 2018). This image does not show India's Chandrayaan-3 which successfully landed on the far side of the Moon near the South Pole in 2023 (Deiss, 2023) and privately owned Intuitive Machines lunar lander, Odysseus, which successfully landed near crater Malapert A in the South Pole in February 2024 (Garner, 2024).

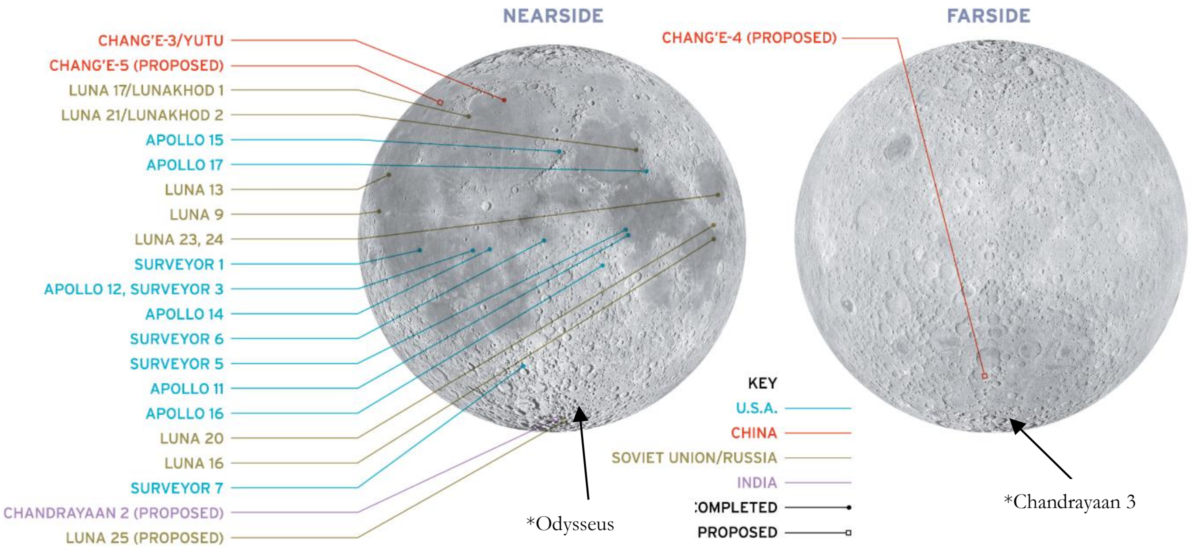

Figure 3-2: A picture of all the lunar landing locations from the first Luna landing in 1959 to China's Chang'e-5 which returned regolith samples in 2020 (TPS, 2018). *Figure adapted from TPS (2018) to show approximate lunar landing locations as of March 2024.

Lunar soil samples were returned by the Apollo, Luna and Chang'e-5 missions. Figure 3-3 is a picture of where the Apollo and Luna regolith sample return missions landed (Cunningham, 2020).

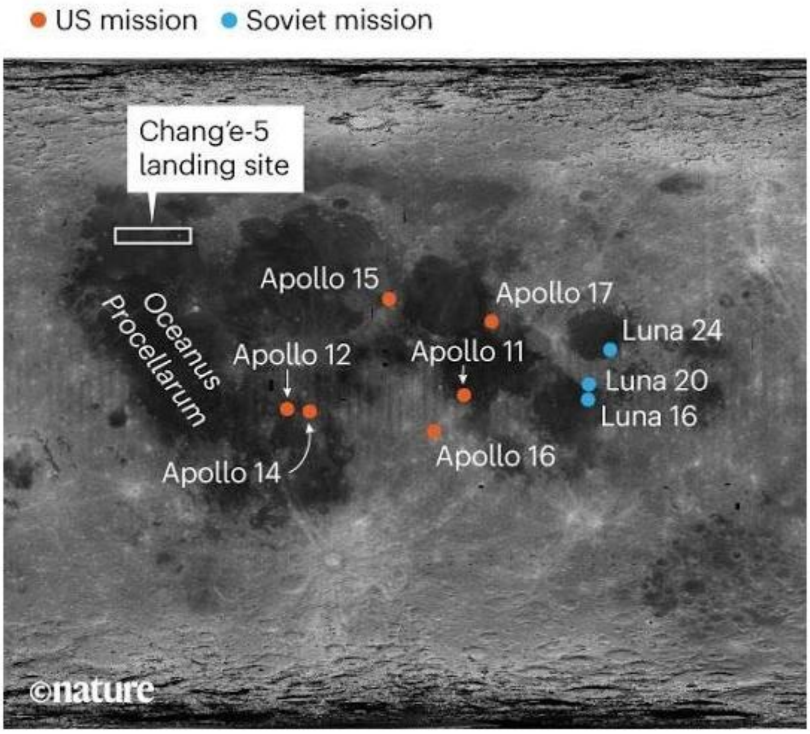

Figure 3-3: A picture of the where the Appollo and Luna regolith sample return missions landed (Cunningham, 2020).

In-situ lunar resources can be broken into four broad categories (Hepp et al., 1994):

1) Mare basaltic volcanic rocks (composed primarily of volcanic ash and lava).
2) Pristine highland rocks (original lunar composition unaffected by impact mixing).

3) Complex breccias and impact melts (with mixed original lunar and meteoritic composition).

4) Lunar regolith composed of unconsolidated debris.

When permanent lunar settlements are established, the likely raw material or feedstock that will be used for lunar base construction, mining, road building, and resource extraction will be lunar regolith (Mendell, 1985; Meurisse & Carpenter, 2020). It could be used directly as an industrial feedstock in a single processing plant (McKay et al., 1991). Regolith has a surficial, unconsolidated, and fine-grained nature. It requires minimal mechanical pre-processing, having been disintegrated by mechanical weathering. It is a source of iron, aluminium and silicon metals (Papike, Simon & Laul, 1982; Hepp et al., 1994). Figure 3-4 (left) shows a picture of Apollo 11 astronaut Edwin "Buzz" Aldrin's boot (for scale) on the upper surface of lunar regolith (Crawford, 2015). This image originally was released by NASA (NASA image AS11-40-5880), but it was taken from of Crawford (2015). (Right) Astronaut and geologist Harrison Schmitt is seen in the Lunar Roving Vehicle during NAS"s Apollo 17 mission (Wamsley, 2022).

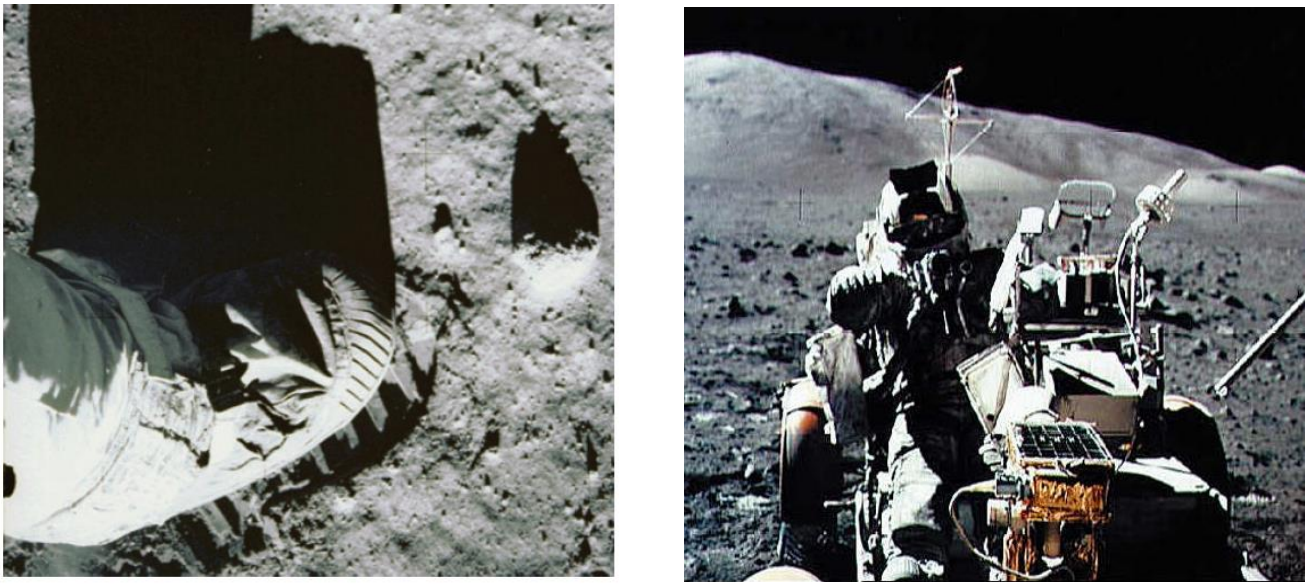

Figure 3-4: (Left) Picture of Apollo 11 astronaut Edwin "Buzz" Aldrin's boot (for scale) on the upper surface of lunar regolith (Crawford, 2015). (Right) Astronaut and geologist Harrison Schmitt is seen in the Lunar Roving Vehicle during NASA's Apollo 17 mission (Wamsley, 2022).

Researchers around the world have conducted extensive studies on particle size distribution, chemical composition, mineral composition, and microscopic morphology of the lunar regolith samples retrieved by these missions (Mitchell et al., 1972; Heiken, Vaniman & French, 1991; Mckay et al., 1991; Zhou et al., 2021, Jia et al., 2021). These studies form the basis from which ISRU processing assumptions are derived.

Figure 3-5 is a picture taken by China's Chang'e-5 lander, which landed on the nearside of the Moon on December 1, 2020 (Amos, 2020). The photo was originally provided by the China National Space Administration (CNSA) by taken from Amos (2020).

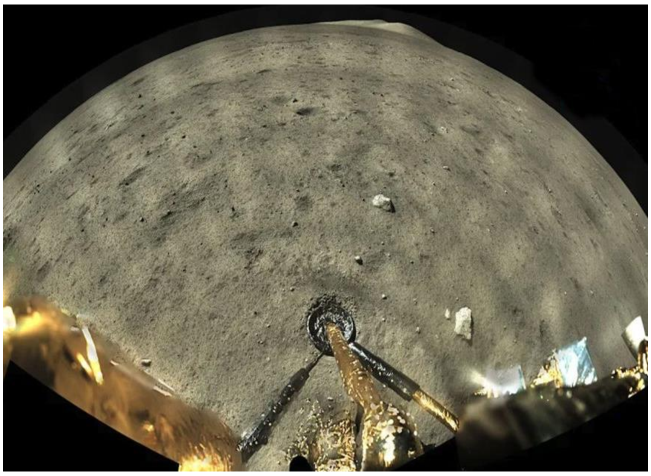

Figure 3-5: Picture of the lunar surface taken by China's Chang'e-5, which landed on the nearside of the Moon (Amos, 2020).

Composition, porosity, pore diameter and particle size are the most important regolith characteristics that will impact the reactor design and operations. These will be discussed further. In-depth studies on other properties and characteristics can be found elsewhere (Mitchell et al., 1972; Papike, Simon & Laul, 1982; Heiken, Vaniman & French, 1991).

3.1 Lunar Regolith Composition

The lunar regolith is a layer several meters thick of unconsolidated debris that covers the underlaying bedrock and forms the interface between the Moon and its space environment. The thickness varies between the mare regions (about 4-5 m thick) and the older highland regions (about 10-15 m thick). The regolith composition may vary widely between locations only a few meters apart (Papike, Simon & Laul, 1982; Heiken, Vaniman & French, 1991; Crawford, 2004; Crawford, 2015; Satish, Radziszewski & Ouellet, 2011; Crawford et al., 2012, Lim & Anand, 2019; Schlüter & Cowley, 2020; Granier et al; 2025).

Figure 3-6 shows the Chang'e-5 probe gathering regolith samples on the Moon (Huaxia, 2022). The photo was originally provided by the CNSA but this image taken from Huaxia (2022).

Figure 3-6: Picture of the Chang'e-5 probe gathering regolith samples on the Moon (Huaxia, 2022).

The major constituents of regolith are aluminium, silicon, iron, titanium, magnesium, calcium and oxygen, which are tightly bound in its oxide form (Papike, Simon & Laul, 1982; Heiken, Vaniman & French, 1991; McKay et al., 1991; Sirk, Sadoway & Sibille, 2010; Crawford, 2015; Zhou et al., 2021).

Figure 3-7 is a map of the variation in chemical composition of lunar regolith by oxide type for three different regions: High-Titanium Mare (yellow), Low-Titanium Mare (cyan), and Highlands (red). The composition data for this map, shown in the figure below, was originally taken from Apollo and Luna missions (Stoeser, Rickman & Wilson, n.d.) and imagery data from Clementine UVVIS instrument (Lucey, Blewett & Jolliff, 2000). This image was taken from Schreiner (2015).

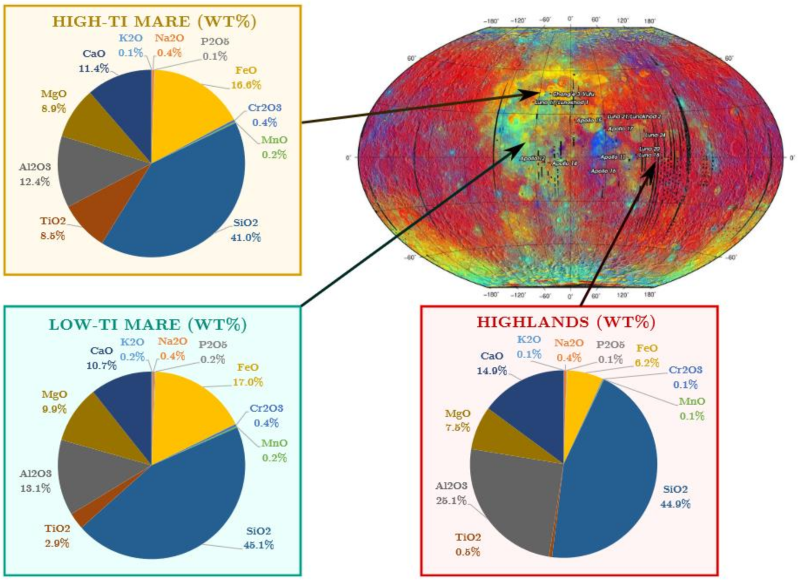

Figure 3-7: The composition of lunar regolith by oxide type for three different regions: High-titanium mare (yellow), low-titanium mare (cyan), and almost titanium-free Highlands (red). The composition data for this map was originally taken from Apollo and Luna missions and imagery data from Clementine UVVIS instrument. Image taken from (Schreiner, 2015).

Nearly all terrestrial commercial metal-extraction plants are designed to process a single feedstock containing a small number of elements and to extract a single metal or, at most, two or three metals (McKay et al., 1991; Allen, Morris & McKay, 1994; Hepp et al., 1994; Landis, 2014). The feedstock is usually concentrated by beneficiation processes before it enters the extraction plant metals (McKay et al., 1991; Allen, Morris & McKay, 1994; Landis, 2014). Mining and beneficiation techniques on the Moon will be different to terrestrial mining due to the lack of freely available water for cooling and lubrication, movement and separation of materials, and solution and precipitation of metals (Heiken, Vaniman & French, 1991; McKay et al., 1991; Hepp et al., 1994; Sadeh & Criswell, 1996; Freundlich' et al., 2005). Economically, it is desirable to have a process that is feedstock-independent to reduce or eliminate this beneficiation stage and to simplify the process (Heiken, Vaniman & French, 1991; McKay et al., 1991; Hepp et al., 1994; Sadeh & Criswell, 1996; Freundlich' et al., 2005; Landis, 2014; Zhou et al., 2021).

Figure 3-8 shows two pictures of a previously unopened regolith sample that was returned on the Apollo 17 mission. (Left) Opening of previously sealed sample that was returned on Apollo 17. (Right) A close-up of Apollo 17 lunar core sample 73001 being taken out of its drive tube in 2019 for the first time since this sample was collected on the surface of the Moon in 1972 at NASA's Johnson Space Centre in Houston (National Aeronautics and Space Administration [NASA], 2022).

Figure 3-8: (Left) Opening in 2019 of a previously sealed sample that was returned on Apollo 17 in 1972. (Right) A close-up of Apollo 17 lunar core sample 73001 (NASA, 2022).

Sen, Ray & Reddy (2005) provide a comparison table on the average lunar regolith composition of the Maria and Highland terrains. Table 3-1, adapted from (Sen, Ray & Reddy, 2005), shows the mean composition of major constituents in lunar regolith between the maria and highlands on the Moon.

Table 3-1: Mean composition of major constituents in lunar regolith and the average composition (adapted from (Sen et al., 2005)).

Constituents	Maria		Highlands		Average regolith Composition
	Apollo 14	Luna 16	Luna 20	Apollo 16	
SiO_2	47,93	41,70	45,40	44,94	44,99
TiO_2	1,74	3,38	0,47	0,58	1,54
FeO	10,37	16,64	7,37	5,49	9,97
MgO	9,24	8,87	9,19	5,96	8,32
CaO	11,19	12,50	13,38	15,57	13,16
Al_2O_3	17,60	15,33	23,44	24,71	20,27

Table 3-1 further illustrates the diversity in composition between different locations (Sen at al., 2005), and highlights the need for a process that is feedstock independent (Papike, Simon & Laul, 1982; Heiken, Vaniman & French, 1991; McKay et al., 1991; Hepp et al., 1994; Sadeh & Criswell, 1996; Freundlich' et al., 2005; Landis, 2014, Lim & Anand, 2019; Granier et al., 2025).

The average regolith composition weight percent in Table 3-1 is used in the computational model presented in this dissertation.

3.2 Lunar Regolith Particle Size

Regolith has the distinct advantage of being pulverized and fine grained, which reduces the need for pre-grinding. The fineness of the feedstock has a great influence on the reaction rate (Zhou et al., 2021). From an economic point of view, this implies that lunar soil is very easy to mine by simple surface mining techniques and will not need to be pulverised or pre-processed as a feedstock (Papike, Simon & Laul, 1982; Mendell, 1985; Landis & Perino, 1989; Heiken, Vaniman & French, 1991; McKay et al., 1991; Allen, Morris & McKay, 1994; Hepp et al., 1994; Landis, 2005; Landis, 2007; Landis, 2014).

Figure 3-9 is a picture showing the fine and unconsolidated nature of regolith particles taken under a microscope (European Space Agency [ESA], 2022).

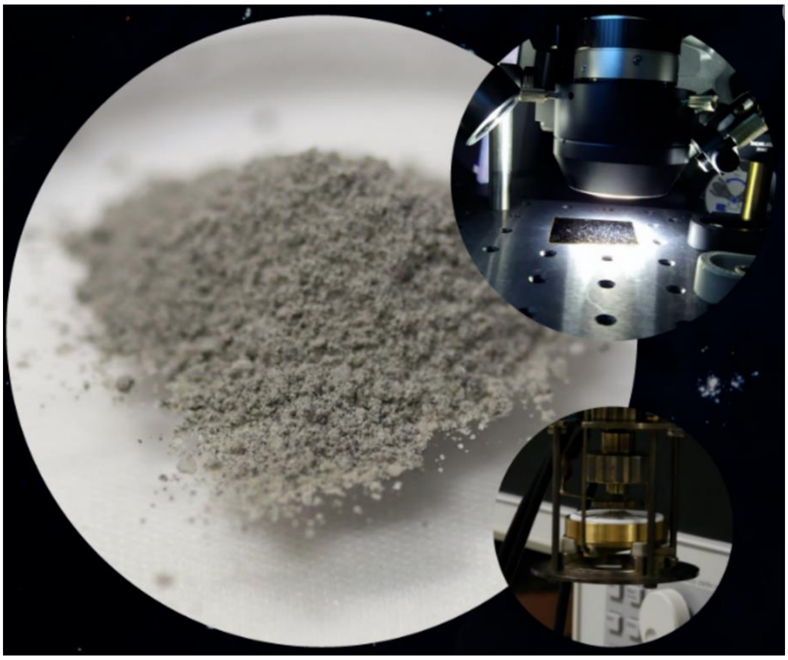

Figure 3-9: Picture showing the unconsolidated and fine nature of lunar regolith (ESA, 2022).

Many investigations of the measured particle size distribution of nearly 350 regolith samples taken in the vicinity of the seven landing sites on the Moon (Apollo 11, 12, 14, 15, 16, and 17, and Luna 24) have been conducted (Carrier, 2003; Zhou et al., 2021). See Figure 3-3 for a map of the landing sites where these samples were collected.

Sieving is the main method of determining the particle size distribution of regolith. It is effective for particle sizes greater than 10 μm. For particles that are smaller than 10 μm, scanning electron microscope (SEM) analysis or Coulter counter methods are usually applied (Papike, Simon & Laul, 1982; Mendell, 1985; Heiken, Vaniman & French, 1991; McKay et al., 1991; Taylor & Carrier, 1992; Allen, Morris & McKay, 1994; Carrier, 2003; Zhou et al., 2021).

There is variation in the reported particle sizes of lunar regolith. The median particle size is reported as 40 μm to 130 μm, with an average of 70 μm. Practically this means that approximately half of the soil (by weight) is finer than the human eye can resolve. Others have reported sizes of up to 166 μm (Papike, Simon & Laul, 1982; McKay et al., 1991, Kiely, Greenberg & Kiely, 2011).

For this study, the average particle size was calculated from the study originally conducted by (Carrier, 2003) and repeated by (Zhou et al., 2021), who compared it to regolith simulants. Figure 3-10 shows the cumulative particle sizes, which are much smaller than the median particle diameter of real lunar soil (41.5–166 μm).

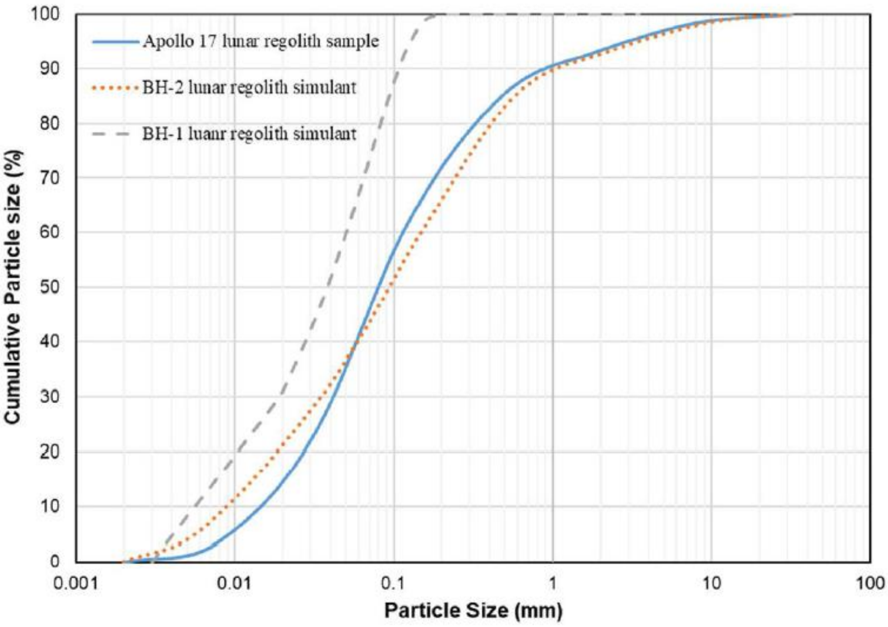

Figure 3-10: Particle size distribution curves of an Apollo 17 regolith sample and two lunar regolith simulants, BH-1 and BH-2. The curve of the Apollo 17 lunar regolith sample was taken from (Carrier, 2003). This figure was taken from (Zhou et al, 2021).

An average particle size of 70 μm was chosen for this computational model (Kiely, Greenberg & Kiely, 2011, Zhou et al, 2021).

3.3 Lunar Regolith Porosity and pore diameter

Porosity and pore diameter of the lunar regolith are critical parameters, as they have a large impact on the reaction and diffusion rates and models that are applicable to the process.

Lunar regolith porosity may be divided into three categories (Heiken, Vaniman & French, 1991; McKay et al., 1991). This is graphically depicted in Figure 3-12:

(1) Intergranular porosity which is the volume of space between individual particles.
(2) Intragranular porosity which is the volume of re-entrant surfaces on the exterior of the particles.
(3) Subgranular porosity which is the volume of enclosed voids within the interior of particles.

Figure 3-11 illustrates SEM images of the regolith returned by Apollo 12 and Apollo 16 missions, from the maria and highland regions (Robens et al., 2008).

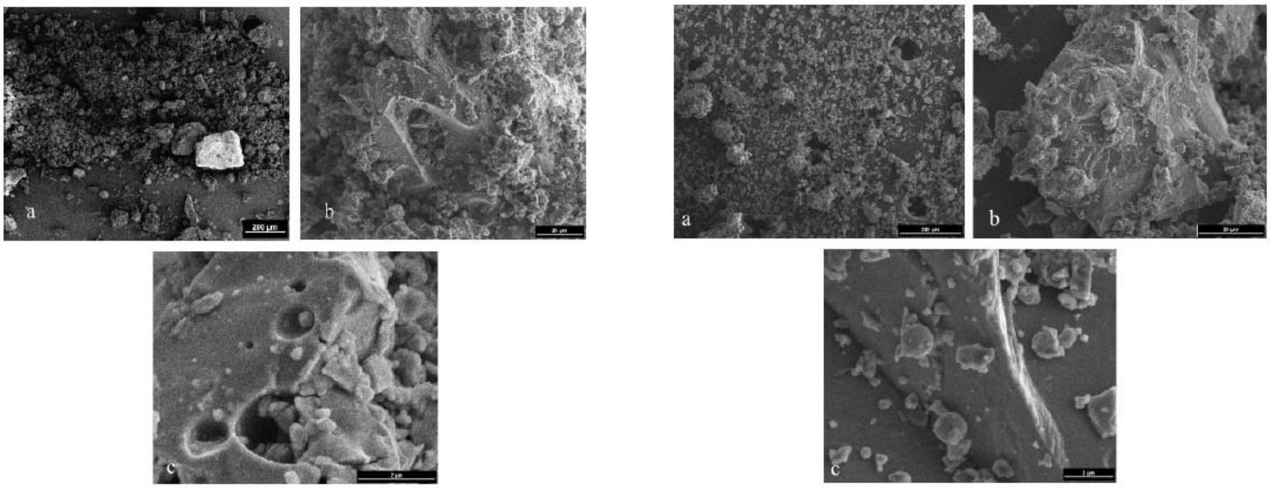

Figure 3-11: Electron micrographs at increasing magnification of lunar regolith sample taken from the inside of the mare basalt region and returned with Apollo 12 (left) and the highland regions, returned with Apollo 16 (right) (Robens et al., 2007).

The intragranular porosity has effects only the bulk density of the lunar soil. The intergranular porosity affects both the bulk density and the relative density. When the soil particles are immersed in a fluid only the intergranular and intragranular space is filled, not the subgranular space. Therefore the actual subgranular porosity of individual lunar soil particles is not well documented in the literature, and additional measurements of subgranular porosity are needed (Heiken, Vaniman & French, 1991; Allen, Morris & McKay, 1994; Pavlou et al., 2017).

Figure 3-12 is a schematic that illustrates the porosity categories found in lunar regolith (Centre for Lunar Science and Exploration [CLSE], n.d.).

Regolith porosity, specific gravity and density estimates that have been made since early in the lunar exploration program (and found in literature) are very varied and are highly dependent on the depth at which the regolith was collected, as well as the shape of the drill bit used in the Apollo 11 drive tube (Mitchell et al., 1972).

The porosity and pore size distribution on lunar regolith simulants was evaluated by Mercury Intrusion Porosimetry (MIP) (Zhou et al, 2021). This technique uses controlled pressure to force mercury into a porous structure. This produces pressure versus intrusion data, which is further analysed to generate volume and size distributions on the internal structure and pore size. The results are shown in Table 3-2 (Zhou et al, 2021).

Table 3-3 is a summary table provided by Mitchell et al. (1972). It summarizes the best estimates of the in-situ average porosity and void ratio in lunar regolith, as it varies with depth below the surface.

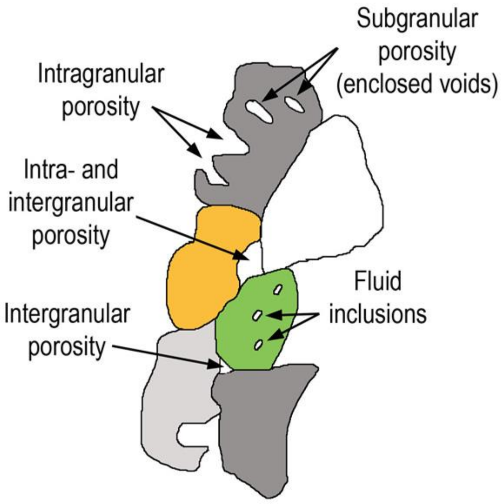

Figure 3-12: Schematic diagram showing the different types of soil porosity produced in the lunar soil by soil particles (CLSE, n.d.).

Table 3-2: Mercury Intrusion Porosimetry (MIP) analysis of selected BH-2 and ground BH-2 geopolymer at the age of 72 hours (Adapted from (Zhou et al., 2021).

Sample	Average pore diameter (nm)	Bulk density (g/ml)	Porosity %
B_v	523.05	1.68	31.45
B_BH-1_v	46.24	1.83	20.76

Table 3-3: Best estimates of lunar soil in situ porosity (inter- and intragranular porosity combined) (adapted from Mitchell et al, 1972).

Depth range (cm)	Average Porosity, n (%)	Average void ratio, e
0-15	52 ± 2	1.07 ± 0.07
0-30	49 ± 2	0.96 ± 0.07
30-60	44 ± 2	0.78 ± 007
0-60	46 ± 2	0.87 ± 0.07

Mitchell et al. (1972) have recommended the following best estimates shown in Table 3-4. These estimates are used in this study. These estimates consider "all the measurements, approximations, analyses, qualifications, and uncertainties described in the preceding sections" (Mitchell et al, 1972, Lim & Anand, 2019).

Table 3-4: The average characteristic values that are used in the mathematical model (Mitchell et al, 1972).

Characteristic	**Value**
Porosity	36.5 %
Void ratio	0.58
Density	2 g/cm^3 or slightly less (for a specific gravity of 3.1) An average density of 1.8 g/cm3 will be used in this study

4. Regolith Furnace Derivation

The reactions that occur within the regolith furnace are classified as non-catalytic gas-solid reactions. These happen between a gas and porous or non-porous solid particle (Levenspiel, 1999; Afshar Ebrahimi, Ale Ebrahim & Jamshidi, 2008; Favergeon et al., 2013). Several conceptual models exist which describe how gas-solid reactions occur. One such model, the Shrinking Core Model (SCM), will be discussed in Section 4.1, as it forms the basis upon which the regolith furnace reaction system is derived. In this work, SCM will be expanded to represent more general gas-solid reactions.

4.1 Shrinking Core Model

The Shrinking Core Model (SCM) is an idealised conceptual model of a simplified gas-solid reaction for non-porous particles. It describes how the gas-solid reaction proceeds for a single chemical reaction, as the solid particle is being consumed for a specific particle size (Levenspiel, 1999; Davis & Davis, 2003; Fogler, 2004; Fedunik-Hofman, Bayon & Donne, 2019; Schlüter & Cowley, 2020). As the particle is consumed, it shrinks and leaves behind a completely converted gas material and inert solid shell, referred to as the "ash" layer. Thus, at any time there exists an unreacted core of material which shrinks in size as the reaction proceeds, and creates an inert ash layer that surrounds the unreacted core (Levenspiel, 1999; Fedunik-Hofman, Bayon & Donne, 2019). Figure 4-1 depicts how the reaction proceeds. For the regolith furnace model, the changing porosity in the regolith particles, as the reaction proceeds, is accounted for. This is an important expansion on the standard SCM.

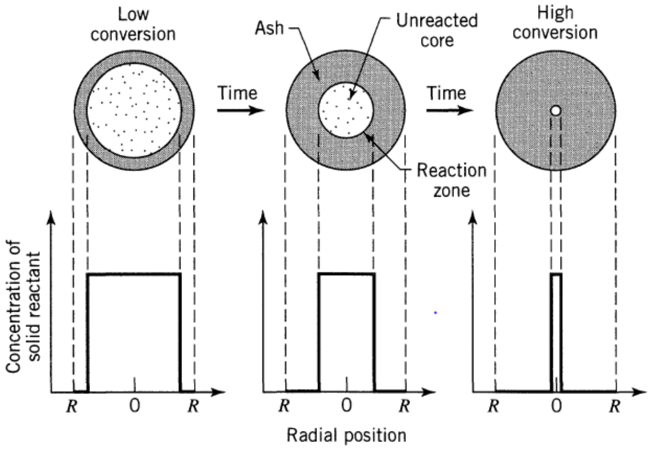

Figure 4-1: Graphical illustration of how the reaction proceeds according to the shrinking core model. The reaction proceeds with a narrow front which moves into the solid particle. The reactant is completely converted as the front passes by. (Taken from Levenspiel, 1999).

The SCM mechanism (five successive steps) for a single reaction is graphically depicted in Figure 4-2.

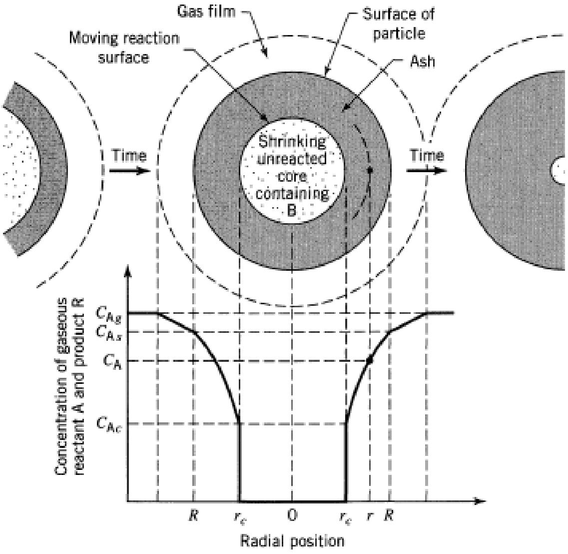

Figure 4-2: Graphical illustration of the five successive steps that can occur in a SCM.

The SCM mechanism is broken into five possible successive steps (Levenspiel, 1999; Fedunik-Hofman, Bayon & Donne, 2019):

1. Step 1: Diffusion of gaseous reactant A through the film surrounding the particle to the surface of the solid.
2. Step 2: Penetration and diffusion of reactant A through the blanket of ash to the surface of the unreacted core.
3. Step 3: Reaction of gaseous reactant A with solid particle at this reaction surface.
4. Step 4: Diffusion of gaseous products through the ash back to the exterior surface of the solid particle.
5. Step 5: Diffusion of gaseous products through the gas film back into the main body of the fluid in the reactor.

A reaction system can either be diffusion controlled or reaction controlled, or a combination of both (Levenspiel, 1999; Fedunik-Hofman, Bayon & Donne, 2019). The diffusion and reaction assumptions influence the theoretical boundary limits of the reaction limit (Levenspiel, 1999; Fogler, 2004; Fedunik-Hofman, Bayon & Donne, 2019). The SCM usually assumes either diffusion or reaction to be dominant.

If the system is diffusion controlled, it implies that the limiting step is the diffusion of the gas through the inert solid ash layer (Levenspiel, 1999; Fogler, 2004). This means that the rate of reaction is so fast that the limiting step is the slower diffusion of the gas through the particle.

If the system is reaction controlled, it implies that the molecules are reacting slower than they are being transported (diffused) to the reaction surface (Fogler, 2004) Hence the reaction rates are the controlling mechanism in the system. Further details on the SCM can be found in Levenspiel (1999; Davis & Davis (2003) and Fogler (2004).

4.2 Regolith Furnace Model

The aim of this work is to develop a robust general gas-solid model of the regolith furnace to determine the exit concentrations of the products from the reactor, the porosity changes through the particle and the conversion exiting the reactor. The model will be used to determine an operating baseline of the system and thereafter will be used to do a parametric sensitivity study on the system, to determine the effect of the critical parameters and various operating regimes they impose on the system. This will form the basis for a detailed reactor design to be done.

The regolith furnace is a complex simultaneous multi-reaction gas-solid reaction system. It reduces the chemical species contained in regolith particles using fluorine gas. The fluorine gas flows into the reactor vessel and reacts with the solid particles for a period of time, at 500 ˚C and 1 atm (Landis & Perino, 1989; Landis et al., 1990; Landis, 2005; Turan et al., 2020).

In other words, the system at hand is complex, with different variables affecting the regolith furnace and is derived to allow for testing the effects of critical parameters on the system and to predict the effects of changes in those parameters on the operating regime of the reactor.

4.2.1 Visualisation of regolith furnace system

Each regolith particle is assumed to be a homogenous mix of six metal oxides that are simultaneously reduced using fluorine to produce oxygen and metal fluorides. The composition of each species is defined in Section 3.1

The six simultaneous reactions are repeated below (Eq 2.1- Eq 2.6):

$$SiO_2(s) + F_2(g) \rightarrow SiF_4(g) + O_2(g) \qquad \text{…(Eq 2-1)}$$

$$TiO_2(s) + F_2(g) \rightarrow TiF_4(g) + O_2(g) \qquad \text{…(Eq 2-2)}$$

$$FeO\ (s) + \frac{3}{2}F_2(g) \rightarrow FeF_3(s) + \frac{1}{2}O_2(g) \qquad \text{…(Eq 2-3)}$$

$$MgO\ (s) + F_2(g) \rightarrow MgF_2(s) + \frac{1}{2}O_2(g) \qquad \text{…(Eq 2-4)}$$

$$CaO\ (s) + F_2(g) \rightarrow CaF_2(s) + \frac{1}{2}O_2(g) \qquad \text{…(Eq 2-5)}$$

$$Al_2O_3(s) + 3F_2(g) \rightarrow 2AlF_3(s) + \frac{3}{2}O_2(g) \qquad \text{…(Eq 2-6)}$$

A single regolith particle is visualised as a porous spherical particle. Figure 4-3(a) (left) is a schematic illustration of how a single regolith particle undergoes fluorine reduction. Figure 4-3(b) (right) shows the semi-batch fluidised bed reactor, which contains the regolith particles and flows fluorine gas through it.

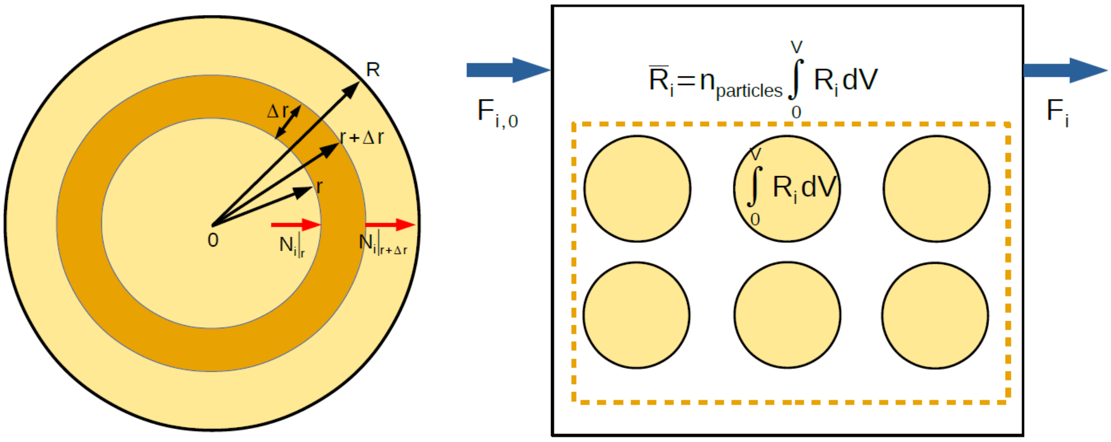

Figure 4-3: (Left) Illustration of a single regolith particle. (Right) The semi-batch fluidised bed reactor showing the reactor feed and exit streams.

The symbols in Figure 4-3 are as follows. N is the molar flux of each species entering and exiting the reaction zone, Δr is the change in radius of the reaction zone is the particle, R is the particle radius, $\bar{R}_i$is the overall reaction rate, $F_{i,0}$ is the initial flowrate into the reactor, F_i is the exit flowrate. This is further explained in the derivation of the system.

The fluorine regolith particle interaction is assumed to occur via the following mechanism:

1. F_2 reactant gas flows into the regolith particle's pores, from the bulk reactor gas.
2. Reaction of F_2 gas with the solid oxides in the regolith occurs in the reaction zone, as illustrated above, and releases the O_2, SiF_4, and TiF_4 and unreacted F_2 gases, and converts the remaining solid oxides into solid metal fluorides which form an inert "ash layer".
3. Diffusion of the O_2, F_2, SiF_4 and TiF_4 gases back through the pores and to the surface, into the bulk gas in the reactor vessel.

The semi-batch fluidised bed reactor is the reactor vessel, which is used for carrying out a variety of multiphase chemical reactions (Levenspiel, 1999; Davis & Davis, 2003; Fogler, 2004, Mebunii. 2022, Cocco, Karri & Knowlton, 2014). This reactor allows the fluorine gas (indicated by $F_{i,0}$ in Figure 4.3 b) to flow through regolith particles bed contained in the reactor vessel thereby fluidising the bed. The gaseous metal fluorides SiF_4 and TiF_4, O_2 and unreacted F_2 exit the reactor in the effluent stream, indicated by F_i in Figure 4.3 b. Once the reaction is completed, the material left in the reactor is the converted solid metal fluorides $FeF_3, AlF_3, CaF_2 \text{ and } MgF_2$.

Details on other reactor configurations can be found elsewhere and are not considered in this work (Levenspiel, 1999; Davis & Davis, 2003; Fogler, 2004).

4.2.2 General Model Assumptions

The regolith furnace system is derived with these general assumptions.

1) Irreversible first-order reactions with respect to gaseous species O_2, F_2, SiF_4 and TiF_4 concentration.
2) The metal oxides in the particle get converted to metal fluorides and form an inert porous solid ash layer for the gas molecules to diffuse through.
3) Knudsen diffusion assumed.
4) The velocity of the F_2 reactant is sufficiently high that the external film resistance can be neglected and therefore the concentration on the surface of the particle is equal to the exit concentration of the reactor effluent stream.
5) The distribution of all solid species in the particle is homogenous.
6) Porosity changes as the reaction proceeds and depends on the local composition of the solid material.
7) The model considers the gases and solids in the particle separately and is tied together with a molar balance over the reactor, to determine the exit concentrations of the product species.
8) The reactor vessel is a semi-batch fluidised bed reactor with a constant reactor volume (V_R), and fluidised solids bed height. The fluidised solids bed height is related to the volume of the solids (V_S).

4.2.3 Gas Phase Mol Balance

The gaseous phase molar balance was derived from first principles and is a system of partial differential equations that are first order in time and second order in position. It has gas species that flow and diffuse in and out of the system.

The gas phase molar balance is described by the equation

$$\frac{\partial(\varepsilon C_{g,i})}{\partial t} = \frac{1}{r^2}\frac{\partial}{\partial r}\left[\varepsilon r^2 D_{e,i}\frac{\partial C_{g,i}}{\partial r}\right] + \bar{R}_{g,i} \qquad \text{...(Eq 4-1)}$$

where ε is the porosity of the particle, $C_{g,i}$ the concentration of the gas species (mol/m^3), r is the radius of the particle (m), $D_{e,i}$ is the diffusion coefficients of the gaseous species (m^2/s), $\bar{R}_{g,i}$ is the overall gas reaction rate for species i (m^3/mol.s). The detailed derivation of Eq 4-1 can be found in Appendix A.

Simplifying Eq 4-1:

$x = \frac{r}{R_p}$; then $r = x \times R_p$; and $dx = R_p dr$

where x is the normalised particle radius and R_p is the particle radius (m).

Assuming a constant $D_{e,i}$ the gas phase molar balance simplifies to:

$$\frac{\partial(\varepsilon C_{g,i})}{\partial t} = \frac{D_{e,i}}{{R_p}^2}\frac{1}{x^2}\frac{\partial}{\partial x}\left[\varepsilon x^2 \frac{\partial C_{g,i}}{\partial x}\right] + \bar{R}_{g,i} \qquad \text{...(Eq 4-2)}$$

The gas phase molar balance is applicable to all the gaseous species ($i = 1{:}4$) in the system, namely, O_2, F_2, SiF_4 and TiF_4.

Knudsen diffusion

The diffusion of fluorine through the regolith particle was assumed to happen via *Knudsen Diffusion*, which occurs when the pore diameter of the particle is smaller than the mean-free-path-length. This implies that the molecules collide with the pore walls within the solid rather than one another, as illustrated in Figure 4-4.

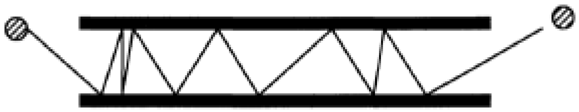

Figure 4-4: Schematic illustrating Knudsen diffusion.

Knudsen diffusivities, D_k, are calculated using the following equation:

$$D_k = 4850 \times d_{pore} \times \left(\frac{T}{M_{wt}}\right)^{0.5} \qquad \text{...(Eq 4-3)}$$

where D_k are Knudsen diffusivities (cm^2/s), T is temperature (K), M_{wt} are molecular weights (g/mol), and d_p is pore diameter (cm).

Knudsen diffusion diffusivities are independent of total pressure, but have a high temperature dependence (Fogler, 2004). When assuming Knudsen diffusion, pressure gradients in the particle can arise since there is no other model of molecular transfer. Pressure gradients would lead to forced flow in the pores to reduce the pressure gradient. The Ergun coefficient for laminar flow in porous media with small pores, such as the regolith particle, is extremely large and thus this flow can be ignored (general assumption 3).

Further details on Knudsen diffusion and other forms of diffusion can be found in elsewhere (Levenspiel, 1999; Davis & Davis, 2003; Fogler, 2004).

4.2.4 Solids Molar Balance

The solid metal oxides (reactant species) are consumed by the reaction, and converted into inert solid metal fluorides, that form an ash fluoride layer. There are no flow terms in the solids molar balance.

The molar balance for solid species is:

$$\frac{\partial}{\partial t}\left[C_{s,i}\right] = \bar{R}_{s,i} \qquad \text{...(Eq 4-4)}$$

where $C_{s,i}$ is the concentration of the solid species (mol/m^3), $\bar{R}_{s,i}$ is the overall solid reaction rate for species i (m^3/mol.s).

The solid species do not diffuse through the particle; they are simply consumed at a position *r*, and this equation is zero order with respect to radius and therefore have no boundary conditions. It depends only on time.

The solids molar balance is applicable to all the solid species $(s_i = 1{:}10)$ in the system, namely, $SiO_2, TiO_2, FeO, MgO, CaO, Al_2O_3, FeF_3, MgF_2, CaF_2, AlF_3$.

4.2.5 Reaction rates

The reaction rate (r_j) for a reaction j classifies and predicts how the reactants are converted into products. It is derived as a function of the reacting materials, concentrations, temperature and pressure at a point in the system and is independent of the type of reactor system (Levenspiel, 1999; Davis & Davis, 2003; Fogler, 2004).

The author could not find any literature on the reaction rates for the six reactions in the regolith furnace system. As such, simplified rate laws were assumed and derived for this model.

The reaction is assumed to be a homogenous uniform reaction throughout the particle (general assumption 5), and therefore assumes a first-order reaction in the gas and solid phase.

The reaction rates for each reaction (*Eq 1 – 6*), link together the gas and solid balances in the particle. The reaction rate is then integrated across all the individual particles (number of particles, N_p) and the volume of the reactor (V_R), to determine the exit concentrations of each species.

The reaction rate, r_j, for reactions j (for *j*=1:6) and ($i = 1{:}\,6$) is a vector and is given by:

$$r_j = k_j C_{F_2} C_{s,i} \qquad \text{...(Eq 4-5)}$$

where k_j is the reaction rate constant for each reaction (m^3/mol.s), $C_{i,1}$ is the fluorine gas molar concentration (mol/m^3) and $C_{s,i}$ is the solid reactants molar concentration (mol/m^3). It is important to note that $C_{s,i}$ is based on the volume of the solid, V_s, and not the volume of the particle, V_p.

The overall reaction rate for the gas phase, $\overline{R_g}$ is a vector of reaction rates for all the gas phase species. It is defined as:

$$\overline{R_g} = \nu_g r_j \qquad \text{...(Eq 4-6)}$$

where ν_g is the stoichiometric coefficient of the reaction system gas species.

The reaction rate for the solid species, $\overline{R_s}$, is a vector of reaction rates for all the solid phase species. It is defined as:

$$\overline{R_s} = \nu_s r_j \qquad \text{...(Eq 4-7)}$$

where ν_s is the stoichiometric coefficient of the reaction system solid species.

$\bar{R}_i$ is the average reaction rate per unit volume:

$$\bar{R}_i = \frac{\int R_i dV}{\int dV} = \frac{\int_0^R R_i 4\pi r^2 dr}{\int_0^R 4\pi r^2 dr} = 3\int_0^1 R_i x^2 dx \qquad \text{...(Eq 4-8)}$$

The reaction is assumed to happen on the surface of the solid particle and happens as the gas diffuses in and out of the particle. The gas exit concentrations on the particle surface are assumed to be the same as the effluent of a well-mixed semi-batch reactor.

4.2.6 Porosity variation with composition

Porosity in the regolith particle is not well known in literature (See Section 2.1.3).

The density of the solid matrix changes when the solid metal oxide is converted into a metal fluoride. That means that the porosity changes as the fluorine reacts with the oxides. Porosity is not constant and is derived with respect to the changing density of the solid phase. This is different to the SCM and makes the model more complex.

Assume a basis of M_0 (kg) of regolith is being fed into the reactor vessel initially. The initial mass fractions $x_{i,0}$, and the densities, $\rho_i \left(\frac{kg}{m^3}\right)$, of the constituents are known from literature.

$V_{s,0}$ is the initial solid volume that depends on composition. It is given by:

$$V_{s,0} = M_0 \sum \frac{x_{i,0}}{\rho_i} \qquad \text{...(Eq 4-9)}$$

The volume of the solid V_s is changing whereas volume of the particle V_p is constant. They are related via the following equation:

$$V_s = (1 - \varepsilon) V_p \qquad \text{...(Eq 4-10)}$$

Particle volume V_p is then related to the initial porosity (ε_0) and initial solid volume ($V_{s,0}$):

$$V_p = \frac{V_{s,0}}{1 - \varepsilon_0} \qquad \text{...(Eq 4-11)}$$

The porosity (ε) after reaction time t, can be estimated by using V_p and the total mass of all species to M with mass fractions x_i:

$$V_p = \frac{M_0 \sum \frac{x_{i,0}}{\rho_i}}{1 - \varepsilon_0} = \frac{V_s}{1 - \varepsilon} = \frac{M \sum \frac{x_i}{\rho_i}}{1 - \varepsilon} \qquad \text{...(Eq 4-12)}$$

Rearranging for ε

$$\varepsilon = 1 - (1 - \varepsilon_0) \left(\frac{M}{M_0}\right) \left(\frac{\sum \frac{x_i}{\rho_i}}{\sum \frac{x_{i,0}}{\rho_i}}\right) \qquad \text{...(Eq 4-13)}$$

Simplifying:

$$\varepsilon = 1 - A \sum \frac{m_i}{\rho_i} \qquad \text{...(Eq 4-14)}$$

where A is a constant that depends only on the initial conditions, and determines the change in porosity:

$$A = \left(\frac{1 - \varepsilon_0}{M_0 \sum \frac{x_{i,0}}{\rho_i}} \right) \quad \text{...(Eq 4-15)}$$

4.2.7 Boundary Conditions

The boundary conditions are only applicable to the gas phase molar balance. There are no boundary conditions for the solid species since they have no spatial derivatives.

There are two boundary conditions, the centre of the particle ($x = 0$) and the surface of the particle ($x = 1$).

The centre boundary conditions at the centre of the particle represents the zero-flux condition, and are given by

$$\left. \frac{\partial C_i}{\partial x} \right|_{x=0} = 0 \quad \text{...(Eq 4-16)}$$

The particle surface boundary condition, in the absence of film resistance (general assumption 4), requires that the surface concentration equals the gas phase concentration on the reactor. This requires a mass balance over the reactor since the surface concentration is coupled to the gas phase concentration.

The system is envisaged as a semi-batch fluidized bed reactor system, that is modelled as an unsteady-state semi-batch fluidised bed Continuous Stirred Tank Reactor (CSTR). A fluidised bed reactor is a reactor that has geometric constraints that form part of the base assumptions. It assumes a constant reactor volume (V_R) and a constant fluidised bed height.

The outer boundary of the particle is assumed to be the same as the exit concentration from the reactor. This becomes the outer boundary condition.

The reactor mass balance:

$$V_R \left. \frac{dC_i}{dt} \right|_{x=1} = F_{i,0} - F_i + \bar{R}_i V_p \quad \text{...(Eq 4-17)}$$

where V_R is the volume of the reactor (m^3), F_i is the molar flowrate (mol/s), $F_{i,0}$ is the initial molar flowrate (mol/s), $\bar{R}_i$ is the overall average reaction rate (m^3/mol.s) and V_p is the volume of the particle (m^3).

$$V_R \frac{dC_i}{dt} = F_{i,0} - F_i + \bar{R}_i V_p \quad \text{...(Eq 4-18)}$$

The ODE needs to be in terms of $C_i$to fit with the particle equations. Therefore, the molar flowrate (mol/s) needs to be converted into a volumetric flowrate Q (m^3/min):

$$0 = Q(t) C_{i,0} - Q C_i + \bar{R}_i V_p - V_r \frac{dC_i}{dt} \quad \text{...(Eq 4-19)}$$

$$0 = Q(t) C_t - Q C_t + \sum \bar{R}_i V_p - \sum V_r \frac{dC_t}{dt} \quad \text{...(Eq 4-20)}$$

Where C_t(mol/m³) is constant, so simplifying and rearranging:

$$Q = Q(t) + \frac{1}{C_t}\sum \bar{R}_i V_p \qquad \text{...(Eq 4-21)}$$

where $Q(t)$ is the flowrate coming out of the reactor (m³/min), and $\bar{R}_i$ is the overall average reaction rate (m³/mol.s). The mass balance is based on molar flowrate, but concentrations are needed in the particle balance. Making the constant pressure assumption for the reactor volume yields:

$$C_{g,i} = \frac{F_i}{\sum F_i}\frac{P}{RT} \qquad \text{...(Eq 4-22)}$$

The mass balance provides the constraint for the boundary condition at the surface, $C_{g,i} = C_{R,i}$ for all species.

4.2.8 Initial Conditions

At $t = 0$, the initial concentrations for gases and solids are $C_{i,0}$.

The reactor and pores are filled with pure O_2. The feed gas contains pure F_2.

The ratio of $\frac{V_p}{V_R}$ is constant.

The gases flow into and out of the system and the boundary conditions are applicable over all time.

4.3 Collocation

The regolith furnace is a system of complex non-linear partial differential equations (4 gas molar balances, and 10 solid molar balances) to determine the concentration of the species as the reaction occurs, and through the regolith particle.

This system can be solved using orthogonal collocation. Application of collocation removes the spatial dependence and converts the equations to first-order ODEs in time or algebraic equations for the boundary conditions. These are then solvable using a differential algebraic equations (DAE) solver.

Collocation only applies to the gas phase molar balance and boundary conditions, which have flux terms. The solids molar balance does not have radial flux, and therefore no collocation is needed.

Figure 4-5 is a picture illustrating the collocation application to the regolith particle balance.

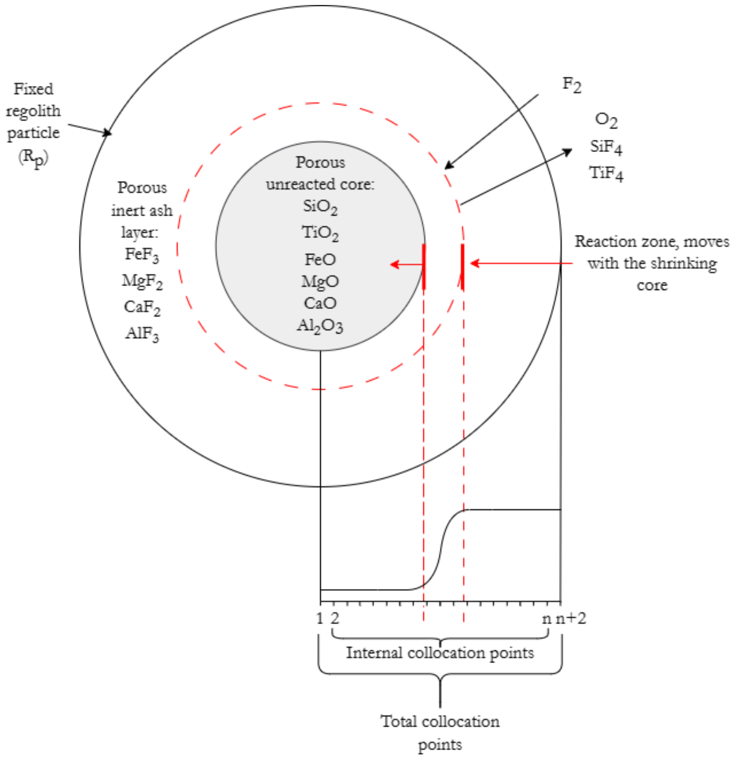

Figure 4-5: Schematic illustration of the collocation application to a regolith particle.

The system is summarized as follows:

$$C_{g,i}\Big|_{i=1:4} = \frac{\partial(\varepsilon C_{g,i})}{\partial t} = \frac{D_{e,i}}{{R_p}^2}\frac{1}{x^2}\frac{\partial}{\partial x}\left[\varepsilon x^2 \frac{\partial C_{g,i}}{\partial x}\right] + \overline{R_g} \qquad \text{...(Eq 4-2)}$$

The first and second derivatives for the interior collocation points (n) can be expanding using the chain rule:

$$\varepsilon\frac{\partial C_{g,i}}{\partial t} + C_{g,i}\frac{\partial \varepsilon}{\partial t} = \frac{\varepsilon D_{e,i}}{R_P^2}\frac{\partial^2 C_{g,i}}{\partial x^2} + \frac{\varepsilon D_{e,i}}{R_P^2}\frac{2}{x}\frac{\partial C_{g,i}}{\partial x} + \frac{D_{e,i}}{R_P^2}\frac{\partial C_{g,i}}{\partial x}\frac{\partial \varepsilon}{\partial x} + \overline{R_g} \qquad \text{...(Eq 4-23)}$$

The concentrations and porosity within the particle change with both position and time. The boundary points are included which gives a total number of points of $(n+2)$. The interior collocation points are used for calculating the concentrations of all gaseous species inside the particles.

Applying collocation to the position, x_k, for species i requires the definition of the concentration matrix of the species to make the calculations clearer. The dynamic concentration of the nodes depends on three variables, $i - th\ species, j - position, k - th\ position\ x_k$. The solution marches forward in time:

$$\varepsilon_k\frac{dC_{g,k,i}}{dt} + C_{g,k,i}\frac{d\varepsilon_k}{dt} = \frac{\varepsilon_k D_{e,i}}{R_P^2}\sum_j B_{k,j}C_{g,k,i} + \frac{\varepsilon_k D_{e,i}}{R_P^2}\frac{2}{x_k}\sum_j A_{k,j}C_{g,k,i} + \frac{D_{e,i}}{R_P^2}\left(\sum_j A_{k,j}C_{g,k,i}\right)\frac{\partial \varepsilon_k}{\partial x} + R_{k,i} \qquad \text{...(Eq 4-24)}$$

where ε_k is the porosity at position x_k. The counter *j* goes over all positions x_k of the spatial coordinate. For the non-symmetric collocation analysis there are $(n+2)$ collocation points, then both boundaries are included in the analysis. Thus the A, B matrices are $(n+2,\ n+2)$ in size and all summations involving A, B and also the weights, w_j will run over $(n+2)$ points. The A, B, x_k and node point (w_j) are obtained from Villadsen & Michelsen (1978).

This equation (Eq 4-24) is repeated for all internal collocation points, for $k = 2{:}n+1$, and calculates all the time gradients at $C_{k,i}$ for all the gas species $i = 1{:}n_g$ at each point k.

The boundary conditions only apply to the gas phase and can be solved by applying collocation.

The centre at $x_{k=1} = 0$ yields, in collocation form:

$$\sum\nolimits_j A_{k,j} C_{j,i} = 0 \qquad \text{...(Eq 4-25)}$$

At the surface $x_{k=n+2} = 1$ yields:

$$0 = Q(t)C_{i,0} - QC_i + \bar{R}_i V_p - V_r \frac{dC_i}{dt} \qquad \text{...(Eq 4-26)}$$

where $\overline{R_\iota}$ is the average reaction rate.

$$\bar{R_\iota} = \frac{\int_0^1 R_{x,i} 4\pi x^2 dx}{\frac{4}{3}\pi} = 3\int_0^1 R_{x,i} x^2 dx = \sum R_{j,i} w_j \qquad \text{...(Eq 4-27)}$$

where w_j are the weights from the collocation analysis. The equation is left in the molar flow rate form.

No collocation needed for the solids balance as there is no radial flux, so at every location x_k

$$\left.\frac{dC_{s,i}}{dt}\right|_{x,i=1:10} = \overline{R_{s,\iota}} \qquad \text{...(Eq 4-28)}$$

The porosity equation is included in the Scilab DAE solver (DASRT), which then calculates the $\frac{d\varepsilon}{dt}$ *and* $\frac{d\varepsilon}{dx}$ variables required in the particle balance. The $\frac{d\varepsilon}{dx}$ term is obtained from collocation.

The final solution is a vector that solves for the exit concentrations of the gas species, solid species and porosity:

$$f|_{x,t} = \begin{pmatrix} \text{center boundary} \\ \text{gas molar balance } (C_{g,i}) \\ \text{solid molar balance } (C_{s,i}) \\ \text{outer boundary} = \text{reactor effluent} \\ \text{Porosity} \end{pmatrix}$$

The SCILAB code can be found in Appendix D.

4.4 Conversion

Conversion ($X_{s,i}$) is defined only for solid reactants, and measures how much of the reactants have been converted to products throughout the reaction. The gas phase is not in steady state, and therefore the conversion of fluorine is not defined.

Conversion of the solid reactants, $SiO_2, TiO_2, FeO, MgO, CaO, Al_2O_3$ is given by:

$$X_{s,i} = 1 - \left(\frac{Average\ C_{s,i}}{C_{s,i,0}}\right) \quad \text{...(Eq 4-29)}$$

4.5 Residence time and contact time

This is a semi-batch fluidised bed reactor. The solids are initially loaded into the reactor, and then the gas is allowed to flow over it, thereby fluidising the bed. As such, the residence time is calculated for the reactor gas flow and the solids contact time separately.

Residence time for the reactor is defined follows:

$$\tau_R = \frac{V_R}{Q_0} \quad \text{...(Eq 4-30)}$$

where V_R is the volume of the reactor (m^3) and Q_0 is the initial gas flowrate into the reactor (m^3/s).

The contact time for the solids time constant is as follows:

$$\tau_S = \frac{V_S}{Q_{F_{2,0}}} = \frac{V_S}{Q_0 \times \frac{C_{F_2}}{C_t}} \quad \text{...(Eq 4-31)}$$

where V_S is the volume of the solid regolith particle (m^3), and $Q_{F_{2,0}}$ is the initial gas flowrate into the reactor (m^3/s).

τ_R and τ_S provide some measure of the rate of contacting that the reactants and solids are undergoing. The residence time for this reaction system is calculated and reported on in the discussion Section 5. We assume the solids spend the same amount of time in the reactor.

4.6 Thiele modulus

The Thiele modulus is a dimensionless number relevant in the design of catalytic reactors. It is a measure of the relative rates of reaction and diffusion within a porous solid particle and is crucial for understanding and optimizing the effectiveness of a catalyst. For the porous solid particles that are undergoing gas-solid reactions, the Thiele modulus provides, at least during the initial stages of the conversions, some indication of the magnitude of the diffusion resistance and its impact on the reaction.

The Thiele modulus (ϕ) compares the rate of the chemical reaction to the rate of diffusion of reactants and products inside and outside of the solid particle. It is usually used to define heterogenous catalytic reaction systems. The Thiele modulus is the measure of the ratio of a surface reaction rate to the rate of diffusion through the solid particle (Fogler, 2004).

$$\phi^2 = \frac{reaction\ time\ constant\ (\frac{1}{s})}{diffusion\ time\ constant\ (\frac{1}{s})} \quad \text{...(Eq 4-32)}$$

A diffusion-controlled system means that the diffusion of the reactants is slower than the reaction rate, whereas in a reaction-controlled system the reaction rate happens slowly and the diffusion of the reactants to the reaction site is fast. In practice, this means that when the Thiele modulus is large (k is big, $D_k$is small and limits the reaction), internal diffusion usually limits the overall rate of reaction; when the Thiele modulus is small, the surface reaction is usually rate-limiting (Levenspiel, 1999; Davis & Davis, 2003; Fogler, 2004).

The Thiele modulus for a catalytic system is calculated at steady state and implies the following:

- ϕ <0.1 implies no diffusion limitations on the reaction as the diffusion is fast compared to the reaction rate. This implies that the concentration of reactants and products within the catalyst particle is relatively uniform. This requires a few collocation points (n<=5), as the concentration profiles will be flat.
- ϕ >100 implies strong diffusion limitations on the reaction as the reaction rate is fast compared to diffusion, leading to significant concentration gradients within the particle. This condition is known as diffusion-limited or transport-limited. This requires many collocation points (n<=50), as the concentration profiles will be very steep.
- 0.1< ϕ <100 implies varying diffusion limitations. This requires collocation points (n) between 15-25.

Figure 4-6 shows how the reaction changes from reaction rate limited to internal diffusion limited as the Thiele modulus increases in a first order spherical catalytic reaction system. The internal effectiveness factor η is a measure of how far the reactant diffuses into the particle before reacting (Fogler, 2004). The internal effectiveness is not calculated in this thesis but is shown here to illustrate how the gradient changes in a reaction system indicating the various controlling regimes.

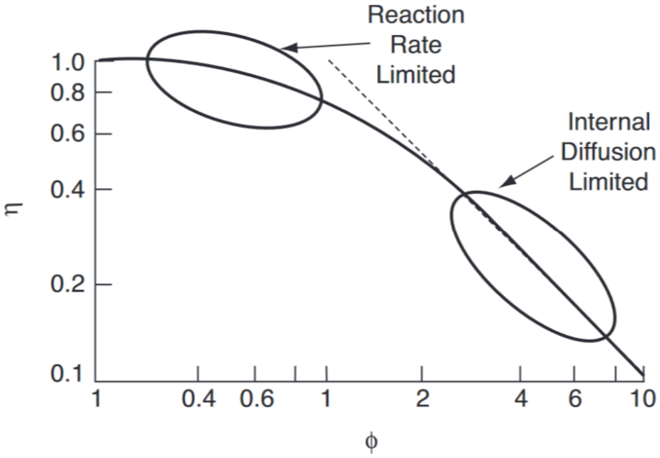

Figure 4-6: A graph showing how the gradient of the internal effectiveness factor η for first order reaction and spherical catalyst shape changes as the Thiele modulus increases (taken from Fogler (2004)).

Visually, the Thiele modulus translates to concentration profiles show in Figure 4-6. This figure was taken from David & Davis (2003). It shows the Thiele modulus on the normalized concentration profiles in a spherical catalyst particle with first-order reaction. The external surface of the particle is located at $\frac{\bar{r}}{R_p} = 1$.

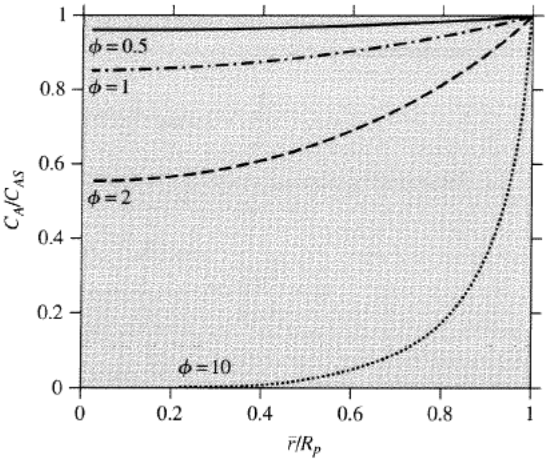

Figure 4-7: The Thiele modulus on the normalized concentration profiles in a spherical catalyst particle with first-order reaction. The external surface of the particle is located at r/Rp =1 (taken from Davis & Davis (2003)).

Figure 4-7 shows that the bigger the Thiele modulus, the steeper the gradient of the concentration line becomes. This shows that the system is experiencing more diffusion limitations, which is explained above. This graph is a point of reference, to help understand what the pseudo-Thiele modulus effect is on the concentration profile calculated in this work.

Fluorine couples all the reactions together, hence, can be explicitly separated from the reaction rates. For higher order reactions, the pseudo-Thiele modulus can be simplified this way, making it not constant with position and time in the particle. It is calculated using the following equations.

$$\phi_i = \sqrt{\frac{kC_{s,0}}{\left(\frac{D_k}{{R_p}^2}\right)}} \qquad \text{...(Eq 4-33)}$$

where $C_{s,0}$ (mol/m³) is the concentration of reactants only, D_k is the calculated Knudsen diffusion, R_p (m³) is the regolith particle radius.

The pseudo-Thiele modulus equation that is calculated for this reaction system is different because it is based on the initial starting solids concentrations. The solids concentration is constantly changing through the particle therefore, the Thiele modulus will also be constantly changing.

The calculated initial pseudo-Thiele modulus for this reaction system is reported in the discussion in Section 5.

4.7 Parameter sensitivity study

The parametric sensitivity study is to look at key design parameters of the reactor. Table 4-1 summarizes all the parameters used to define the regolith furnace reactor.

Table 4-1: Summary of the baseline parameters used to define the regolith furnace reactor.

Parameter	Value
V_R (m³)	1
V_S (m³)	0.48
V_R: V_S	2
Initial Porosity (ε)	0.35
Initial mass flowrate Q_0 (m³/s)	1000
Initial mass of regolith M_0 (g)	1000000
Particle radius R_p (m)	3.5x10^{-5}
Particle Pore diameter d_p (cm)	1x10^{-6}
Rate constants $k_{j=1:6}$ (m³/mol.s)*	1

The fluidised bed reactors have geometric constraints and assumptions. It assumes a constant reactor volume and a constant fluidised bed height. The fluidised bed height is the height that the solids rise to when the gas is flowed through from the bottom of the reactor, thereby fluidising the bed. This implies a constant reactor volume (V_R) to solids volume (V_S) ratio.

Typically, fluidised beds assume that the volume of the reactor is approximately 2.5 times the volume of the solids. (Fogler, 2004, Cocco, Karri & Knowlton, 2014). For this study, based on the particle sizes, we have assumed the volume of the reactor is equal to 2 times the volume of the solids, see Table 4.1.

V_R, V_S and the ratio of V_R: V_S are fixed and will not be varied in the parameter study.

The temperature and pressure are predefined by Landis and Perino (1989) and are assumed constant. The pressure and temperature affect the total concentration of the system but due to the limited knowledge of the system reaction parameters, T and P are not varied here.

The initial mass of regolith is also assumed constant, due to the conserved total concentration. Furthermore, the initial mass of the regolith will affect the volume of the reactor and the fluidised bed height, which are assumed to be fixed.

In the particle, ε_0 and d_p are assumed to be fixed variables, based on literature values.

The particle size (R_p), initial flowrate (Q_0) and the reaction rates (k_j) are chosen to be varied and to analyse the effect it has on the reaction system. By varying these parameters, we will be able to analyse under which operational regime the system will be governed by:

1. Diffusion controlled.
2. Reaction controlled.
3. Feed rate controlled.

These three regimes provide sufficient conceptual information that will enable postulation of a possible reactor configuration that will generate pure O_2 and SiF_4.

5. Analysis of the base case system results

The aim of this study was to develop a robust model of the regolith furnace that would determine the exit concentration of a semi-batch fluidised bed reactor in which solid regolith particles are reduced by fluorine. In this chapter we present that application of the model to a base case system. A parameter sensitivity study will then be conducted to see how the system responds.

The baseline for the system is defined in Table 4-1. It assumes that the system is left to react to completion. The fixed parameters were chosen based on literature values. The variable parameters Q_0, k_j and R_p were chosen to show a good variation in the concentrations of the gaseous and solid species with position and time. This allows for a good interpretation of the system and its operating regimes.

The model generates a large volume of data, and these have been placed in three groups to facilitate better interpretation. The concentrations of the reactants and products of the gas phase species, (group 1 – gases) $F_2, O_2, SiF_4 and\ TiF_4$ are reported together.

There are 10 solid species, and therefore cannot be reported on in the same graphs. As such, they are broken into four reactant species, (group 2 – solid oxides, reactants) $SiO_2, TiO_2, FeO, MgO, CaO\ \ and\ Al_2O_3$ in one set. And the four solid products species, (group 3–- solid fluorides, products) $FeF_3, MgF_2, CaF_2\ and\ AlF_3$ in one set.

The baseline system is discussed in detail and the key responses that best describe the system are determined. Thereafter only the key responses are presented in the parametric study. The full set of graphs from the parametric study can be found in Appendix C.

5.1 Gas reactants and products concentrations

Figure 5-1 (a-d) shows how the gas concentration changes over reaction time, for each gas species.

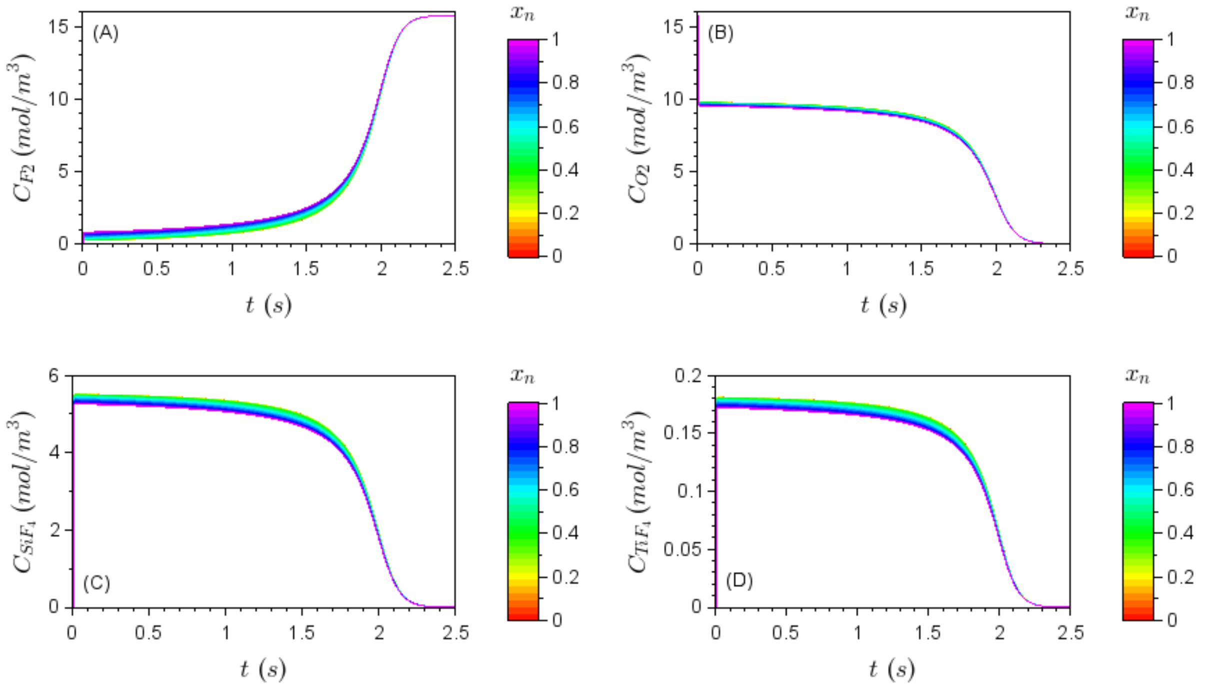

Figure 5-1: Graphs (A-D) showing how the gas concentration changes over reaction time, for each gas species for the baseline parameters.

The four graphs show that the reaction goes to completion after 2.5 seconds. The colour bar on the side of each figure shows the position in the particle of each concentration profile, where $x_n = 1$ is the outer surface of the particle, which is equal to the exit concentration of the reactor and $x_n = 0$ is the centre point of the particle.

Each colour represents a slice at a particular position as a function of time. The purple line is the concentration at the surface of the particle as a function of time while the red line is the concentration at the centre of the particle as a function of time.

The model assumes that the reactor is filled with pure oxygen during start-up, which is equal to the total concentration of 15.7 mol/m^3 when the F_2 is instantaneously added to the reactor, the F_2 is instantaneously almost completely consumed by the reaction and in the process produces gaseous products at the concentrations shown. This is why there is an initial decrease in the oxygen concentration profile at the beginning of the reaction from 15.7 to 9.6 mol/m^3.

Initially, the fluorine is completely consumed. However, as time progresses the reaction rate slows down and can be observed by the increasing concentration of fluorine over time in the system. When the fluorine concentration rises to the total concentration of the system, 15.7 mol/m^3, the reaction is over. The slope of the fluorine increases over time, and the slopes of the oxygen, silicon tetrafluoride and titanium tetrafluoride decrease as they are products. They decrease over time and eventually reach zero when the reaction is completed. There are no more products being produced because the regolith particle is completely converted to fluorides.

The profiles of the product gases follow the same trends because the reaction rates for each reaction are the same.

The reaction time is 2.5 seconds. This is a short reaction time but given the small particle size and porosity of the regolith particles, it is not unfeasible. Terrestrially, in fluidised bed reactors there are reactions that can occur within a few seconds. Fluidised Catalytic Cracking (FCC) and acrylonitrile production (Cocco, Karri & Knowlton, 2014) and polymerisation processes typically take place in a matter of seconds in fast fluidizing gases (Cocco, Karri & Knowlton, 2014).

The base case product profiles in the gas phase show a steady production rate of the product gases over the initial reaction time. This is the desired operating regime to produce a steady state production of maximum concentration of oxygen. This will allow for easier downstream processing. It also allows for continuous production of product gases by using a multiple semi-batch reactor system in parallel, which will allow reloading of the particle from the first vessel, as the reaction continuous in the other vessels.

Under these operating conditions, there is only a slight variation in the concentration through the particle, as indicated by the spacing between the colour lines in Figure 5-1. Figure 5-2 shows how the gas concentrations varies through the particle at each time slice and allows closer inspection of the concentration profiles and the effect of diffusion on the reaction.

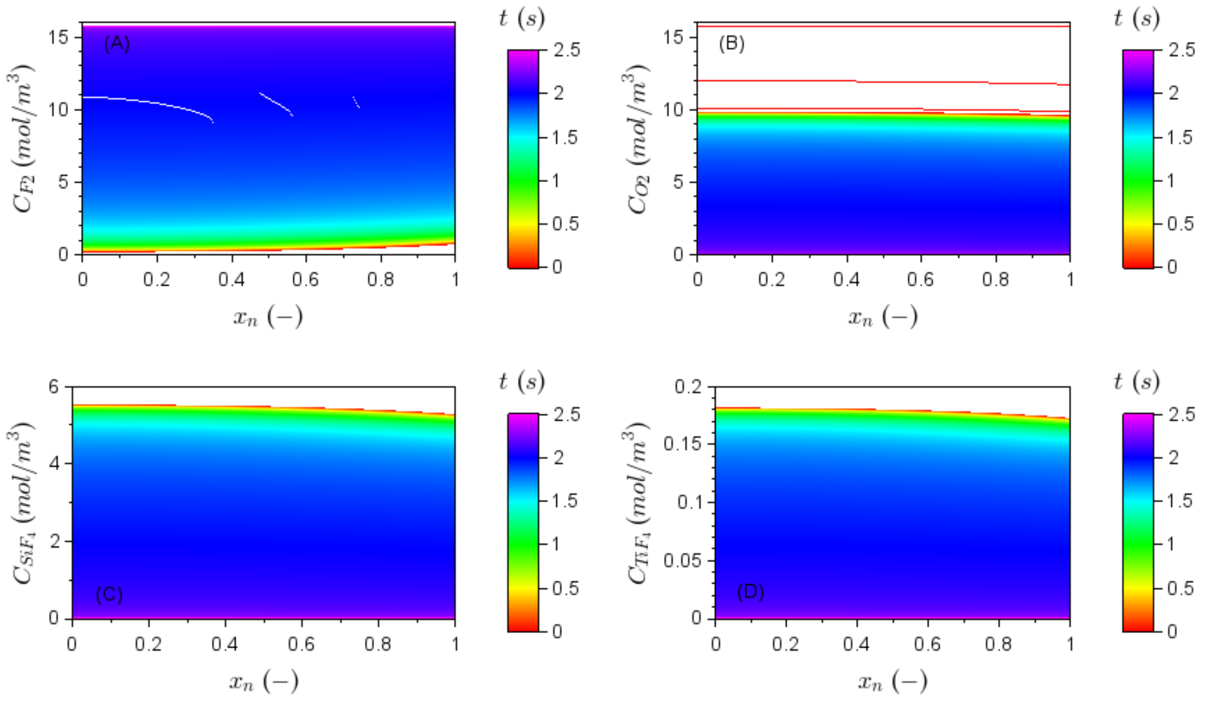

Figure 5-2: Graphs (A-D) showing how the gas concentration varies through the particle for the baseline parameters.

These graphs shows that variation of the concentrations through the particle, starting from the centre of the particle as it moves through to the surface of the particle, at $x_n = 1$. The colour bar shows the time progression of the reaction, with the red indicating the start of the reaction at $t = 0$ and the purple line indicating the end of the reaction at $t = 2.5$ seconds. Each line represents a colour which represents a constant time slice through the particle.

Although the concentration profiles of the gases are almost flat, indicating negligible diffusion limitations, it can be seen that the initial concentration profile of SiF_4 and TiF_4 is steeper than for F_2 and O_2. This is because the diffusion coefficient for the heavy gases is smaller than for the light gases, since D_k is proportional to $\sqrt{\frac{1}{M_{wt}}}$, and as shown by the ratio of the Knudsen diffusion coefficients.

$$D_{TiF_4} = \left(\sqrt{\frac{M_{wt(TiF_4)}}{M_{wt(O_2)}}}\right) \times D_{O_2} = \left(\sqrt{\frac{32}{124}}\right) \times D_{O_2} = 0.5 \times D_{O_2}$$

The fluorine concentration profile through the particle, at $t = 0$, shows no fluorine at the centre of the particle and the lowest concentration on the surface of the particle. The profiles are more prominent when the reaction rate is the highest. Hence diffusion limitations are more likely to impact the reaction. However, with increasing reaction time, the reaction rate slows down as the solid is consumed and the reaction is less likely to be impacted by diffusion limitations, which is observed in the nearly horizontal profiles near the end of the reaction (the blue to purple lines). There is a small concentration gradient through the particle. This implies that the fluorine is being consumed faster at the start of the reaction. The fluorine is reacting marginally faster at the surface before it can diffuse through to the centre the particle. As the reaction proceeds, the profile becomes completely flat meaning that the concentration of fluorine at the surface is the same as the centre.

The product gases mirror the fluorine profile, and all the product gases follow the same trend. Therefore, only the oxygen trends will be discussed in detail. The oxygen concentration throughout the particle has a flat profile, indicating that the oxygen concentration is the same at the surface of the particle and at the centre of the particle, leading to a constant production of pure oxygen over the reaction time.

The rate of consumption of fluorine is at least 2-3 times higher than the production of oxygen as can be noted from the reaction stoichiometry. In other words, silicon dioxide is larger than silicon tetrafluoride therefore it requires twice as much fluorine. Since the reaction rate of fluorine is much higher than oxygen, the diffusion limitations are more likely to impact the concentration profile of fluorine, and this can be clearly seen in the figure in which the fluorine initial concentration profile is steeper than that of oxygen. Note, that the D_k for oxygen and fluorine are very similar, unlike for titanium fluoride, so there are two effects here that act in different ways. This shows that there are small diffusion limitations.

The concentrations are maximum at the beginning of the reaction, but then go to zero as the reaction proceeds. However, the amount of oxygen produced is the same as all the oxygen contained in the regolith and can actually be found by integrating $\int (QC_{o_2})\,dt$.

The concentrations of each product are based on the molar composition of the particle which is based on the stoichiometric composition. More simply, the concentrations that are achieved are based on the initial composition of the solid oxide within the regolith particle. The concentration of titanium tetrafluoride is very small in comparison to the silicon tetrafluoride because there is more silicon dioxide than titanium dioxide in the regolith particle.

Figure 5-3 shows how the various gas concentrations vary over reaction time and position in the particle. The colour bar represents the concentration of the gas species, in the z-axis.

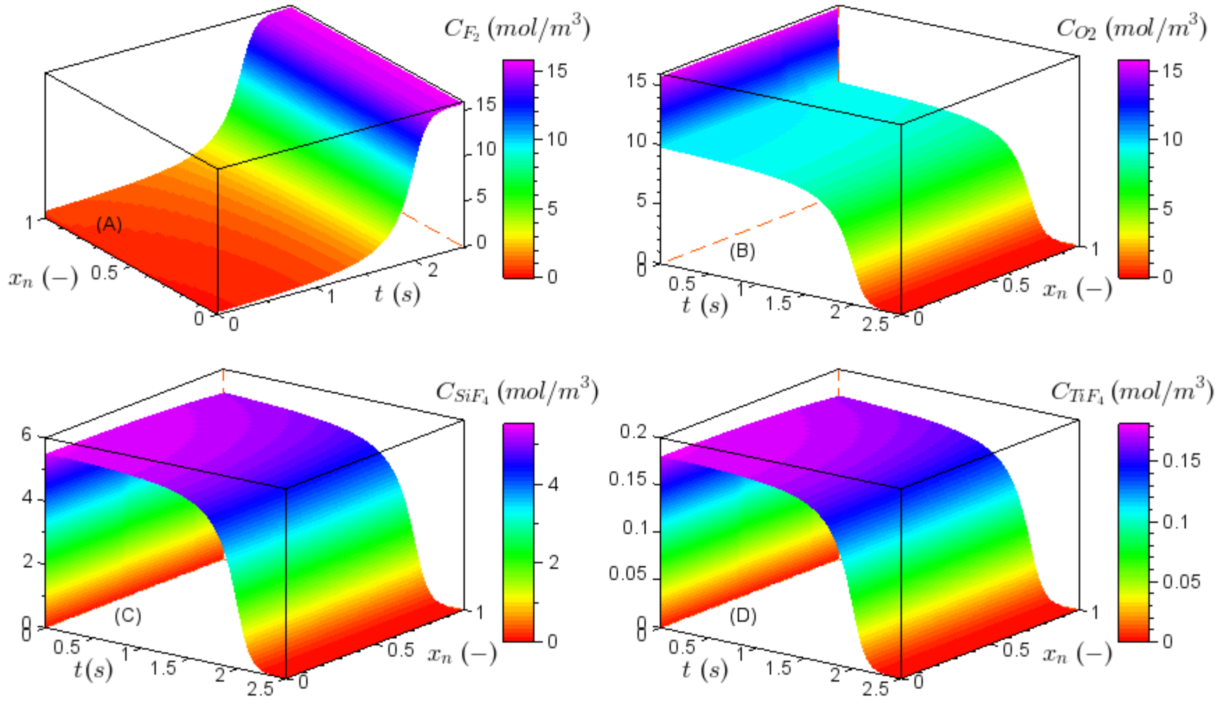

Figure 5-3: 3D graphs (A-D) show how the gas concentrations varies over reaction time and position in the particle for the baseline parameters.

These figures show the combined effects of position and time which have been previously discussed. Although these trends are visible in these figures, it is much easier to observe trends with time and position by looking at slices of the data using 2D plots, as shown above in Figs 5-1 and 5-2. These 2D plots will then form the basis of further comparison of trends as a function of parameters.

The trend for the product gases is the same, therefore in the parametric sensitivity analysis only fluorine and oxygen graphs will be shown.

5.2 Solid reactants concentration

Figure 5-4 shows how the solid reactant concentration varies over time.

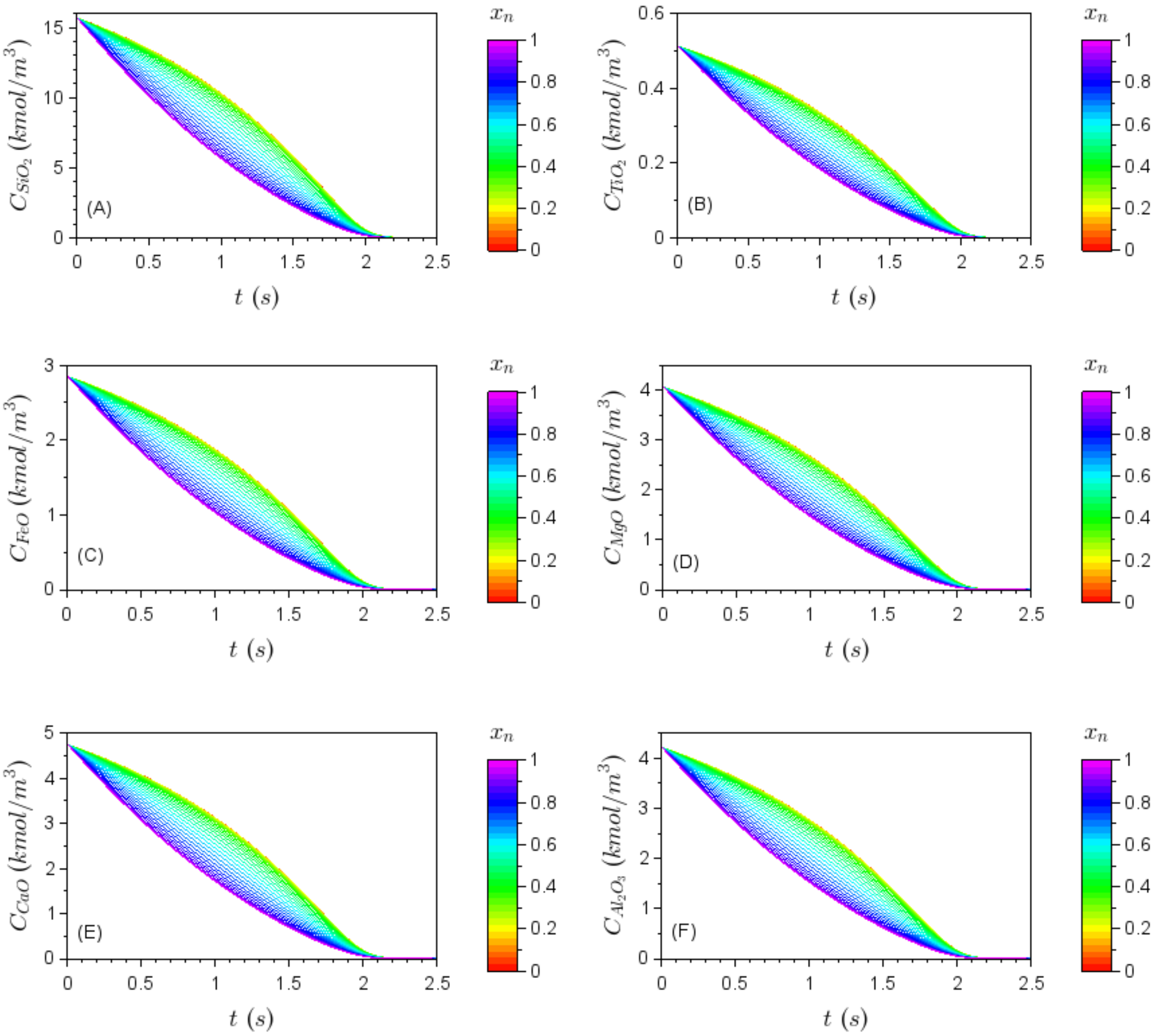

Figure 5-4: Graphs (A-F) showing how the solid reactant concentrations varies over time for the baseline parameters.

These graphs show the concentration variation of the solid reactants over the reaction time of 2.5 seconds. The colour bar shows the variation of the concentration through the particle. The red colour is the centre of the particle, and the purple line is the outer surface of the particle, same as the gas concentration graphs.

The trends for each solid reactant are the same, however the molar concentrations are different and are based on the molar composition of the regolith particle.

The profile shows a decreasing concentration over the reaction time because the reactants are getting consumed and converted to products. The concentration on the outer surface changes more rapidly than the concentration of the centre, suggesting that diffusion might be limiting the reactions. However, the concentration profile of the gaseous species are almost negligible, indicating that gas concentrations are not limiting, and can be seen by comparing the gap between the gas phase species in Figure 5.1 with the gap of the solid concentrations in Figure 5-4.

Figure 5-5 shows how the solid reactant concentration varies through the particle at each point in time.

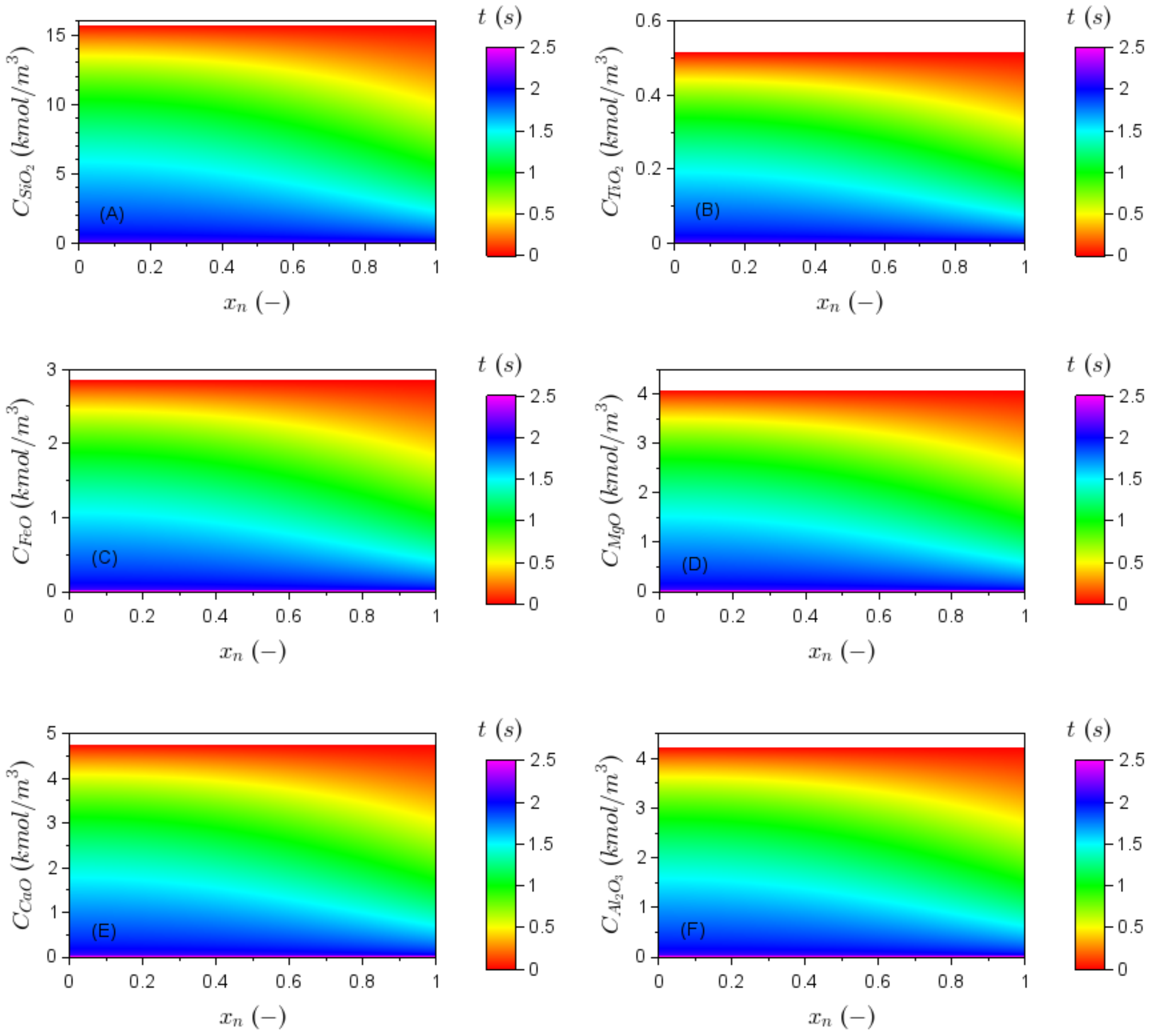

Figure 5-5: Graphs (A-F) showing how the solid reactant concentration varies through the particle for the baseline parameters.

The solid reactant concentration as it varies throughout the particle in shown in Figure 5-5. The gradients are shown by the slope of the colour lines across the particle (x-axis). The gradients show that even though there is no diffusion of the solids, the outer surface of the particle has a lower concentration than the centre of the particle. This is because the fluorine concentration on the surface of the particle is so low (almost zero) at the beginning, the reaction rate is slow and hence diffusion limitations are small. The fluorine gas concentration profile leads to the reaction rate profile which leads to the solids concentration profile which reflect the fluorine gas concentration profile. The purple line, indicating the end of the reaction time, shows that the concentrations are zero. This shows that the particle is spent, and the reaction is over.

Figure 5-6 shows how the solid reactant concentrations vary over reaction time and position in the particle. The colour bar represents the concentration of the gas species, in the z-axis.

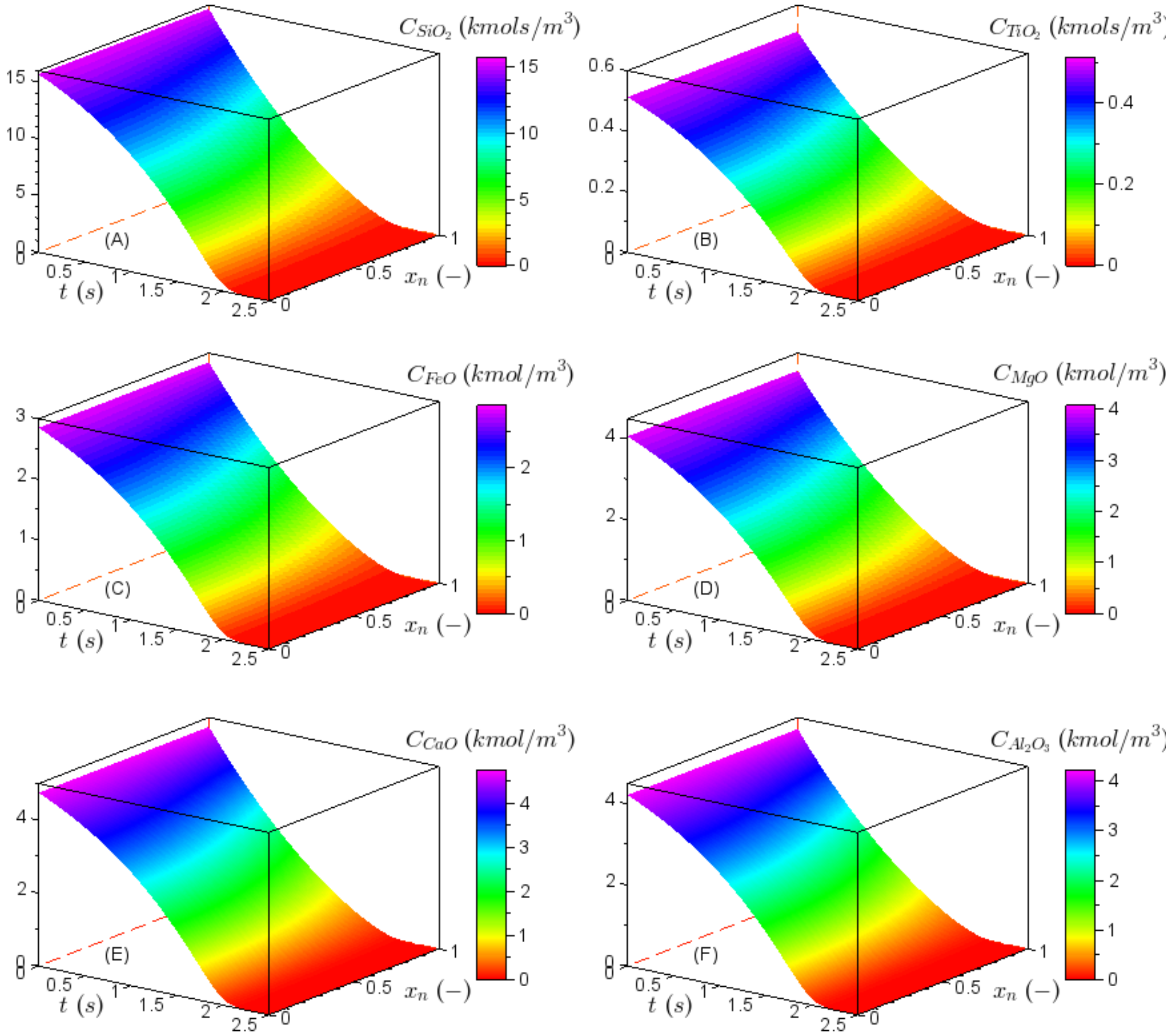

Figure 5-6: 3D graphs (A-F) show how the solid reactant concentrations varies over reaction time and position in the particle for the baseline parameters.

5.3 Solid products concentrations

Figure 5-7 shows how the solid product concentrations vary over time.

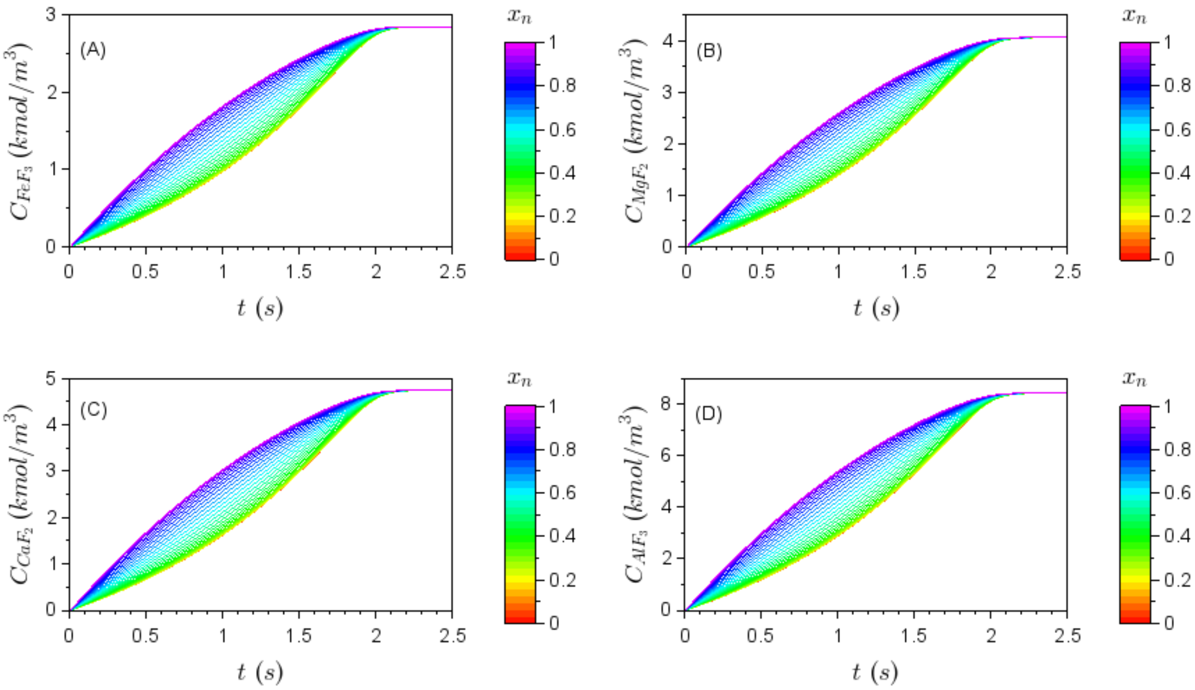

Figure 5-7: Graphs (A-D) showing how the solid product concentrations change over time for the baseline parameters.

The curves of the solid products mirror to the solid reactants, as they are being produced while the reactants are being consumed. The graphs for all the solid products follow the same trend.

Figure 5-8 shows how the solid product concentrations change through the particle as a function of time slices. The trends in Figure 5-8 mirror that of the solid products in Figure 5-75. The gradient in the concentration profiles of the solid products is much more prominent than the gas products. All the product gases follow the same trend.

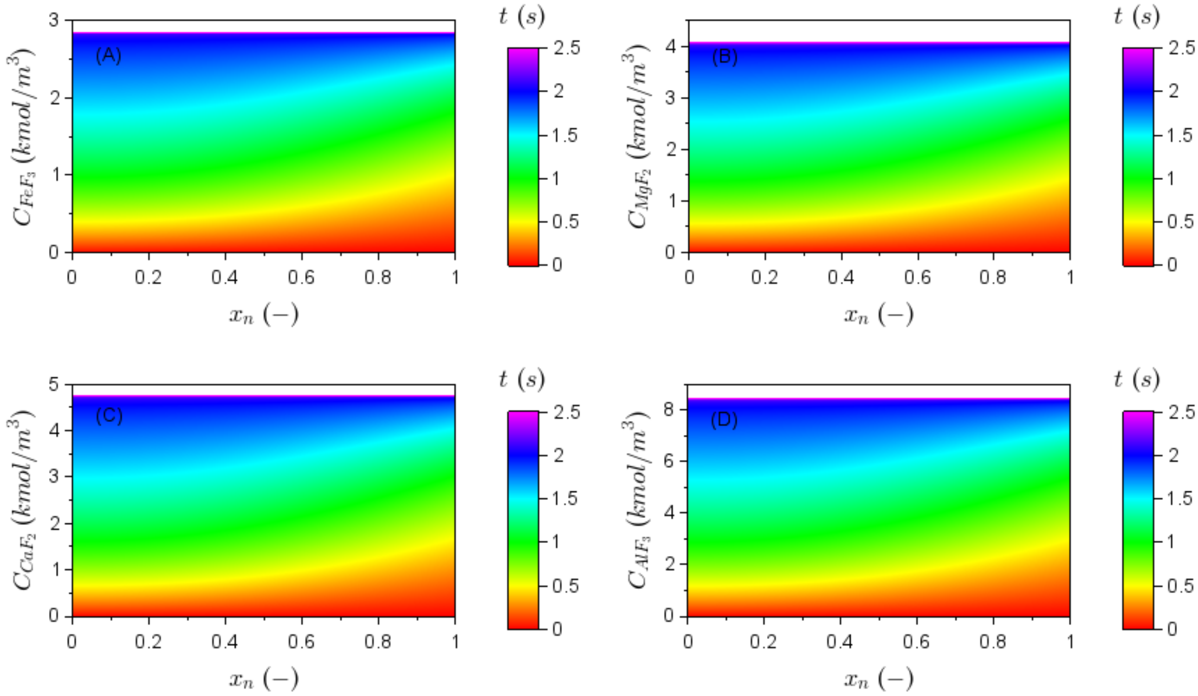

Figure 5-8: Graphs (A-D) showing how the solid product concentrations change through the particle for the baseline parameters.

Figure 5-9 shows how the solid reactant concentrations vary over reaction time and position in the particle. The colour bar represents the concentration of the gas species, in the z-axis.

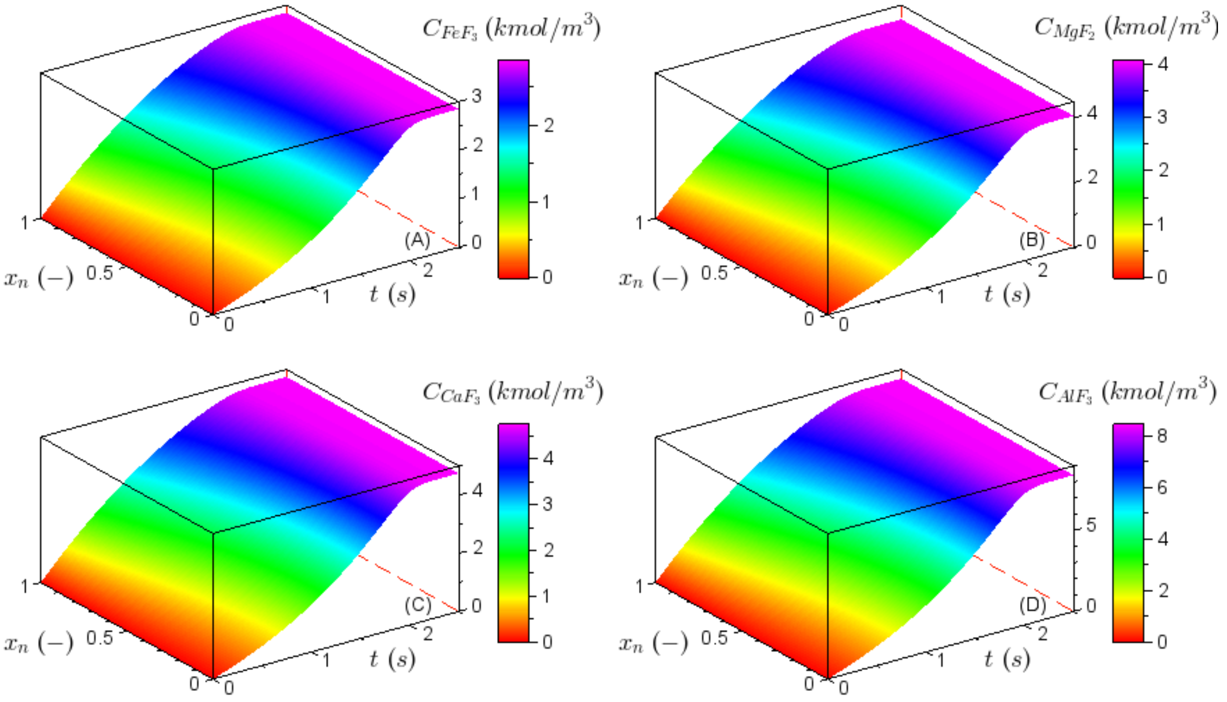

Figure 5-9: 3D graphs (A-D) showing how the solid reactant concentrations varies over reaction time and position in the particle for the baseline parameters.

5.4 Porosity variations

The porosity was assumed to vary as the reaction proceeds. Figure 5-10 shows how (a) the porosity varies as with time, (b) through the particle and (c) 3D graph for the baseline parameters.

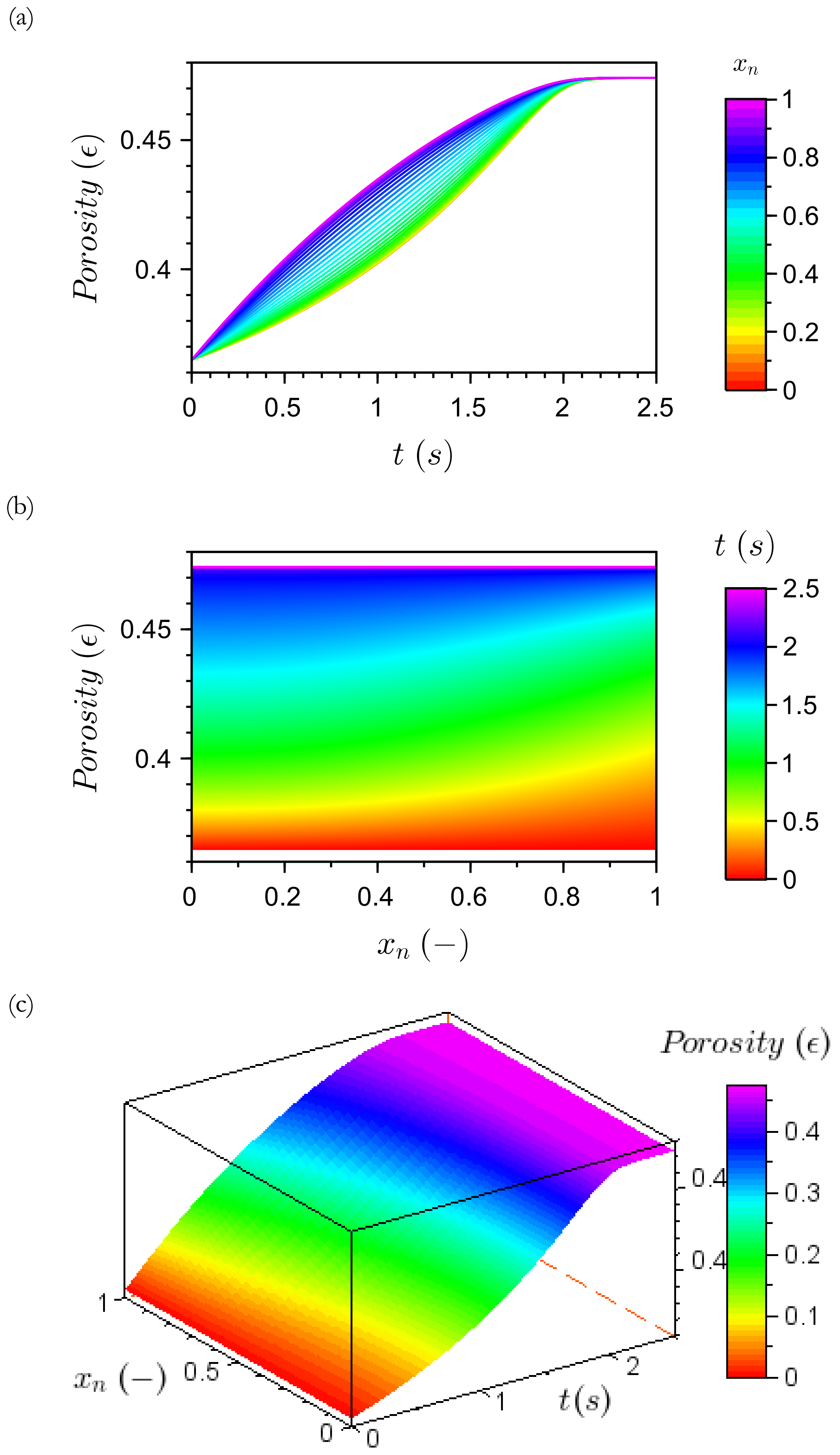

Figure 5-10: Graphs showing (a) the porosity variations over time, (b) through the particle and (c) the 3D graph for the base case parameters.

The porosity over reaction time graph, Figure 5-10(a), shows how the porosity varies as the reaction proceeds, the colour bar shows the variation through the particle. The profile indicates that the porosity increases as the reaction proceeds, and it reaches a maximum porosity of 47% at the end of the reaction.

The porosity variation through the particle graph, Figure 5.10(b), shows how the porosity varies through the particle, as the reaction proceeds. The colour bar shows the reaction time variation. The slope of the curve shows that the porosity is greater at the surface of the particle then at the centre of the particle. This indicates that porosity is increasing as the reaction proceeds.

The porosity profile has the same shape as the concentration plots of the products (Figure 5.7 and 5.8). This is so since the reaction rate of all the species is approximately the same. They all have the same reaction rate constants, and the diffusion coefficients are not significantly different to have a major impact.

5.5 Conversion of solid reactants

The conversion of the solid reactants was calculated. Figure 5-11 shows the conversion of the solids as the reaction proceeds.

Conversion is calculated for each solid reactant in the system. They all follow the same pattern because each reaction has the same reaction rate and only minor deviation due to differences in diffusion of species.

The system reaches 100% conversion of the solids in the system, this is expected because the reaction stops once the solid oxide is completely converted to fluoride. This was one of the base assumptions when defining the reaction rate, as there was no literature on specific reaction rates.

There is a linear conversion profile for majority of the reaction time, and it tapers at the end as the particle is completely consumed. The rate is defined by equation 4-5.

$$r_j = k_j C_{F_2} C_{s,i} \qquad \text{...(Eq 5-1)}$$

This is the reason that the conversion tapers towards the end. C_g is very small and as the reaction proceeds C_S also get smaller. The reaction is second order and hence its asymptotes to zero.

The conversion of each solid reactant follows the same trend. Therefore, the effects of the parametric sensitivity study on SiO_2 will be discussed in detail.

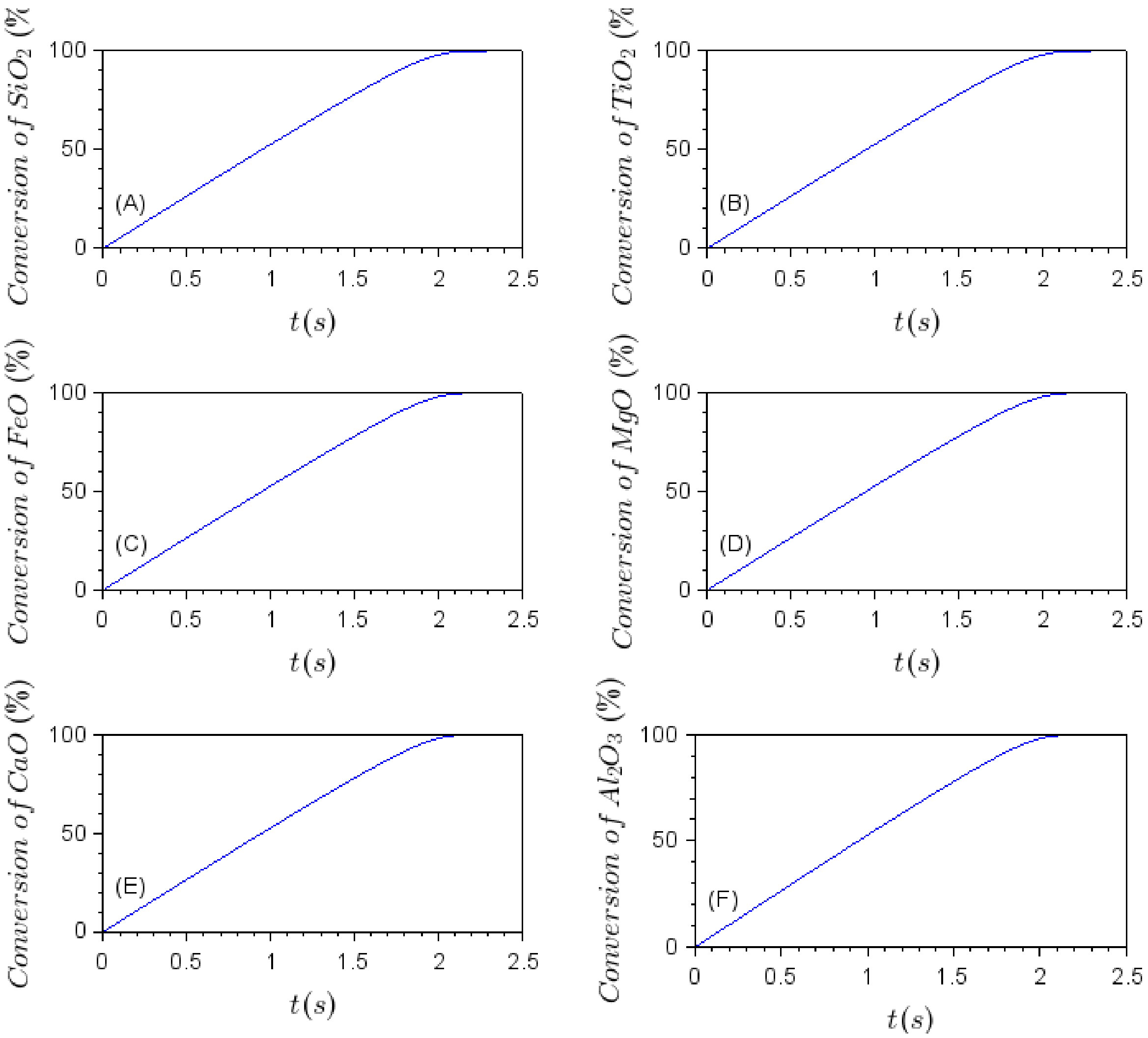

Figure 5-11: Graphs showing the conversion of solid reactants as the reaction proceeds for the baseline parameters.

The residence time and contact time were calculated and are reported in Table 5-1.

Table 5-1: Calculated residence time and contact time.

RT	Value
τ_R (s)	0.001
τ_S (s)	0.000488

The reaction is very fast to only require such a low contact time. The fluorine is almost all converted at the initial conditions. This is because of the chosen rate equations, in which the $C_g \times C_s$ actually yields large values and thus high reaction rates. But since the molecular weight of the solid and the gas differ by about a factor of a 1000, the reaction time for complete conversion at these flow rates without diffusion limitations would be of the order of seconds.

The pseudo-Thiele modulus was calculated for each reactant, based on the initial conditions. These are reported in Table 5-2.

Table 5-2: Calculated initial pseudo-Thiele modulus number for the base case model.

Reactant Name	Calculated Pseudo-Thiele Modulus
R1	0.937
R2	0.169
R3	0.399
R4	0.477
R5	0.516
R6	0.486

The Thiele modulus is usually calculated for catalytic reaction systems which operate at steady state and are therefore not time dependant. This system, however, is a batch process which is at unsteady state. The $C_{s,i}$ is constantly changing which means that the Thiele modulus in the system will be constantly changing over the reaction time.

The pseudo-Thiele modulus was calculated based on the initial solid reactant concentrations. It is a maximum at the beginning, and it will only get smaller. It provides some indication to the potential diffusion limitations that might arise in the initial stages of the reaction. It is calculated and reported as this is a common measure used in reactor design.

The pseudo-Thiele modulus for the base case system is less than 1 at the start of the reaction and this indicates that the system has very little diffusion limitations and indicating that the base case is operating under a reaction limited regime.

6. Analysis of the parametric sensitivity study

Only three variables were tested in the parametric study, namely volume flowrate (Q_0) of the incoming feed stream, reaction rate coefficient (k_j) and particle radius (R_p) according to Table 6-1.

The parameters were varied, and the effects are discussed below. Only the effects on F_2, O_2, SiO_2 and conversion of SiO_2 are discussed. The graphs of the other species can be found in Appendix C.

When varying each parameter, the other parameters were kept the same as the base case.

Table 6-1: Summary of the sensitivity parameters that were varied.

	Figure label				
	a	b	c	d	e
Volumetric flowrate (Q_0) in m³/s	1	10	100	1000*	10000
Reaction rate coefficient (k_j) in (m3/mol.s)	0.01	0.1	1*	10	100
Particle radius (R_p) in μm	0.35	3.5	35*	350	700

*Indicates the values from the base case parameters.

6.1 Effect of feed flowrate

The flowrate was varied according to Table 6-1, and the results are displayed and discussed below. The results are presented in sequential order. The general trend of the profiles is important when doing the parametric analysis.

Figure 6-1 shows the effect that the flowrate has on the concentration of fluorine over time. And Figure 6-2 shows the effect that flowrate has on the fluorine concentration through the particle, as the reaction proceeds.

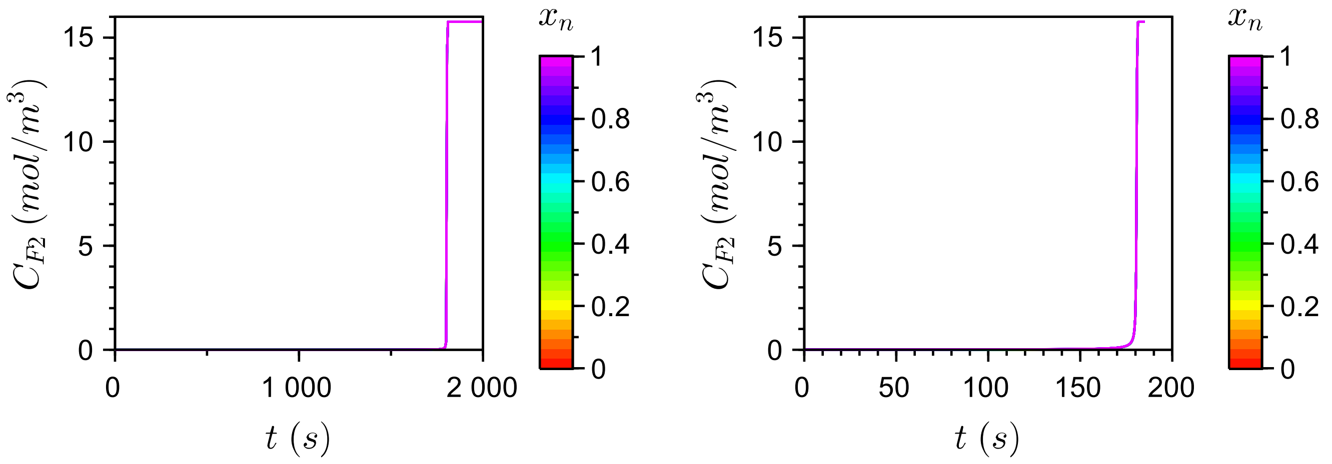

(a) Q_0=1 m³/s (b) Q_0=10 m³/s

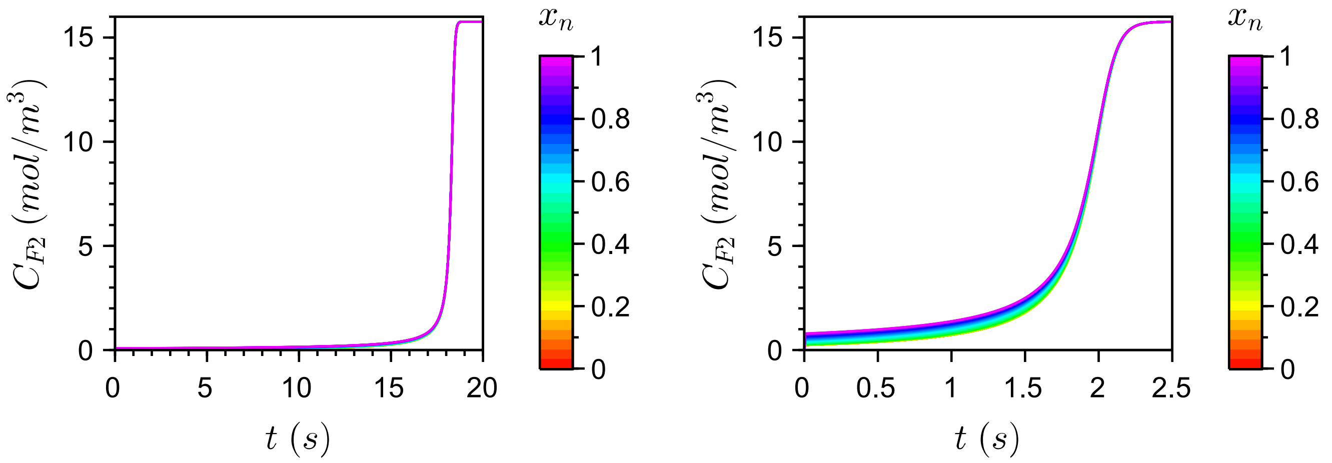

(c) Q_0=100 m³/s (d) Q_0=1000 m³/s

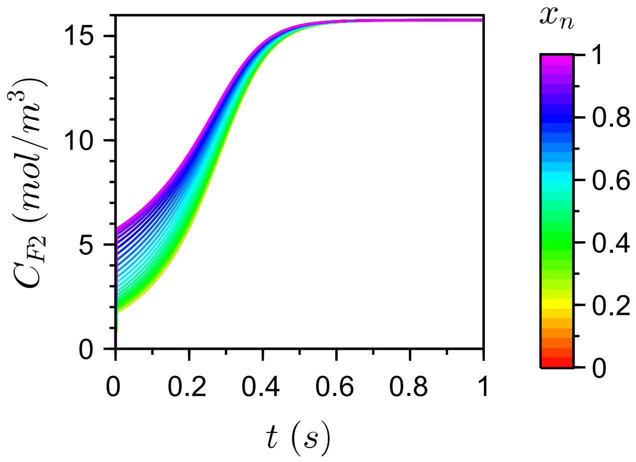

(e) Q_0=10000 m³/s

Figure 6-1: Graphs showing the effect of flowrate on fluorine concentration over time.

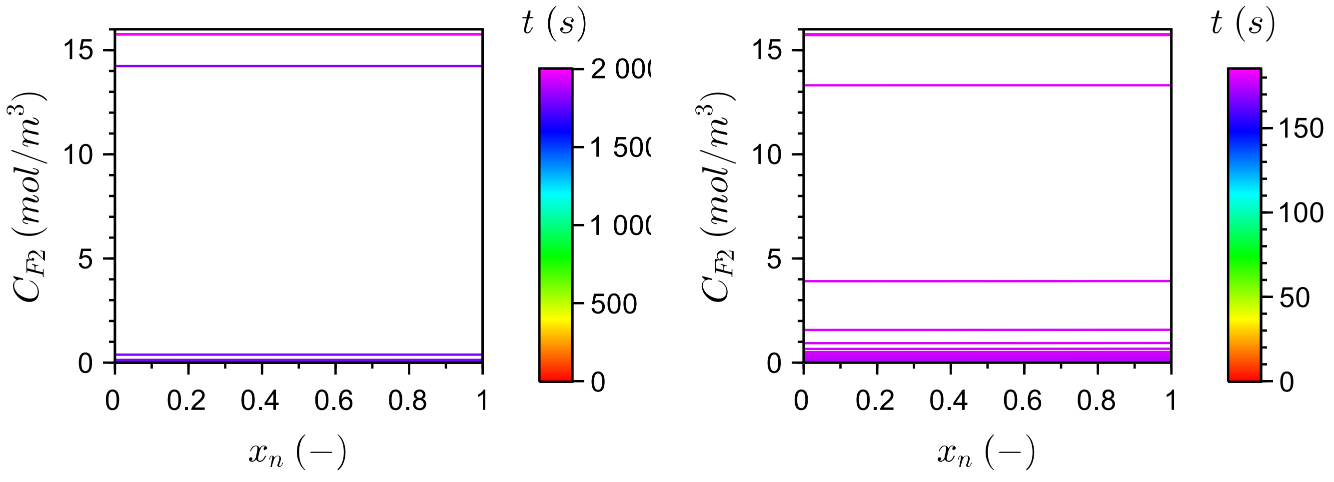

(a) Q_0=1 m³/s

(b) Q_0=10 m³/s

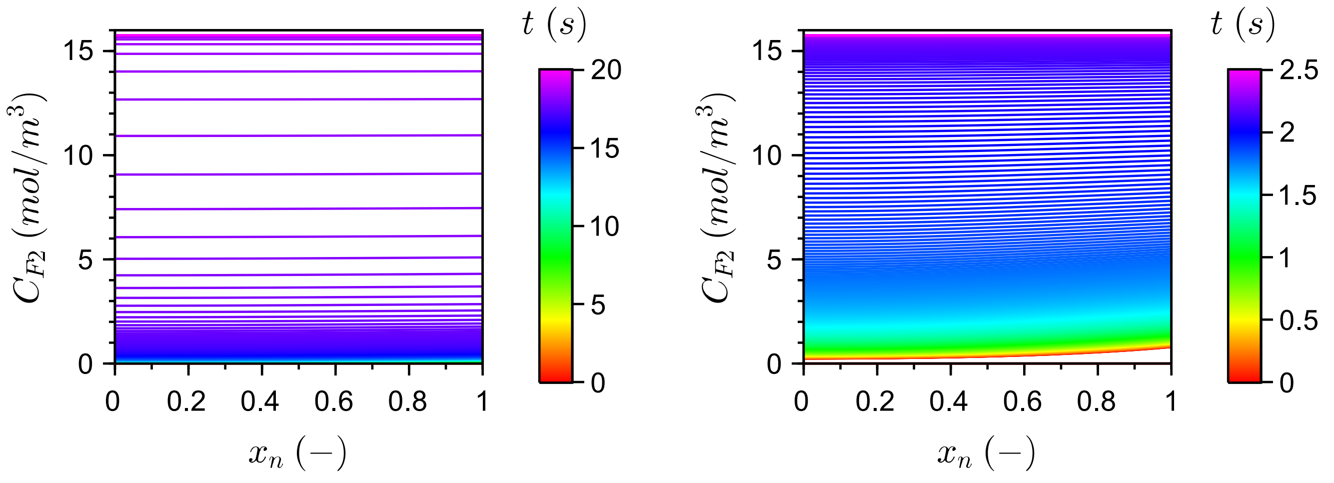

(c) Q_0=100 m³/s

(d) Q_0=1000 m³/s

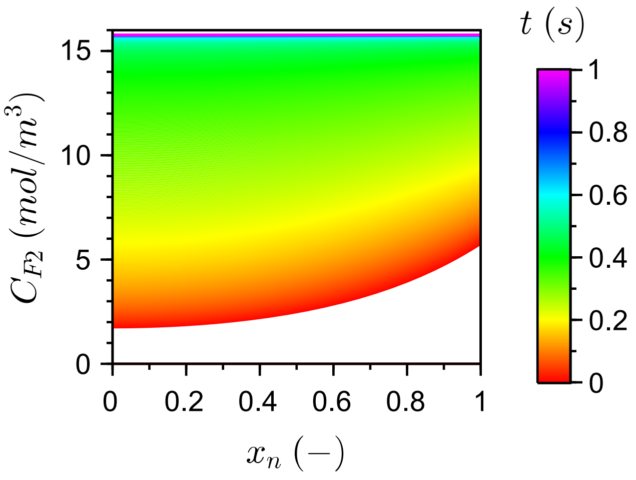

(e) Q_0=10000 m³/s

Figure 6-2: Graphs showing the effect of flowrate on fluorine concentration through the particle.

The trends over time and through the particle, show that as the flowrate decreases, the reaction time increases. The low flowrates, Figure 6-1(a-c) and Figure 6-2(a-c), show that there is no variation of fluorine through the particle. The gradient is zero and the line is flat all through the reaction time. This means that the concentration of fluorine is the same everywhere in the particle, and that the fluorine is being consumed throughout the particle at the same time, so there are no diffusion limitations. In other words, a low flowrate limits the amount of fluorine that is fed into the system and there is not enough fluorine to react to the core. This leads to low reaction rates, and thus flat concentration profiles which imply a reaction-controlled system with no diffusion limitations. In other words, the fluorine concentration is almost zero, so the reaction rate is almost zero and therefore diffusion is no longer limiting.

As the flowrate is increased, Figure 6-1(d-e) and Figure 6-2(d-e), the reaction time decreases and the fluorine concentration gradient through the particle increases. There is more fluorine at the surface of the particle, than at the centre of the particle. The more fluorine, the faster the reaction rate which produces more gas products in a shorter space of time and would increase the diffusion limitations in the system. Even with a reaction time of 1s, there are still little diffusion limitations.

Figure 6-3 shows the effect that flowrate has on oxygen concentration over time. And Figure 6-4 shows the effect of flowrate on the concentration of oxygen through the particle, as the reaction proceeds.

These profiles mirror the fluorine concentration profiles because oxygen is being produced as the fluorine and solids are being consumed.

They show that as the flow rate is decreased, there is a constant production of oxygen, i.e., there is no concentration gradient through the particle as the reaction proceeds. This is the desired operating regime, as it a maximum oxygen concentration in the exit gas stream. The flat profile indicates that the system is reaction controlled, with little diffusion limitations. The oxygen production is constant due to the amount of fluorine being fed into the system as noted above. At very high flowrates, we see an increase in the concentration gradient between the surface and the centre of the particle. This shows that the diffusion limitations increase, even at the shortest reaction time, as the flowrate increases. Under these conditions fluorine contaminates the product stream.

The general trend shows that as the flowrate increases, the reaction time decreases and that the diffusion limitations increase which decreases the pure oxygen that is produced. Flat profiles produce maximum oxygen concentration and are preferred. Therefore, a slower flowrate is a better operating regime.

Although the concentration of oxygen is maximised, the flowrate of oxygen is minimised. Therefore, the production rate of oxygen is greatly reduced at the expense of producing a highly concentrated oxygen stream that is not contaminated by fluorine. Note that the separation of oxygen and fluorine is difficult, while the separation of oxygen from silicon tetrafluoride and titanium tetrafluoride is easy due to the large difference in molecular properties.

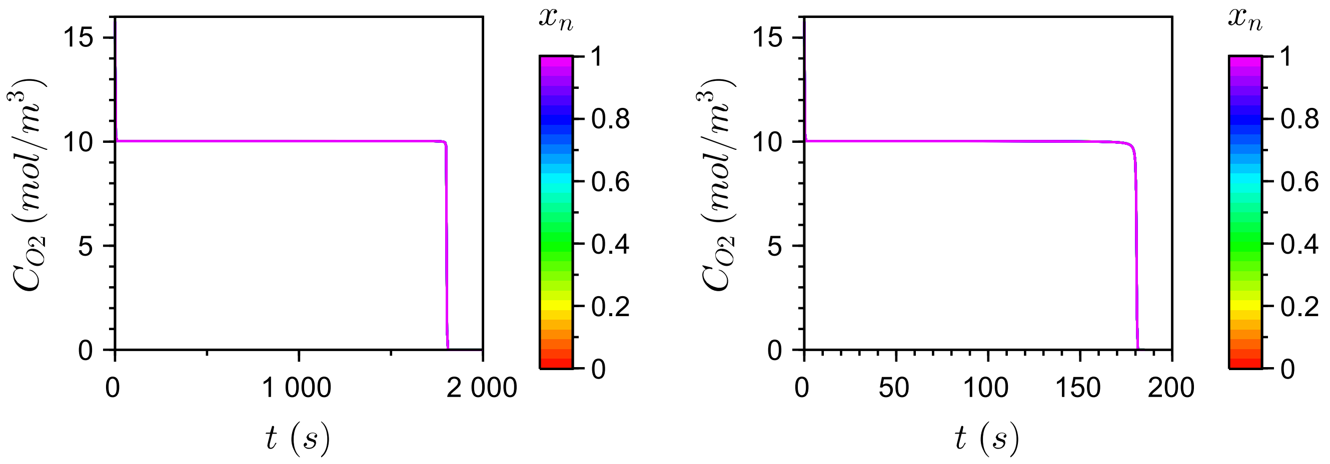

(a) Q_0=1 m³/s (b) Q_0=10 m³/s

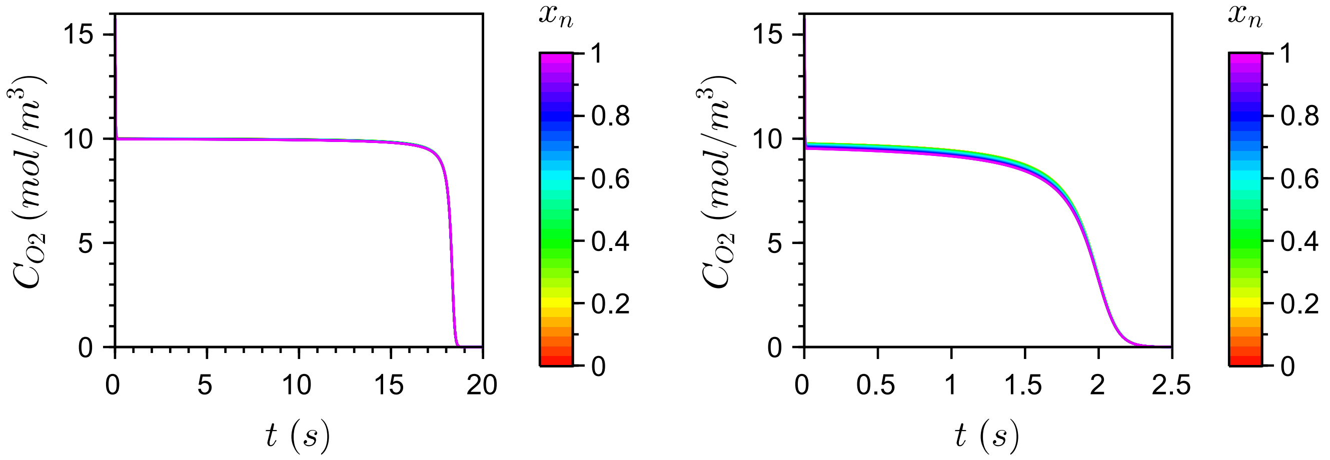

(c) Q_0=100 m³/s (d) Q_0=1000 m³/s

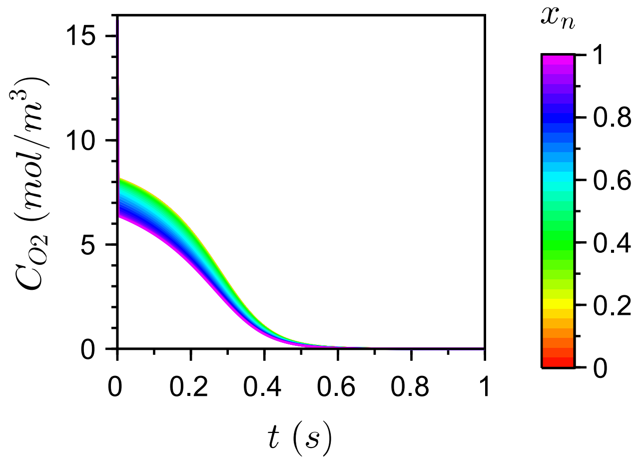

(e) Q_0=10000 m³/s

Figure 6-3: Graphs showing the effect of flowrate on oxygen concentration over time.

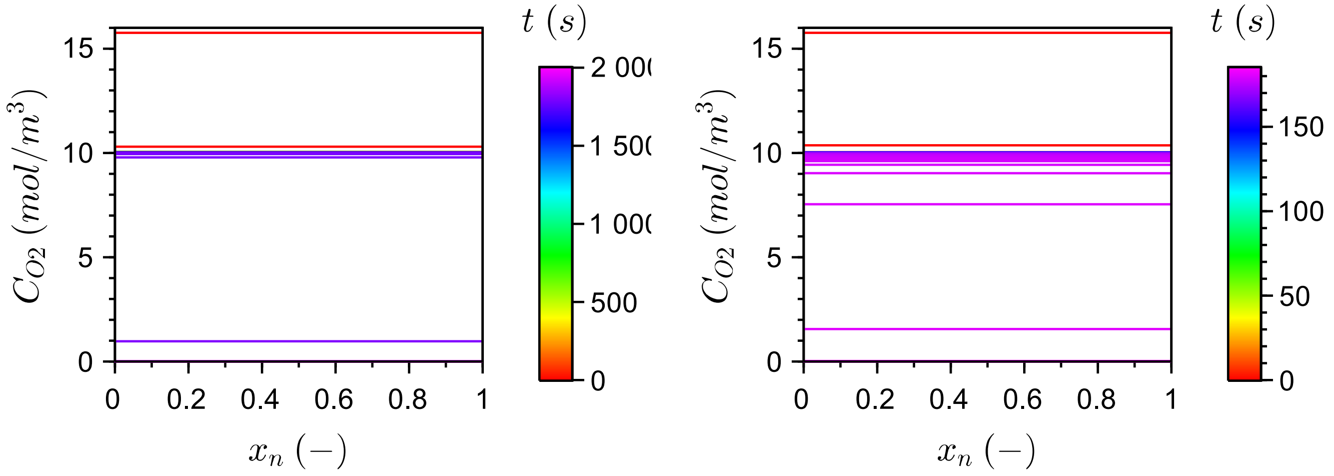

(a) Q_0=1 m³/s

(b) Q_0=10 m³/s

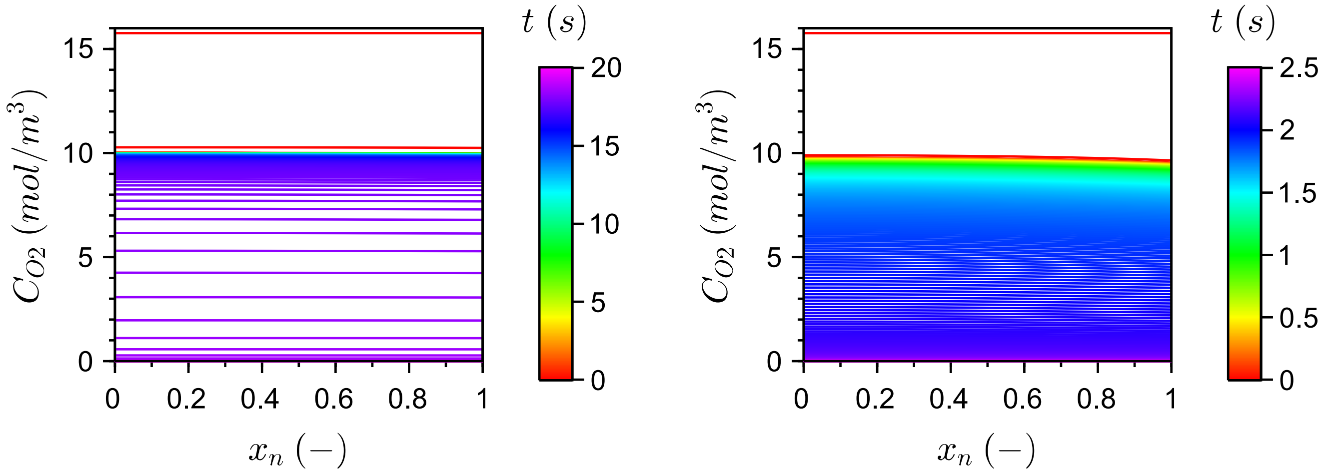

(c) Q_0=100 m³/s

(d) Q_0=1000 m³/s

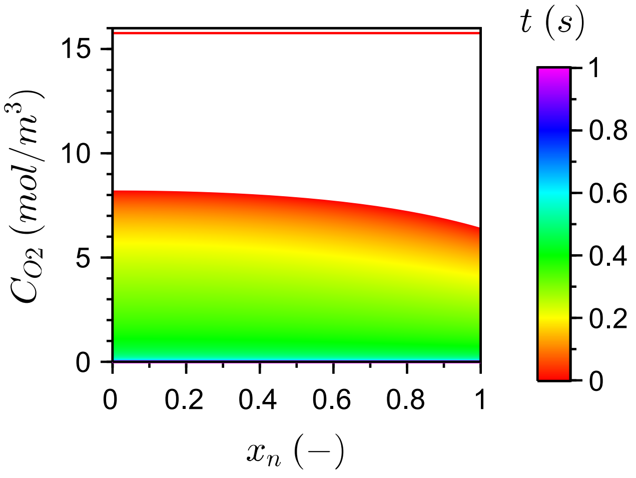

(e) Q_0=10000 m³/s

Figure 6-4: Graphs showing the effect of flowrate on oxygen concentration through the particle.

Figure 6-5 shows the effect of flowrate on the silicon dioxide concentration over time.

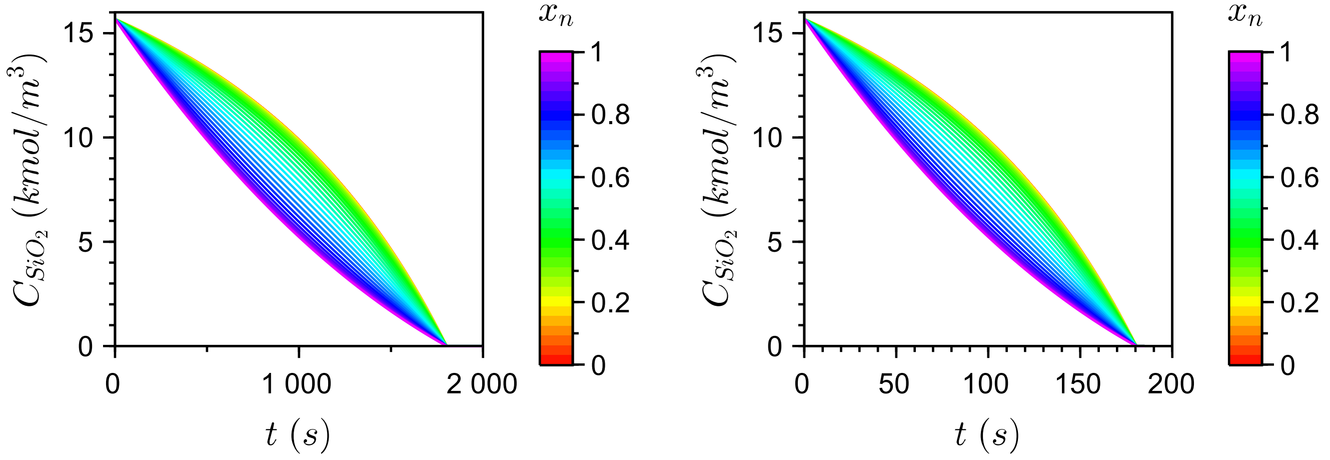

(a) Q_0=1 m³/s (b) Q_0=10 m³/s

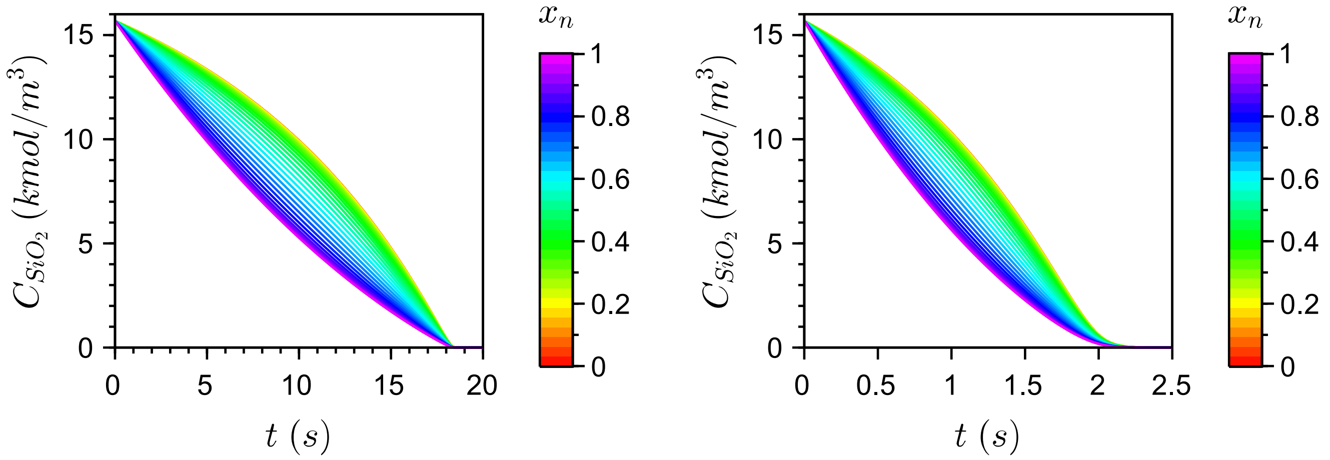

(c) Q_0=100 m³/s (d) Q_0=1000 m³/s

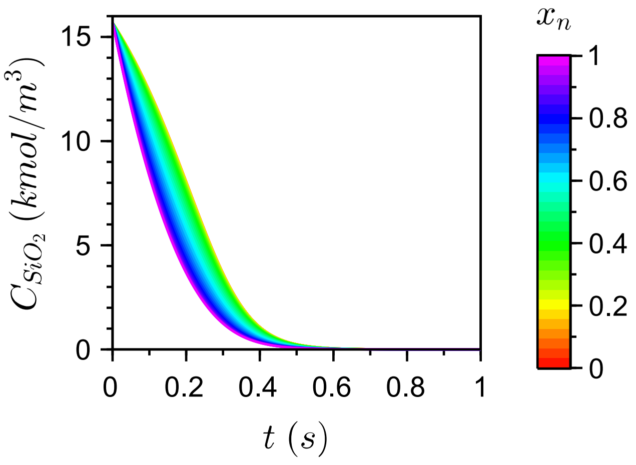

(e) Q_0=10000 m³/s

Figure 6-5: Graphs showing the effect of flowrate on silicon dioxide concentration over time.

Figure 6-6 shows the effect of flowrate on the silicon dioxide concentration through the particle.

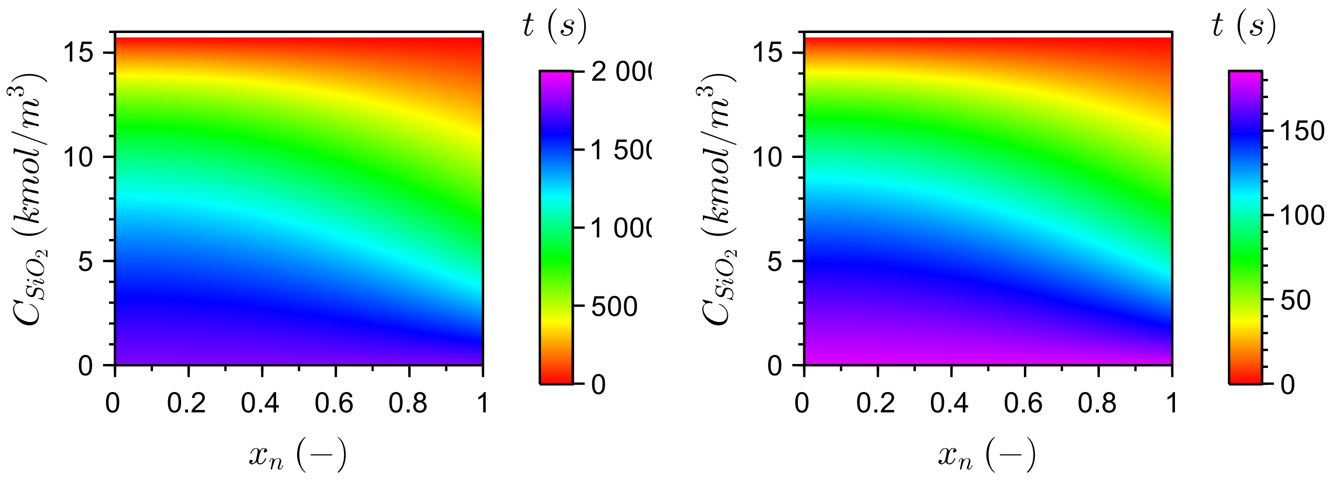

(a) Q_0=1 m³/s

(b) Q_0=10 m³/s

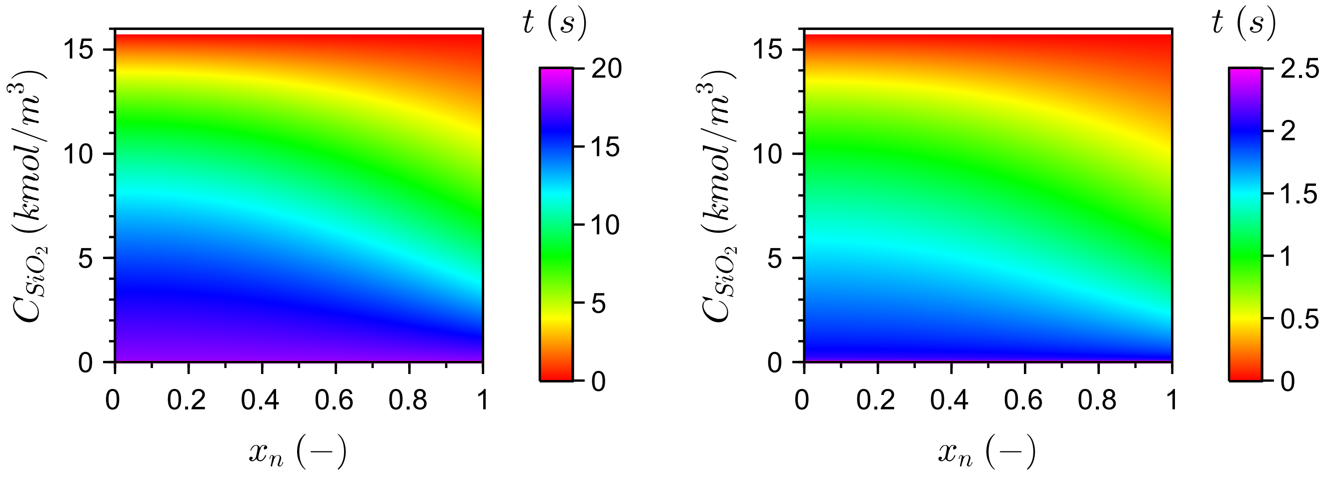

(c) Q_0=100 m³/s

(d) Q_0=1000 m³/s

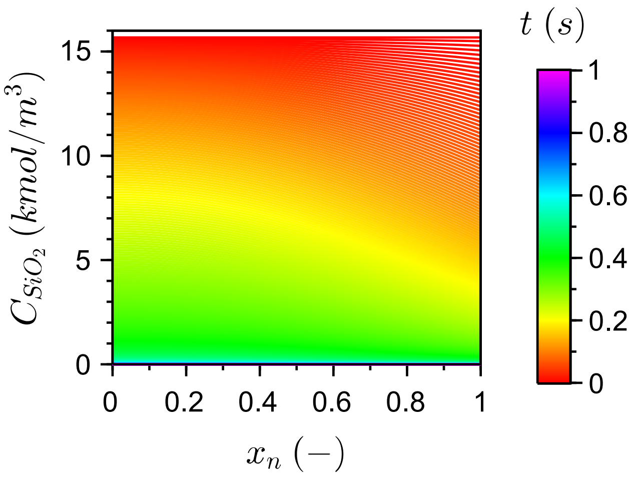

(e) Q_0=10000 m³/s

Figure 6-6: Graphs showing the effect of flowrate on silicon dioxide concentration through the particle.

The solid is evenly consumed in all cases. The concentration profile is almost the same for all the flow rates. This corresponds to the small variation in the concentration observed between fluorine and oxygen even at the high flow rates. Thus, under these conditions the particle is nearly uniformly consumed.

As the flowrate is increased, the trend shows that the silicon dioxide (reactant) concentration is lower at the surface and higher at the centre. The solids aren't diffusing; therefore, the concentration gradient is a result of the fluorine concentration gradient on the surface. The solids reflect the gas concentration profiles. The gas concentration profile leads to the reaction rate concentration profile which leads to the solids concentration profile and porosity in the particle.

The variation over time shows more clearly that the concentration variation through the particle becomes smaller at the higher flowrates. There is not much change in the variation of the concentration gradients at the lower flowrates over the reaction time, shown in Figure 6-6(a-d). At the highest flowrate, Figure 6-6(e), it shows that majority of the conversion happens at the beginning of the reaction, and as it proceeds it reaches zero. The solids' reaction is completed in under 1 second, showing that the solids are consumed very fast due to the high concentration of fluorine being fed into the system.

The little variation in the gas phase concentration profile with position, notwithstanding that the fluorine concentration increases many times inside the pores, thus greatly increasing the reaction rate with the increasing flow rate. So, a small variation in the gas phase concentration with position is not sufficient to produce a reaction front.

The same results are obtained for iron fluoride and for porosity and they mirror those of the reactants. The iron fluoride is a solid product, and these graphs mirror the silicon dioxide profiles which is the solid reactant. The trend shows that as the flowrate is increased, the reaction time decreases and the concentration through the particle surface and centre boundaries are reduced. The reaction time for the highest product is less than 1 second.

The solid product is higher at the surface and lower at the centre of the particle. The solids aren't diffusing, as mentioned above. The products are a result of the reactants being consumed and converted. This is therefore dependent on the fluorine concentration which effects the reaction rate.

The graphs are note shown here, and can be found in Appendix C.

Figure 6-7 shows the effect that flowrate has on conversion of silicon dioxide over time.

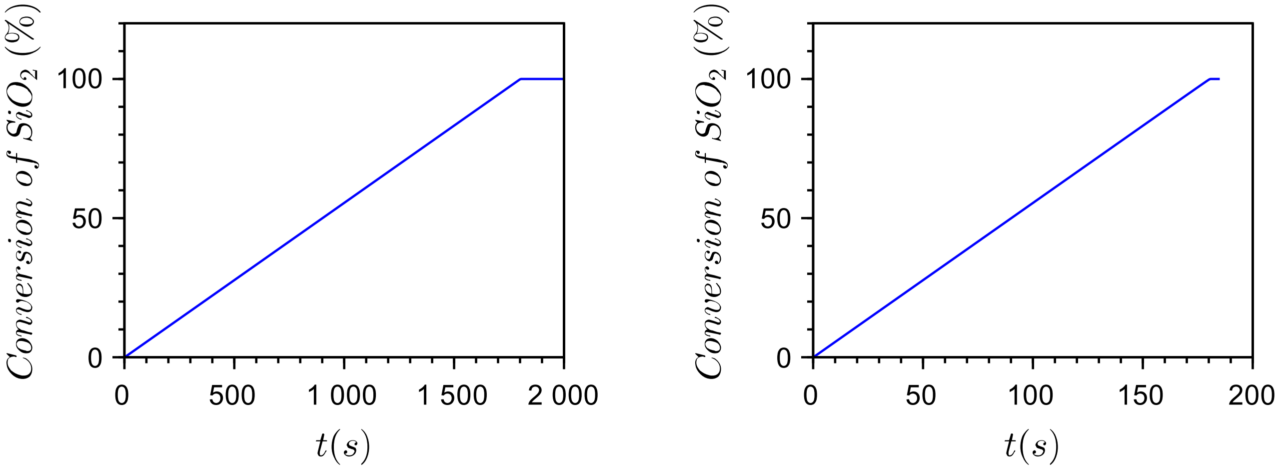

(a) Q_0=1 m³/s (b) Q_0 =10 m³/s

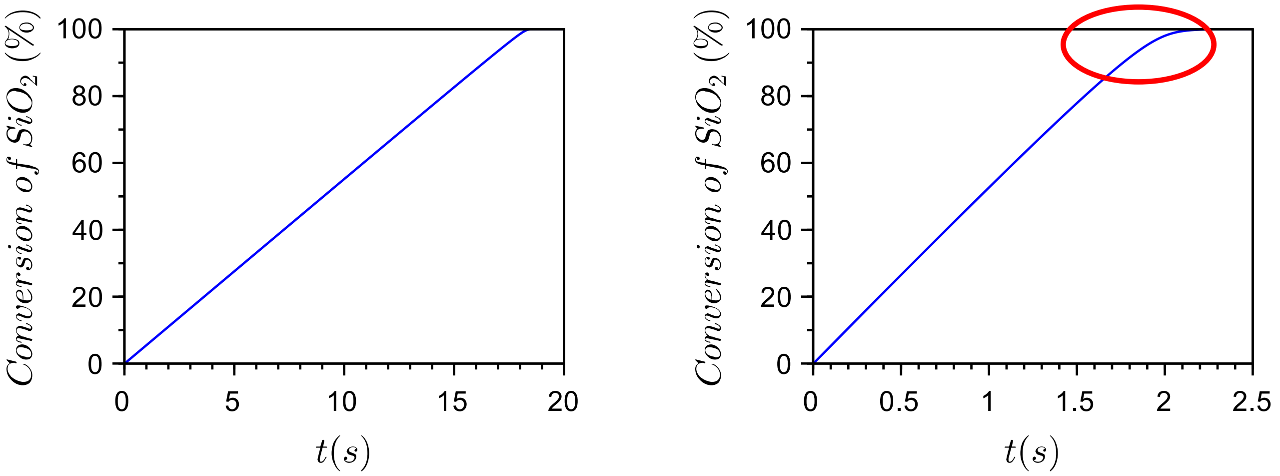

(c) Q_0=100 m³/s (d) Q_0=1000 m³/s

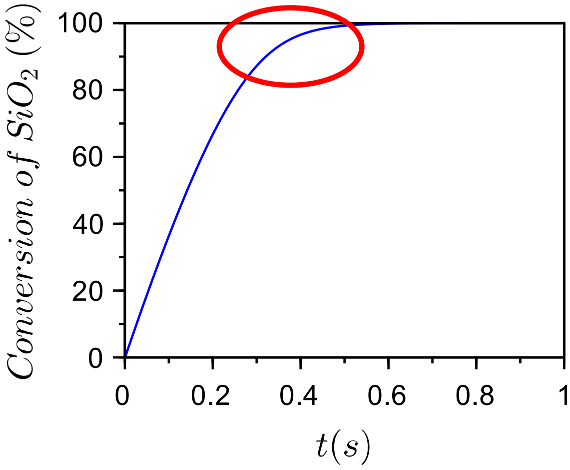

(e) Q_0=10000 m³/s

Figure 6-7: Graphs showing the effect of flowrate on conversion of silicon dioxide over time. The red circles indicate when the system become reaction rate controlled, due to the increased fluorine flowrate.

The conversion of the solid reactants is not related to the solid phase concentration profiles, as initially thought. The concentration of the solids hardly changes. In Figures 6-1(a-c) to 6-4(a-c), the gas concentration profiles are completely flat, and these show a very sharp end point to the reaction. The concentration of gas phase is approximately constant across the particle and that the reaction rate is proportional to the amount of active solid in the matrix, hence the linear profile. The reaction rate depends on the amount of fluorine that can be supplied in the feed. Once the gas phase experiences even mild diffusion limitations, the supply of reactants to the reaction zones in the particle are no longer dependent only on feed rate, but also on the concentration profile. The reaction rate then varies as the particle is consumed and asymptotes to 100 % conversion.

Figure 6-8 was plotted in scilab to illustrate the shape of the conversion gradients over time for a CSTR reactor when the film diffusion is controlling, the ash diffusion is controlling, and the reaction rate is controlling the reaction system.

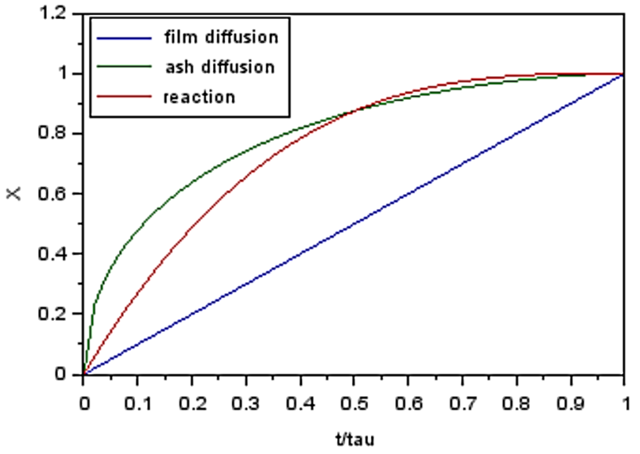

Figure 6-8: Graph illustrating the shape of the conversion gradients over time for a CSTR reactor when the different regimes are controlling the reaction system. Film diffusion represents the feed limiting regime, ash diffusion represents the diffusion controlling regime.

The concentration graphs are plotted to complete conversion. Furthermore, the model uses a CSTR and therefore we get varying conditions, and the gas concentration keeps changing, depending on the reaction rate and feed rate. This shows that the feed flowrate limiting condition mimics the film limiting diffusion when the gas concentration is very low.

Figure 6-7(d) shows that at a high flowrate, the reaction rate controls, and the supply of fluorine is limiting. It shows that the theoretical time required for complete conversion at 100% fluorine consumption in the reactor without the effect of diffusion limitations is approximately 1.8 seconds. This is based on the molar flow rate of the fluorine and stoichiometric amount required to convert the oxides in the reactor to fluorides. Figure 6-7(e) has a more linear initial region, also showing a reaction-controlled regime.

An analogy can be drawn with the CSTR mole balance:

$$\frac{C_A}{C_{A,0}} = \frac{1}{1+\left(\frac{k_{eff}V}{Q}\right)} \qquad \text{...(Eq 6-1)}$$

Here $C_{A,0}$ and V are fixed. Then to get $C_A = 0$, which is the condition to get 100 % fluorine across the reactor, it requires either a k_{eff} that is very large or a Q that is very small (large $\tau = \frac{Q}{V}$, long residence time) at $Q = 10000$ m/s, it should take 0.18 seconds but $k_{eff}$is not large enough.

When film diffusion is limiting, then the surface concentration of fluorine will be very small. This is also what happens when the flow rate of fluorine is not high enough. So, film resistance is limiting and the flow limitation in a CSTR lead to identical responses.

Table 6-2 shows the change in the residence time distribution in the system as the flowrate is varied.

Table 6-2: Summary of the effect of flowrate on the residence time and contact time of the system.

Flowrate (Q_0) (m^3/s)	τ_R (s)	τ_S (s)
1	1	0.488
10	0.1	0.049
100	0.01	0.005
1000 (baseline)	0.001	0.0005
10000	0.0001	0.00005

The table shows that as the flowrate increases the residence time and contact time of the reactor and the solid become smaller, meaning the particles spend less time in the reactor reacting. This is because the fluorine into the system is increased, which leads to very fast reaction rates. since the molecular weight of the solid and the gas differ by about a factor of a 1000, the reaction time for complete conversion at these flow rates without diffusion limitations would be of the order of seconds/milliseconds.

The Thiele modulus remains unchanged, as the diffusion and reaction rate were not varied. The reaction is very fast to require such a short contact time. The fluorine is almost all converted at the initial conditions. This is because of the chosen rate equations, in which the $C_g \times C_s$ actually yields large values and this high reaction rates. But since the molecular weight of the solid and the gas differ by about a factor of a 1000, the reaction time for a complete conversion at these flowrates without diffusion limitations would be of the order of seconds.

The pseudo-Thiele modulus was calculated for each reactant, based on the initial conditions. These are reported in Table 5-2.

6.2 Effect of reaction rate constant

The reaction rates k_j was varied according to Table 6-1, and the results are displayed and discussed below. The results are presented in sequential order.

The reaction rate does not affect the residence time distributions, but it does affect the pseudo-Thiele modulus, and is discussed at the end of this section.

Figure 6-9 are graphs showing the effect of reaction rate constants on the concentration of fluorine over time. And Figure 6-10 are graphs showing the effect of reaction rate constants on the fluorine concentration through the particle.

Figure 6-9(a) shows that at a very slow reaction rate the fluorine concentration profile does not go down.

Figure 6-9(d-e) shows the reaction time does not reduce below 1.8 seconds, even if the reaction rate constant is made much bigger than 100 m^3/mol.s. This represents the diffusion limited reaction rate in which the reaction rate can be considered infinitely fast, getting closer to the SCM, at least in the initial time of the reaction.

Furthermore, Figure 6-9(e) shows that for more than half the reaction time, fluorine does not reach the centre of the particle. It is consumed faster that it can diffuse into the particle. As the reaction proceeds it slows down and the fluorine that can then reach the core. This is typical of shrinking core type reactions, where the reaction rate is almost instantaneous and the rate of diffusion to the reaction front controls the rate of reaction. This is why as the reaction rate constant becomes greater than 10, there is almost no reduction in the reaction time, because the reaction time is determined by the rate of diffusion of fluorine.

There is the second effect of the reactor flow rate which controls the concentration of fluorine on the surface of the particle, it's the competition between k_{eff} and residence time τ. From the CSTR design equation (Eq 5-1), when $k_{eff} \times \tau \gg 1$ then the fluorine concentration is low on the external surface. If fluorine concentration is close to zero on the external surface, this ensures the minimum reaction time for complete conversion given $k_{eff} \times \tau$, which in this ccase is 1.8 seconds. Here τ is not changing. So as long as $k_{eff} \times \tau \gg 1$, by whatever means, the reaction time will approach 1.8 seconds and will never go below this.

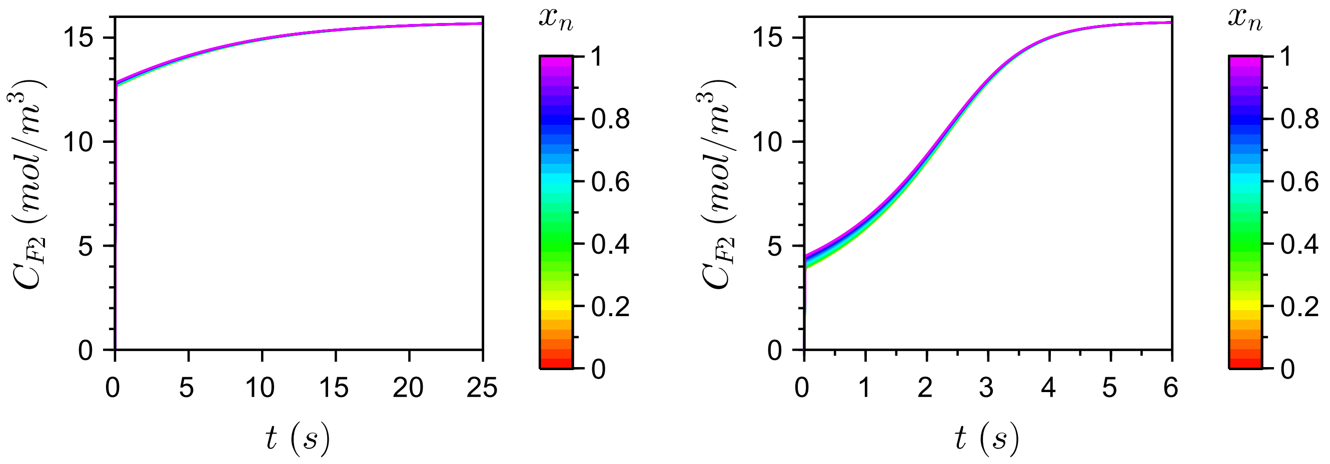

(a) k_j=0.01 (m³/mol.s)

(b) k_j=0.1 (m³/mol.s)

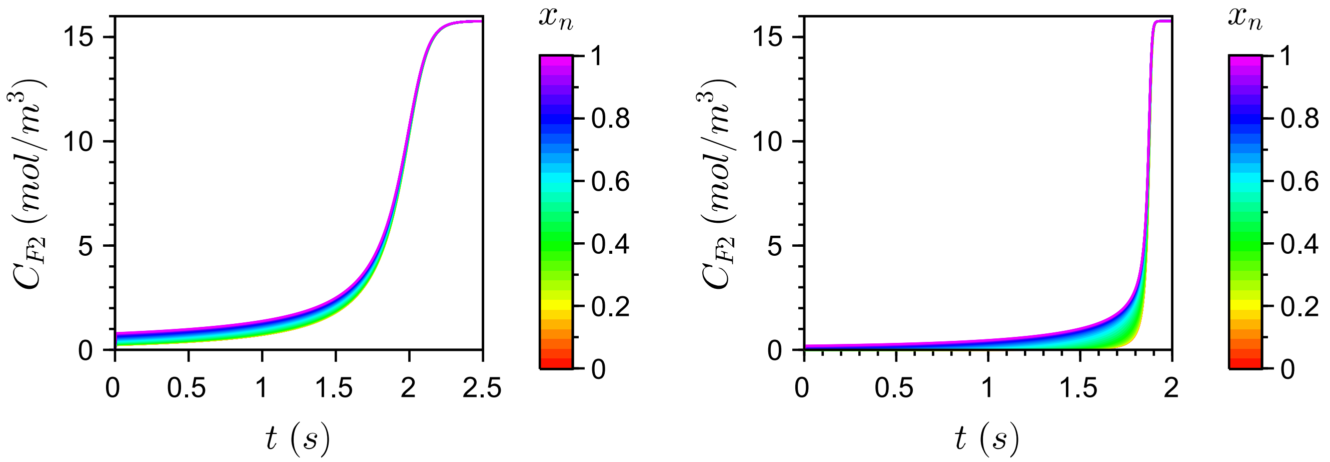

(c) k_j=1 (m³/mol.s)

(d) k_j=10 (m³/mol.s)

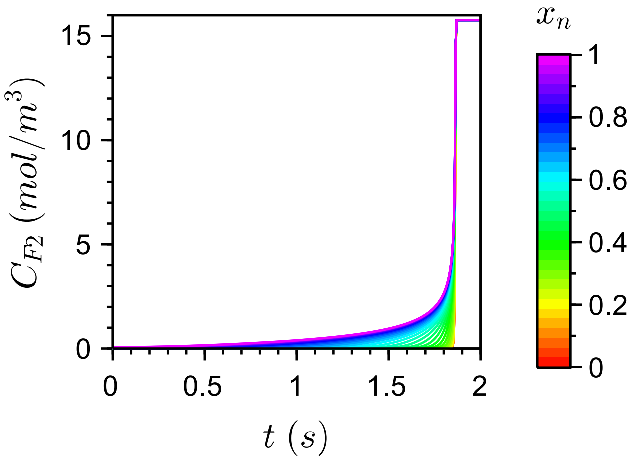

(e) k_j=100 (m³/mol.s)

Figure 6-9: Graphs showing the effect of reaction rate constant on fluorine concentration over time.

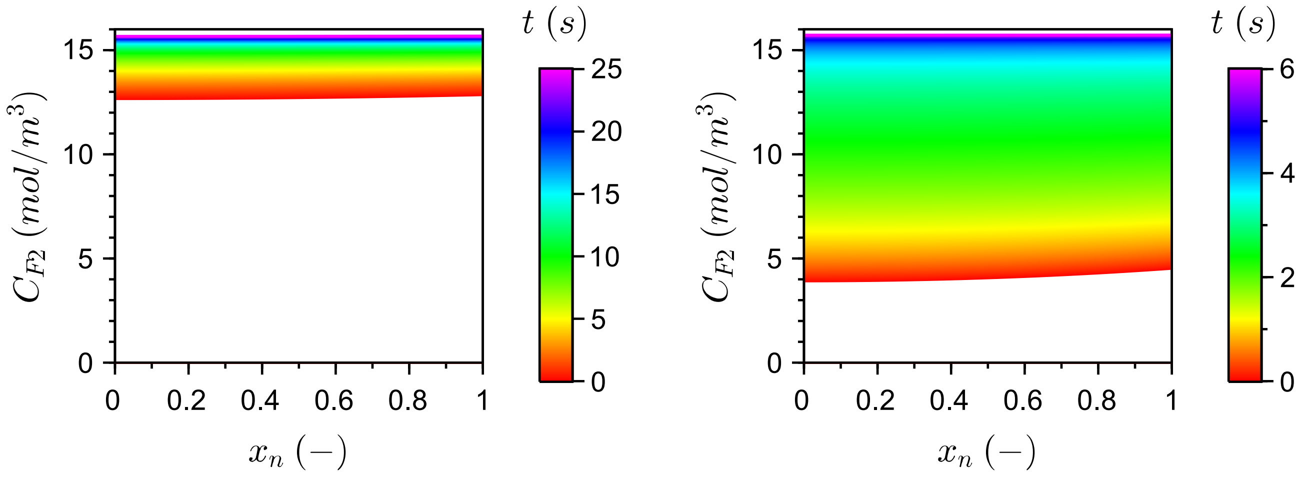

(a) k_j=0.01 (m³/mol.s) (b) k_j=0.1 (m³/mol.s)

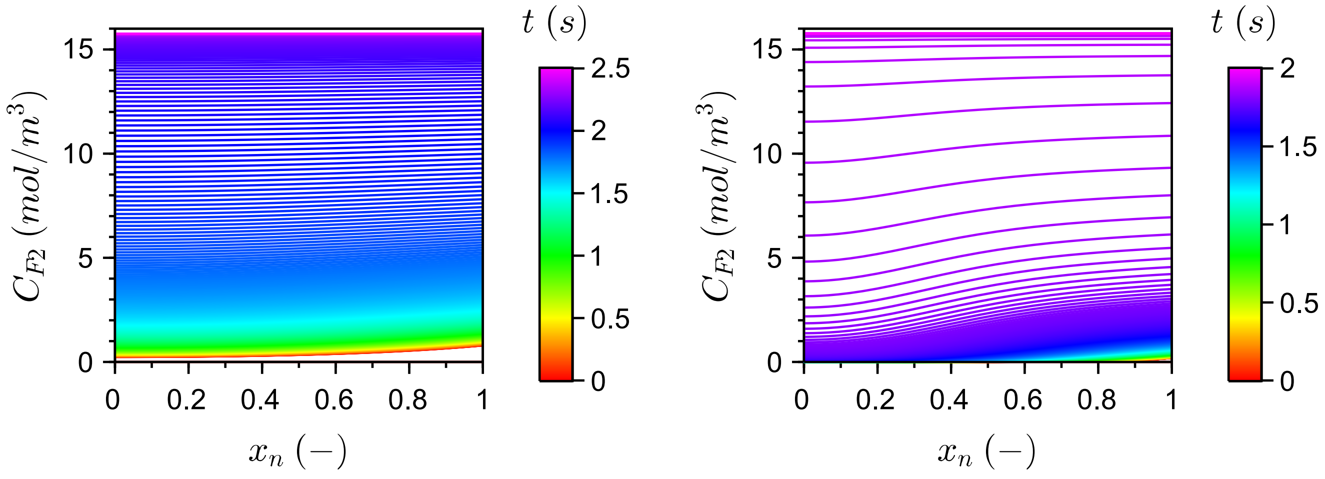

(c) k_j=1 (m³/mol.s) (d) k_j=10 (m³/mol.s)

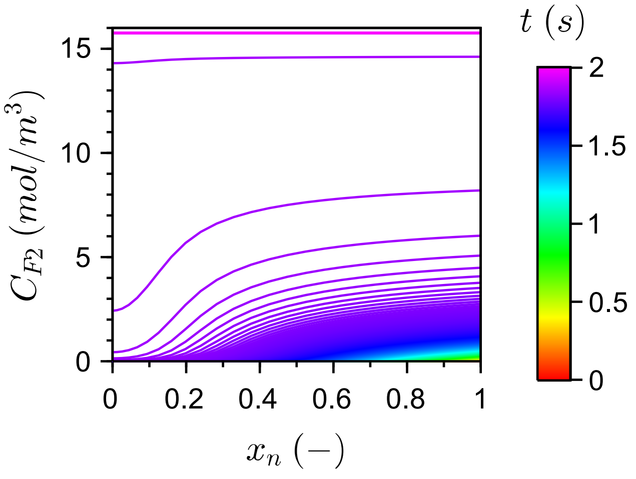

(e) k_j=100 (m³/mol.s)

Figure 6-10: Graphs showing the effect of reaction rate constant on fluorine concentration through the particle.

However, diffusion limitations can prevent k_{eff} from getting larger even as k_j is made larger, this is what we see and it suggests only mild diffusion limitations, even though the profiles are very steep (not easy to see) and actually the diffusion limitations are high. So, the flow rate becomes limiting and hides the magnitude of the diffusion effects. This is very subtle. The diffusion limitations are better observed when the particle size is varied.

The general trend shows that as the reaction rate is decreased, there is a lower limit, the diffusion-controlled reaction is increased. This is true for all reaction species in the system. There are two effects:

1. The high reaction rate constant means that the fluorine cannot penetrate the particle. This leaves less solid to react with. In contrast. the smaller rate constant ensures that the fluorine can react with the entire solid in the particle.
2. When the flow rate is increased, and the higher external fluorine concentration will penetrate all the way through the particle increasing the reaction rate. This would have minimal effect on the diffusion limited reaction, since the concentration of fluorine at the reaction front would remain close to zero.

The effects of the reaction rate are significant. At the lowest reaction rate, the concentration profile through the particle is flat, showing the same concentration of fluorine throughout the particle. The starting concentration of fluorine is higher for the lower reaction rate constant, as seen in Figure 6-10(a). This has less fluorine through the particle. As the reaction rate is increased, the concentration through the particle is still flat however the starting concentration of fluorine is much lower, as seen in Figure 6-10(b). The slow reaction rate constant has a slow reaction rate which means that there is more fluorine in the system to contaminate the oxygen.

As the reaction rate constant is increased further, there is a small concentration gradient at the beginning of the reaction. But the profile becomes horizontal as the reaction proceeds. This shows that the fluorine is consumed everywhere and the variation through the particle becomes more significant. This shows an increase in the diffusion limitations. This will be more clearly visible if the y-axis is converted to a log axis.

Figure 6-11 shows the effect of reaction rate constant on oxygen concentration over time. Figure 6-12 shows the effect of reaction rate constant on oxygen concentration through the particle.

These graphs mirror that fluorine concentration graphs, as oxygen is a product that is produced as the fluorine reacts with the particle. At small reaction rate constants, the concentration of oxygen through the particle is flat, showing a constant concentration through the particle at the various reaction rate constants. The concentrations are small, but the gradient is steep, so fluorine does not reach the centre of the particle. This is due to a fast reaction rate.

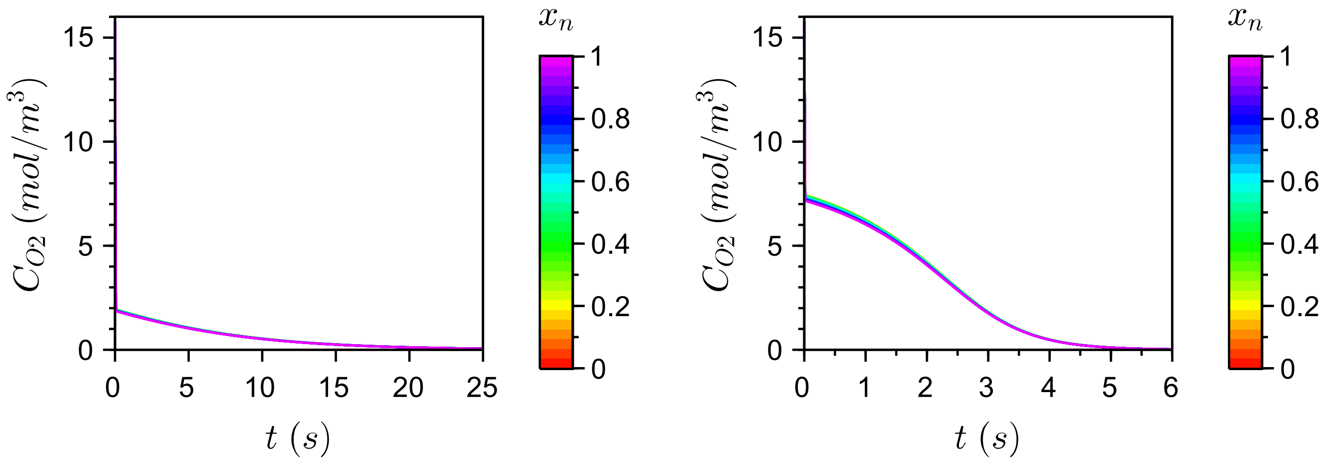

(a) k_j=0.01 (m3/mol.s)

(b) k_j=0.1 (m3/mol.s)

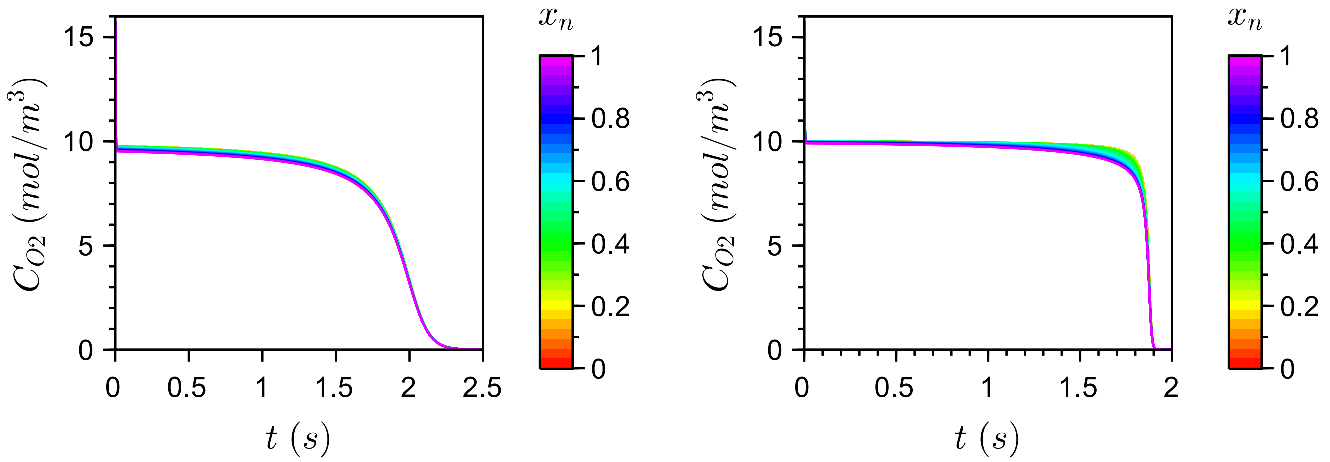

(c) k_j=1 (m3/mol.s)

(d) k_j=10 (m3/mol.s)

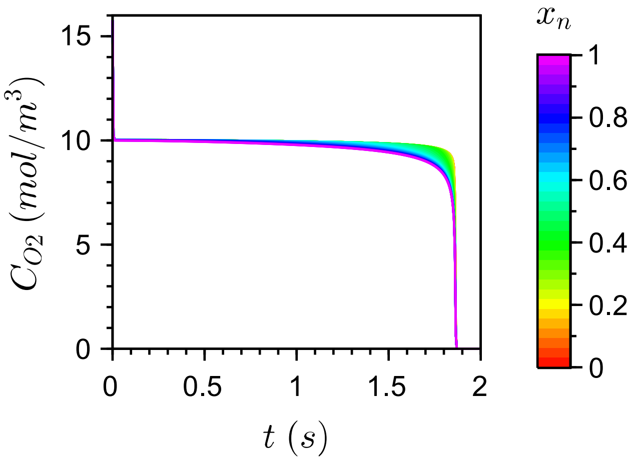

(e) k_j=100 (m3/mol.s)

Figure 6-11: Graphs showing the effect of reaction rate constant on oxygen concentration over time.

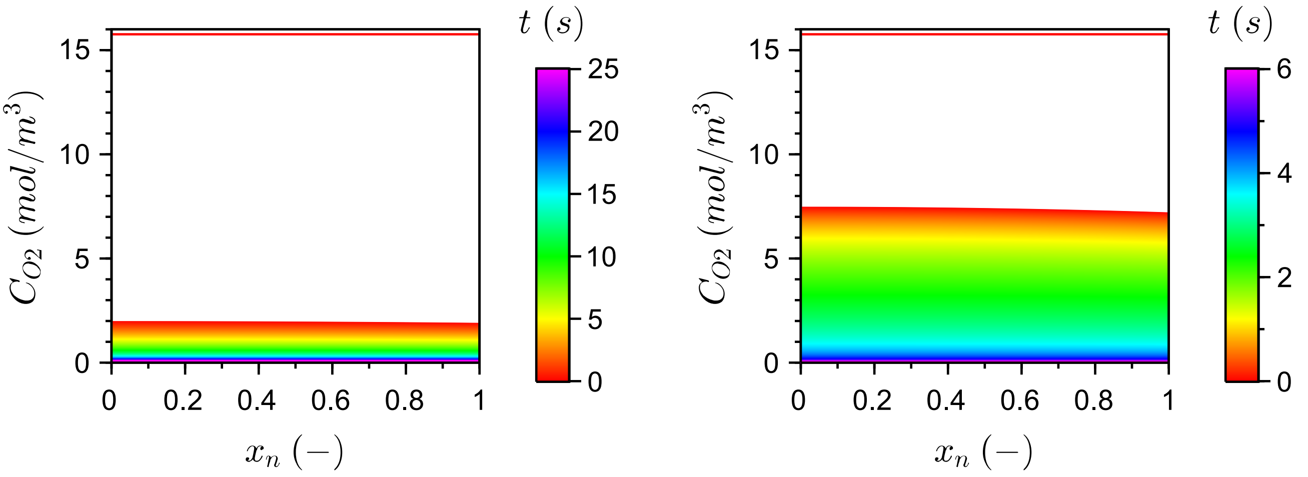

(a) k_j=0.01 (m3/mol.s) (b) k_j=0.1 (m3/mol.s)

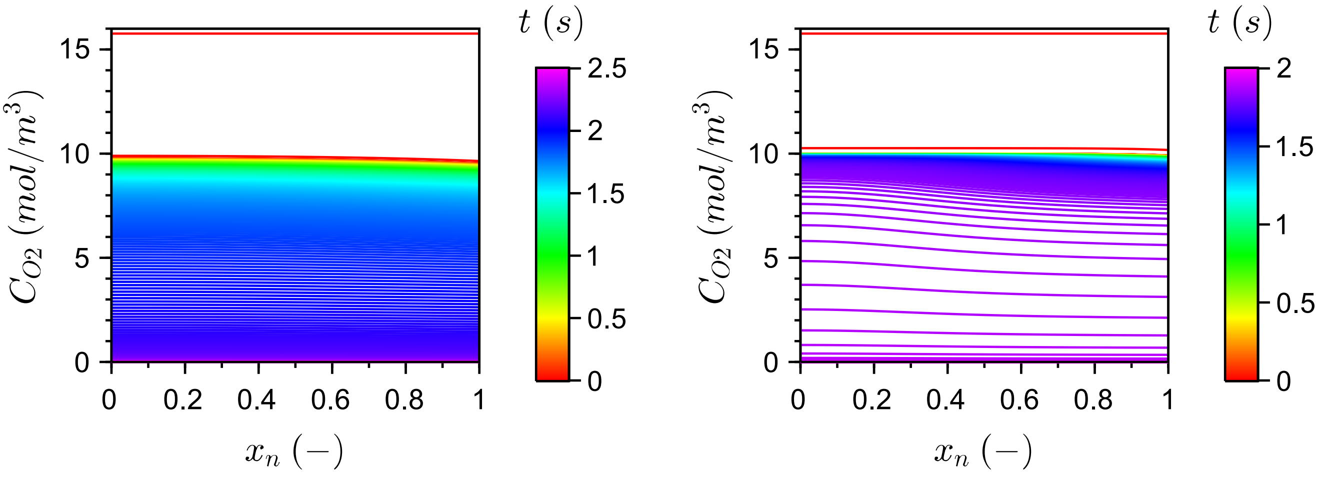

(c) k_j=1 (m3/mol.s) (d) k_j=10 (m3/mol.s)

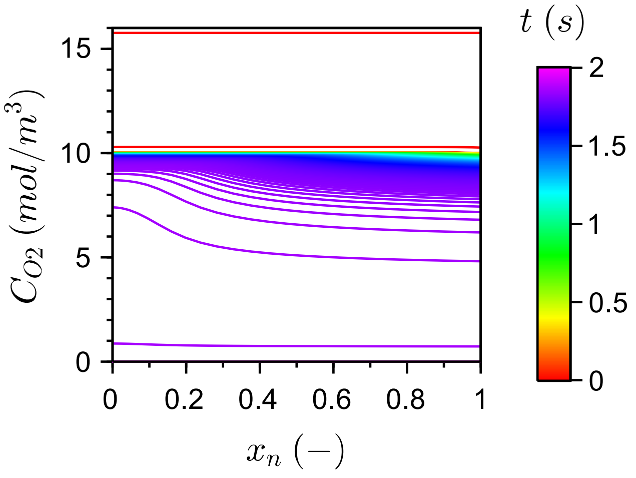

(e) k_j=100 (m3/mol.s)

Figure 6-12: Graphs showing the effect of reaction rate constant on oxygen concentration through the particle.

There are strong diffusion limitations that are not evident because the fluorine concentration is too low. The reactor residence time is hiding the true diffusion effects from being visible. Furthermore, Figure 6-12(a-b) show that the reaction rate is too slow to convert all the oxygen. This implies that the k_{eff} is too small and so $k_{eff} \times \tau$ is approximately 1. The reactor residence time is hiding the true diffusion effects from being visible.

Figure 6-13 shows the effect of reaction rate constant on the silicon dioxide concentration over time. And Figure 6-14 shows the effect of reaction rate constant on the silicon dioxide concentration through the particle.

The solid reactant concentrations show more detailed than the gas concentrations. The fluorine concentration is too low to see its impact on high reaction rates. The solids show clearly that the fluorine does not reach the centre of the particle and you get a reaction from progressing into the particle, like a shrinking core model. As the reaction rate increases, the solid reactant concentration profile over time and through the particle changes significantly. However, the solids do not diffuse. The profiles of the solids are due to the fluorine concentration into the system.

At the low reaction rate constants, the silicon dioxide has a flat profile through the particle, the same as fluorine concentration profile which is also high here. As the reaction rate constant is increased, the silicon dioxide concentration gradient through the particle increases significantly. It becomes steeper and looks like a wave moving through the particle over time. The concentration at the surface is smaller than at the centre. The reaction rate constant increases the reaction rate. It closely approximates an instantaneous reaction, and access into the particle is a result of gaseous reactants diffusing into the particle. As the reaction rate increases, the fluorine gets consumed before it gets to the centre of the particle. The fluorine experience strong diffusion limitations which give rise to the steep gradients, that resemble a wave front, both over time and through the particle. The Knudsen diffusion and the model formation do not account for the interaction between diffusion species, for that one would need a Maxwell-Stefan formulation.

At the highest reaction rate constant, shown in Figure 6-10(e), the reaction front resembles the shrinking core model. This happens because the fluorine is consumed by reaction before it can reach the centre of the particle. The slope of the profile is almost constant across the whole particle.

Figure 6-13 shows the effect of the reaction rate constant on conversion of silicon dioxide over time.

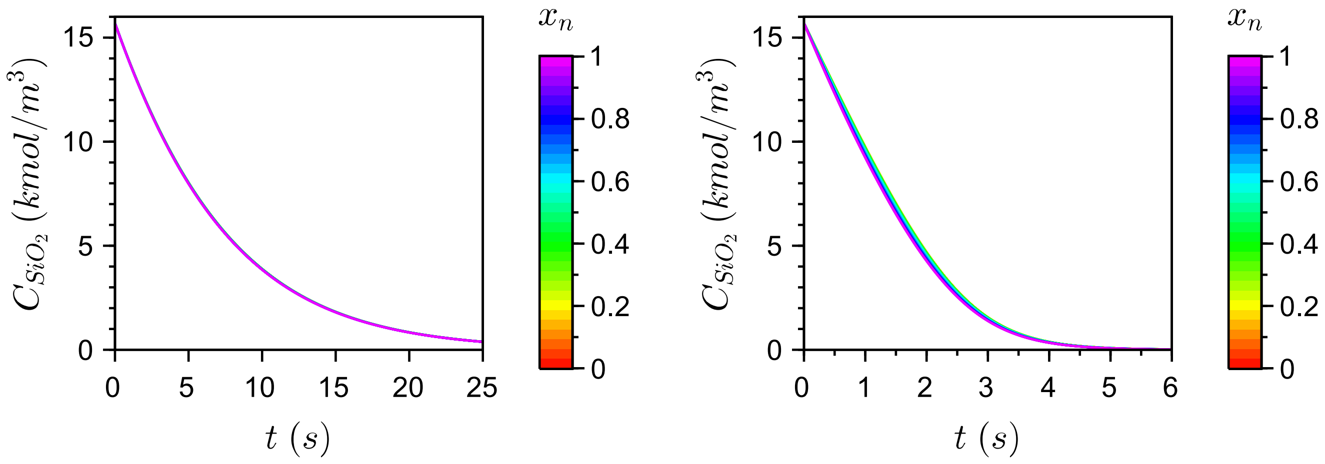

(a) k_j=0.01 (m3/mol.s)

(b) k_j=0.1 (m3/mol.s)

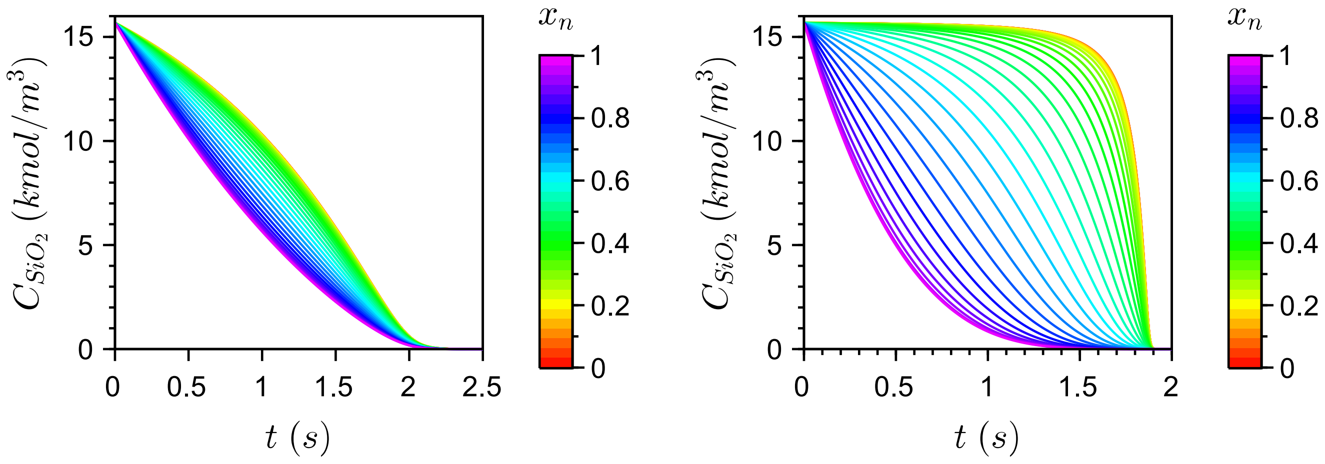

(c) k_j=1 (m3/mol.s)

(d) k_j=10 (m3/mol.s)

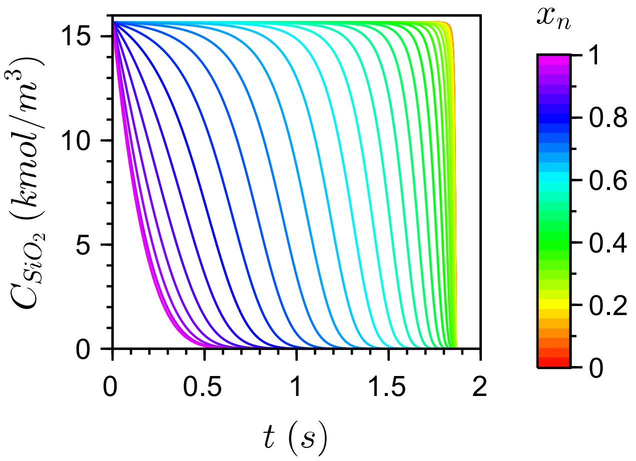

(f) k_j=100 (m3/mol.s)

Figure 6-13: Graphs showing the effect of reaction rate constant on the silicon dioxide concentration over time.

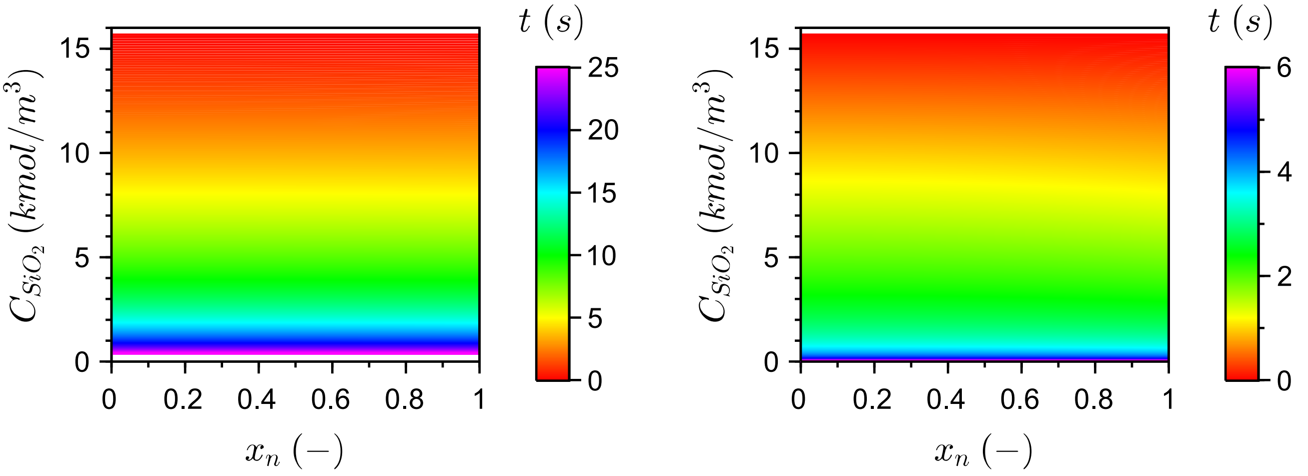

(a) k_j=0.01 (m3/mol.s) (b) k_j=0.1 (m3/mol.s)

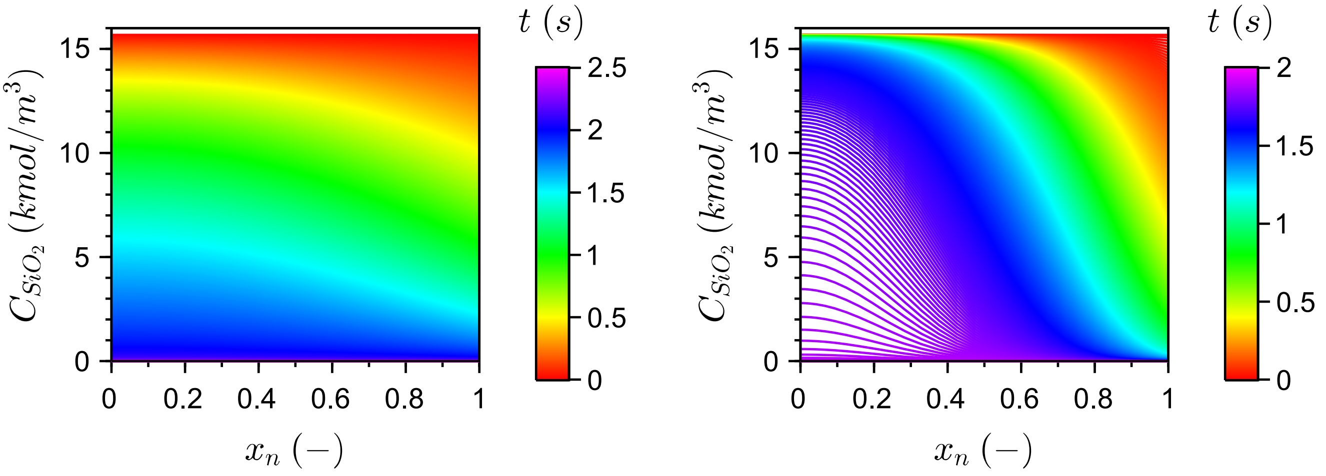

(c) k_j=1 (m3/mol.s) (d) k_j=10 (m3/mol.s)

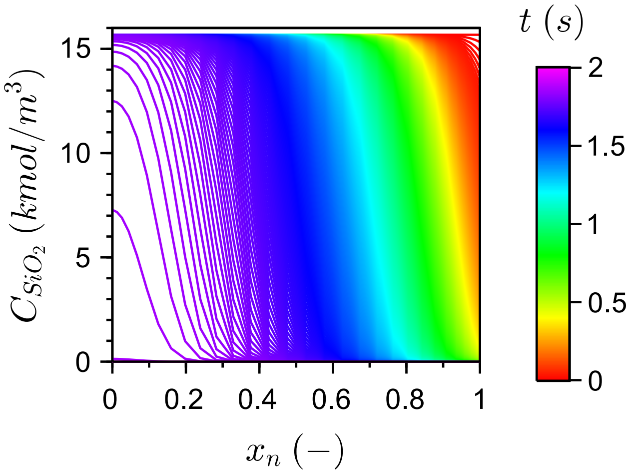

(e) k_j=100 (m3/mol.s)

Figure 6-14: Graphs showing the effect of reaction rate constant on the silicon dioxide concentration through the particle.

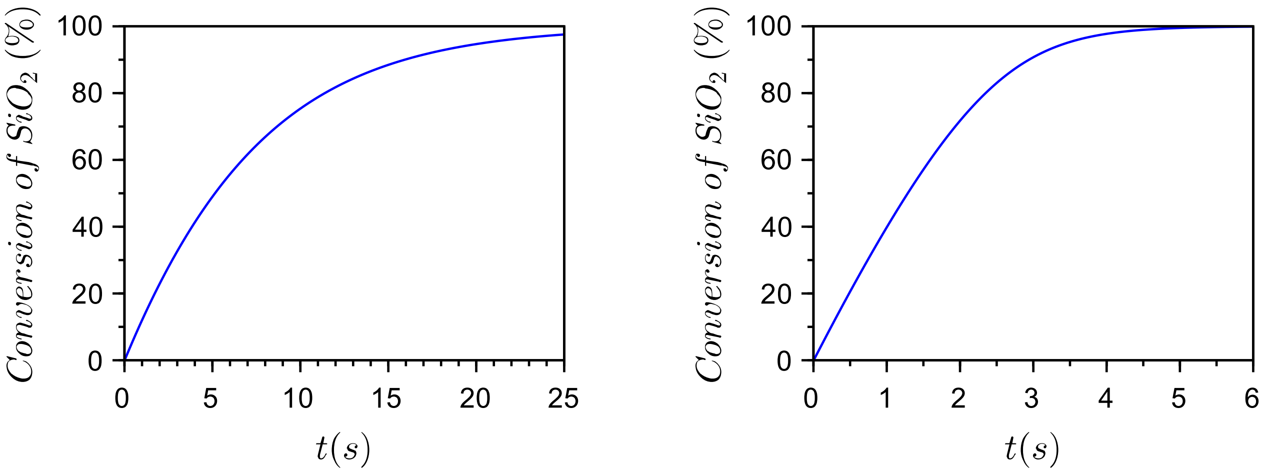

(a) k_j=0.01 (m3/mol.s) (b) k_j=0.1 (m3/mol.s)

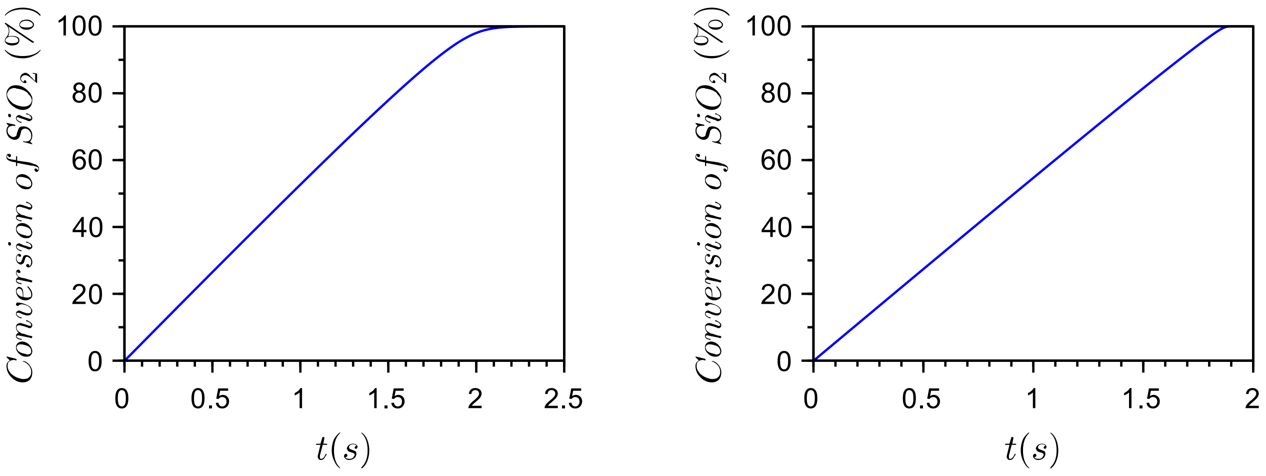

(c) k_j=1 (m3/mol.s) (d) k_j=10 (m3/mol.s)

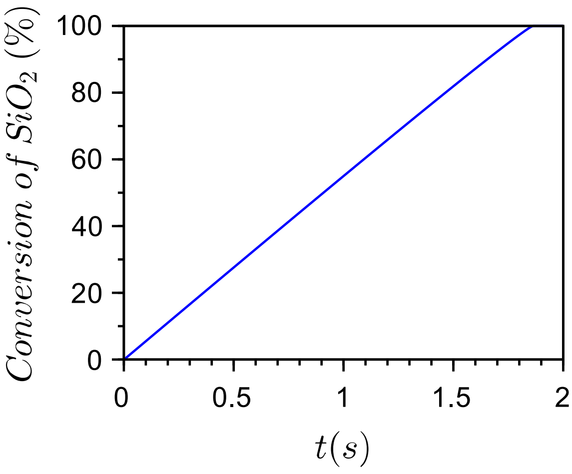

(e) k_j=100 (m3/mol.s)

Figure 6-15: Graphs showing the effect of reaction rate constant has on conversion of silicon dioxide over time.

The trend shows that as the reaction rate constant is increased, the gradient of the conversion becomes steeper and more linear. At the low reaction rates, the gradient is concave. The conversion happens faster at the beginning of the reaction, as slows down towards the end and the diffusion limitation becomes negligible, so the graphs approach 1 asymptotically like the slow reaction ones. This shows the reaction-controlled regime is controlling the reaction system. As the reaction rate constant increases becomes linear, and the conversion progresses at the same rate as the reaction proceeds, showing that the system become more diffusion controlled.

Figure 6-15(a) shows no mass transfer limitations and a reaction-controlled conversion. The conversion proceeds via a second-order reaction. As the reaction rate constant is increased, the system becomes more diffusion controlled and the conversion profile starts changing shape, shown in Figure6-15(b).

Figure 6-15(c-d) shows that the system changes from mass transfer limited at short reaction times to reaction limited at long reaction times, since the reaction slows down over time, the diffusion limitations become negligible. The more linear the initial region, and the steeper the slope, the more likely diffusion will control the reaction rate and the conversion.

Figure 6-15(e) conversion profile shows that the system is diffusion-controlled reaction which is a nearly instantaneous reaction. The conversion proceeds via a shrinking core model. There must be some diffusion limitations in the system or else the reaction time would be closer to 1.8 seconds. This means the k_{eff} increases to an upper limit at which the reaction becomes completely limited by diffusion.

The residence time is not affected by the reaction rate and is not reported here.

The pseudo-Thiele modulus is affected by the change in the reaction rate. Table 6-3 summarizes the changes in the calculated pseudo-Thiele modulus for each variation.

Table 6-3: Summary of the calculated pseudo-Thiele modulus for each reaction rate.

Reactant Name	Φ a. $k_{1\text{-}6}$=0.01	Φ b. $k_{1\text{-}6}$=0.1	Φ (base case) c. $k_{1\text{-}6}$=1	Φ d. $k_{1\text{-}6}$=10	Φ e. $k_{1\text{-}6}$=100
R1	0.094	0.296	0.937	2.963	9.368
R2	0.017	0.054	0.169	0.536	1.694
R3	0.040	0.126	0.399	1.263	3.995
R4	0.048	0.151	0.477	1.508	4.770
R5	0.052	0.163	0.516	1.630	5.155
R6	0.049	0.154	0.486	1.537	4.859

If you look at the CSTR equation, Eq 5-1, $k_{eff} = \eta \times k$, where η is the effectiveness factor. The larger Thiele modulus means a smaller η and k_{eff}. However, the situation is more complicated. $k_{eff} = \eta \times k_j$. As k_j increases, Thiele modulus and η decreases, which means that k_{eff} increases much slower than k_j.

Again, the pseudo-Thiele modulus increases as the reaction rate increases, but it does not follow the expected catalyst limits and definitions shown in Section 4.6 and Figure 4-6. At the low reaction rates, the small pseudo-Thiele modulus shows that there are no diffusion limitations, and the profiles are flat. As the reaction rate is increased, the pseudo-Thiele modulus increases, and the system has increased diffusion limitations, and the profiles get steeper.

6.3 Effect of particle size

The particle size R_p was varied according to Table 6-1, and the results are displayed and discussed below. The results are presented in sequential order.

The particle radius does not affect the rate constant of the system and the reaction rate. It does affect the pseudo-Thiele modulus and thus will influence the diffusion resistance experienced by the reaction. This is reported and is discussed at the end of this section.

Figure 6-16 shows the effect particle size has on fluorine concentration over time. And Figure 6-17 shows the effect particle size has on fluorine concentration through the particle.

At a small particle size, we see no mass transfer limitations. The reaction cannot proceed faster than under these conditions, the rate of reaction is limited by the supply of fluorine. The supply of fluorine is slow enough to not introduce diffusion limitations, as seen in Figure 6-16(a-b). As the particle size increases, there is strong diffusion limitations in the system. The reaction rate is slowed down a lot because of the relationship to the particle size $\left(R_p{}^2\right)$, so the effect becomes evident very fast.

Figure 6-17(a-b) shows the fluorine concentration remains low in the particle, so there is no concentration gradient. The fluorine is not limited by diffusion but is limited by the supply of fluorine from the feed. The reaction proceeds as a reaction front, fluorine cannot penetrate the particle as the diffusion is too slow and the reaction consumes the fluorine before it can penetrate the particle. As the reaction proceeds, the reaction rate slows down, and the gradient becomes less steep, as seen in Figure 6-17(e).

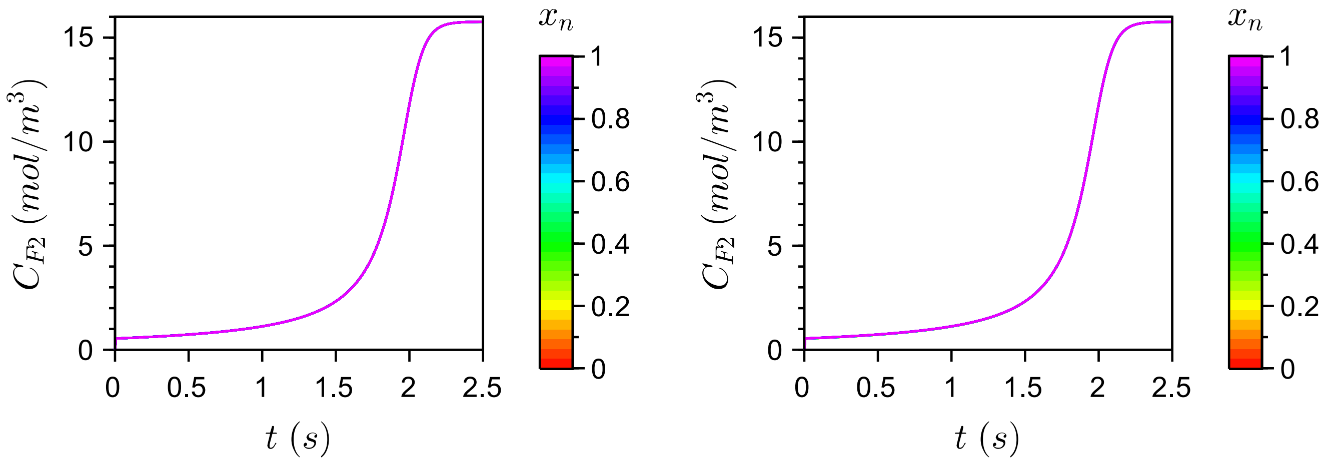

(a) R_p=0.35 μm

(b) R_p=3.5 μm

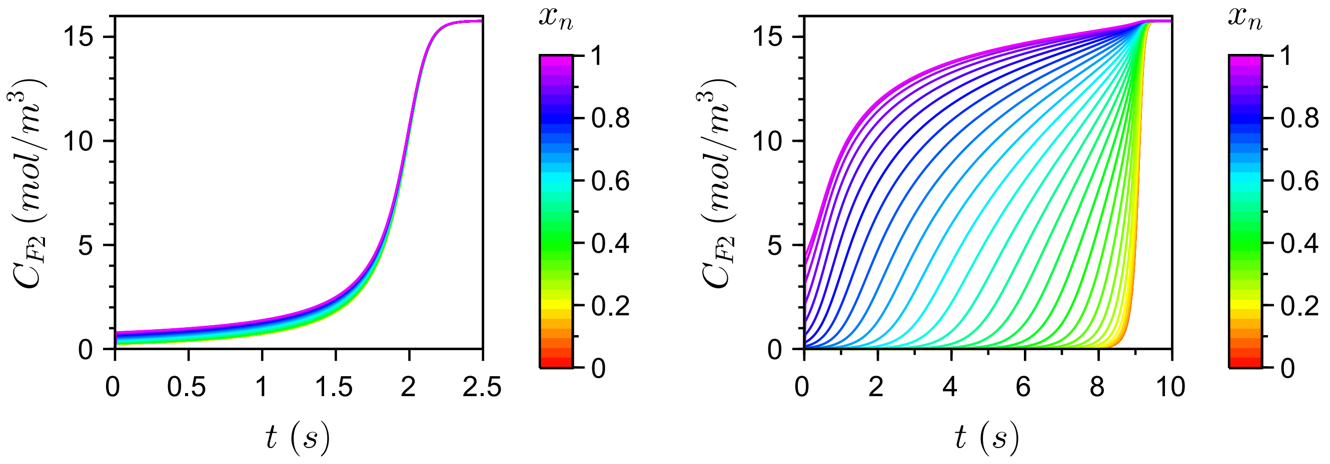

(c) R_p=35 μm

(d) R_p=350 μm

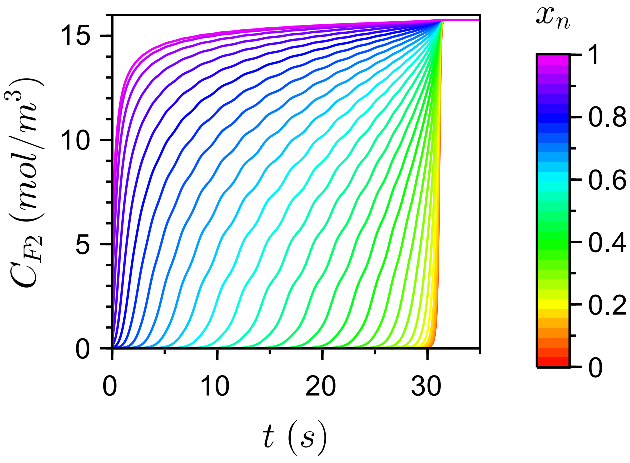

(e) R_p=700 μm

Figure 6-16: Graphs showing the effect of particle size on fluorine concentration over time.

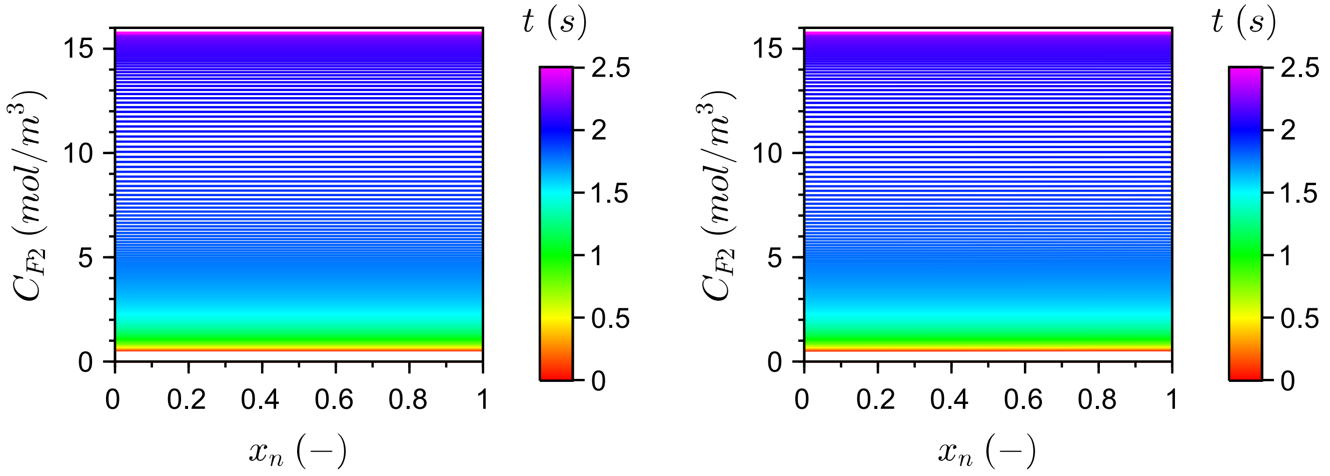

(a) R_p=0.35 μm (b) R_p=3.5 μm

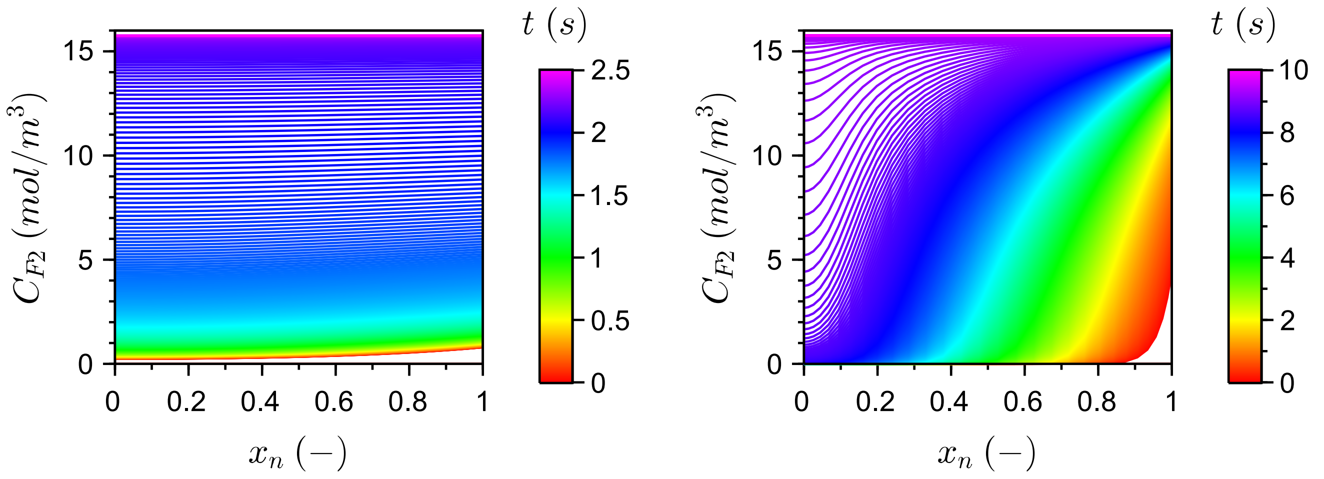

(c) R_p=35 μm (d) R_p=350 μm

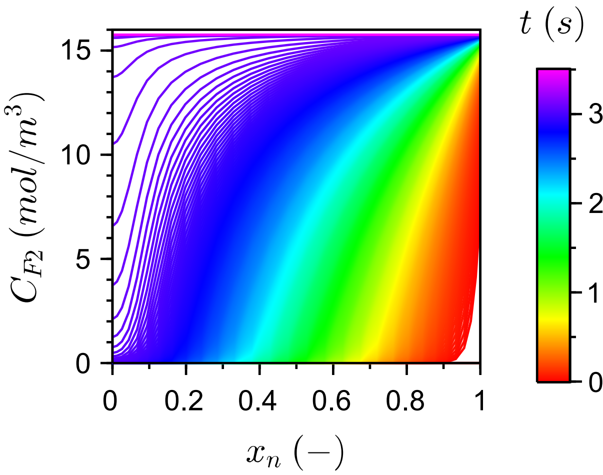

(e) R_p=700 μm

Figure 6-17: Graphs showing the effect of particle size on fluorine concentration through the particle.

The particle size has a significant effect on the fluorine concentration profile over time. The trend shows that increasing particle size increases the reaction time. The gradient becomes steeper and starts to resemble a wave through the particle, like a SCM. The bigger particle takes more time to react.

At small particle sizes, there is no concentration gradient through the particle. The profiles are flat through the particle. This shows that the particle is reaction controlled. The reaction is slower than the diffusion of fluorine through the particle. The reaction is limited by the supply of reactant from the feed, for example, if you increase the feed rate you will increase the reaction rate.

Figure 6-18 shows the effect of particle size on the oxygen concentration profile over time. And Figure 6-19 shows the effect of particle size on the oxygen concentration through the particle.

These graphs mirror the fluorine concentration over time graphs, as oxygen is being produced as the particle and fluorine are being consumed. As the particle size is increased, the profiles become steeper, and the diffusion limitations become more prominent. As the particle size increases, the concentration of oxygen on the surface is lower than the oxygen concentration at the centre of the particle.

When the particle size is small, the concentration gradient through the particle is flat. There is no difference in the concentration between the surface and centre of the particle, indicating that the reaction happens at the same rate all through the particle. And a constant production of maximum oxygen concentration over the reaction time.

As the particle size increases, the gradients through the particle become steeper, showing that the diffusion limitations increase. The concentration of oxygen at the surface of the particle is less than the oxygen concentration at the centre of the particle. The reaction is faster at the surface, producing more oxygen which prevents the fluorine from diffusion to the centre of the particle.

The oxygen concentration at the particle surface ($x_n = 1$) is the concentration in the reactor. At the largest particle size (Figure 6-18(e)) shows that the oxygen concentration is very low, so the product stream will contain high amounts of fluorine.

Particle size is diffusion limiting because oxygen and products can’t diffuse out faster than they are being produced as the reaction proceeds.

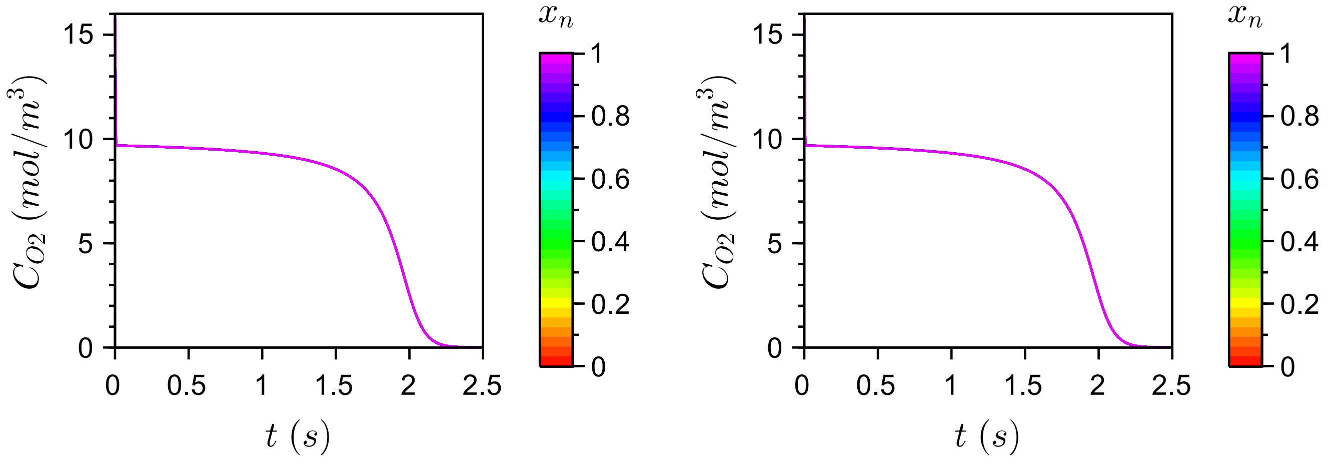

(a) R_p=0.35 μm (b) R_p=3.5 μm

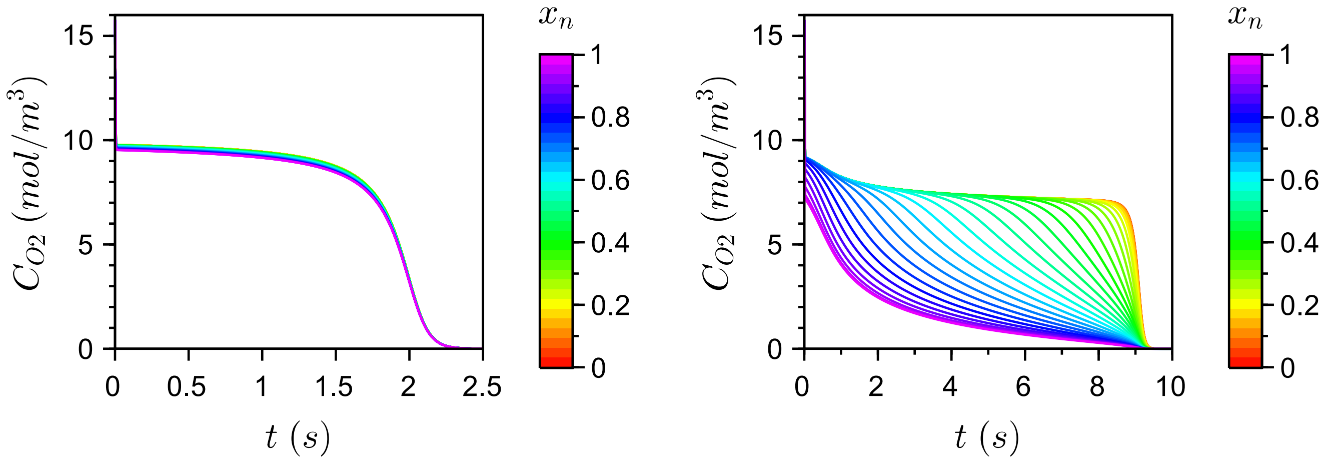

(c) R_p=35 μm (d) R_p=350 μm

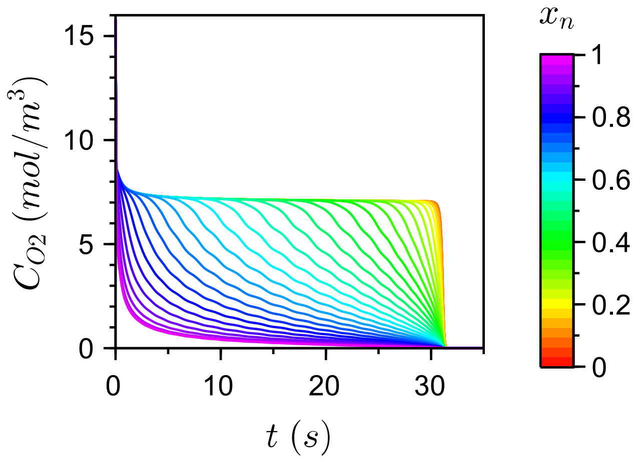

(e) R_p=700 μm

Figure 6-18: Graphs showing the effect of particle size on oxygen concentration over time.

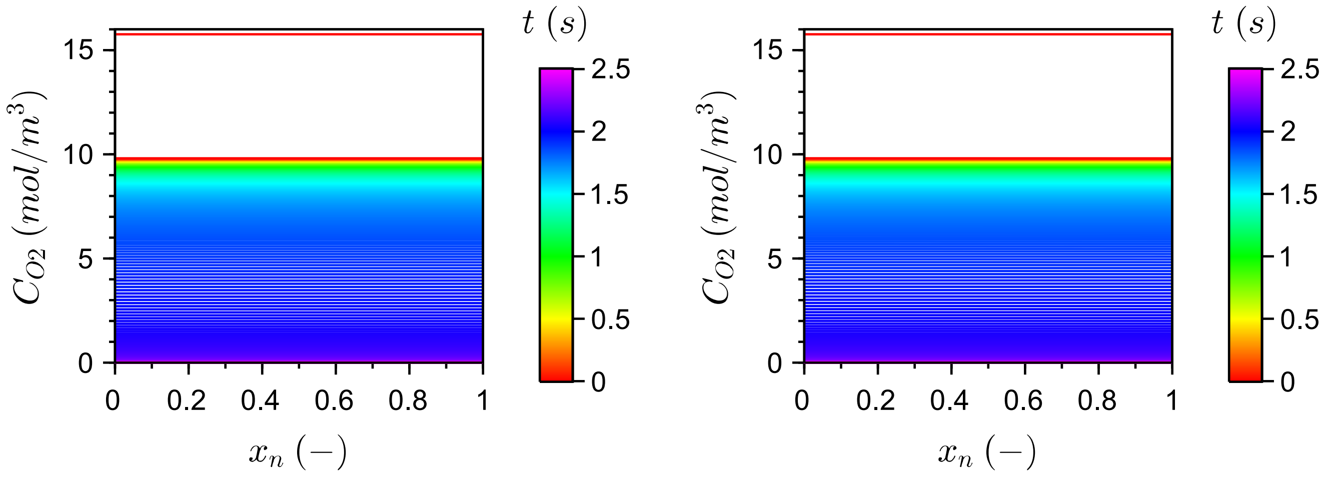

(a) R_p=0.35 μm

(b) R_p=3.5 μm

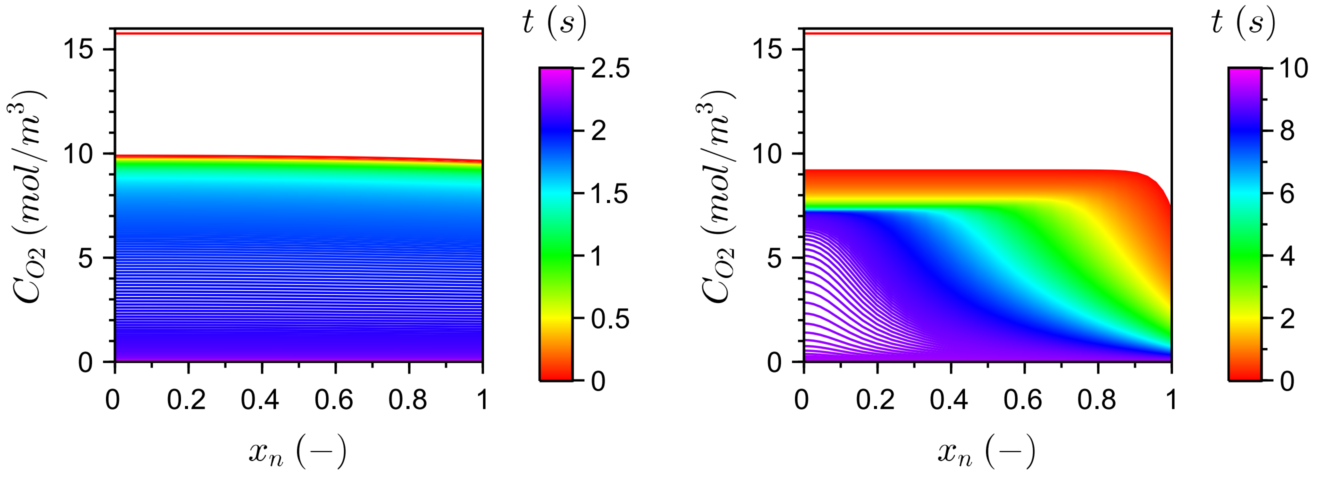

(c) R_p=35 μm

(d) R_p=350 μm

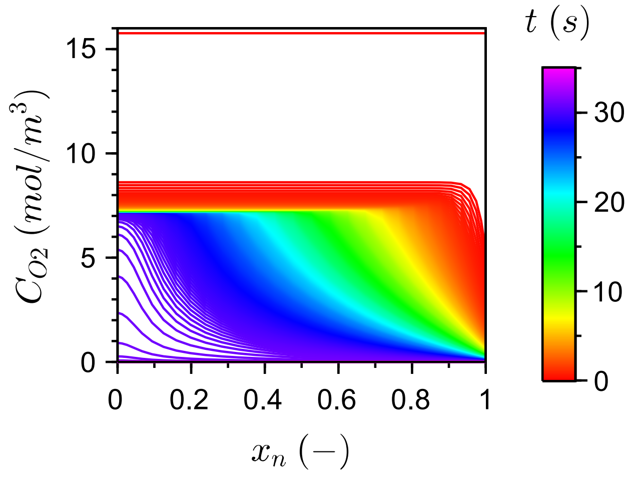

(e) R_p=700 μm

Figure 6-19: Graphs showing the effect of particle size on the oxygen concentration through the particle.

Figure 6-20 shows the effect of particle size on silicon dioxide concentration over time. And Figure 6-21 shows the effect of the of particle size on silicon dioxide concentration through the particle.

When the particle size is small, it shows flat profiles through the particle and a linear decrease with time. As the particle size is increased, the profiles become very steep. The silicon dioxide at the surface is lower than at the centre of the particle. The solids profile is due to the gas concentration profiles. When the particle size is small, the fluorine concentration is constant through the system which leads to a constant reaction rate profile, and even consumption of the silicon dioxide in the particle and a linear decrease with time.

As the particle size increases the concentration profiles become steeper and start to resemble the SCM. The reaction rate constant has not changed, in fact the reaction rate has slowed down, it is taking longer to react. There is now a much longer reaction path, while the rate of diffusion has not changed. This means that fluorine cannot make it all the way to the centre of the particle before it is consumed because the reaction path is too long. The reactants in the big particles have to diffuse orders of magnitude further to effect complete conversion than for the small particles.

Figure 6-22 shows the effect that particle size has on conversion of the silicon dioxide over time.

As the particle size increases the conversion gradient becomes less linear and more concave. This shows that the conversion gradient changes as the diffusion limitations increase in the system.

Since the reactants are limited by diffusion, the reaction time does not increase linearly with increasing particle size. The size was increased in factors of 10, and there is no time increase until the particle size is in the order of magnitude of 10^{-4}. At this point, and as it increases by factors of 10, the time increases from 2.5 seconds to 10 seconds to 35 seconds. This shows that the reaction time is not linearly increasing with particle radius increases. It is flat at first, and then increases exponentially. This is true for all the concentration profiles.

As the particle size increases, the conversion profile starts to resemble the shrinking core model, as seen in Figure 6-22(e). The shape of the gradient resembles that of the reaction rate control system shown in reference Figure 6-8.

The pseudo-Thiele modulus is affected by the change in the particle size. Table 6-3 summarizes the changes in the calculated pseudo-Thiele modulus for each variation.

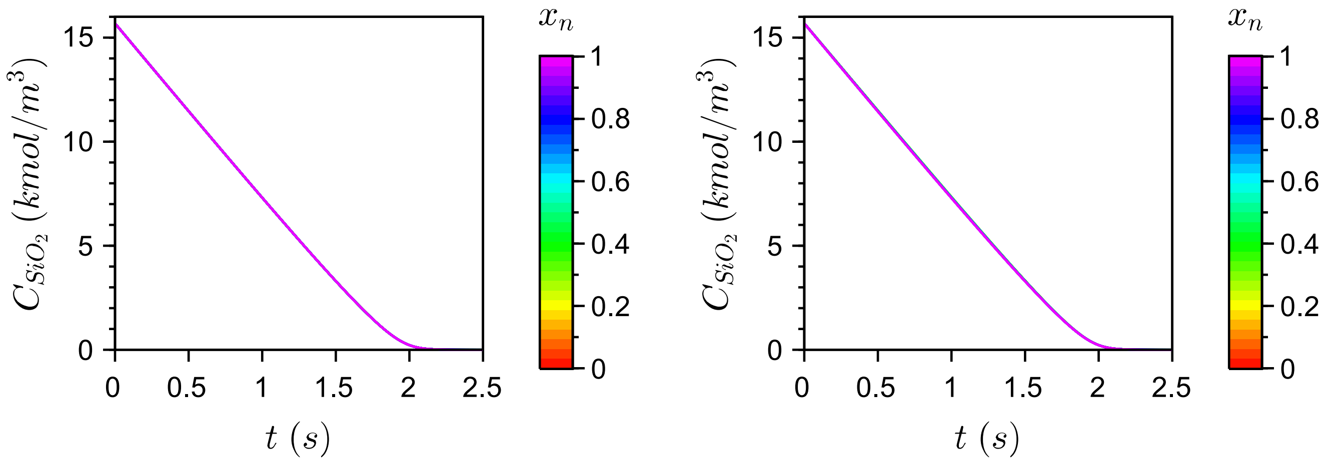

(a) R_p=0.35 μm

(b) R_p=3.5 μm

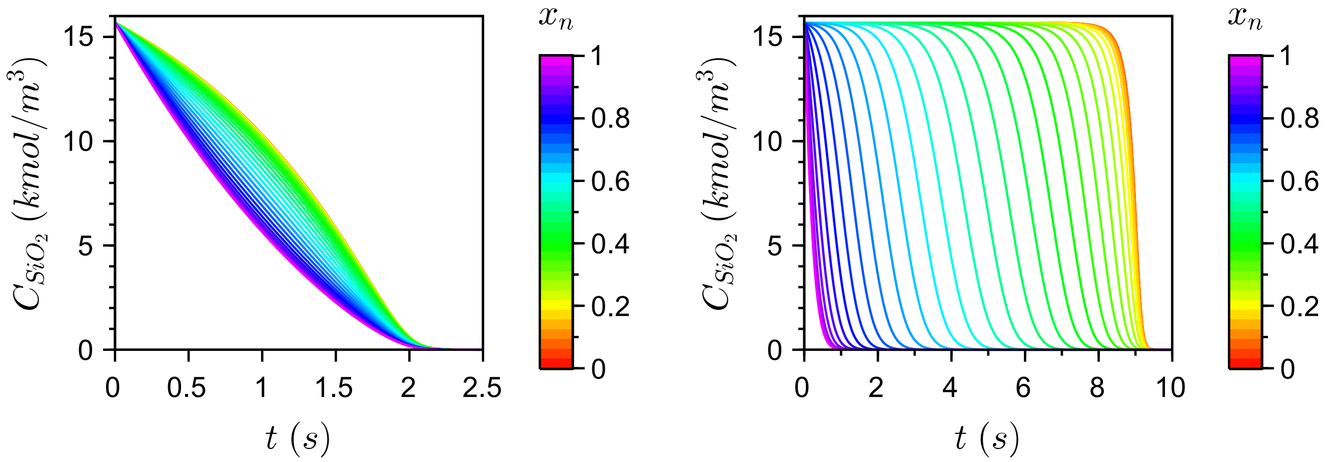

(c) R_p=35 μm

(d) R_p=350 μm

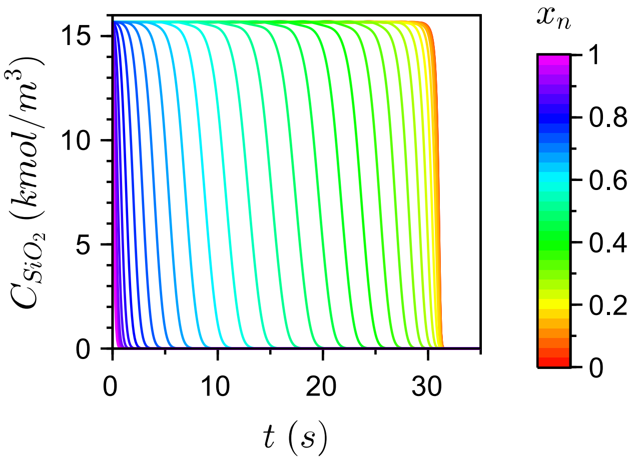

(e) R_p=700 μm

Figure 6-20: Graphs showing the effect of particle size on silicon dioxide concentration over time.

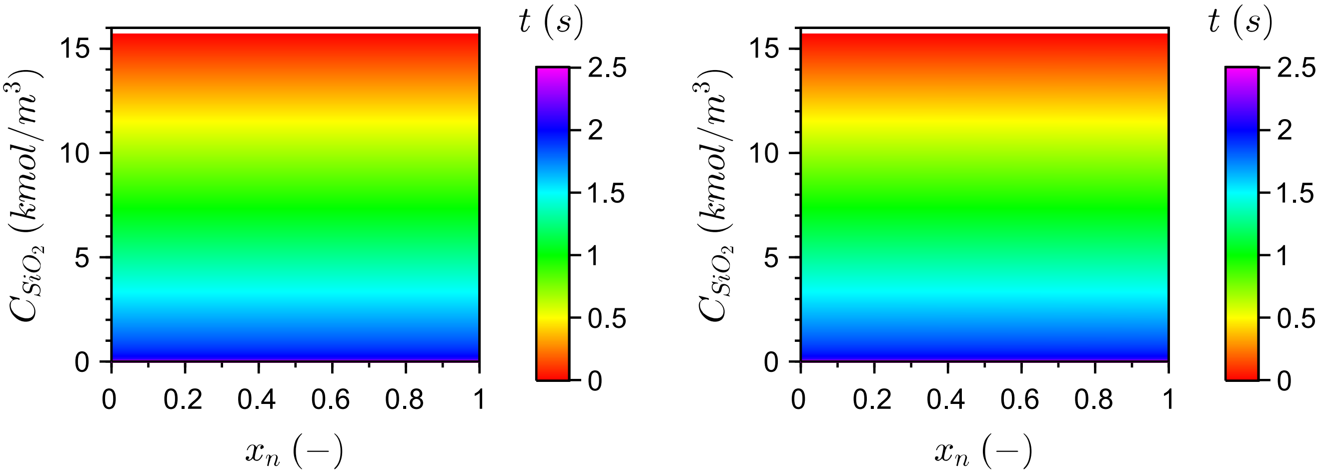

(a) R_p=0.35 μm

(b) R_p=3.5 μm

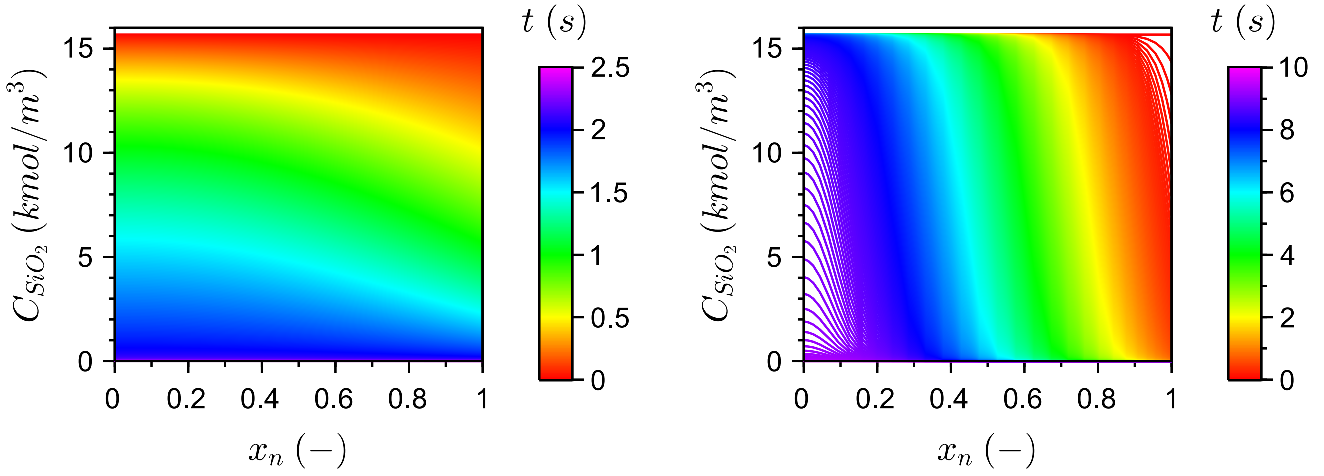

(c) R_p=35 μm

(d) R_p=350 μm

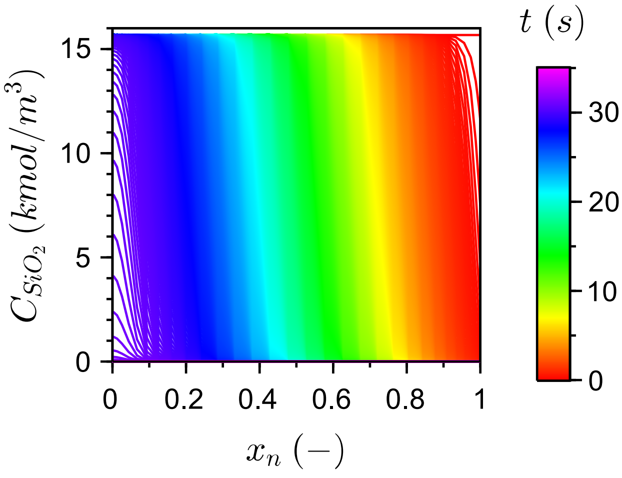

(e) R_p=700 μm

Figure 6-21: Graphs showing the effect of particle size on silicon dioxide concentration through the particle.

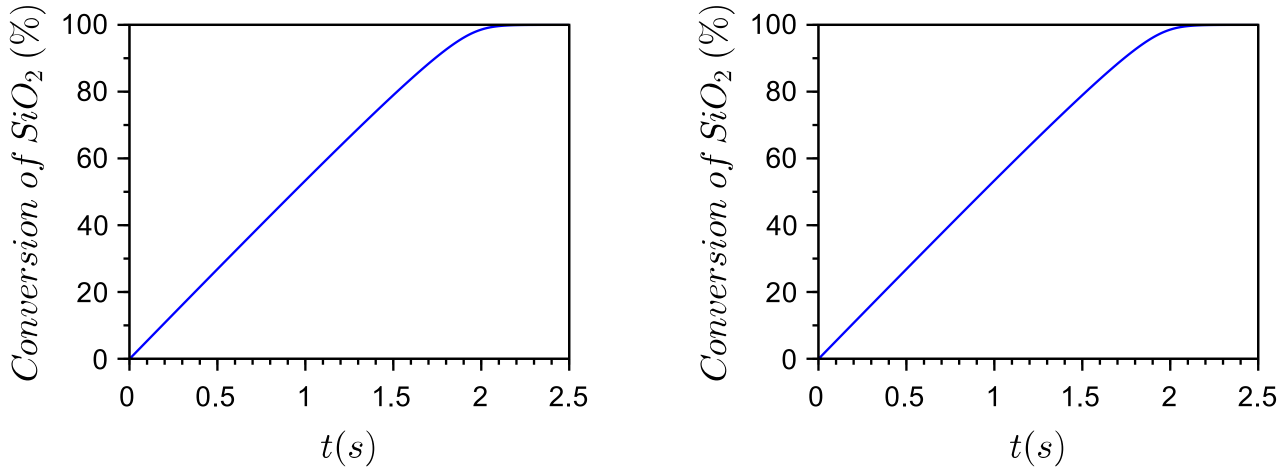

(a) R_p=0.35 μm (b) R_p=3.5 μm

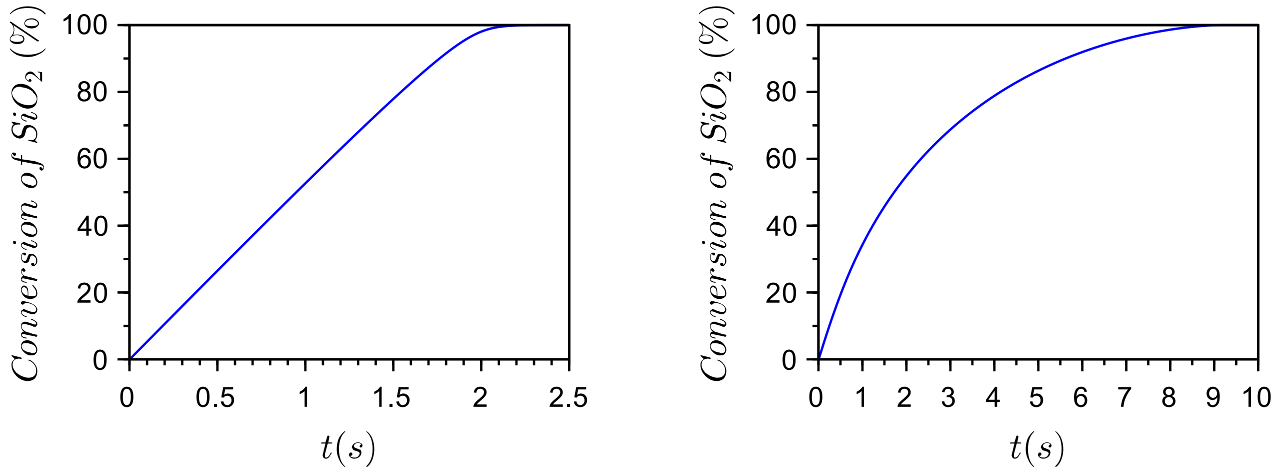

(c) R_p=35 μm (d) R_p=350 μm

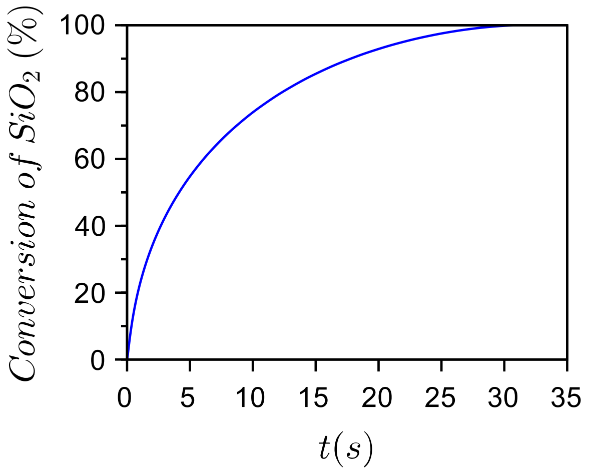

(e) R_p=700 μm

Figure 6-22: Graphs showing the effect that particle size has on the conversion of silicon dioxide.

Table 6-4: Summary of the calculated pseudo-Thiele modulus for each particle size.

Reactant Name	Φ a. R_p=0.35 μm	Φ b. R_p=3.5 μm	Φ (base case) c. R_p=35 μm	Φ d. R_p=350 μm	Φ e. R_p=700 μm
R1	0.009	0.094	0.937	9.368	18.737
R2	0.001	0.017	0.169	1.694	3.389
R3	0.004	0.040	0.399	3.995	7.989
R4	0.005	0.048	0.477	4.770	9.540
R5	0.005	0.052	0.516	5.155	10.310
R6	0.005	0.049	0.486	4.859	9.718

The pseudo-Thiele modulus increases with an increase in the particle size. This shows an increase in the diffusion limitations in the system and leads to a variation between the surface and centre species concentrations and porosity.

6.4 Effect of all three parameters by reaction time

In the previous sections, the effect of varying each parameter was analysed in isolation. In this section, they will be analysed jointly, according to a fast reaction time and a slow reaction time. Table 6-5 summarizes each parameter and the reaction times. Analysing the system according to reaction time will also aid in the design of the reactor configuration system.

Table 6-5: Summary of each parameter and the reaction times.

	Flow rate	Reaction rate	Particle size
Reaction time			
$t = 2.5\ s$	$Q_0 = 1000$ m³/s	$k_j = 10$ m³/mol.s	$R_p = 3.5\ \mu m$
$t = 20\ s$	$Q_0 = 100$ m³/s	$k_j = 0.01$ m³/mol.s	$R_p = 700\ \mu m$

Figure 6-23 shows the effect each parameter has on the fluorine and oxygen concentration through the particle over a short reaction time. Figure 6-24 shows the effect each parameter has on the silicon dioxide concentration and through the particle and conversion profile over a short reaction time.

At the fast reaction time, Figure 6-23(a, c and e) shows almost flat fluorine concentration profiles through the particle. The oxygen profiles in Figure 6-23(b, d and f) mirror the fluorine profiles. Therefore, there is a constant production of oxygen through the particle at the slow reaction time and under these conditions. The slight gradient in the concentration profiles implies that there are still slight diffusion limitations in the system under these conditions. The most diffusion limitations are experienced when the system is reaction-controlled, as seen in Figure 6-23(c-d).

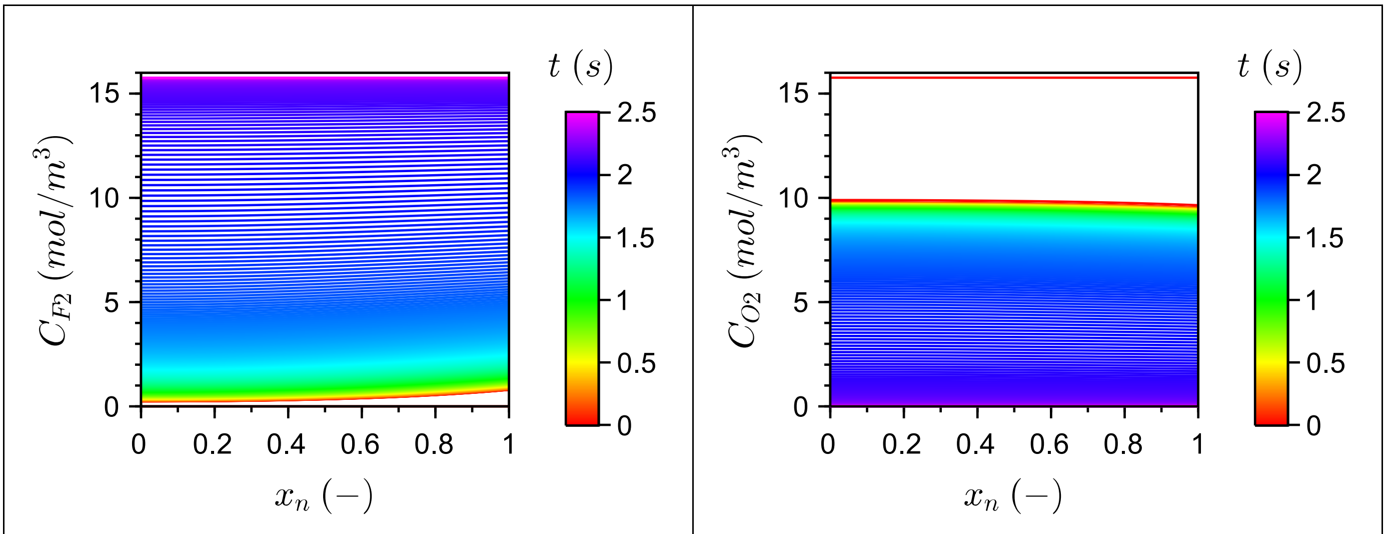

(a) $Q_0 = 1000\ m^3/s$ (b) $Q_0 = 1000\ m^3/s$

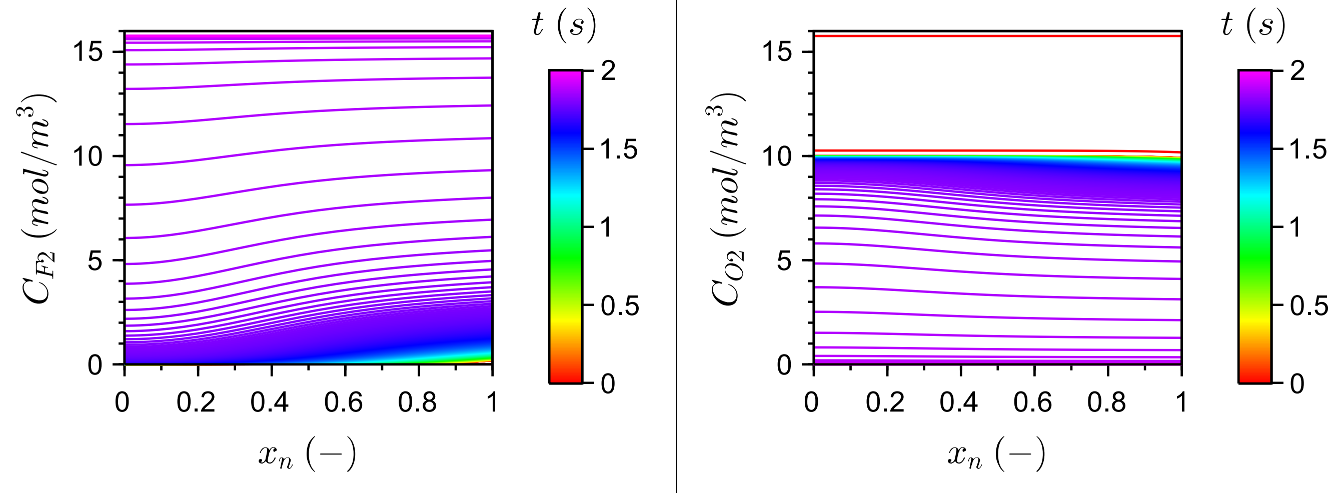

(c) k_j=10 (m³/mol.s) (d) k_j=10 (m³/mol.s)

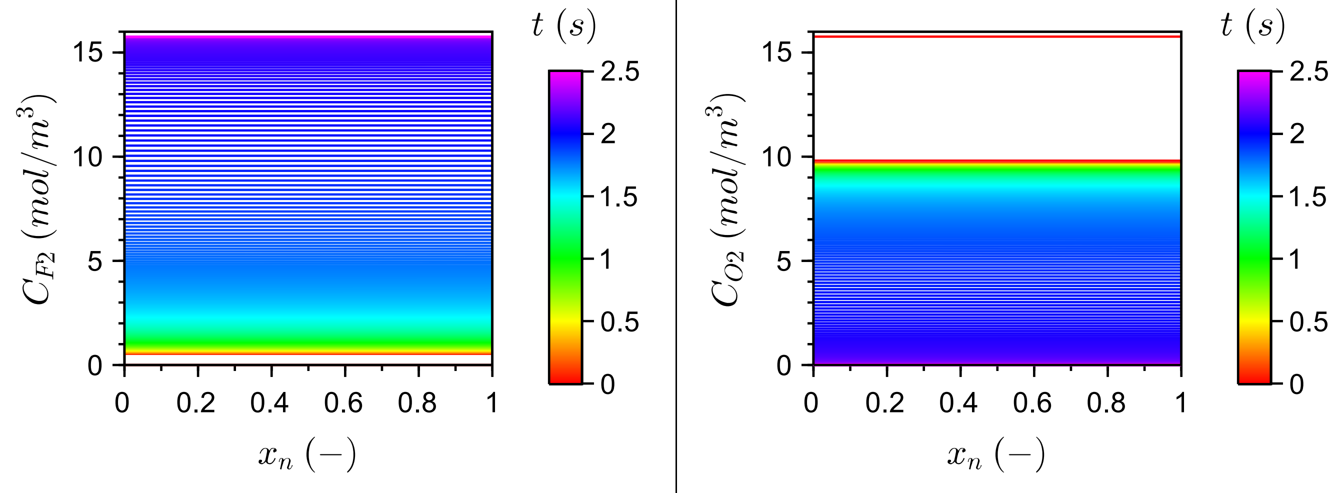

(e) R_p=3.5 μm (f) R_p=3.5 μm

Figure 6-23: Graphs showing the effect each parameter has on the fluorine and oxygen concentration over a short reaction time.

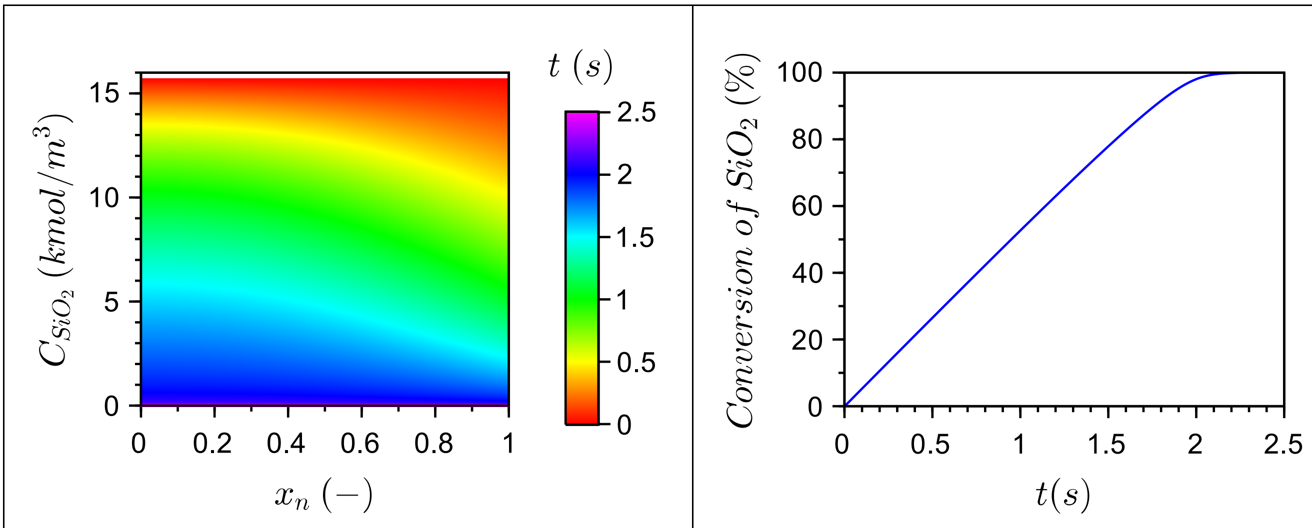

(a) $Q_0 = 1000\ m^3/s$ (b) $Q_0 = 1000\ m^3/s$

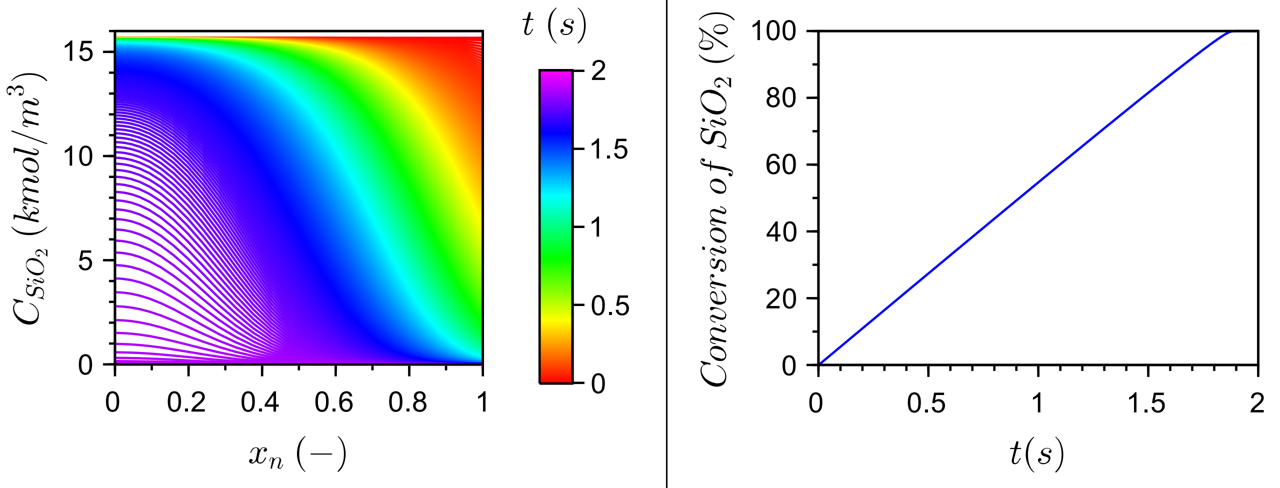

(c) k_j=10 (m³/mol.s) (d) k_j=10 (m³/mol.s)

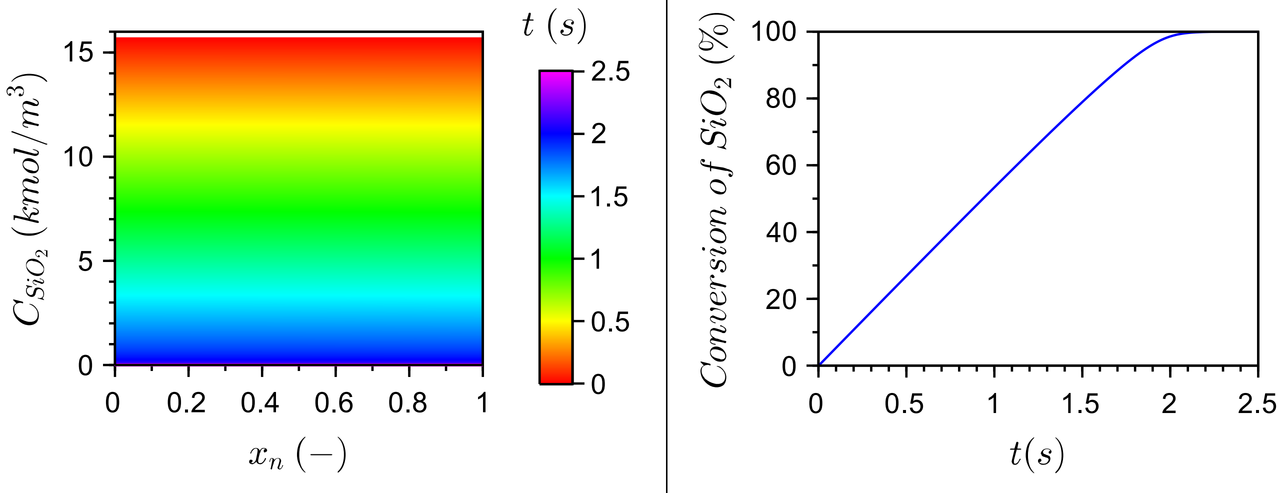

(e) R_p=3.5 μm (f) R_p=3.5 μm

Figure 6-24: Graphs showing the effect each parameter has on silicon dioxide concentration and conversion profile over a short reaction time.

The solid reactant concentrations show more detailed changes in the concentration gradients through the particle than the gas concentrations when the parameters are varied at the fastest reaction time. This is because there is a higher concentration of solids being produced, when compared to the gas species. The solids aren't diffusing; therefore, the concentration gradient is a result of the fluorine concentration gradient on the surface. The reaction-controlling system has the most prominent gradients, as seen in Figure 6-24(c) and resembles the SCM. It shows that the concentration of the silicon dioxide is lower at the surface, indicating that it is very quickly reacting with the fluorine on the surface faster than the fluorine is diffusing into the particle. When the particle size is small, the fluorine concentration is constant through the system, which leads to a constant reaction rate profile, with even consumption of the silicon dioxide in the particle and a linear decrease (in what?) with time.

At the short reaction time, the conversion profiles for the flowrate and small particle size show that the system is slightly reaction-rate controlled, as seen in Figure 6-24(b and f). The gradient becomes slightly concave at the end of the reaction. However, looking across the parameters, the conversion profiles are almost identical, at a short reaction time.

The most desirable operating conditions will be using the smallest particle size or the high flowrate, which gives consistent oxygen production over the reaction time, with very little diffusion limitations. It should be noted that a high flowrate may pose practical challenges such as, but not limited to, high pressure drops and pumping costs, heat transfer limitations, fluid mixing and material compatibility and erosion.

Figure 6-25 shows the effect each parameter has on the fluorine and oxygen concentration through the particle over a long reaction time. Figure 6-26 shows the effect each parameter has on the silicon dioxide concentration and through the particle and conversion profile over a short reaction time.

The fluorine and oxygen profile at the large particle size parameter shows significant diffusion limitations in Figure 6-25(e and f). Figure 6-25(e) shows the fluorine concentration at the surface is higher than at the centre of the particle. Figure 6-25(f) mirrors the fluorine profiles. This leads to an impure product stream, which will require a lot the fluorine to be separated further downstream in the process.

The system responds differently to each parameter at a longer reaction time, each operating under a different regime. The medium flowrate and small reaction rate have flat oxygen concentration profiles, as seen in Figure 6-25(b and d). This shows that the system has little diffusion limitations. The continuous production of oxygen is the desirable operating regime, as it leads to minimal fluorine in the product stream. The large particle size shows that the system experiences diffusion limitations because the fluorine is not able to reach the centre of the particle before being consumed and starts to resemble a SCM. This is shown by the steep profiles in Figure 6-25(e and f).

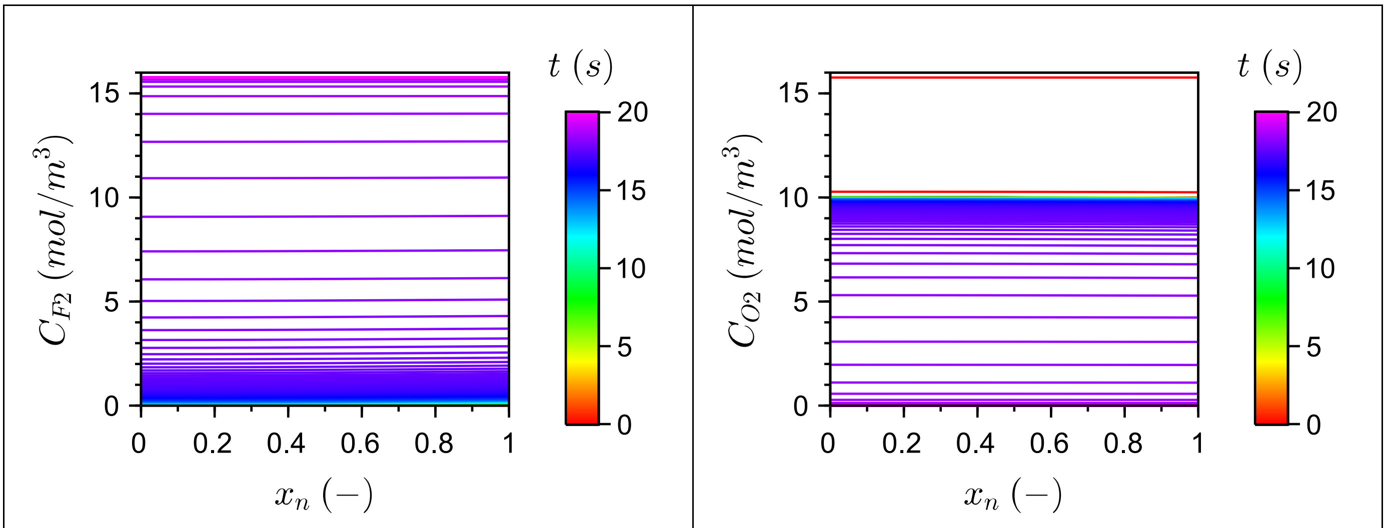

(a) $Q_0 = 100\ m^3/s$

(b) $Q_0 = 100\ m^3/s$

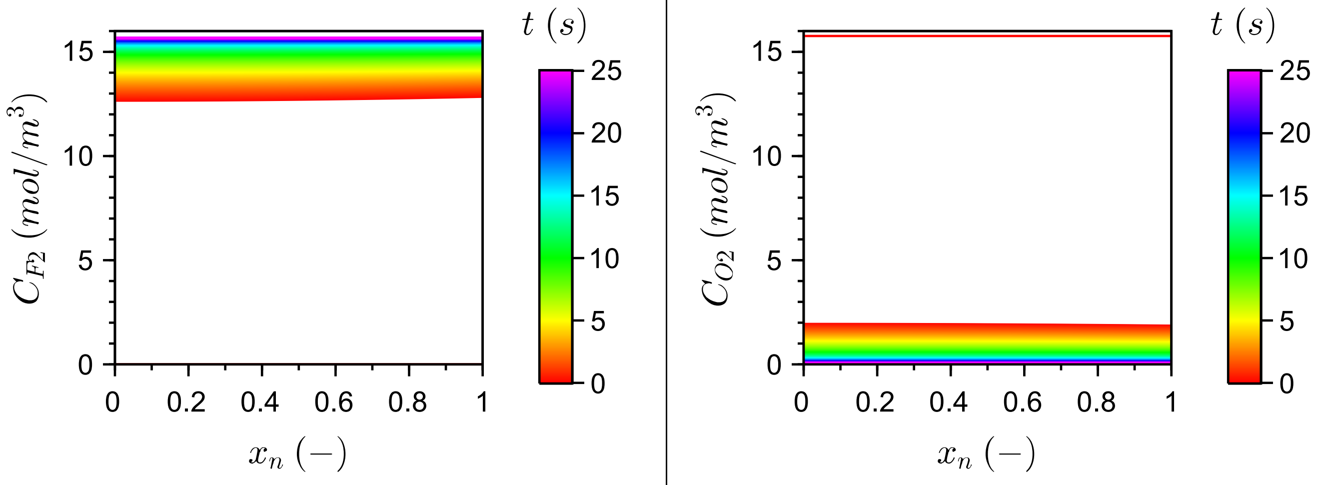

(c) k_j=0.01 (m³/mol.s)

(d) k_j=0.01 (m³/mol.s)

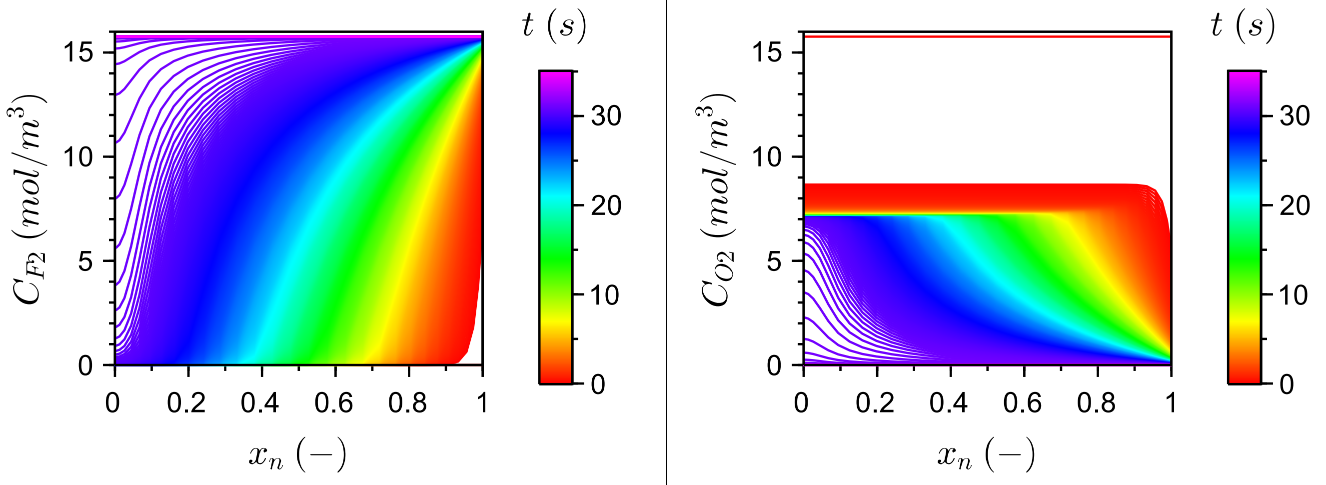

(e) R_p=700 μm

(e) R_p=700 μm

Figure 6-25: Graphs showing the effect each parameter has on fluorine and oxygen concentration over a long reaction time.

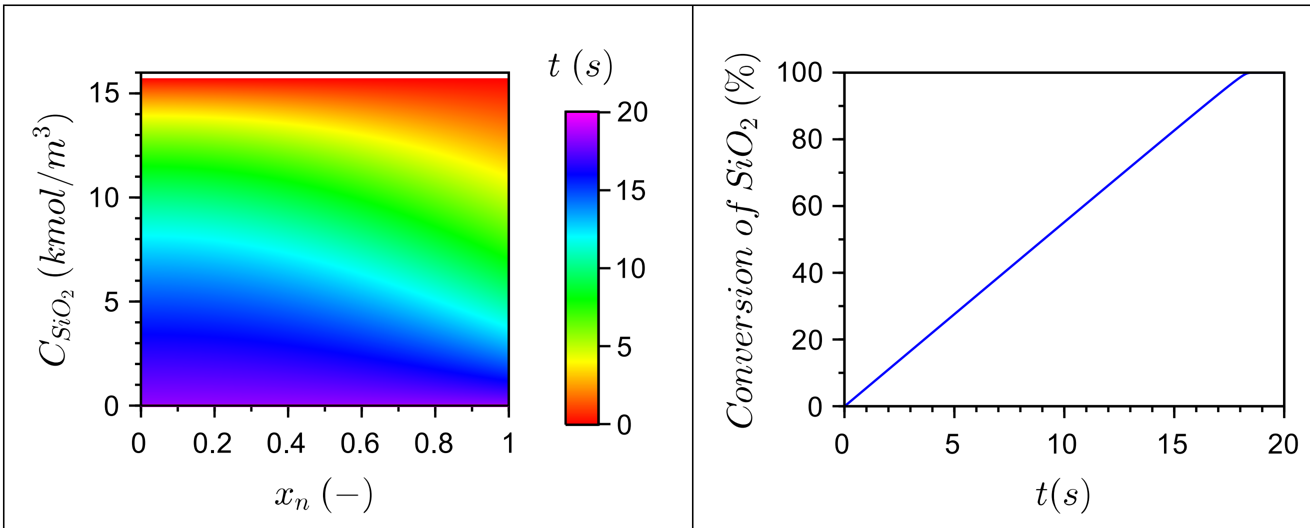

(a) $Q_0 = 100\ m^3/s$ (b) $Q_0 = 100\ m^3/s$

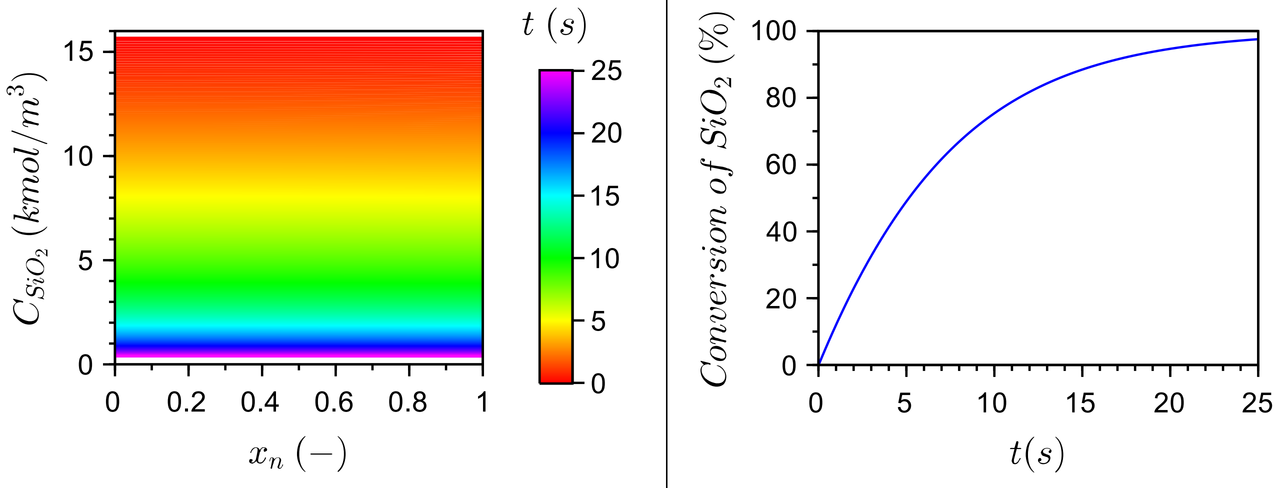

(c) k_j=0.01 (m^3/mol.s) (d) k_j=0.01 (m^3/mol.s)

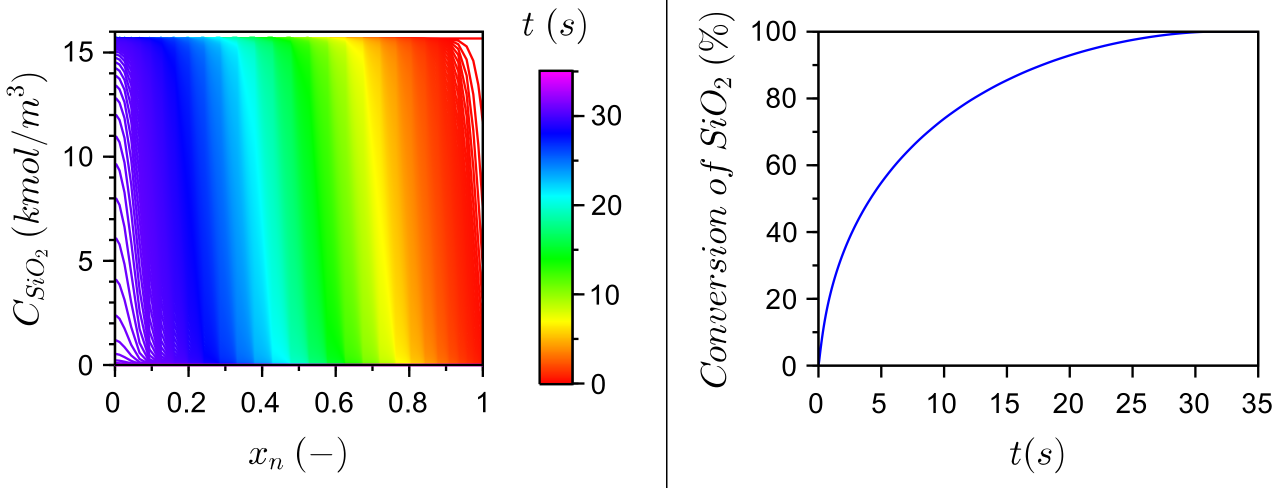

(e) R_p=700 μm (e) R_p=700 μm

Figure 6-26: Graphs showing the effect each parameter has on silicon dioxide concentration and conversion profiles over a long reaction time.

At the fast reaction time, the conversion at the high particle size and the low reaction rate happens faster at the beginning of the reaction and slows down towards the end and the diffusion limitation becomes negligible, so the graphs approach 1 asymptotically like the slow reaction ones. This shows that the reaction-controlled regime is controlling the reaction system resembling the SCM, as seen in Figure 6-26(e and f).

6.5 Summary

The effect of varying the parameters on the three operating regimes can be summarized as follows:

1) Changing the flowrate changes the dynamics of the system, as it changes how much fluorine is fed into the system, through which diffusion limitations arise.
2) As the flow rate is increased, the reaction time decreases as the system moves from a flow-limited conversion to diffusion-limited conversion.
3) The concentration of oxygen is maximised at the low feed flowrates, however the production rate of oxygen is greatly reduced. It comes at the expense of producing a highly concentrated oxygen stream that is not contaminated by fluorine, which is difficult to separate.
4) The concentration profile of the solids is almost the same for all the flow rates, showing that it is quite evenly consumed. This corresponds to the small variation in concentration observed in fluorine and oxygen even at the high flow rates.
5) The rate constant increases the reaction rate. Increasing the reaction rate constant, reduces the reaction time for complete conversion and the system moves from a reaction-controlled conversion to a diffusion limited conversion. It starts to behave very closely to a shrinking core model.
6) Even if the reaction rate is increased to more than 100 m3/mol.s, the reaction time does not reduce below approximately 1.8 seconds. This represents the diffusion limited reaction rate in which the reaction rate can be considered infinitely fast, getting closer to the SCM model.
7) As the particle size increases, the reaction rate slows down and the system moves from reaction control to diffusion control and sharp concentration fronts are obtained in the solid concentrations, similar to those that are expected from SCM. The reaction time increases as the particle size increases.
8) The desired operating regime will be achieved when the oxygen profile is flat, producing a pure oxygen stream; this happens at the small particle sizes.

7. Conclusions and recommendations for future work

The aim of this work was to derive a robust gas-solid reaction system that describes the operation of a regolith furnace for the reduction of lunar regolith. The model is able to describe how a regolith particle, which consists of a mix of metal oxides, is reduced by fluorine gas to produce metal fluorides. The model incorporates the varying porosity of the particle, and the concentration profiles of the reactants in a multiple reaction system with diffusion limitations. There is no known reaction rate or diffusion data for this system, therefore values were assumed, and a parametric study was conducted to test the sensitivity of the system to changes in critical parameters and determine the optimum operating regimes.

The base case results showed that the reaction happens within 2.5 seconds and reaches 100% conversion of all solid reactants. It shows a flat concentration profile of oxygen being produced, both through the particle and over time. This implies very few diffusion limitations in the system. This is desired, as it implies minimal contamination of the stream with fluorine, which is difficult to separate out further downstream. The conversion of the particle was calculated for each solid reactant, and they all follow the same pattern because each reaction has the same reaction rate and only minor deviation due to differences in diffusion of species. The reaction is very fast and therefore required a low residence time and solids contact time. The fluorine is almost fully consumed and converted at the initial conditions, leading to a high reaction rate.

A parametric sensitivity study was conducted on the effect that varying Q_o, k_j and R_p have on the system. The values where varied and compared against the base case. The analysis showed that the optimum operating regime is when maximum oxygen is being produced consistently through the particle, shown by a flat oxygen concentration profile through the particle and over time.

This scenario occurred when the volumetric flowrate was set to 100 m^3/s. It showed that under these conditions, maximum oxygen was produced under no reaction control and no diffusion control limitations. It showed the steepest cut-off when compared to the other parameters. At this flowrate, there is a better production rate of oxygen when compared to lower flowrates.

The psuedo-Theile modulus is an indicator of the starting point of the reaction only. It is used in heterogenous systems as an indicator for how the reaction control and diffusion control effect the system. The calculated values, across the varying parameters, showed that the system does not follow the expected catalytic limits and definitions. The calculated pseudo-Theile modulus of less than 1 (when $Q = 100\ m^3/s$ and $R_p = 3.5\ \mu m$) gave rise to maximum oxygen conversion profiles, showing very little diffusion effects in the system.

This model provides a good basis for further development. The following are suggestions on how it could be developed further:

- The system should be expanded to test different fixed-bed reactor volumes, bed height ratios and different reactor types.
- The system is currently assumed to be isothermal. It should be expanded to incorporate heats of reaction for an adiabatic system.
- Thereafter it should be expanded to incorporate an energy balance and a fluid balance, to do a complete reactor design.
- The reaction kinetics of the model could be improved and made more complex.
- The parametric study should be expanded to include more variables to better understand the systems response and operating regimes.
- The reactions should be examined in more detail. They should be expanded to include any side reactions that may occur from metals reacting with the oxygen in the system to form oxide-fluoride alloys at the particle interfaces.
- Further experimental work should be done using regolith simulants to test the reaction kinetics of the system, and these should be incorporated into the model to validate and improve it going forward. This will be able to provide data on the expected conversion [rate/behaviour/characteristics/…?] of the particle.
- The porosity of the system and the model should be improved to link it to porosity in the inert solid matrix. Regolith porosity is not well understood, and further testing and experimentation is recommended to improve the ability to model how the solid will react.

References

Afshar Ebrahimi, A., Ale Ebrahim, H. & Jamshidi, E. 2008. *Solving partial differential equations of gas–solid reactions by orthogonal collocation*. Computers & Chemical Engineering. 32(8):1746–1759. DOI: 10.1016/j.compchemeng.2007.08.017.

Allen, C., Morris, R. & McKay, D. 1994. *Experimental reduction of lunar mare soil and volcanic glass*. Journal of Geophysical Research: Planets. 99(E11):23173–23185. DOI: 10.1029/94JE02321.

Amos, K. 2020. *China's Chang'e-5 Moon mission returns colour pictures*. Available: China's Chang'e-5 Moon mission returns colour pictures - BBC News

Anand, M., Crawford, I., Balat-Pichelin, M., Abanades, S., van Westrenen, W., Péraudeau, G., Jaumann, R. & Seboldt, W. 2012. *A brief review of chemical and mineralogical resources on the Moon and likely initial in situ resource utilization (ISRU) applications*. Planetary and Space Science. 74(1):42–48. DOI: 10.1016/j.pss.2012.08.012.

Balasubramaniam, R., Gokoglu, S. & Hegde, U. 2010. *The reduction of lunar regolith by carbothermal processing using methane*. International Journal of Mineral Processing. 96(1–4):54–61. DOI: 10.1016/j.minpro.2010.06.001.

Bennett, N. J., Ellender, D., & Dempster, A. G. 2020. *Commercial viability of lunar In-Situ Resource Utilization (ISRU)*. Planetary and Space Science, 182. https://doi.org/10.1016/j.pss.2020.104842

Billingham, J., Gilbreath, W., O'Leary, B. & Gossett, B. 1979. *Space resources and space settlements*. Technical papers derived from the 1977 Summer Study at NASA Ames Research Centre. Moffett Field, California Study, (NASA SP-428):300.

Burt, D. 1992. *Lunar mining of oxygen using fluorine*. In Lunar and planetary exploration. V. 2. 423–428. Available: https://ntrs.nasa.gov/citations/19930004792.

Carrier, W. 2003. *Particle Size Distribution of Lunar Soil*. Journal of Geotechnical and Geoenvironmental Engineering. 129(10):956–959. DOI: 10.1061/(ASCE)1090-0241(2003)129:10(956).

Centre for Lunar Science and Exploration [CLSE]. n.d. *Classroom illustrations: Lunar surface environment*. Available: Lunar Surface Environment (usra.edu)

Chi, G., Zhang, Z., Tang, J., Jiang, S., Lu, Z., Zhang, W., Tian, Y., & Deng, Z. 2024. *Quantitative sampling and thermal extraction of the lunar regolith for lunar volatile exploration: Method and validation*. Acta Astronautica, 220, 274–282. https://doi.org/10.1016/j.actaastro.2024.04.029

Cocco, R., Karri, S.B.R. & Knowlton, T. 2014. *Introduction to Fluidization.* American Institute of Chemical Engineers (AIChE). 21–29.

Crawford, I. 2004. *The scientific case for renewed human activities on the Moon.* Space Policy. 20(2):91–97. DOI: 10.1016/j.spacepol.2004.02.007.

Crawford, I. 2015. *Lunar resources: A review.* Progress in Physical Geography: Earth and Environment. 39(2):137–167. DOI: 10.1177/0309133314567585.

Crawford, I., Anand, M., Cockell, C., Falcke, H., Green, D., Jaumann, R. & Wieczorek, M. 2012. *Back to the Moon: The scientific rationale for resuming lunar surface exploration.* Planetary and Space Science. 74(1):3–14. DOI: 10.1016/j.pss.2012.06.002.

Cunningham, P.J. 2020. *China shoots the moon.* Available: China Shoots the Moon - Counter Information (counterinformationblog.blogspot.com)

Curreri, P., Ethridge, E., Hudson, S., Miller, T., Grugel, R., Sen, S. & Sadoway, D. 2006. P*rocess demonstration for lunar ISRU - molten oxide electrolysis.* (NASA/TM—2006–214600). Marschell Space Flight Centre: NASA.

Cutler, A. & Krag, P. 1985. *A carbothermal scheme for lunar oxygen production.* Washington D.C.: Lunar and Planetary Institute. 559–569.

Davis, G., Montes, C. & Eklund, S. 2017. *Preparation of lunar regolith based geopolymer cement under heat and vacuum.* Advances in Space Research. 59(7):1872–1885. DOI: 10.1016/j.asr.2017.01.024.

Davis, M. & Davis, R. 2003. *Fundamentals of chemical reaction engineering.* International ed. (McGraw-Hill chemical engineering series). Boston: McGraw-Hill.

Deiss, H. 2023. *NASA's LRO Observes Chandrayaan-3 Landing Site.* Available: NASA's LRO Observes Chandrayaan-3 Landing Site - NASA

The European Space Agency (ESA). 2022. *Lunar regolith testing.* Available: ESA - Lunar regolith testing.

Favergeon, L., Morandini, J., Pijolat, M. & Soustelle, M. 2013. *A General Approach for Kinetic Modelling of Solid-Gas Reactions at Reactor Scale: Application to Kaolinite Dehydroxylation.* Oil and Gas Science and Technology – Revue d'IFP Energies nouvelles. 68(6):1039–1048. DOI: 10.2516/ogst/2012018.

Fedunik-Hofman, L., Bayon, A. & Donne, S. 2019. *Kinetics of Solid-Gas Reactions and Their Application to Carbonate Looping Systems.* Energies. 12(15):2981. DOI: 10.3390/en12152981.

Fogler, H. 2004. *Elements of Chemical Reaction Engineering.* Third Edition ed. New Delhi: Prentice-Hall of India.

Freedman, R. A. 2008. *Comparing Lunar Highlands and Maria.* Available: Comparing Lunar Highlands and Maria | Actforlibraries.org

Freundlich', A., Ignatiev', A., Horton', C., Duke, M. & Sibille, L. 2005. *Manufacture of solar cells on the moon.* IEEE. 794-797.

Gao, Y., Phipps, A., Taylor, M., Crawford, I., Ball, A., Wilson, L., Parker, D., Sweeting, M., et al. 2008. *Lunar science with affordable small spacecraft technologies: MoonLITE and Moonraker.* Planetary and Space Science. 56(1):367-377.

Garner, R. 2024. *NASA's LRO Images Intuitive Machine's Odysseus Lander.* Available: NASA's LRO Images Intuitive Machine's Odysseus Lander - NASA

Granier, J., Cutard, T., Pinet, P., le Maoult, Y., Chevrel, S., Sentenac, T., & Favier, J. J. 2025. *Selective laser melting of partially amorphous regolith analog for ISRU lunar applications*. Acta Astronautica, 226, 66–77. https://doi.org/10.1016/j.actaastro.2024.10.024

Guerrero-Gonzalez, F. J., & Zabel, P. 2023. *System analysis of an ISRU production plant: Extraction of metals and oxygen from lunar regolith*. Acta Astronautica, 203, 187–201. https://doi.org/10.1016/j.actaastro.2022.11.050

Hanmer, S. n.d. *Moon 1: Highlands, Lowlands and Lavas.* Available: Moon I : Highlands & Lowlands (simonhanmer52.ca).

Hartley-Parkinson, R. 2019. *World's first private craft to try and land on the moon crashes onto its surface*. Available: Space IL's Beresheet crashes as it tries to land on moon's surface | Metro News.

Haskin, A. 1985. *Toward a spartan scenario for use of lunar materials.* In Lunar Bases and Space Activities for the 21st century. 435–443.

Haskin, A., Colson, O., Lewis, H. & Semkow, W. n.d. *Electrolytic smelting of lunar for oxygen, iron, and silicon.* 2nd conference on Lunar Bases and Space Activities. 411-422

Heiken, G., Vaniman, D. & French, B. Eds. 1991. *Lunar sourcebook: a user's guide to the Moon.* Houston, Texas: Cambridge university press.

Hepp, A., Linne, D., Landis, G., Wadel, M. & Colvin, J. 1994. *Production and Use of Metals and Oxygen for Lunar Propulsion.* Journal of Propulsion and Power. 10(6):834–840. DOI: 10.2514/3.51397.

Huaxia. 2022. *China's Chang'e-5 completes sampling on moon.* Available: China's Chang'e-5 completes sampling on moon - Xinhua | English.news.cn (xinhuanet.com).

Jia, B., Fa, W., Xie, M., Tai, Y. & Liu, X. 2021. *Regolith Properties in the Chang'E-5 Landing Region of the Moon: Results from Multi-Source Remote Sensing Observations.* Journal of Geophysical Research: Planets. 126(7). DOI: 10.1029/2021JE006934.

Jones, A. n.d. *What is the moon made of?* Available: Overview | Composition – Moon: NASA Science.

Just, G., Smith, K., Joy, K. & Roy, M. 2020. *Parametric review of existing regolith excavation techniques for lunar In Situ Resource Utilisation (ISRU) and recommendations for future excavation experiments.* Planetary and Space Science. 180:104746. DOI: 10.1016/j.pss.2019.104746.

Keaton, P. 1985. *A Moon Base/Mars Base Transportation Depot. In Lunar Bases and Space Activities of the 21st Century.* Houston: Lunar and Planetary Institute. 141–154. Available: https://ui.adsabs.harvard.edu/abs/1985lbsa.conf..141K/abstract.

Kiely C, Greenberg G, Kiely CJ. 2011. *A new look at lunar soil collected from the sea of tranquillity during the Apollo 11 mission.* Microscopy and Microanalysis. 17(1):34-48. Available: A new look at lunar soil collected from the sea of tranquility during the Apollo 11 mission - PubMed (nih.gov)

Kring, D. 2006. *Parameters of Lunar Soils.* Space Sciences Lunar Exploration Initiative. 29.

Landis, G. 2005. *Materials Refining for Solar Array Production on the Moon.* Space and Electric Power for Humanity, the Fourth International Symposium on Space Means for Power Utilities, and the Third Wireless Power Transmission Conference cosponsored by the Canadian Aeronautics and Space Institute (CASI) and the Société des Electriciens et des Electroniciens (SEE). Glenn Research Centre, Cleveland, Ohio (NASA/TM—2005-214014):25.

Landis, G. 2007. *Materials refining on the Moon.* Acta Astronautica. 60:906–915. DOI: 10.1016/j.actaastro.2006.11.004.

Landis, G. 2011. *Calcium Reduction as a Process for Oxygen Production from Lunar Regolith.* In 49th AIAA Aerospace Sciences Meeting including the New Horizons Forum and Aerospace Exposition. Orlando, Florida: American Institute of Aeronautics and Astronautics. DOI: 10.2514/6.2011-701.

Landis, G. 2014. *Resource production on the Moon.* In Planetary and Terrestrial Mining Sciences Symposium. Golden CO.

Landis, G., Bailey, S., Brinker, D. & Flood, D. 1990. *Photovoltaic power for a lunar base.* Acta Astronautica. 22:197–203.

Landis, G. & Perino, M. 1989. *Lunar production of solar cells.* In 9th Biennial SSI. New Jersey: NASA Technical Memorandum 102102. 18.

Levenspiel, O. 1999. *Chemical reaction engineering.* 3rd ed. New York: Wiley.

Lim, S., & Anand, M. 2019. *Numerical modelling of the microwave heating behaviour of lunar regolith.* Planetary and Space Science. 179. https://doi.org/10.1016/j.pss.2019.104723

Lu, X., Ma, R., Wang, C. & Yao, W. 2016. *Performance analysis of a lunar based solar thermal power system with regolith thermal storage.* Energy. 107:227–233. DOI: 10.1016/j.energy.2016.03.132.

Lucey, P.G., Blewett, D.T. & Jolliff, B.L. 2000. *Lunar iron and titanium abundance algorithms based on final processing of Clementine ultraviolet-visible images.* Journal of Geophysical Research: Planets. 105(E8):20297–20305. DOI: 10.1029/1999JE001117.

McKay, D., Heiken, G., Basu, A., Blanford, G., Simon, S., Reedy, R., French, B. & Papike, J. 1991. *The lunar regolith: Chapter 7.* In Lunar Sourcebook. 285–356.

Mebunii, C. E. 2022. *15 types of pyrolysis reactors and their features explained.* Available: 15 Types of Pyrolysis Reactors and their Features Explained - Felsics.com

Mendell, W. 1985. *Lunar bases and space activities for the 21st century.* Washington D.C.: Lunar and Planetary Institute.

Meurisse, A., & Carpenter, J. 2020. *Past, present and future rationale for space resource utilisation.* Planetary and Space Science. 182. Elsevier Ltd. https://doi.org/10.1016/j.pss.2020.104853

Mitchell, J., Houston, W., Scott, R., Costes, N., Carrier, W. & Bromwell, L. 1972. *Mechanical properties of lunar soil: density, porosity, cohesion, and angle of internal friction.* In Third Lunar Science Conference. V. 3. The M.I.T. Press. 3235–3253.

Najafi, M. & Nikoukhah, R. 2006. *Modelling and Simulation of Differential Equations in Scicos.* The Modelica Association. (Modelica):9.

The National Aeronautics and Space Administration (NASA). 2022. *Fifty years later, curators unveil one of last sealed apollo samples*. Available: Fifty Years Later, Curators Unveil One of Last Sealed Apollo Samples - NASA.

Papike, J., Simon, S. & Laul, J. 1982. *The lunar regolith: chemistry, mineralogy, and petrology*. Reviews of Geophysics and Space Physics. 20(4):761–826.

Pavlou, P., Pavlou, D., Möller, K. & Maharaj, R. 2017. *A Reactor Model for the Conversion of Regolith Using Fluorine Gas*. BSc. in Chemical Engineering. University of Cape Town.

Rasera, J. N., Cilliers, J. J., Lamamy, J. A., & Hadler, K. 2020. *The beneficiation of lunar regolith for space resource utilisation: A review*. Planetary and Space Science. 186. Elsevier Ltd. https://doi.org/10.1016/j.pss.2020.104879

Rice, E. & Gustafson, R. 2000. *Review of current indigenous space resource utilization (ISRU) research and development*. In 38th Aerospace Sciences Meeting and Exhibit. Reno, NV, U.S.A.: American Institute of Aeronautics and Astronautics. DOI: 10.2514/6.2000-1057.

Rice, R. & Do, D. 1995. *Applied mathematics and modelling for chemical engineers*. (Wiley series in chemical engineering). New York: Wiley.

Robens, E., Bischoff, A., Schreiber, A. & Unger, K. 2008. *Investigate of surface properties of lunar regolith Part II*. Journal of Thermal Analysis and Calorimetry. 94(3):627–631.

Robens, E., Bischoff, A., Schreiber, A., Dąbrowski, A. & Unger, K.K. 2008. *Investigation of surface properties of lunar regolith: Part III*. Journal of Thermal Analysis and Calorimetry. 94(3):627–631. DOI: 10.1016/j.apsusc.2006.12.098.

The Planetary Society. 2018. *Lunar landing sites maps for The Planetary Report*. Available: Lunar landing sites map for The Planetary… | The Planetary Society.

Sacksteder, K. & Sanders, G. 2007. *In-Situ Resource Utilization for Lunar and Mars Exploration*. In 45th AIAA Aerospace Sciences Meeting and Exhibit. Reno, Nevada: American Institute of Aeronautics and Astronautics. DOI: 10.2514/6.2007-345.

Sadeh, W. & Criswell, M. 1996. *Infrastructure for a lunar base*. Advances in Space Research. 18(11):139–148. DOI: 10.1016/0273-1177(96)00102-0.

Sanders, G. 2005. *NASA In-Situ Resource Utilization (ISRU) Capability Roadmap Final Report*. NASA. Rev 1.

Sanders, G., Larson, B., Sacksteder, K., Mclemore, C. & Johnson, K. 2007. *Lunar In-situ Resource Utilization: Development and Implementation – December 13.* NASA

Sargeant, H. M., Abernethy, F. A. J., Barber, S. J., Wright, I. P., Anand, M., Sheridan, S., & Morse, A. 2020. *Hydrogen reduction of ilmenite: Towards an in situ resource utilization demonstration on the surface of the Moon.* Planetary and Space Science, 180. https://doi.org/10.1016/j.pss.2019.104751

Satish, H., Radziszewski, P. & Ouellet, J. 2011. *A review of mining technologies for space.* Proceedings of the Canadian Engineering Education Association (CEEA). (August, 15). DOI: 10.24908/pceea.v0i0.3879.

Schlüter, L., & Cowley, A. 2020. *Review of techniques for In-Situ oxygen extraction on the moon*. Planetary and Space Science. 181. Elsevier Ltd. https://doi.org/10.1016/j.pss.2019.104753

Schreiner, S. 2015. *Molten regolith electrolysis reactor modelling and optimisation of ISRU systems.* Master of Science in Aerospace Engineering. Massachusetts Institute of Technology.

Schwandt, C., Hamilton, J., Fray, D. & Crawford, I. 2012. *The production of oxygen and metal from lunar regolith.* Planetary and Space Science. 74(1):49–56. DOI: 10.1016/j.pss.2012.06.011.

Sebolt, W., Linger, S., Hoernes, S., Grimmeisen, W., Lekies, R., Herkelmann, R. & Burt, D. 1993. *Lunar Oxygen Extraction Using Fluorine.* Available: https://www.researchgate.net/publication/224799042_Lunar_Oxygen_Extraction_Using_Fluorine/link/00b7d52963a7eb2910000000/download.

Sen, S., Ray, C. & Reddy, R. 2005. *Processing of lunar soil simulant for space exploration applications.* Materials Science and Engineering A. 6.

Šeško, R., Lamboley, K., Cutard, T., Grill, L., Reiss, P., & Cowley, A. 2024. *Oxygen production by solar vapor-phase pyrolysis of lunar regolith simulant.* Acta Astronautica, 224, 215–225. https://doi.org/10.1016/j.actaastro.2024.08.009

Shaltens, R. & Boyle, R. 1995. Initial results from the solar dynamic (SD) ground test demonstration (GTD) project at NASA Lewis. *Proceedings of the conference on "30th Intersociety Energy Conversion Engineering Conference."* 31 July - 4 August. Orlando, Florida. 12.

Simon, T. & Sacksteder, K. 2007. *NASA in-situ resource utilisation (ISRU) development and incorporation plans.* Technology Exchange Conference. Galveston. Texas.

Sirk, A., Sadoway, D. & Sibille, L. 2010. *Direct Electrolysis of Molten Lunar Regolith for the Production of Oxygen and Metals on the Moon.* ECS Transactions. 28(6):367–373. DOI: 10.1149/1.3367929.

Song, L., Xu, J., Fan, S., Tang, H., Li, X., Liu, J. & Duan, X. 2019. *Vacuum sintered lunar regolith simulant: Pore-forming and thermal conductivity.* Ceramics International. 45(3):3627–3633. DOI: 10.1016/j.ceramint.2018.11.023.

Stancati, M., Jacobs, M., Cole, K. & Collins, J. 1991. *In-situ propellant production - alternatives for mars exploration.* (NASA CR 187192 SAIC-91/1052). NASA Lewis Research Center.

Stoeser, D.B., Rickman, D.L. & Wilson, S. n.d. *Design and Specifications for the Highland Regolith Prototype Simulants NU-LHT-1M and -2M.*

Taylor, G. & Martel, L. 2003. *Lunar prospecting.* Advance in Space Research. 31(11):2403–2412. DOI: 10.1016/S0273-1177(03)00549-0.

Taylor, L. & Carrier, W. 1992. *Production of Oxygen on the Moon: Which Processes Are Best and Why.* AIAA Journal. 30(12):2858–2863. DOI: 10.2514/3.48974.

Taylor, L. & Meek, T. 2005. Microwave Sintering of Lunar Soil: Properties, Theory, and Practice. Journal of Aerospace Engineering. 18(3):188–196. DOI: 10.1061/(ASCE)0893-1321(2005)18:3(188).

Toutanji, H., Evans, S. & Grugel, R. 2012. *Performance of lunar sulphur concrete in lunar environments.* Construction and Building Materials. 29:444–448. DOI: 10.1016/j.conbuildmat.2011.10.041.

Turan, E., Stein, S., Maharaj, R. & Möller, K. 2020. *A flow sheet for the conversion of lunar regolith using fluorine gas.* Advances in Space Research. 65(7):1852–1862. DOI: 10.1016/j.asr.2020.01.014.

van Boekel, M. & Tijskens, L. 2001. *Kinetic modelling. In Food Process Modelling.* Elsevier. 35–59. DOI: 10.1533/9781855736375.1.35.

Villadsen, J. & Michelsen, M. 1978. *Solution of Differential Equation Models by Polynomial Approximation.* Englewood Cliffs, New Jersey: Prentice-Hall, Inc.

Wamsley, L. 2022. *NASA is just now opening a vacuum-sealed sample it took from the moon 50 years ago.* Available: NASA is opening a vacuum-sealed sample it took from the moon 50 years ago : NPR.

Wanta, K., Astuti, W., Perdana, I. & Petrus, H. 2020. *Kinetic study in atmospheric pressure organic acid leaching: shrinking core model versus lump model.* Minerals. 10(7):613. DOI: 10.3390/min10070613.

Wattles, J. 2023. *Here's what India's historic lunar lander found on the moon — and what's next.* Available: What India's Chandrayaan-3 found on the moon — and what's next | CNN.

Zhou, S., Yang, Z., Zhang, R., Zhu, X. & Li, F. 2021. *Preparation and evaluation of geopolymer based on BH-2 lunar regolith simulant under lunar surface temperature and vacuum condition.* Acta Astronautica. 189:90–98. DOI: 10.1016/j.actaastro.2021.08.039.

Appendix A - Detailed derivations

Gas Phase Molar Balance

Molar balance, for species *i*, around the reaction zone (Red box in Figure 4-5):

$$Rate\ of\ accumulation_i|r = Flow\ In_i|r + Flow\ Out_i|(r+\Delta r) + Generation/Consumption|_i$$

Where N_i is the mol of species *i*

$$N_i = V_G C_i = (\varepsilon 4\pi r^2 \Delta r)C_i$$

And

$$Flow\ In_i|r = Area_{Gas}\ \times\ Flux|r$$

$$Flow\ Out_i|_{r+\Delta r} = Area_{Gas}\ \times\ Flux|_{r+\Delta r}$$

Flux at r refers to the movement of the species due to mass transfer.

And

$$Generation/consumption_i =\ V_p r_i$$

V_p is the volume of a Regolith particle, and is defined as: $V_P = 4\pi r^2 \Delta r$

The overall gas species mol balance:

$$\frac{\partial N_i}{\partial t} = \ (\varepsilon 4\pi r^2 D_{e,i})\frac{\partial C_i}{\partial r}\bigg|_r - (\varepsilon 4\pi r^2 D_{e,i})\frac{\partial C_i}{\partial r}\bigg|_{r+\Delta r} + (4\pi r^2 \Delta r)R_i$$

$$\frac{\partial((\varepsilon 4\pi r^2 \Delta r)C_i)}{\partial t} = (\varepsilon 4\pi r^2 D_{e,i})\frac{\partial C_i}{\partial r}\bigg|_r - (\varepsilon 4\pi r^2 D_{e,i})\frac{\partial C_i}{\partial r}\bigg|_{r+\Delta r} + (4\pi r^2 \Delta r)R_i$$

Appendix B – Solution matrix formulation

To solve the derived reaction system, the equations need to be written in vector format. This will assume that the reaction rate for each species has been calculated. Using a DAE solver like DASKR, these equations are written as:

$$f_i = 0 = G(C) - \sum \frac{dC_i}{dt}$$

Where G(C) are general expressions as a function of C and $\frac{dC_i}{dt}$ are left implicitly within the equation set. When the $\frac{dC_i}{dt}$ terms are zero, then the equations are algebraic.

Using the collocation formulation, the objective is to write all the balances in the above form using matrix algebra. This greatly enhances the performance of the model.

Consider species *i* only, then working from the centre outwards:

$$f_{k=1} = \sum\nolimits_j A_{k,j}\, C_{j,i}$$

The internal gas phase values are:

$$f_{k=2:n+1} = \frac{\varepsilon_k D_{e,i}}{R_p^2} \sum\nolimits_j B_{k,j} C_{j,i} + \frac{\varepsilon_k D_{e,i}}{R_p^2} \frac{2}{x_k} \sum\nolimits_j A_{k,j} C_{j,i} + \frac{D_{e,i}}{R_p^2} \left(\sum\nolimits_j A_{k,j} C_{j,i} \right) \frac{\partial \varepsilon_k}{\partial x} + R_{k,i} - \varepsilon_k \frac{dC_{k,i}}{dt} - C_{k,i} \frac{d\varepsilon_k}{dt}$$

The surface is:

$$f_{k=N+2} = F_{i,0} - F_i + 3V_s \sum\nolimits_k \left(R_k x_k^2 w_k \right)$$

$$f_{k=N+2} = C_{k,i} - \frac{F_i}{\sum F_i} \frac{P}{RT}$$

The reactor balance is:

The solid phase balances are:

$$f_{k=1:n+2} = R_{s,k,i} - (1 - \varepsilon_k) \frac{dC_{s,k,i}}{dt} + C_{s,k,i} \frac{d\varepsilon_k}{dt}$$

Three different regions where defined: the gas phase in the particle (Cg), the solid phase in the particle (Cs) and the reactor gas phase (F). Then build 3 vector/matrix equations that solve each region. Then variables are defined as:

$$C_g = \begin{bmatrix} C_{1,1} & \cdots & C_{1,m} \\ \vdots & \ddots & \vdots \\ C_{n+2,1} & \cdots & C_{n+2,m} \end{bmatrix}$$

$$C_s = \begin{bmatrix} C_{s,1,1} & \cdots & C_{s,1,n} \\ \vdots & \ddots & \vdots \\ C_{s,n+2,1} & \cdots & C_{s,n+2,n} \end{bmatrix}$$

$$\varepsilon = [\varepsilon_1 \quad \cdots \quad \varepsilon_m]^T$$

Similarly, there will be a matrix of $\frac{dC_{k,i}}{dt}$ and $\frac{dC_{s,k,i}}{dt}$ for each mode and each species and $\frac{d\varepsilon}{dt}$ for each species. There is $m=4$ gas phase species and $n=10$ solid phase species. Then each region was divided into its elements and was simplified with vector mathematics.

Appendix C – All parametric study results

Flowrate variation results - $Q_0 = 1\ m^3/s$

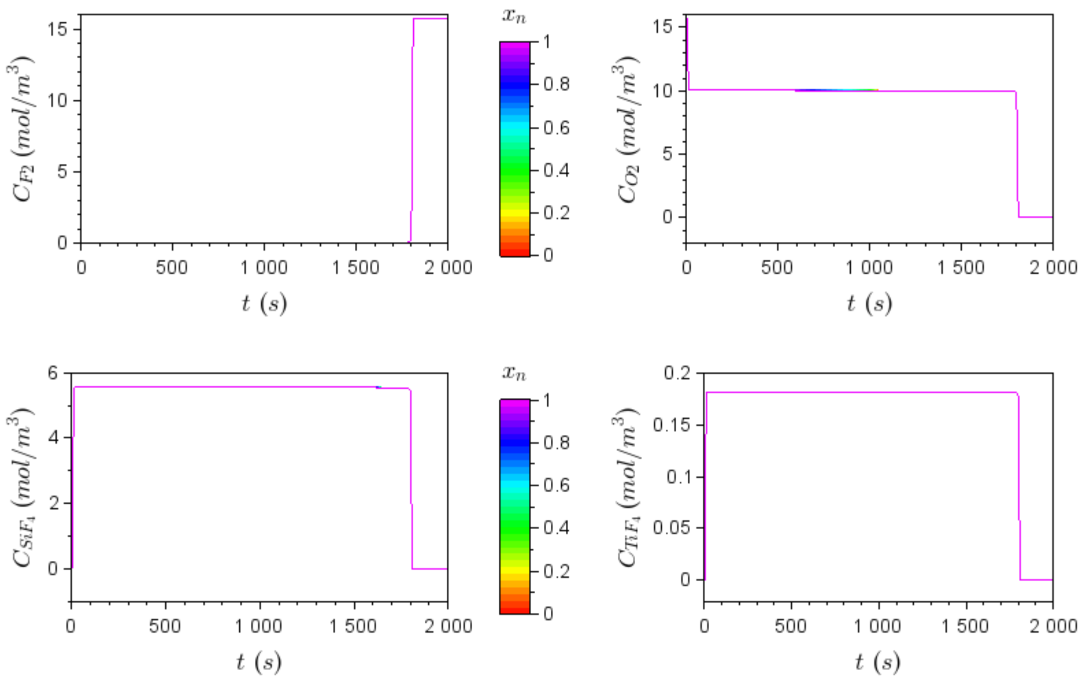

C 1: Effect of flowrate = 1 m^3/s on gas concentrations over time.

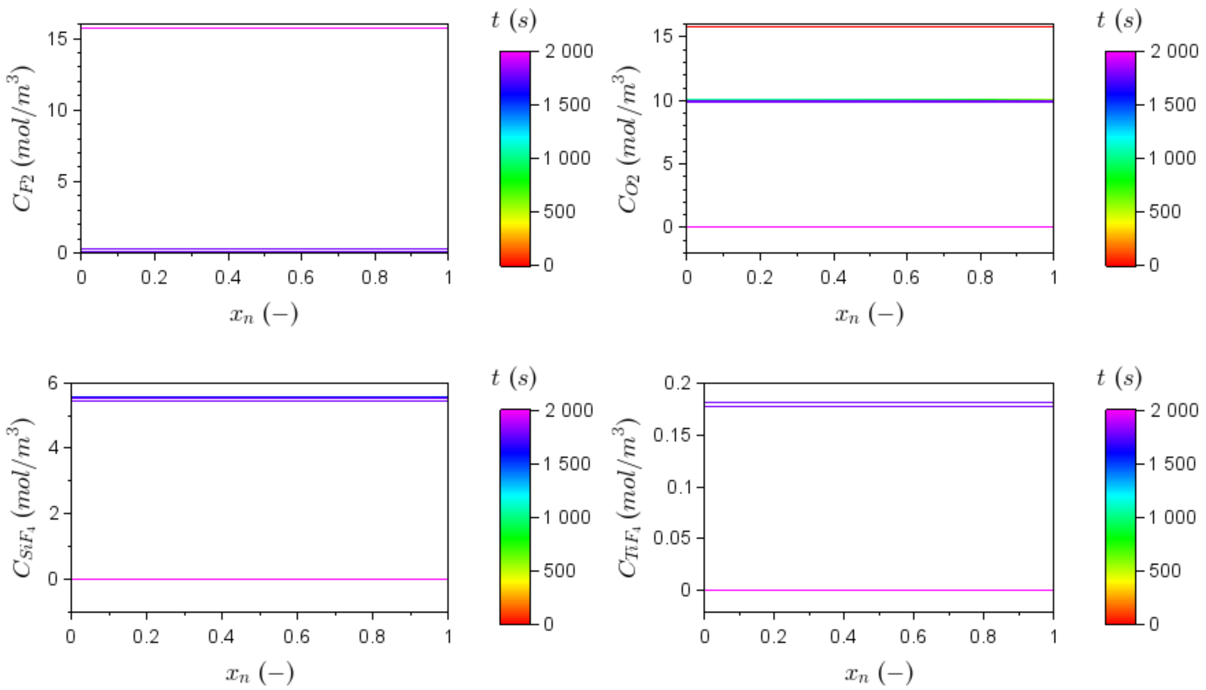

C 2: Effect of flowrate = 1 m³/s on gas concentrations through the particle.

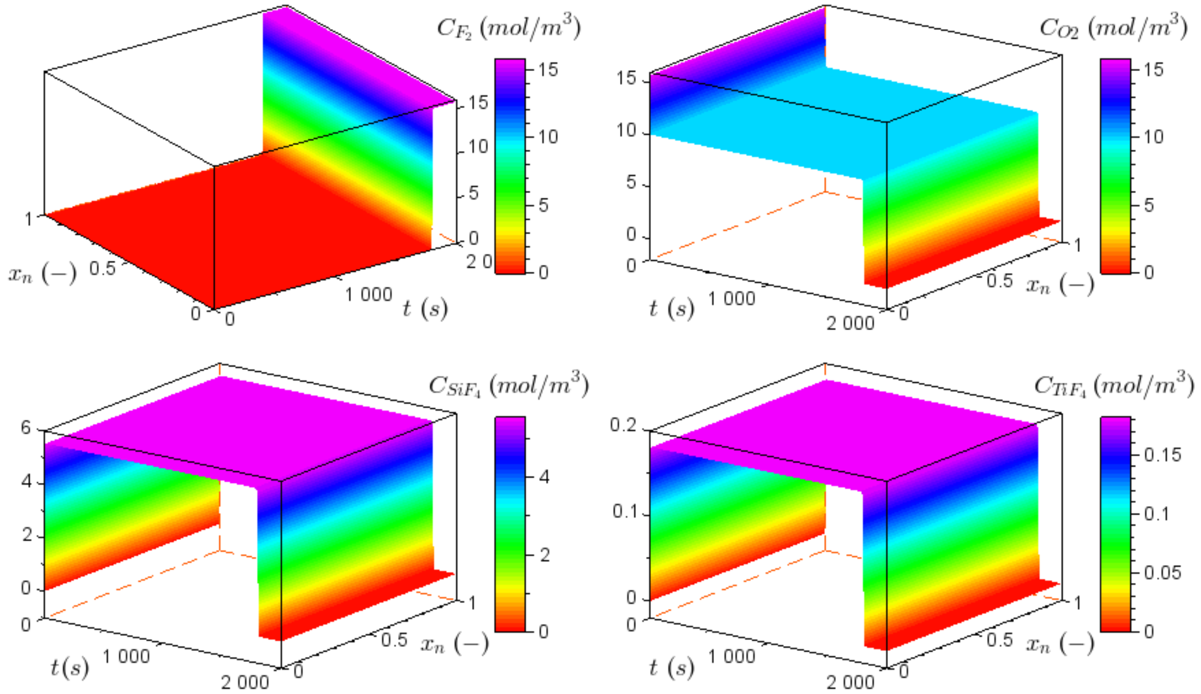

C 3: Surface graphs showing the effect of flowrate = 1 m³/s on gas concentrations.

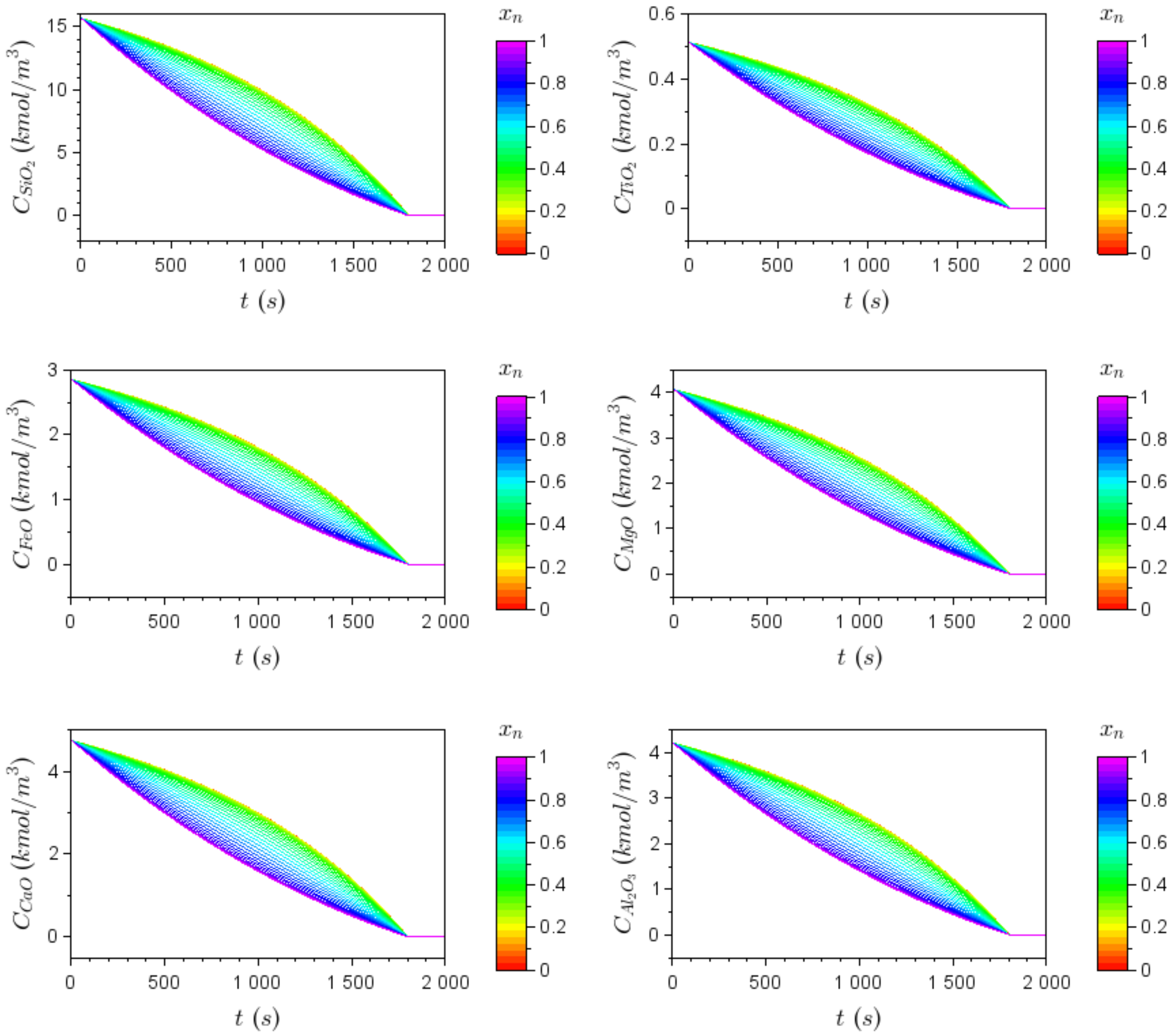

C 4: Effect of flowrate = 1 m³/s on solid reactant concentrations over time.

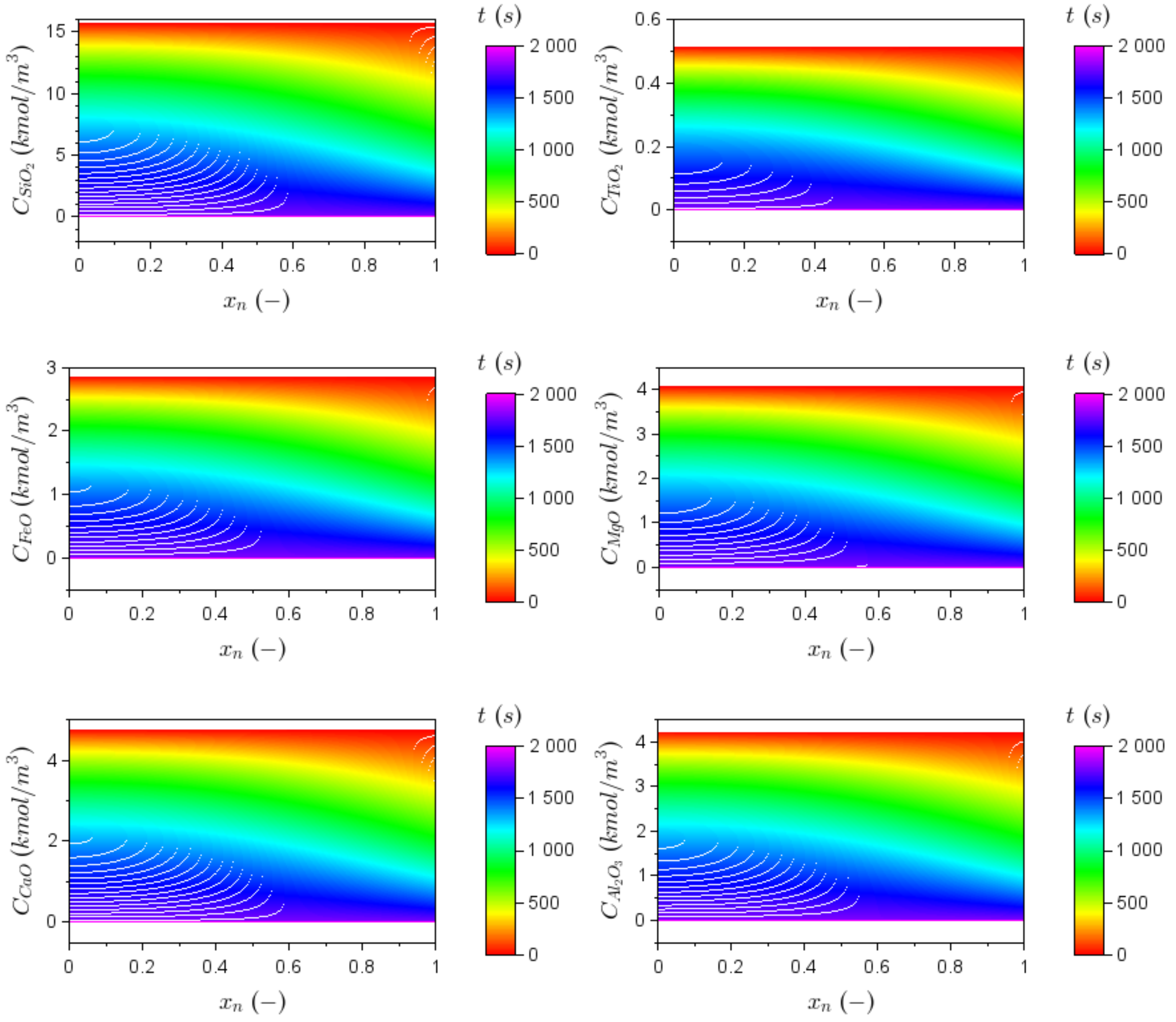

C 5: Effect of flowrate = 1 m^3/s on solid reactant concentrations through the particle.

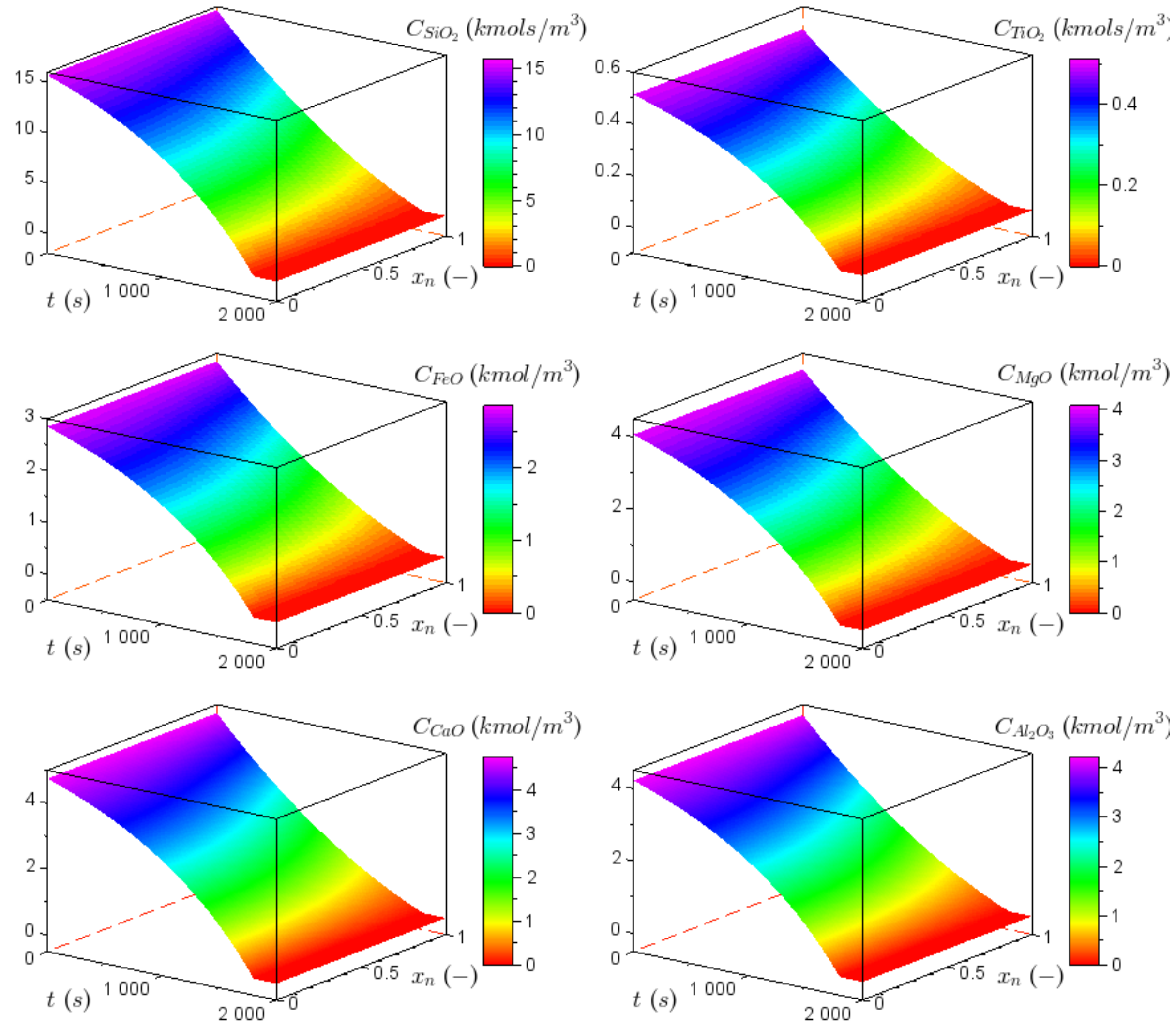

C 6: Surface graphs showing the effect of flowrate = 1 m^3/s on solid reactant concentrations.

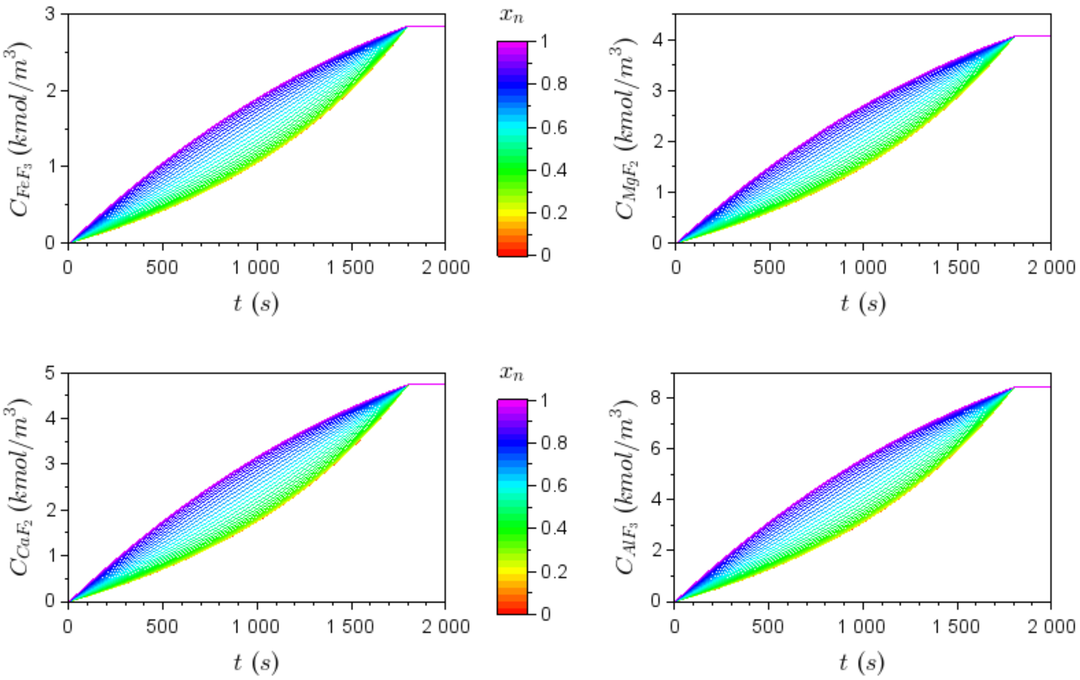

C 7: Effect of flowrate = 1 m³/s on solid products concentrations over time.

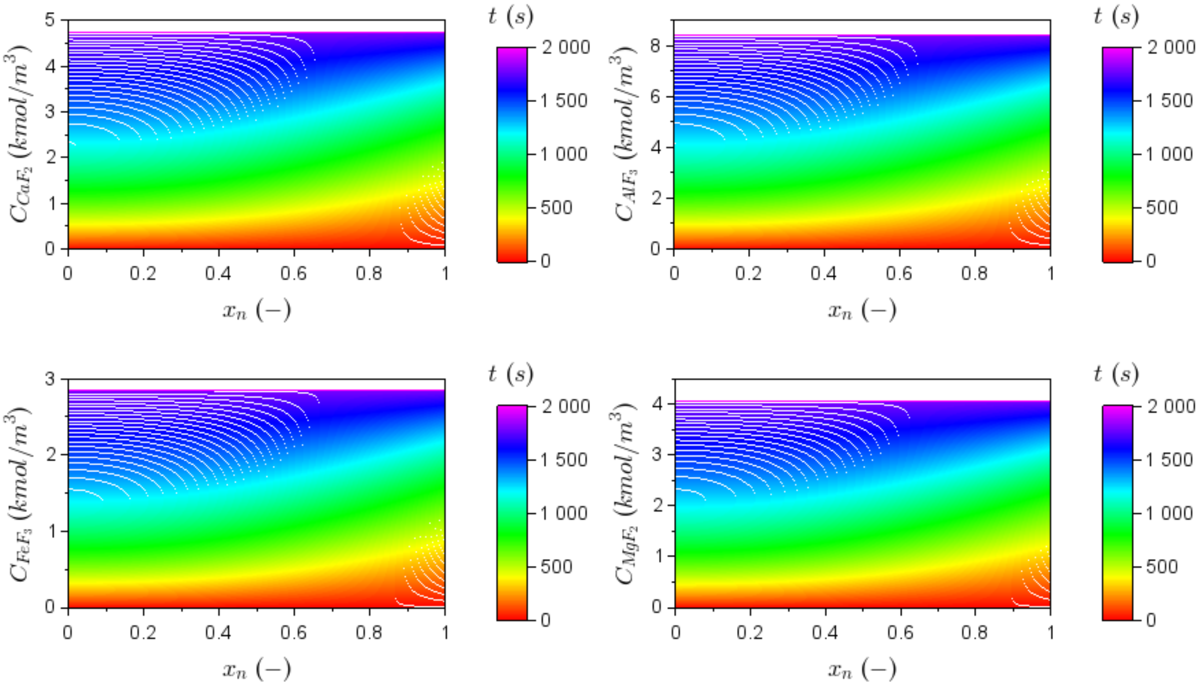

C 8: Effect of flowrate = 1 m³/s on solid products concentrations over through the particle.

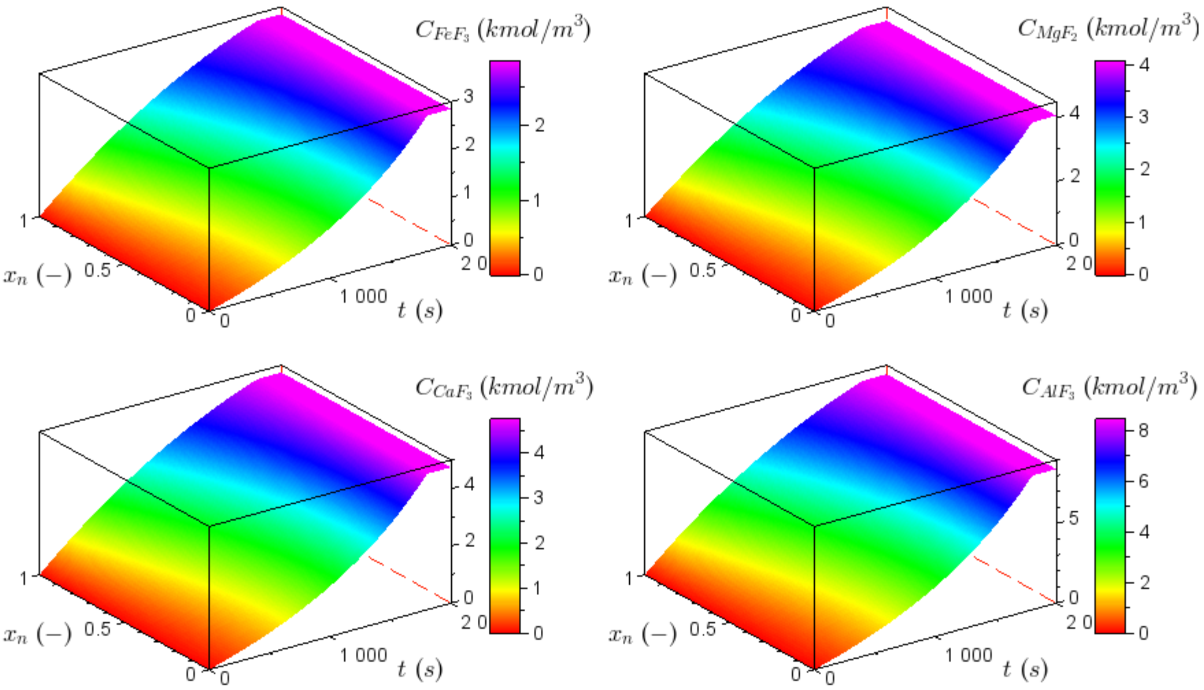

C 9: Surface graphs showing the effect of flowrate = 1 m³/s on solid products concentrations.

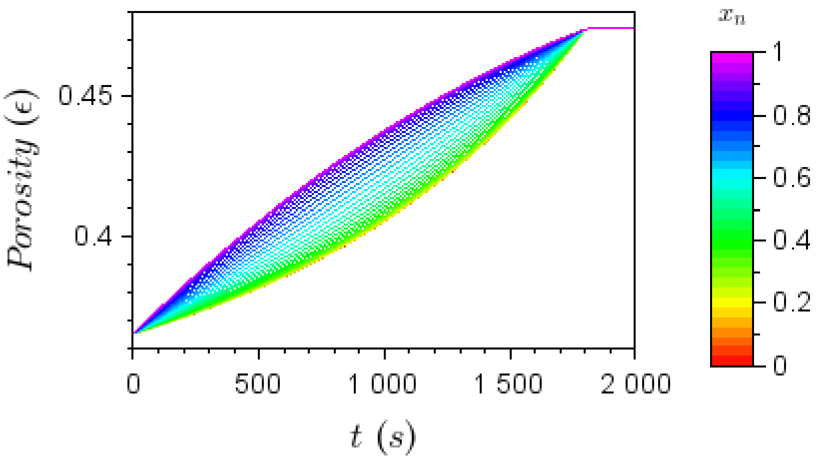

C 10: Effect of flowrate = 1 m³/s on porosity over time.

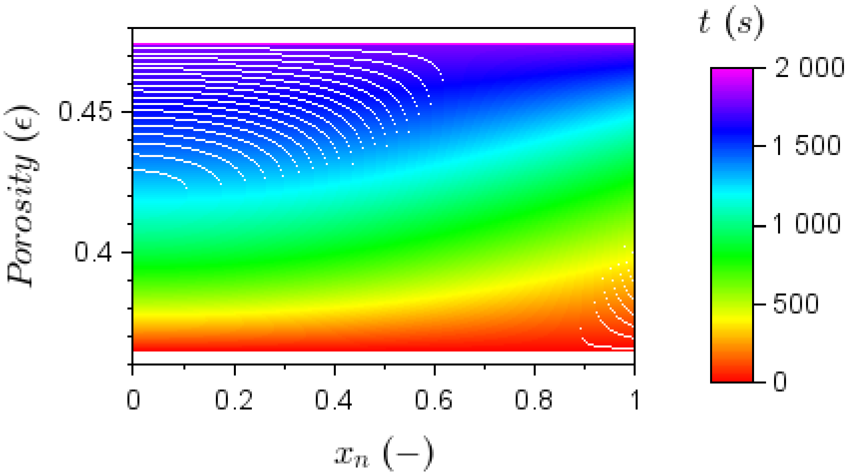

C 11: Effect of flowrate = 1 m³/s on porosity through the particle.

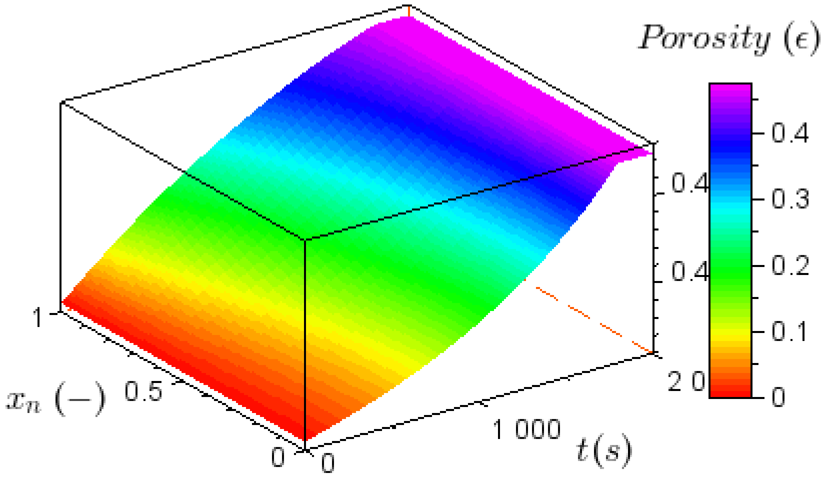

C 12: Surface graphs showing the effect of flowrate = 1 m³/s on porosity.

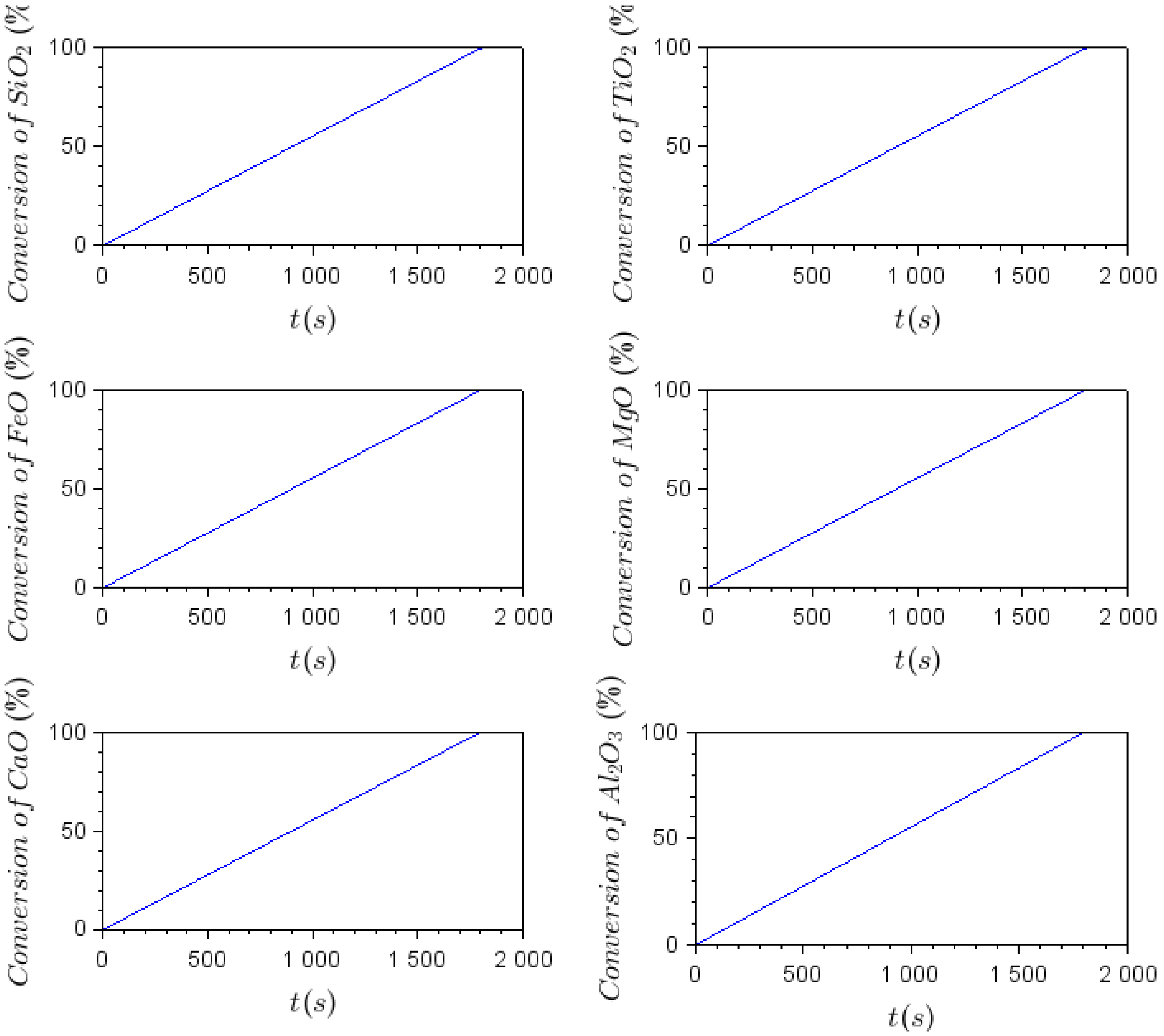

C 13: Effect of flowrate = 1 m^3/s on conversion over time.

Flowrate variation results - $Q_0 = 10\ m^3/s$

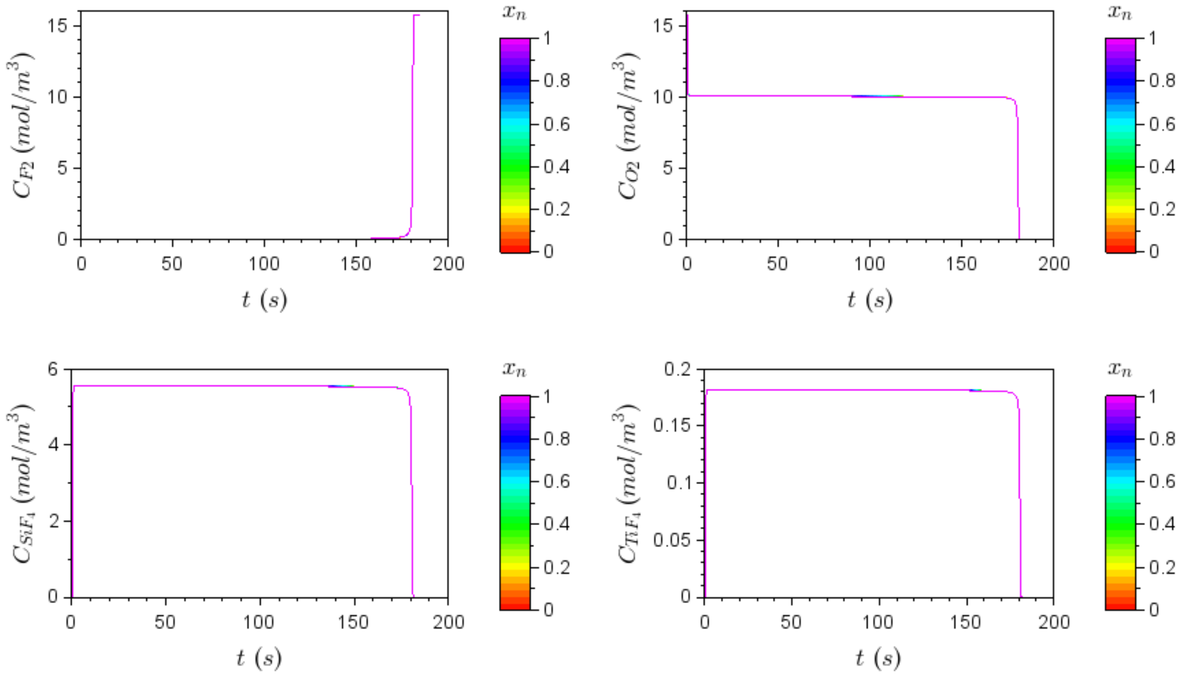

C 14: Effect of flowrate = 10 m³/s on gas concentrations over time.

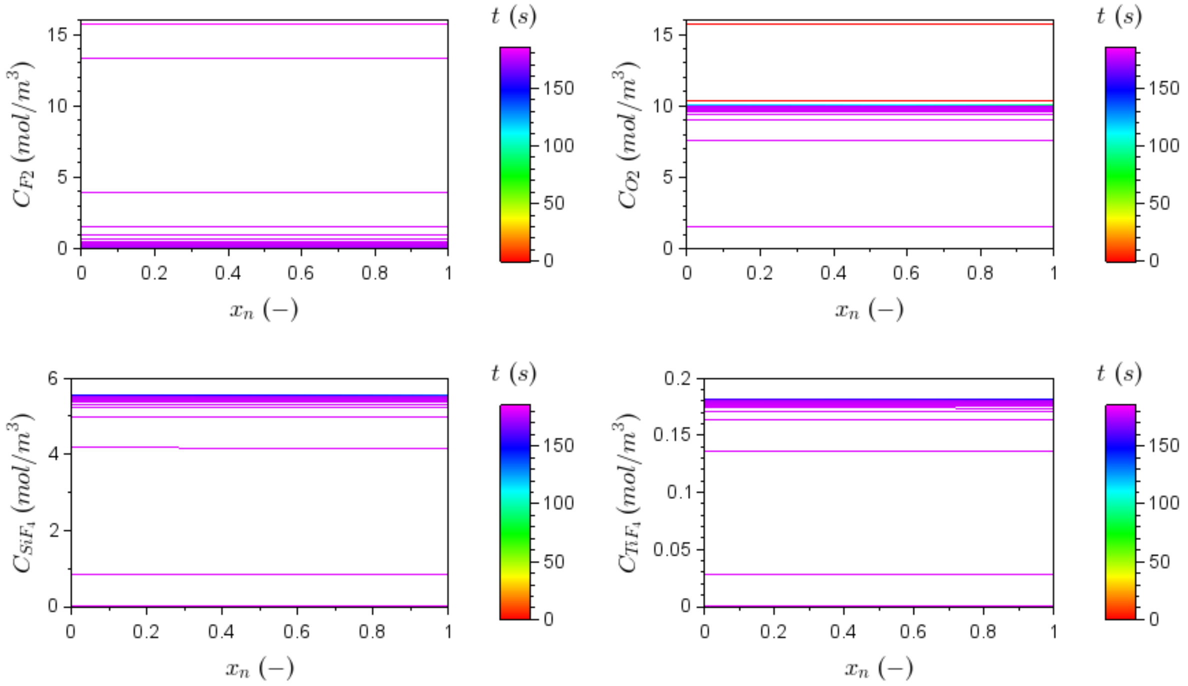

C 15: Effect of flowrate = 10 m³/s on gas concentrations through the particle.

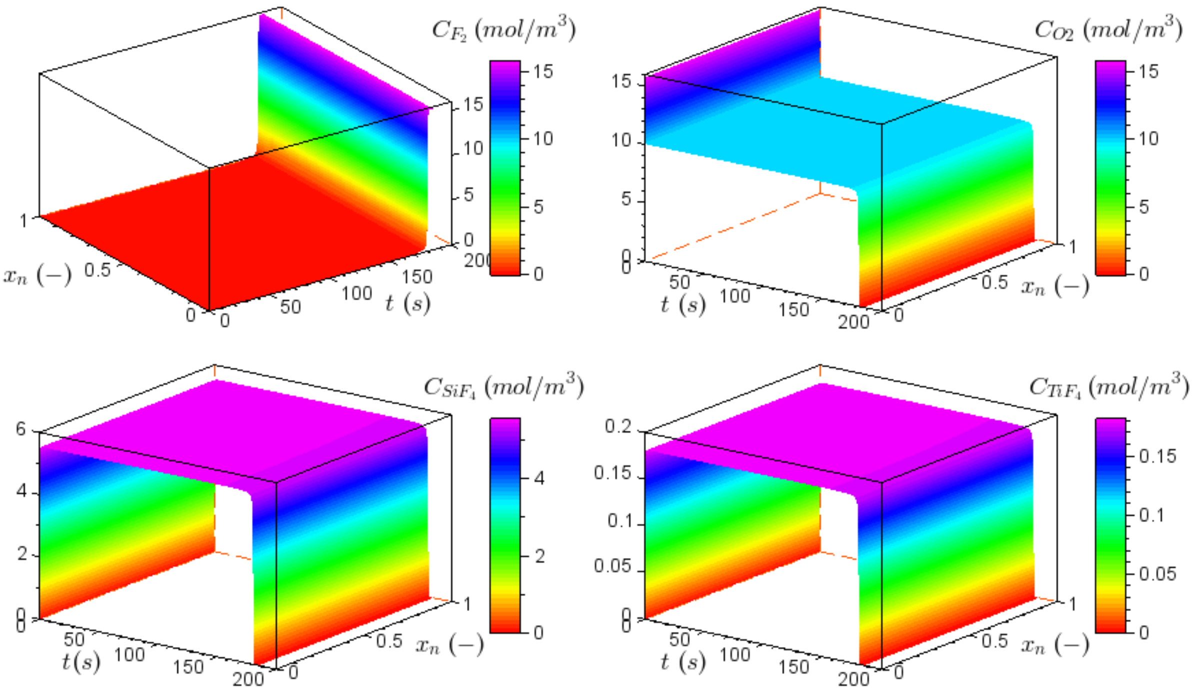

C 16: Surface graphs showing the effect of flowrate = 10 m³/s on gas concentrations.

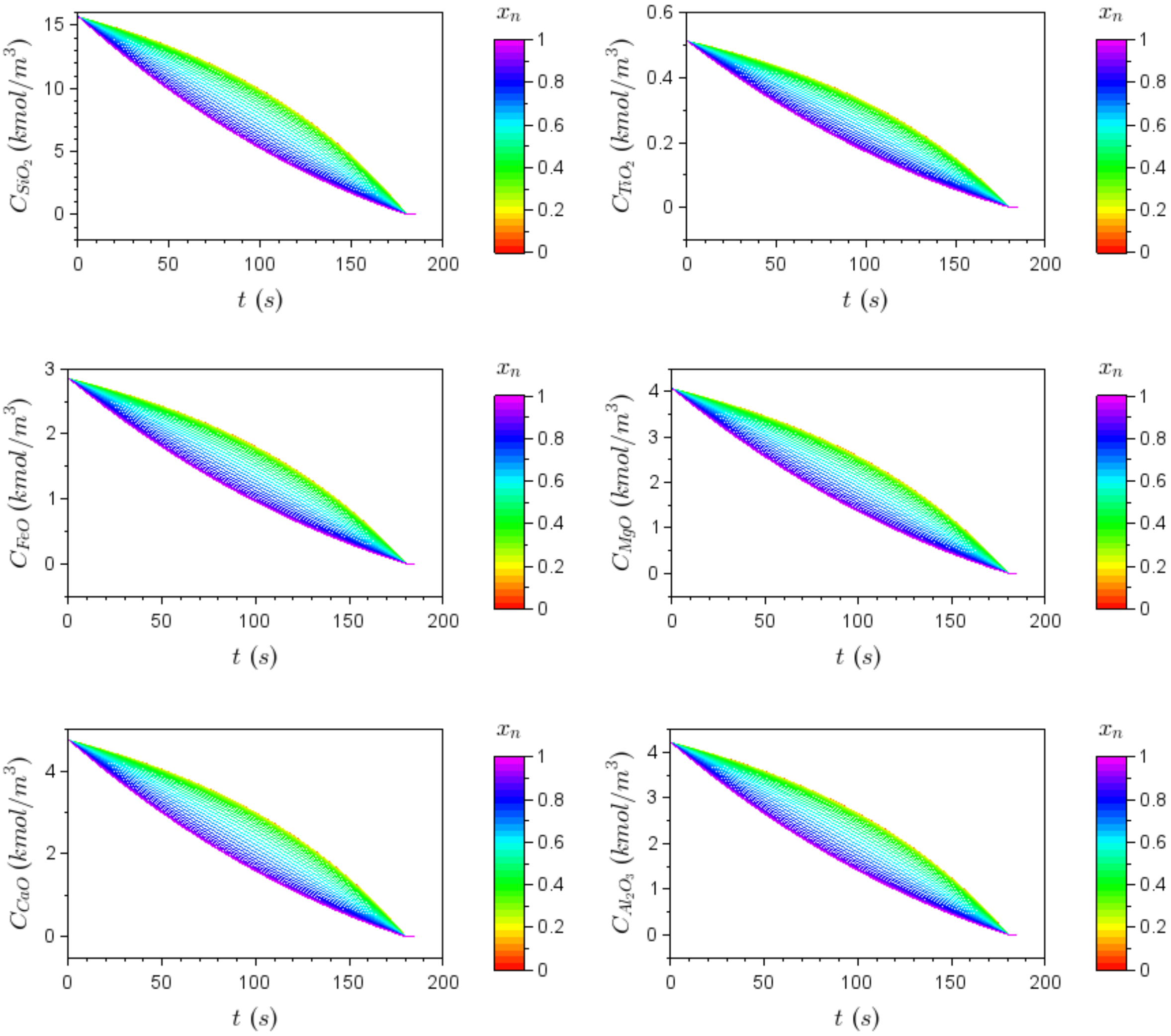

C 17: Effect of flowrate = 10 m^3/s on solid reactant concentrations over time.

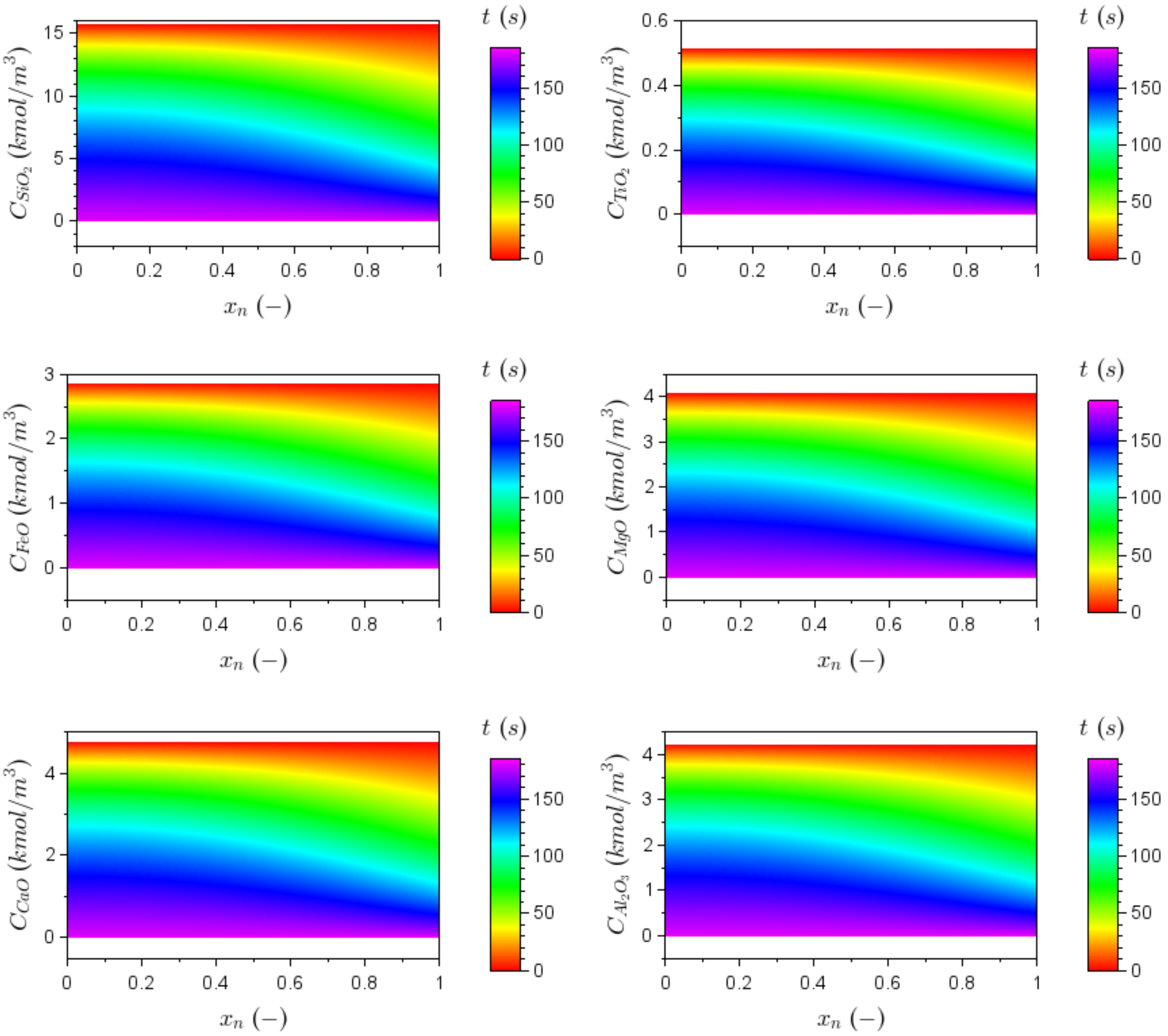

C 18: Effect of flowrate = 10 m^3/s on solid reactant concentrations through the particle.

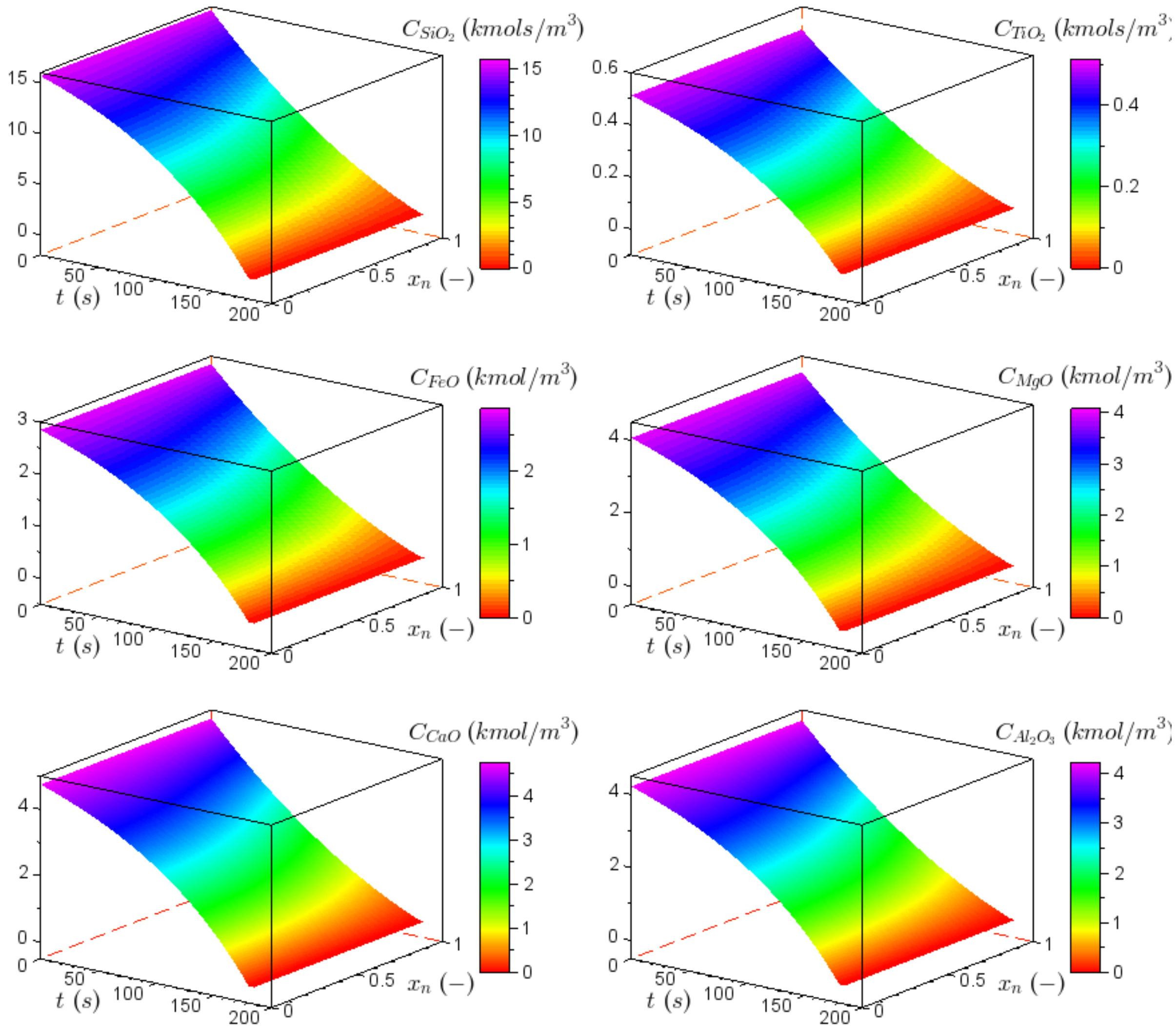

C 19: Surface graphs showing the effect of flowrate = 10 m³/s on solid reactant concentrations.

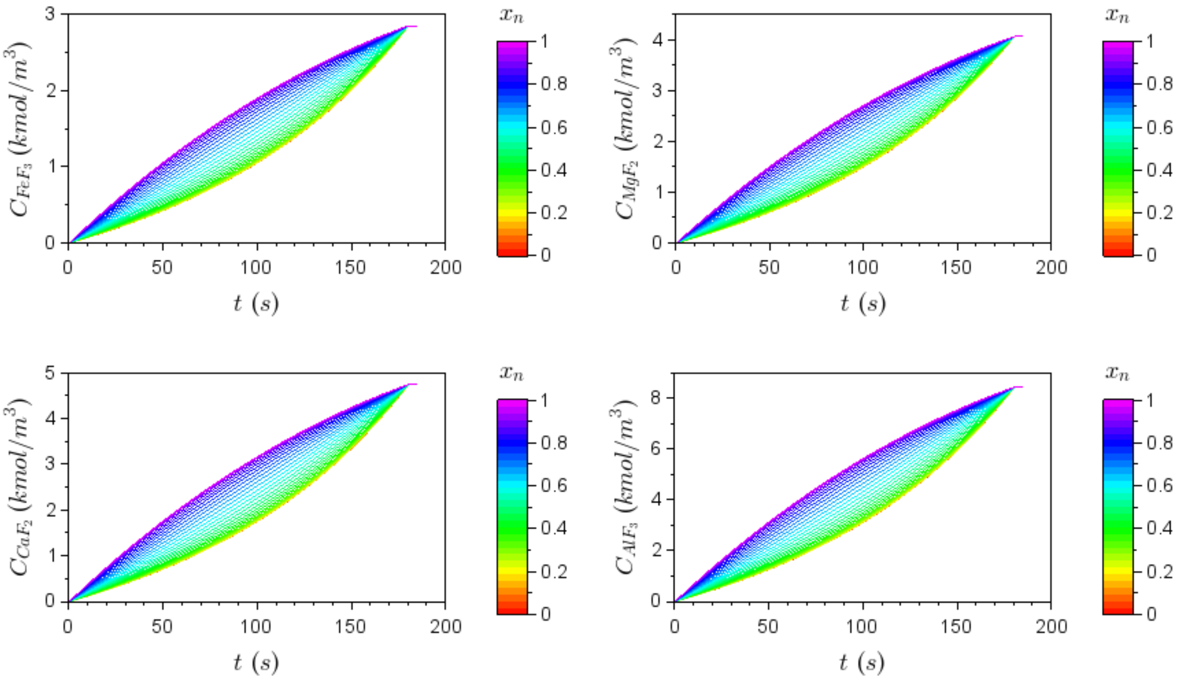

C 20: Effect of flowrate = 10 m³/s on solid products concentrations over time.

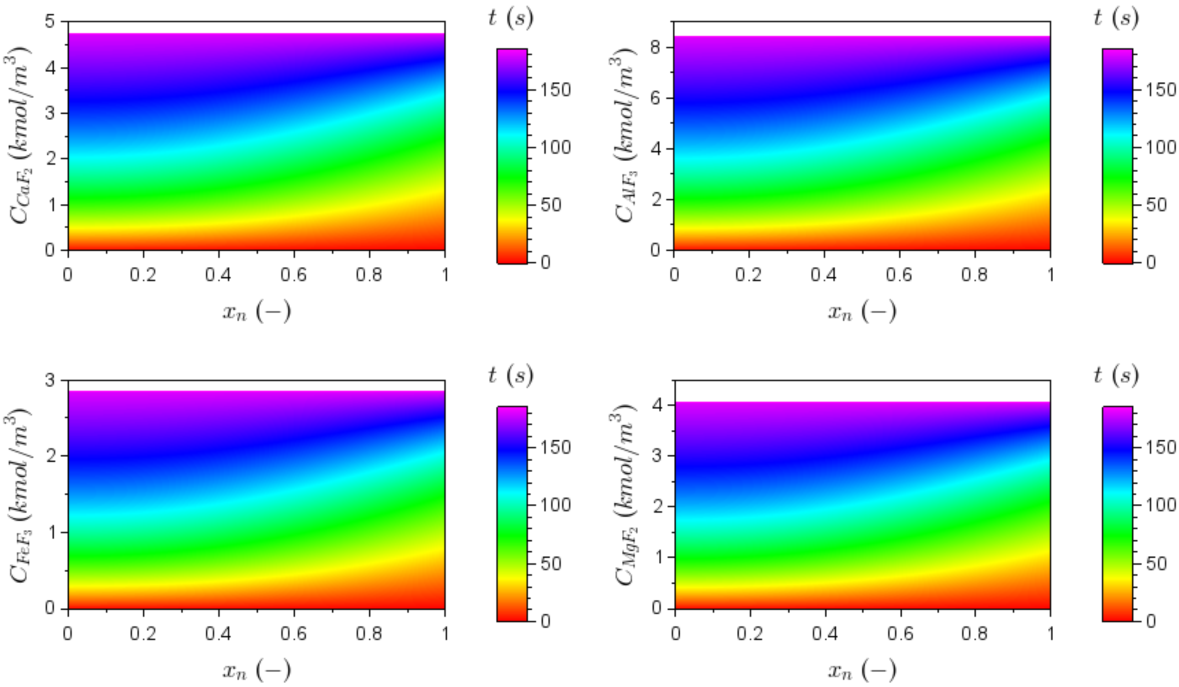

C 21: Effect of flowrate = 10 m³/s on solid products concentrations through the particle.

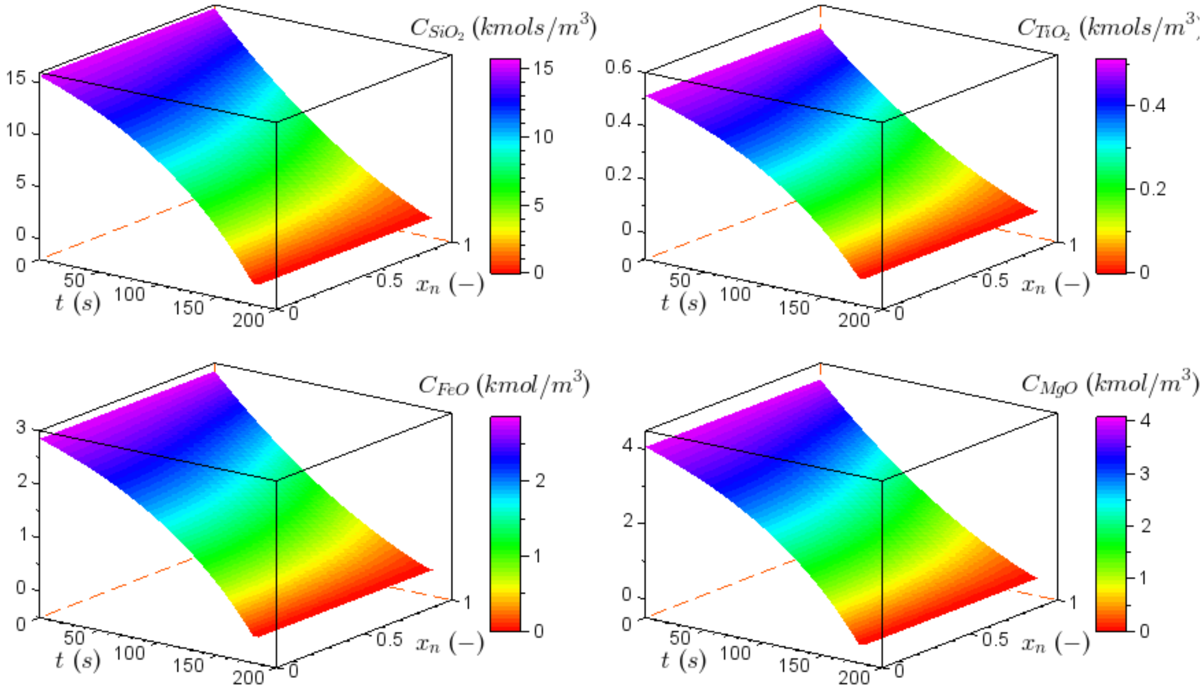

C 22: Surface graphs showing the effect of flowrate = 10 m^3/s on solid products concentrations.

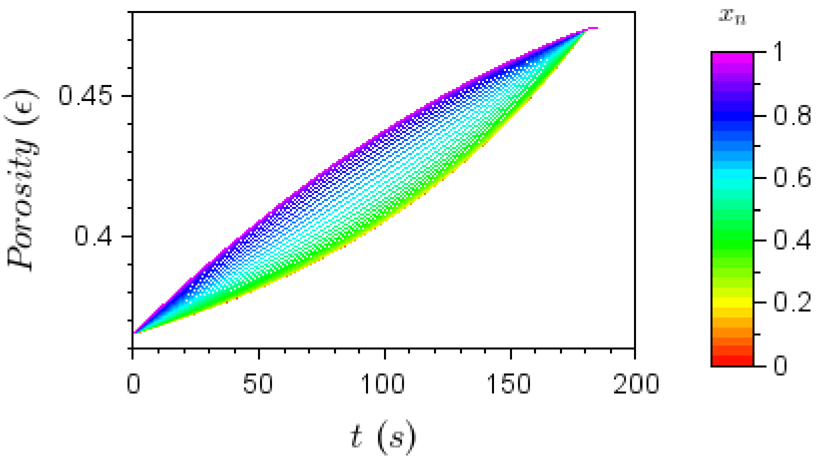

C 23: Effect of flowrate = 10 m³/s on porosity over time.

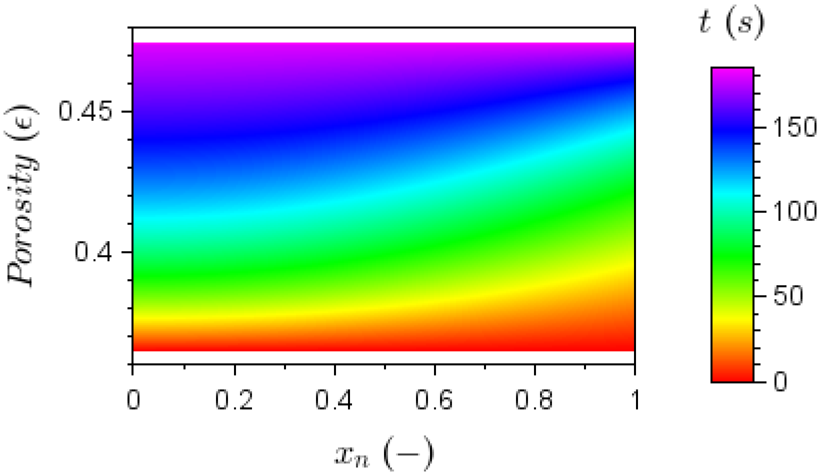

C 24: Effect of flowrate = 10 m³/s on porosity through the particle.

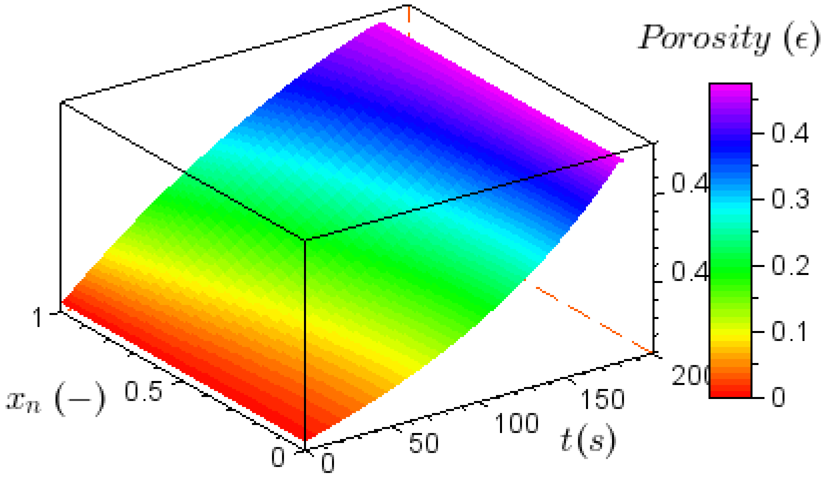

C 25:Surface graphs showing the effect of flowrate = 10 m³/s on porosity.

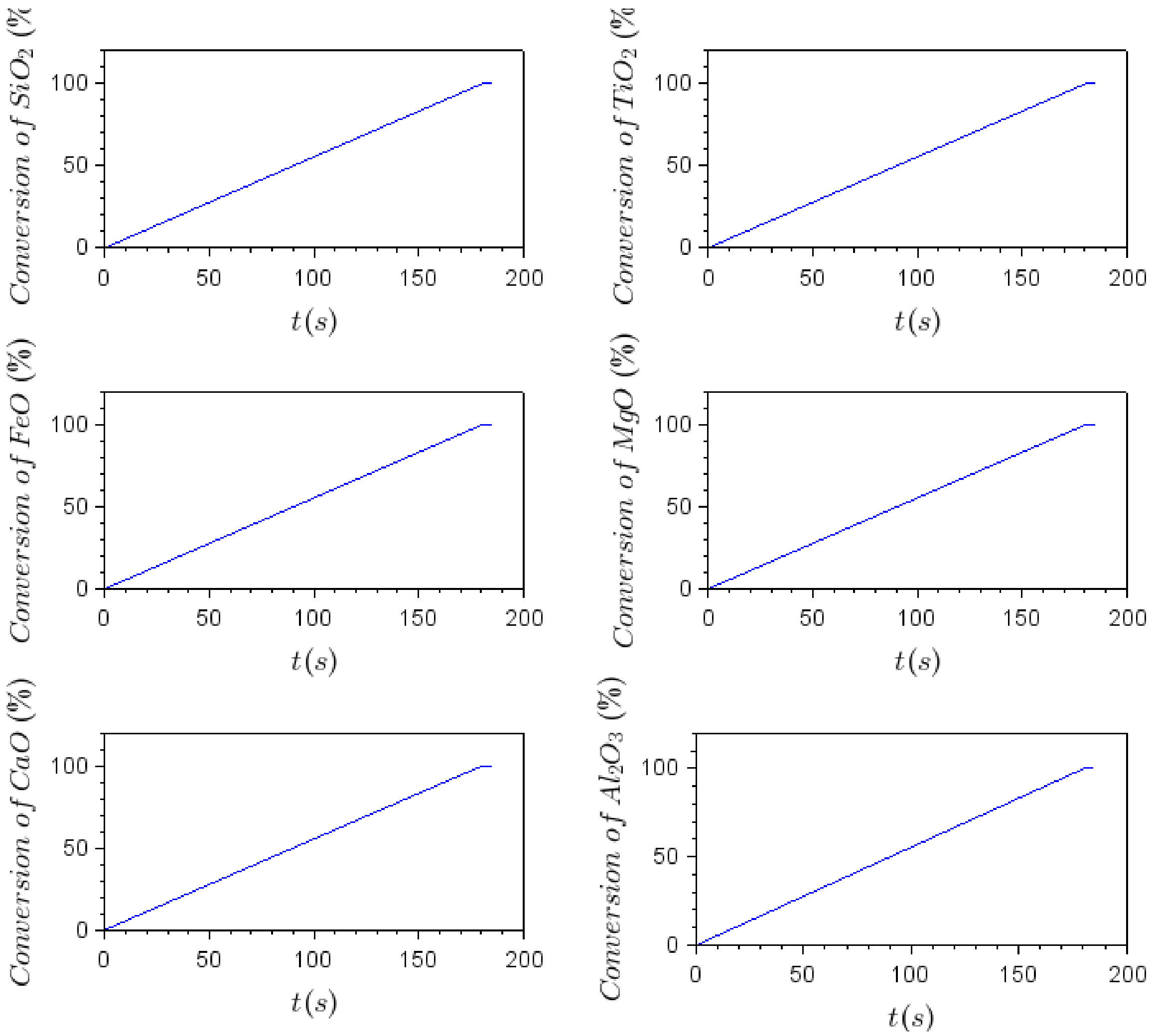

C 26: Effect of flowrate = 10 m³/s on conversion over time.

Flowrate variation results - $Q_0 = 100\ m^3/s$

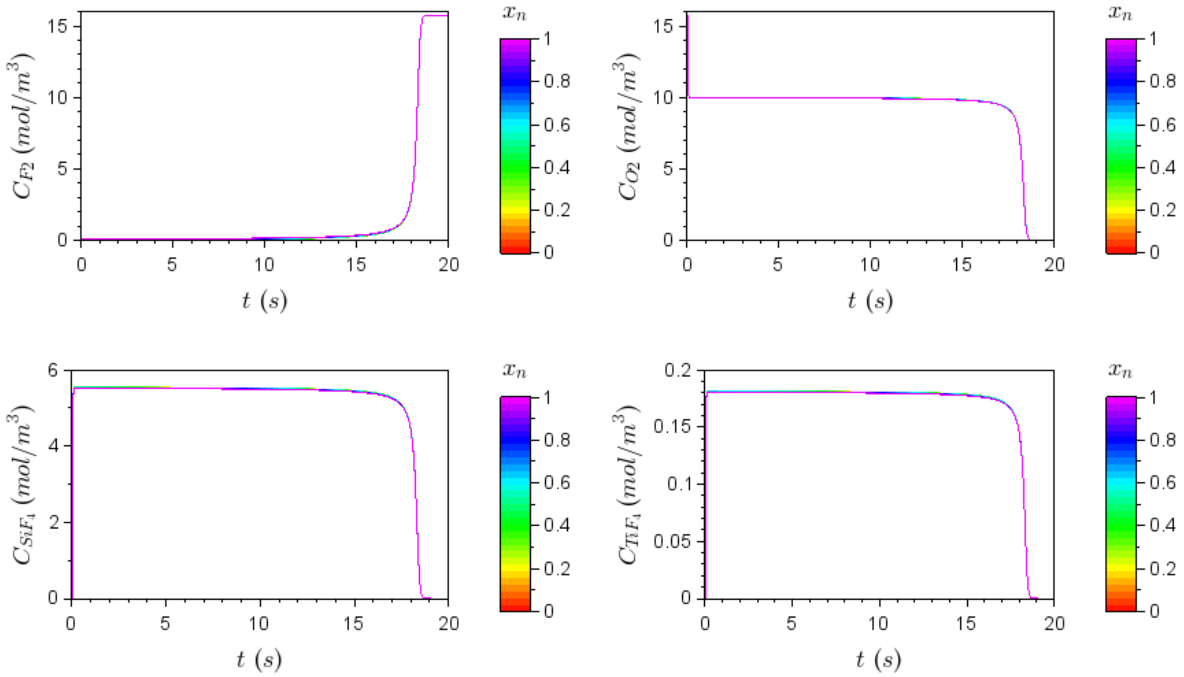

C 27: Effect of flowrate = 100 m³/s on gas concentrations over time.

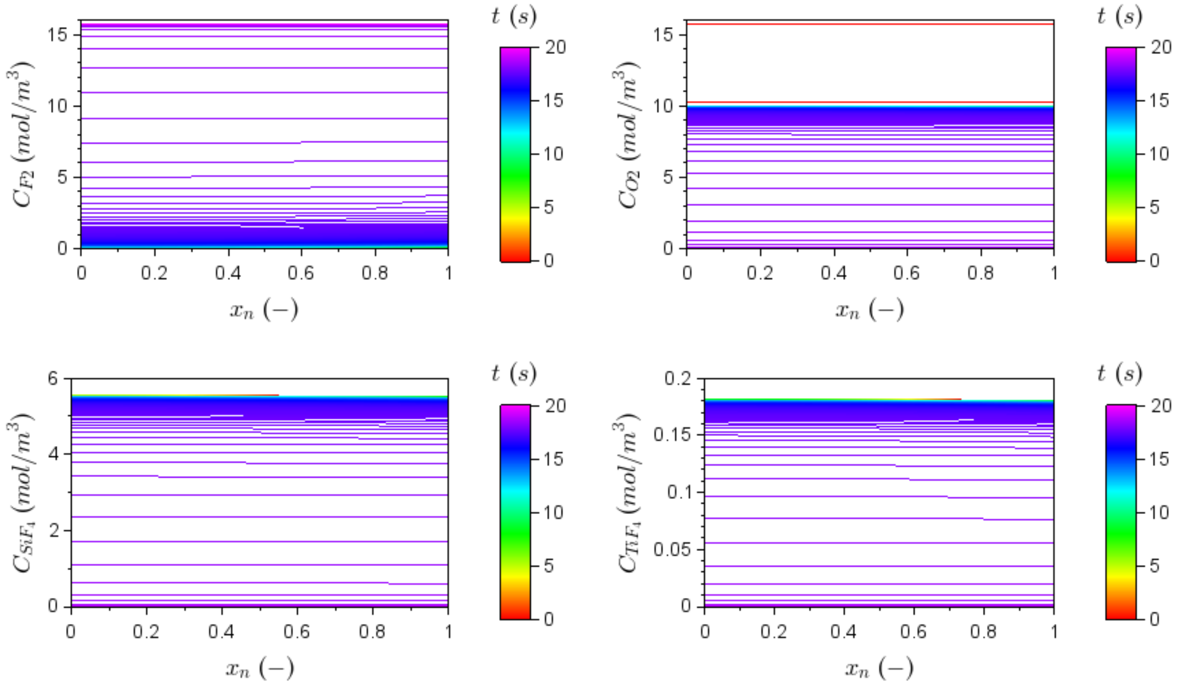

C 28: Effect of flowrate = 100 m³/s on gas concentrations through the particle.

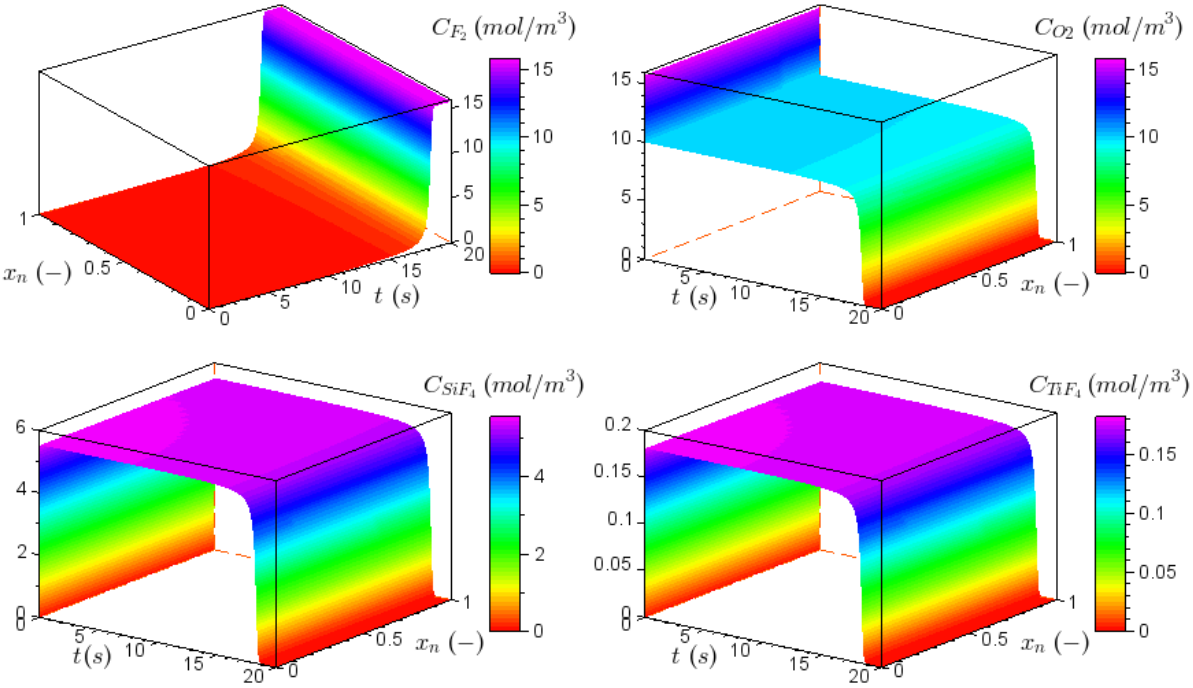

C 29: Surface graphs showing the effect of flowrate = 100 m^3/s on gas concentrations.

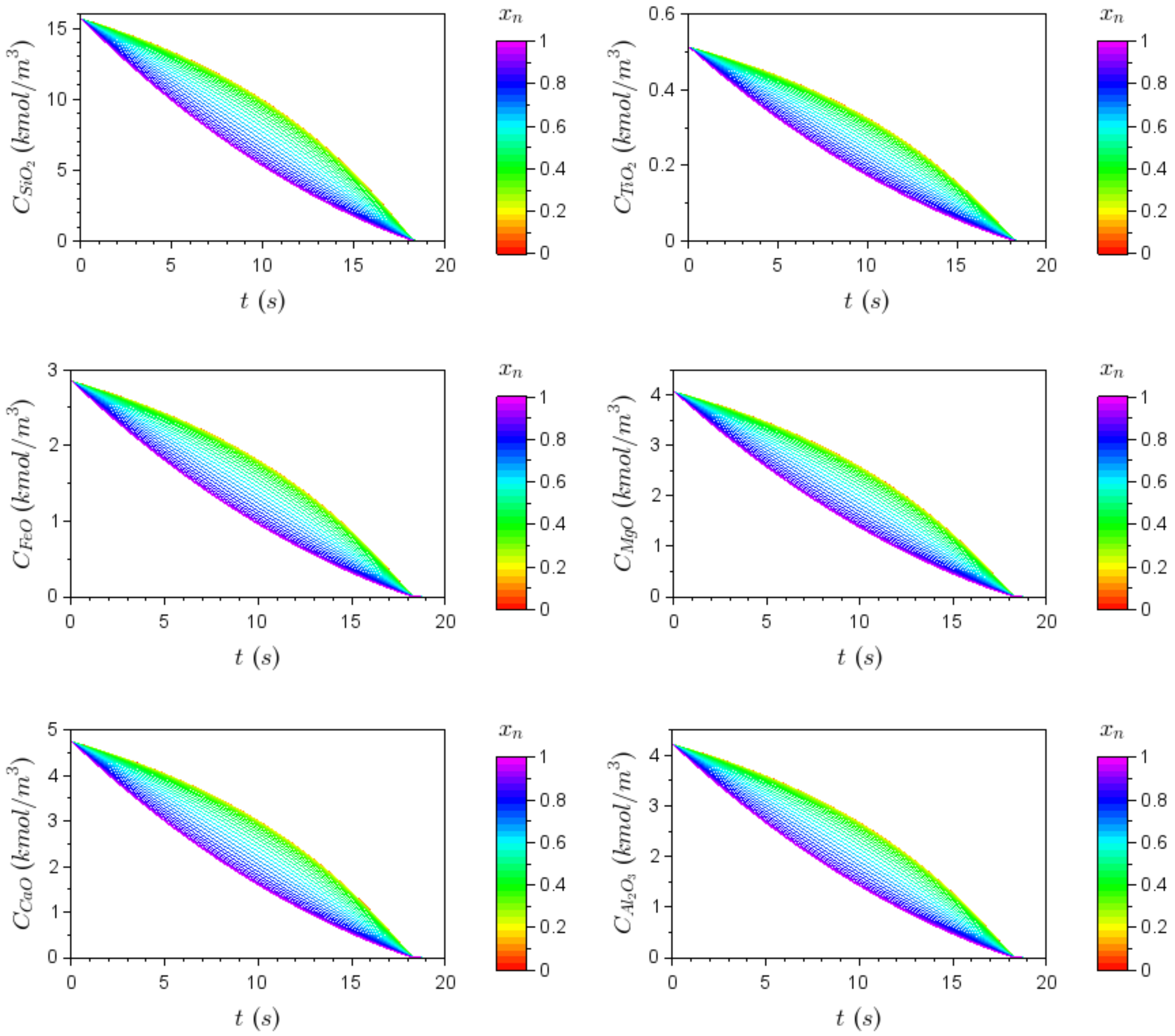

C 30: Effect of flowrate = 100 m^3/s on solid reactant concentrations over time.

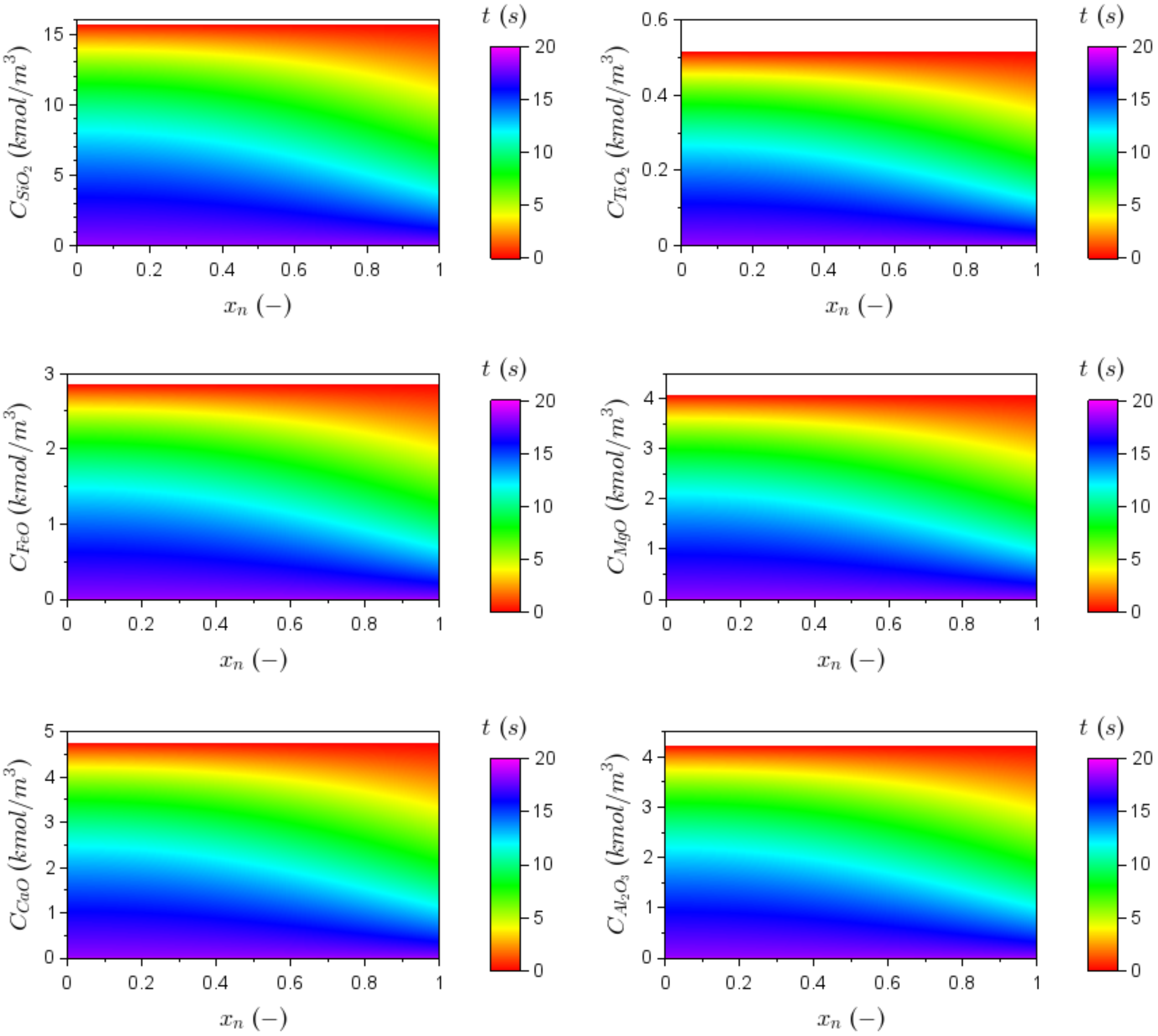

C 31: Effect of flowrate = 100 m^3/s on solid reactant concentrations through the particle.

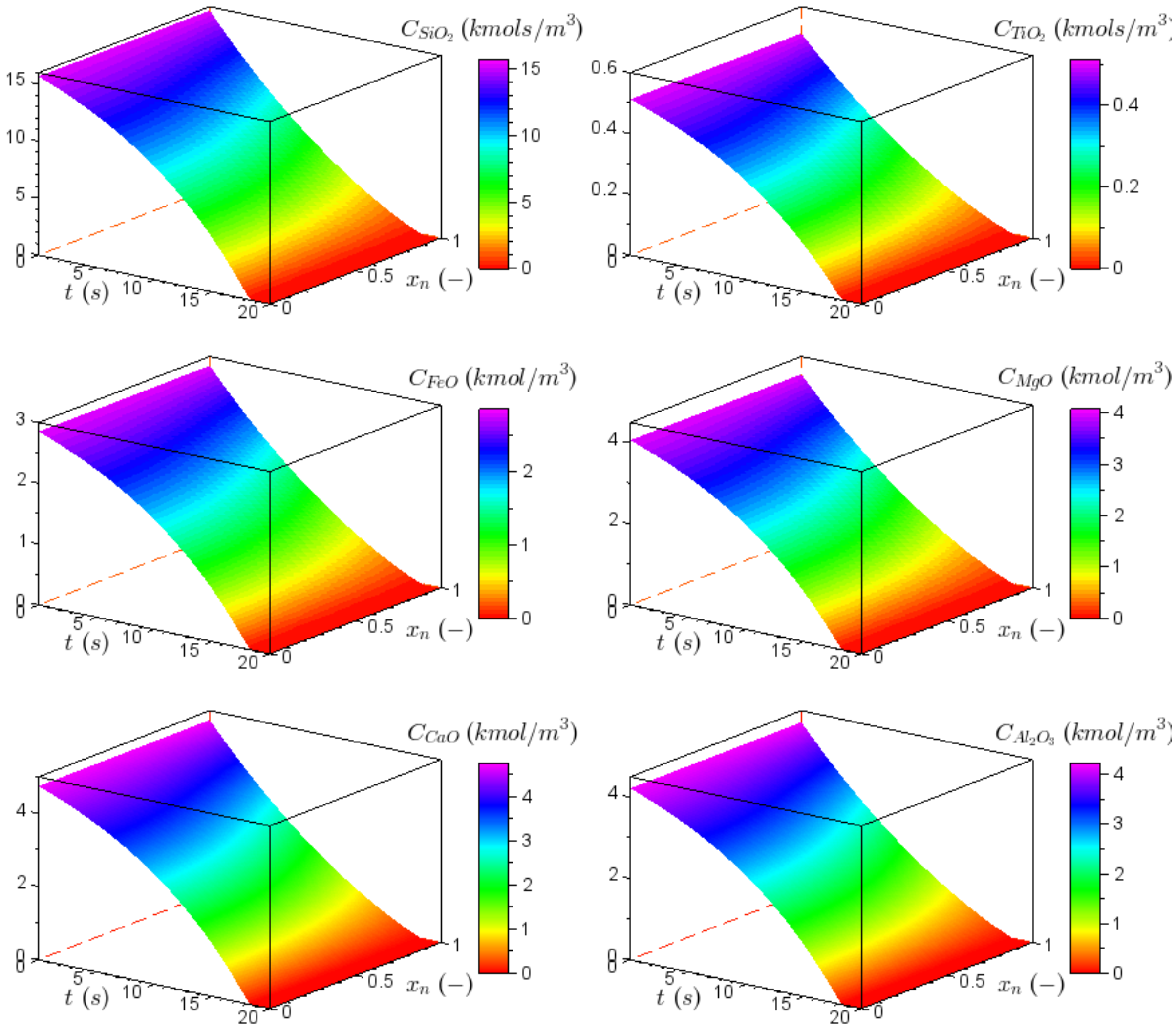

C 32:Surface graph showing the effect of flowrate = 100 m³/s on solid reactant concentrations.

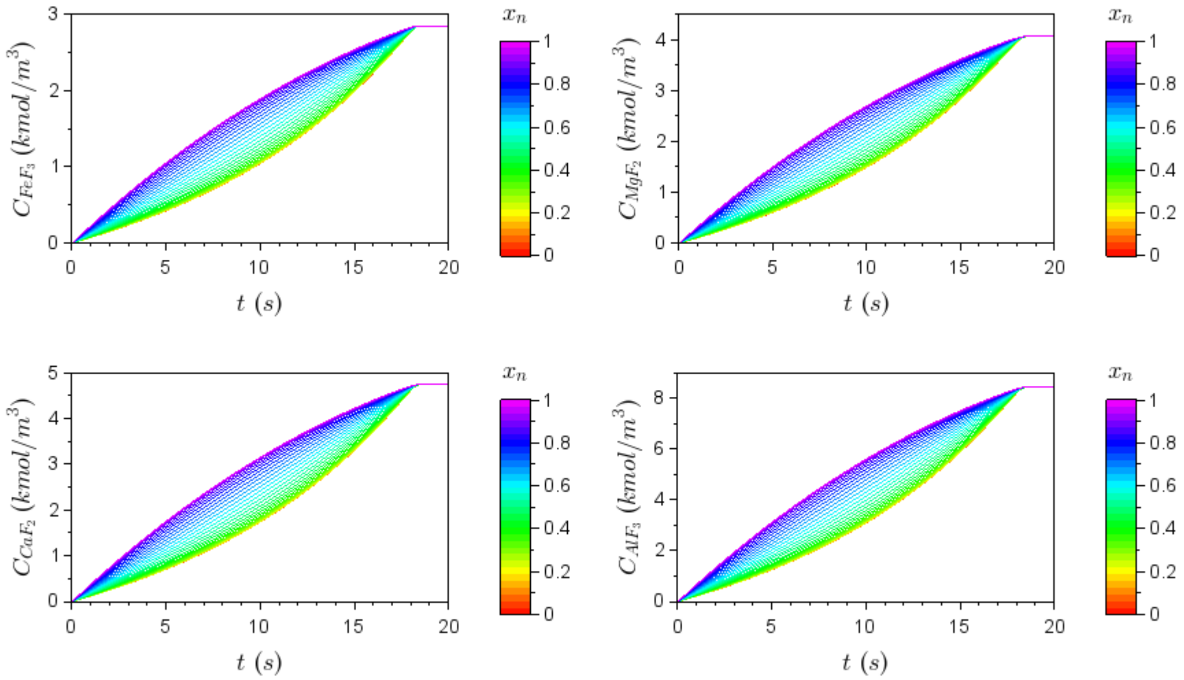

C 33: Effect of flowrate = 100 m³/s on solid products concentrations over time.

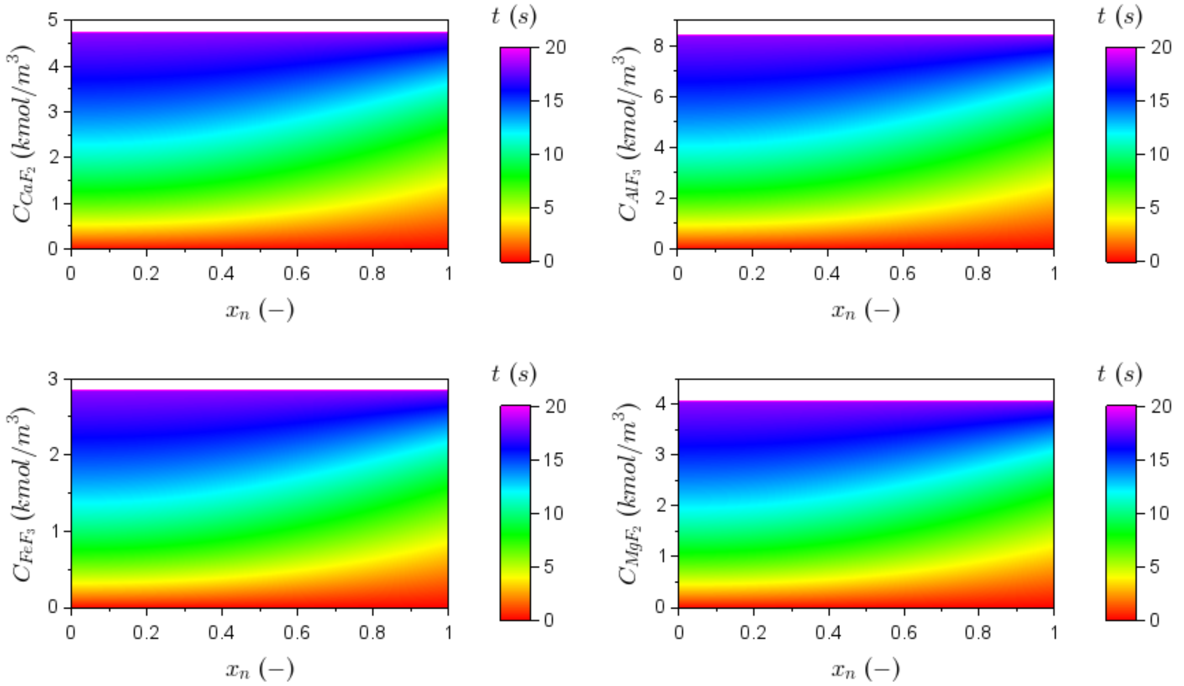

C 34: Effect of flowrate = 100 m³/s on solid products concentrations through the particle.

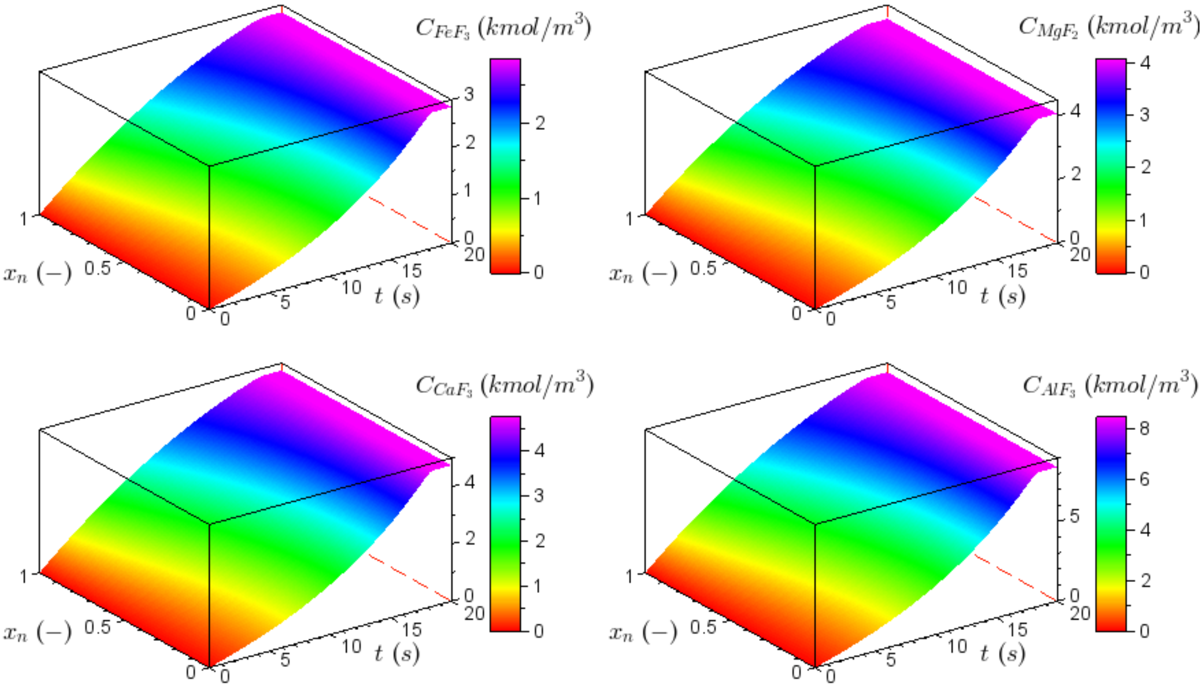

C 35: Surface graphs showing the effect of flowrate = 100 m^3/s on solid products concentrations.

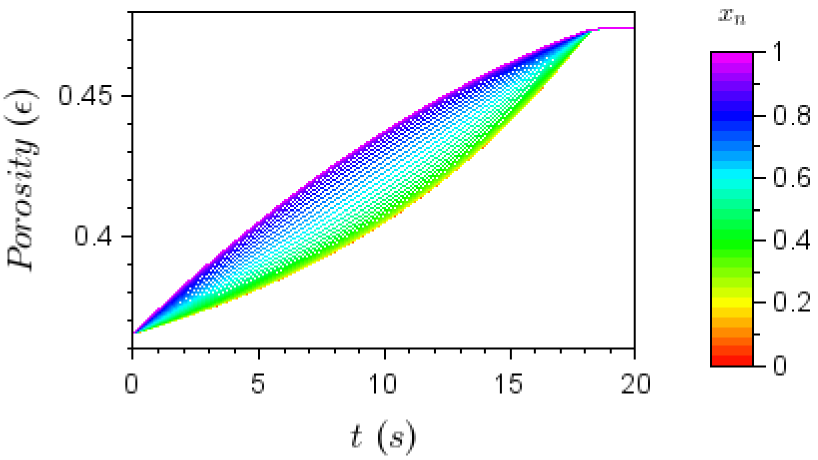

C 36: Effect of flowrate = 100 m³/s on porosity over time.

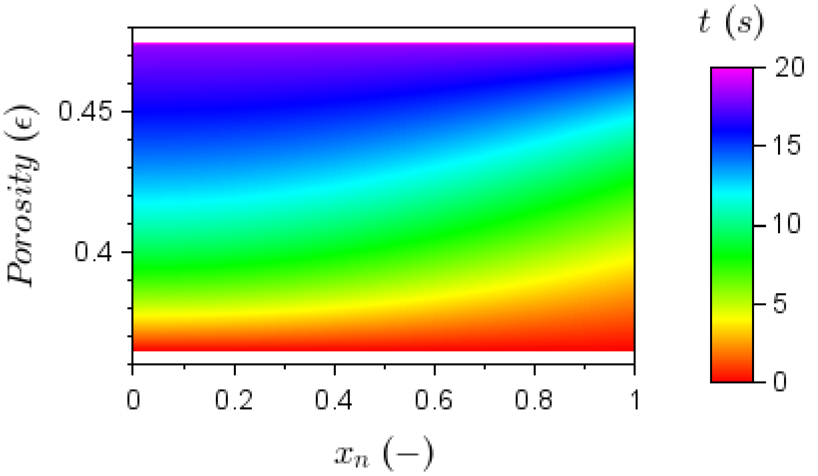

C 37: Effect of flowrate = 100 m³/s on porosity through the particle.

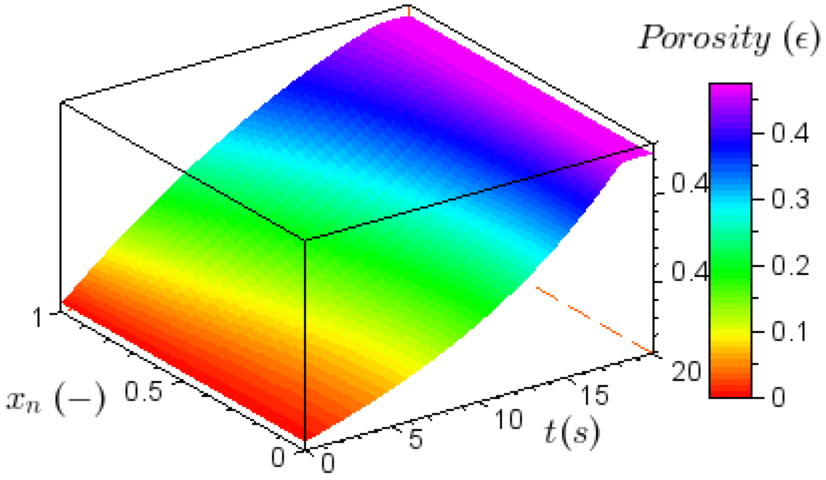

C 38: Surface graphs showing the effect of flowrate = 100 m³/s on porosity.

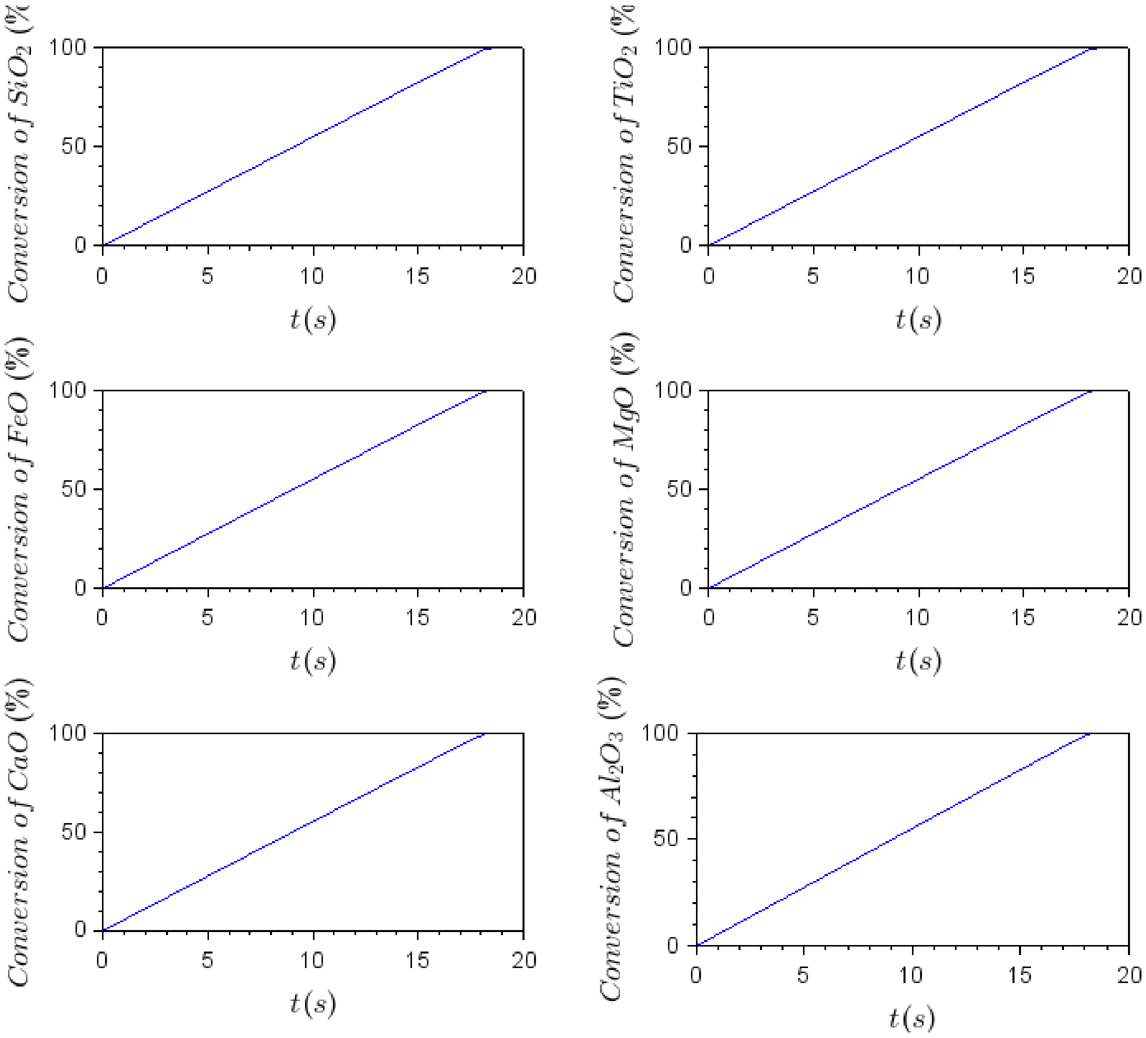

C 39: Effect of flowrate = 100 m^3/s on conversion over time.

Flowrate variation results - $Q_0 = 10000\, m^3/s$

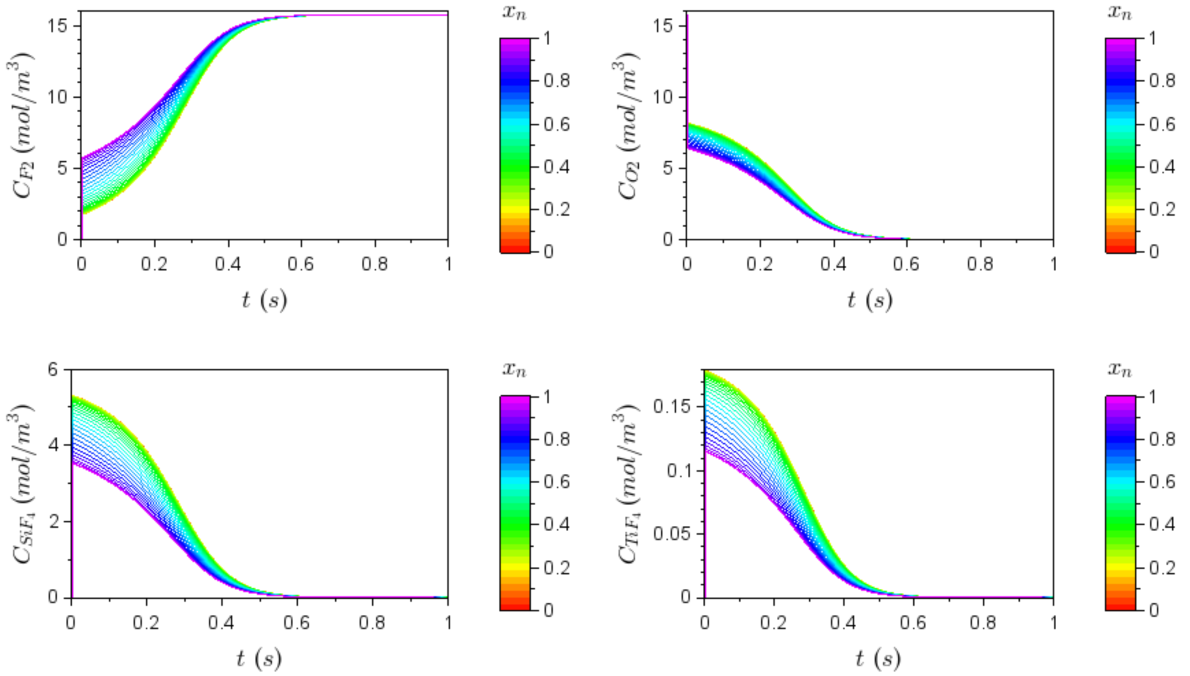

C 40: Effect of flowrate = 10000 m^3/s on gas concentrations over time.

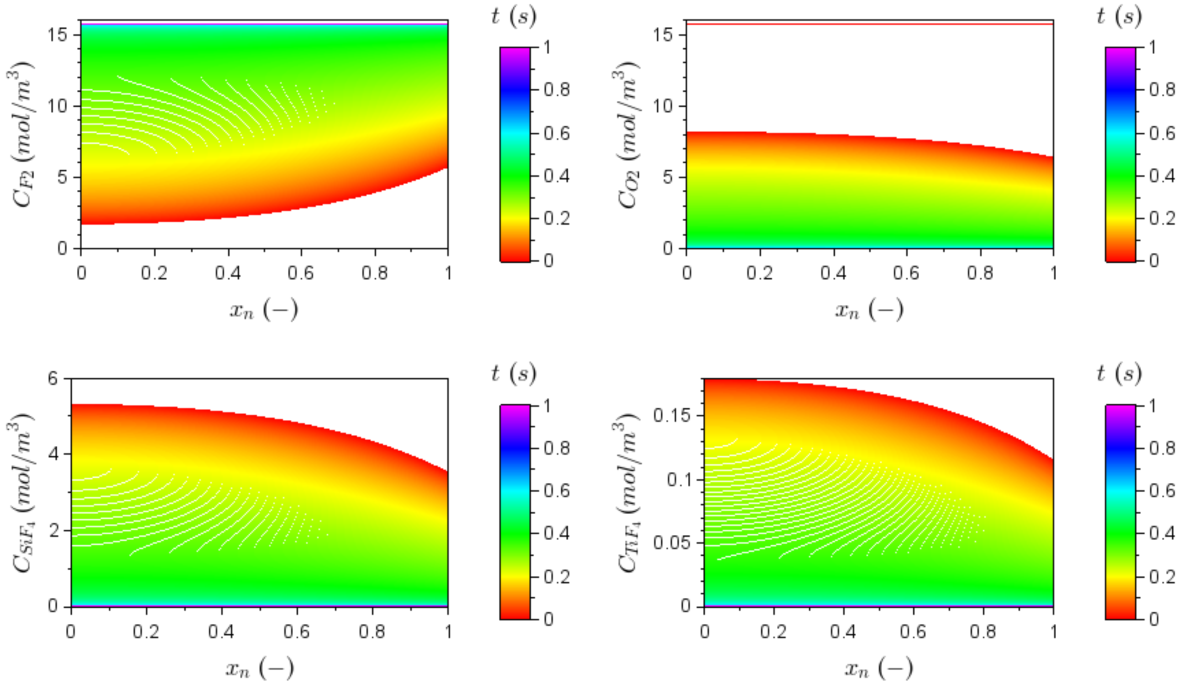

C 41: Effect of flowrate = 10000 m^3/s on gas concentrations through the particle.

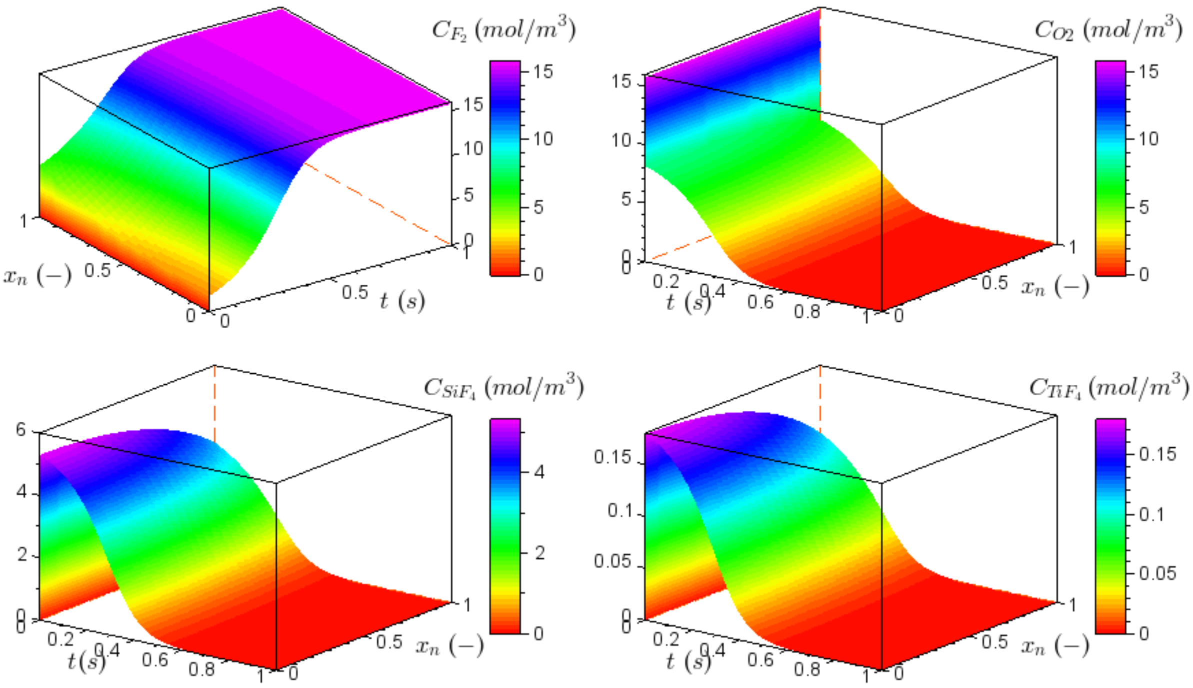

C 42: Surface graphs showing the effect of flowrate = 10000 m^3/s on gas concentrations.

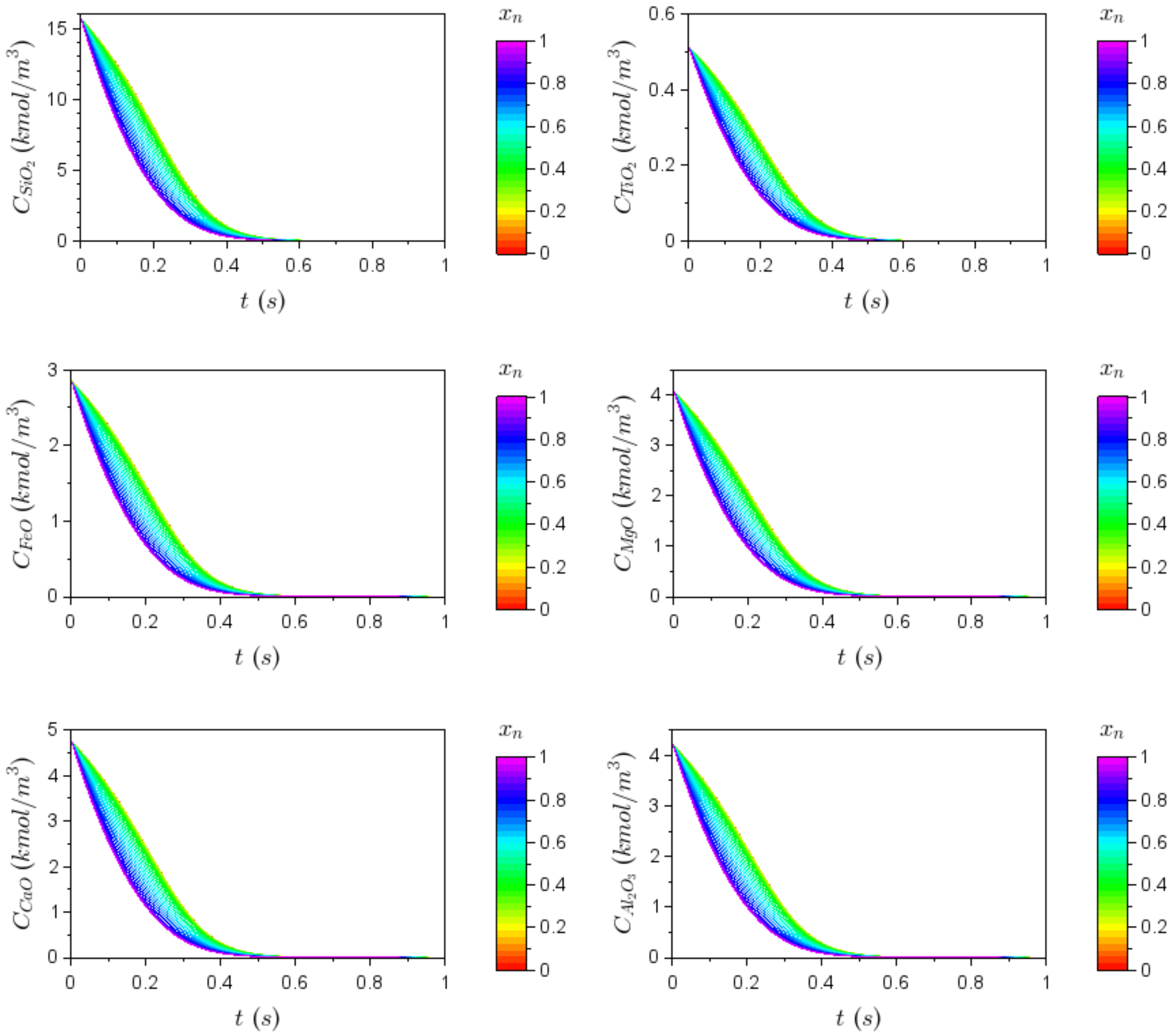

C 43: Effect of flowrate = 10000 m^3/s on solid reactant concentrations over time.

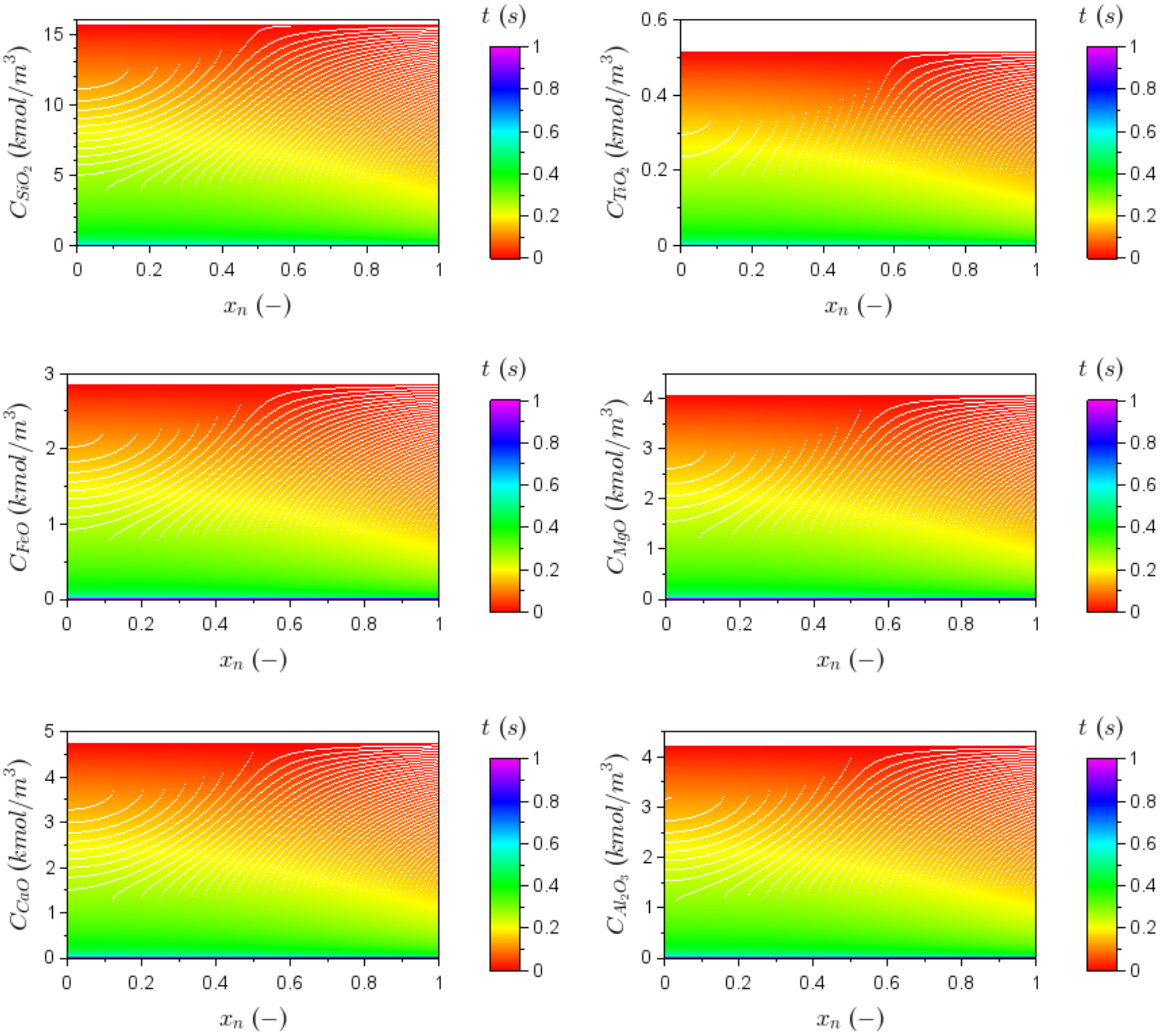

C 44: Effect of flowrate = 10000 m³/s on solid reactant concentrations through the particle.

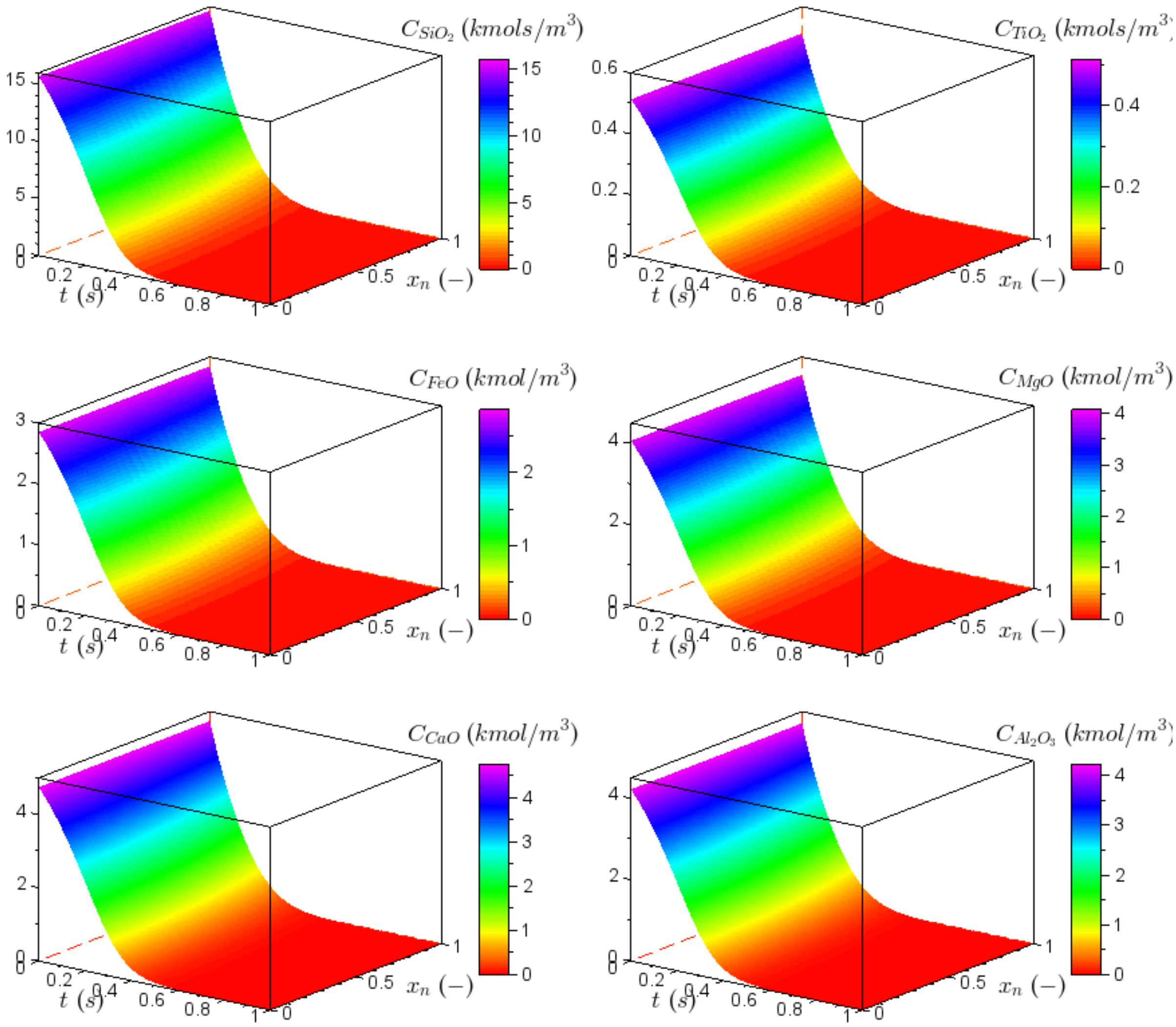

C 45: Surface graph showing the effect of flowrate = 10000 m^3/s on solid reactant concentrations.

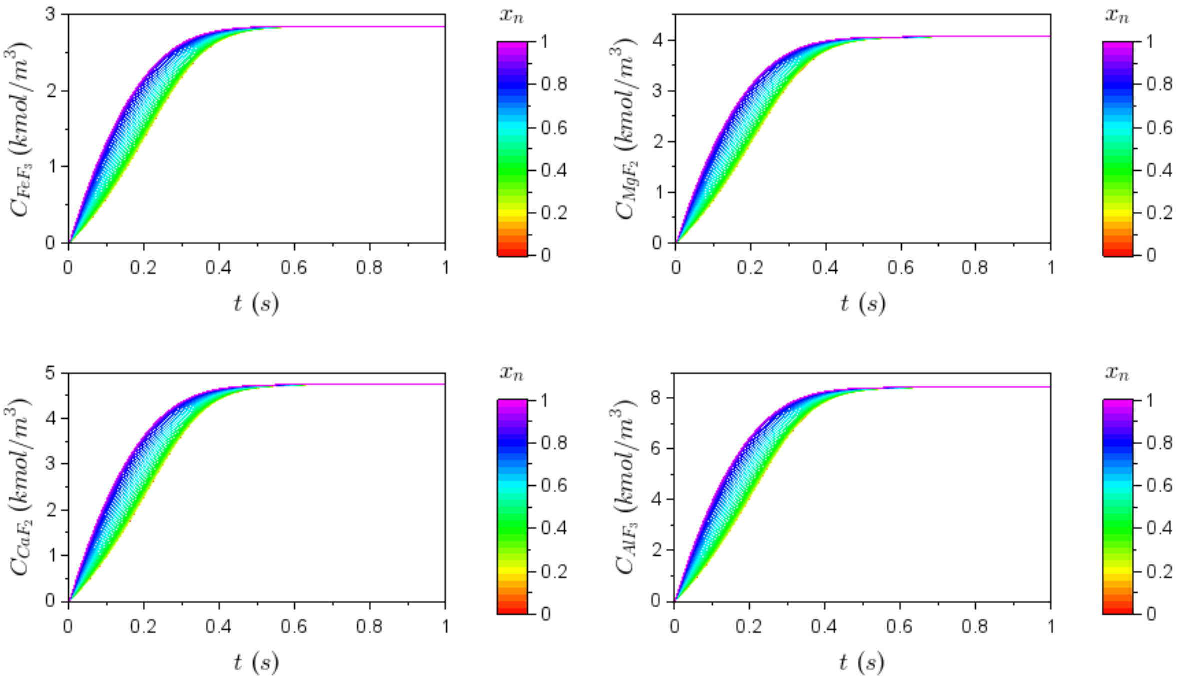

C 46: Effect of flowrate = 10000 m³/s on solid products concentrations over time.

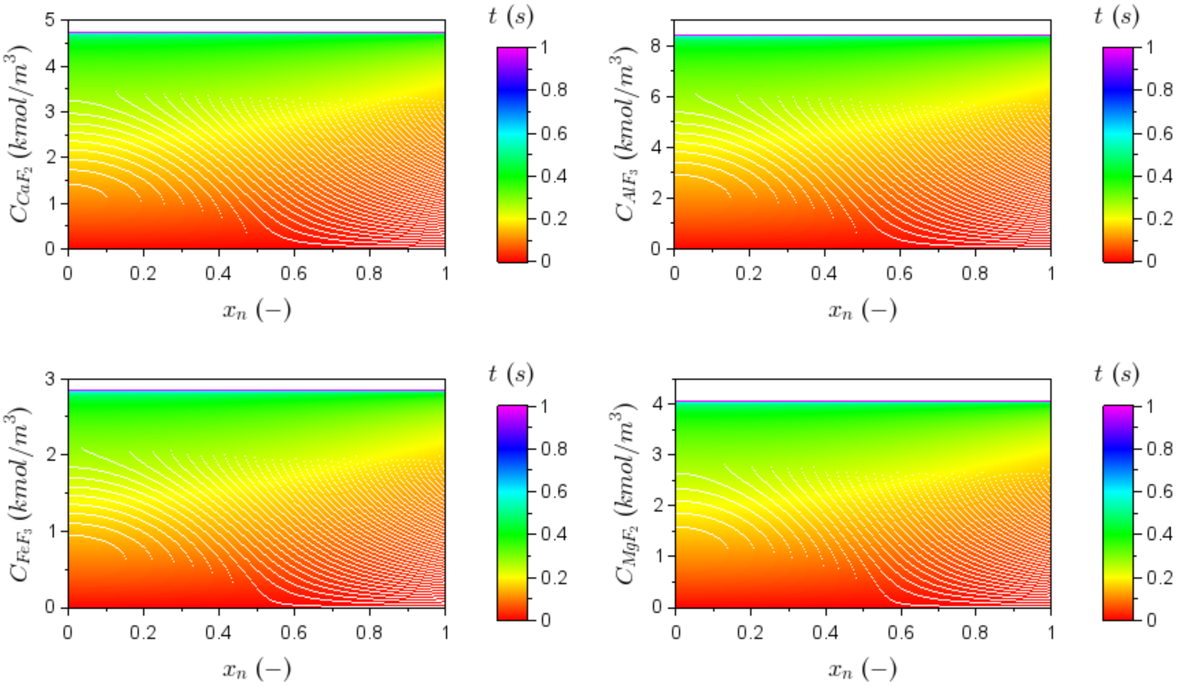

C 47: Effect of flowrate = 10000 m³/s on solid products concentrations through the particle.

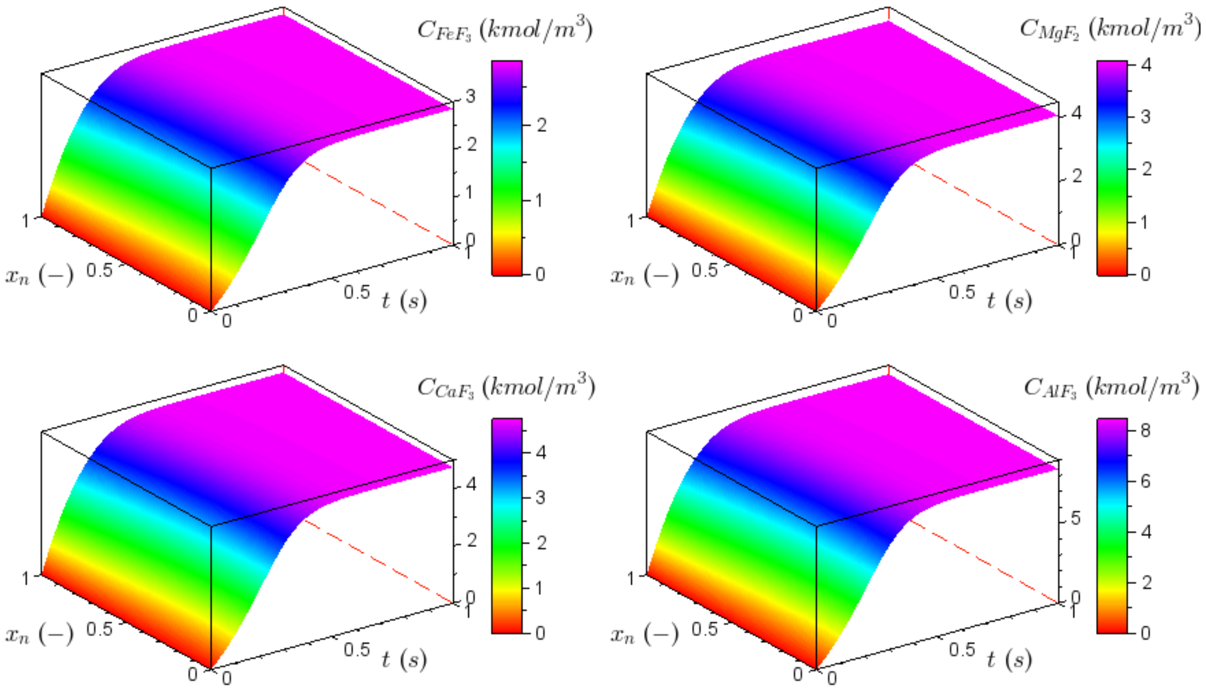

C 48: Surface graphs showing the effect of flowrate = 10000 m^3/s on solid products concentrations.

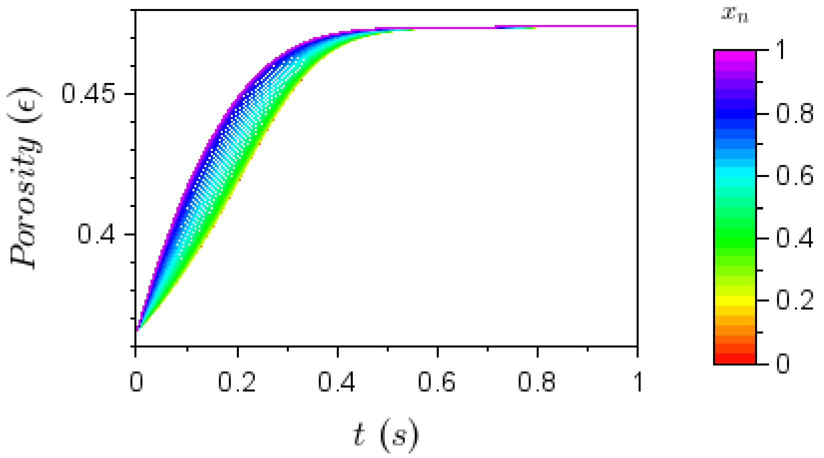

C 49: Effect of flowrate = 10000 m^3/s on porosity over time.

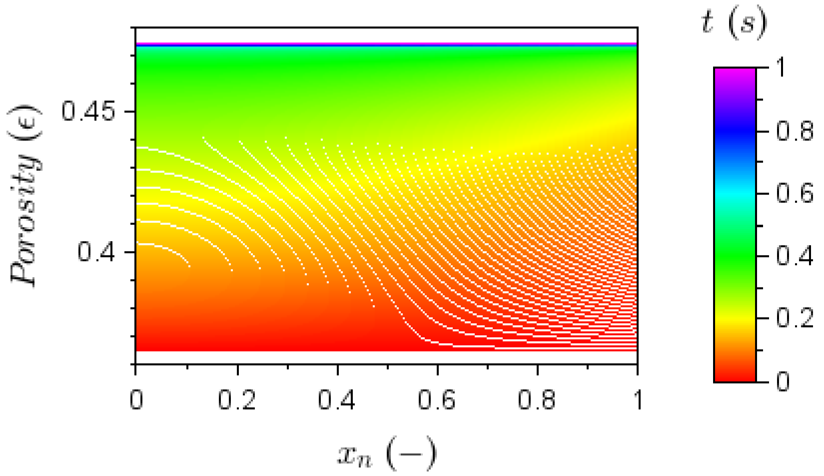

C 50: Effect of flowrate = 10000 m^3/s on porosity through the particle.

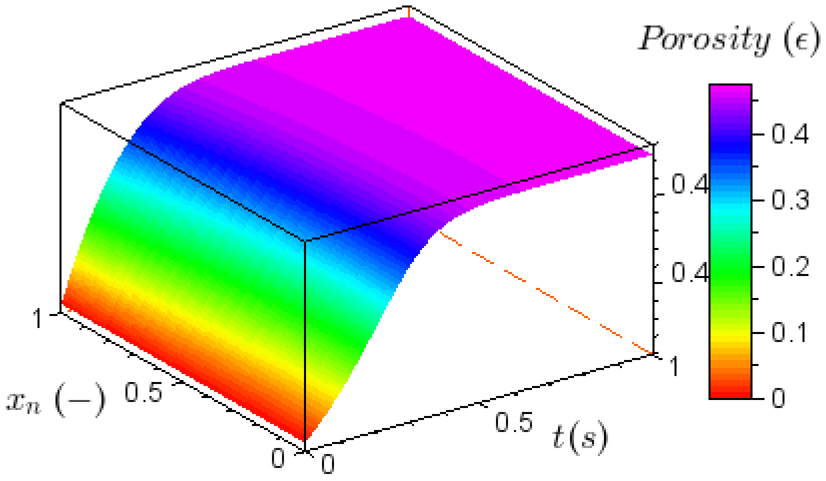

C 51: Surface graphs showing the effect of flowrate = 10000 m^3/s on porosity.

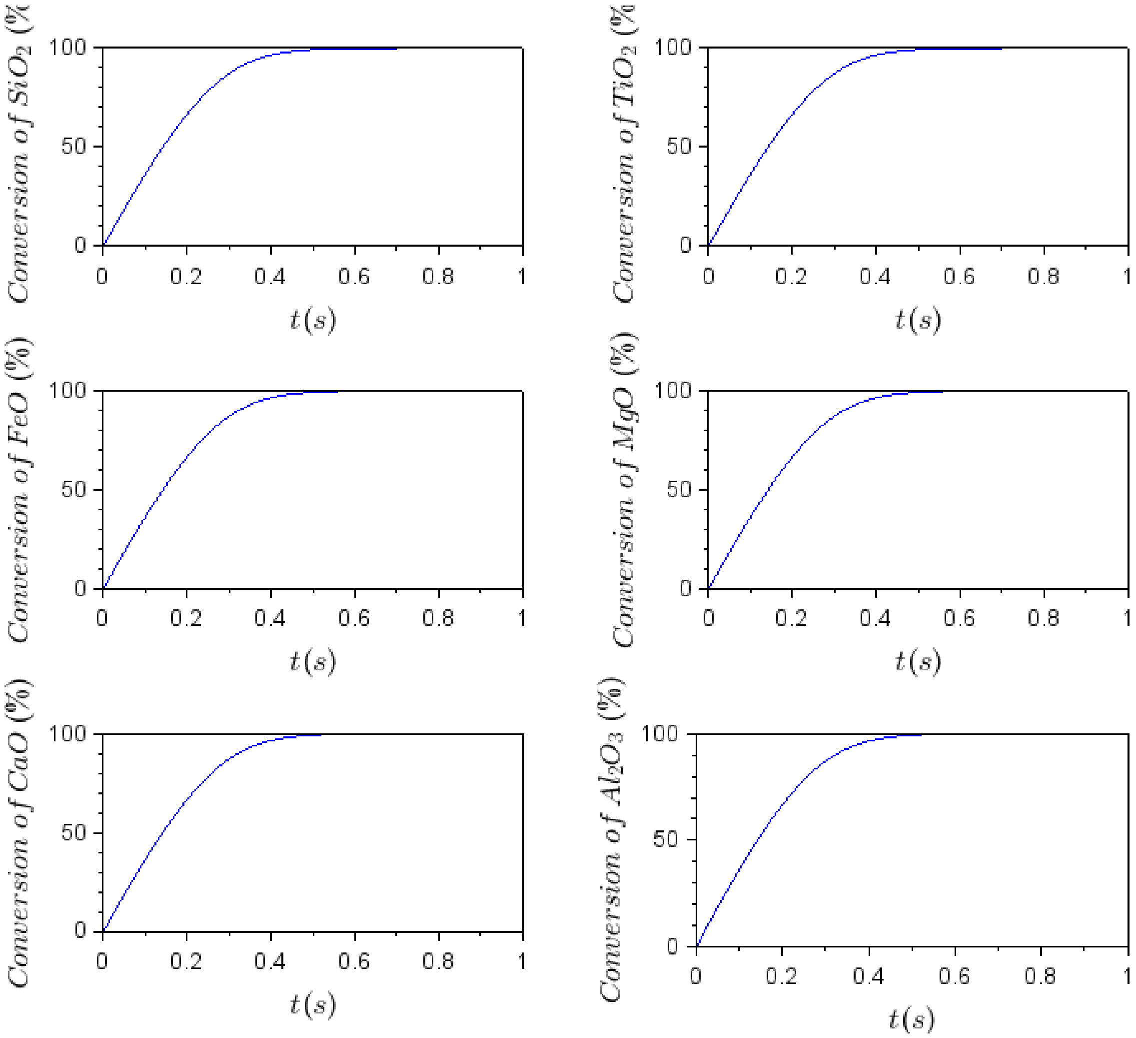

C 52: Effect of flowrate = 10000 m³/s on conversion over time.

Reaction rate constant variation - $k_j = 0.01\ 1/s$

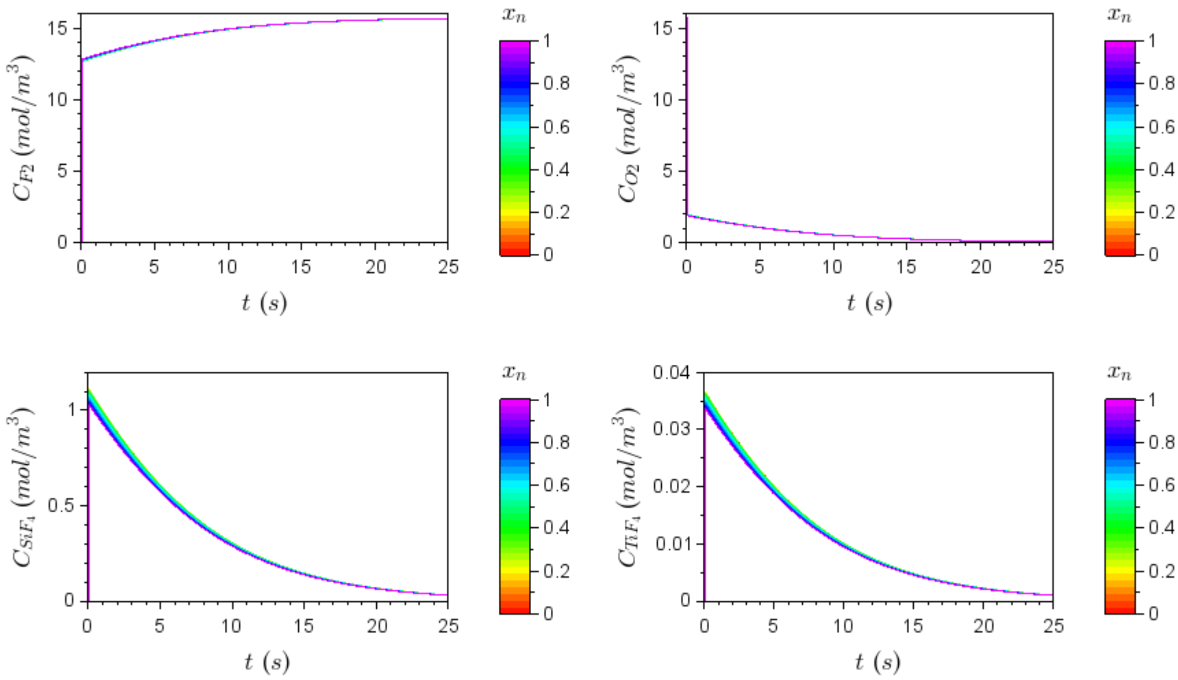

C 53: Effect of reaction rate constant = 0.01 (m3/mol.s) on gas concentrations over time.

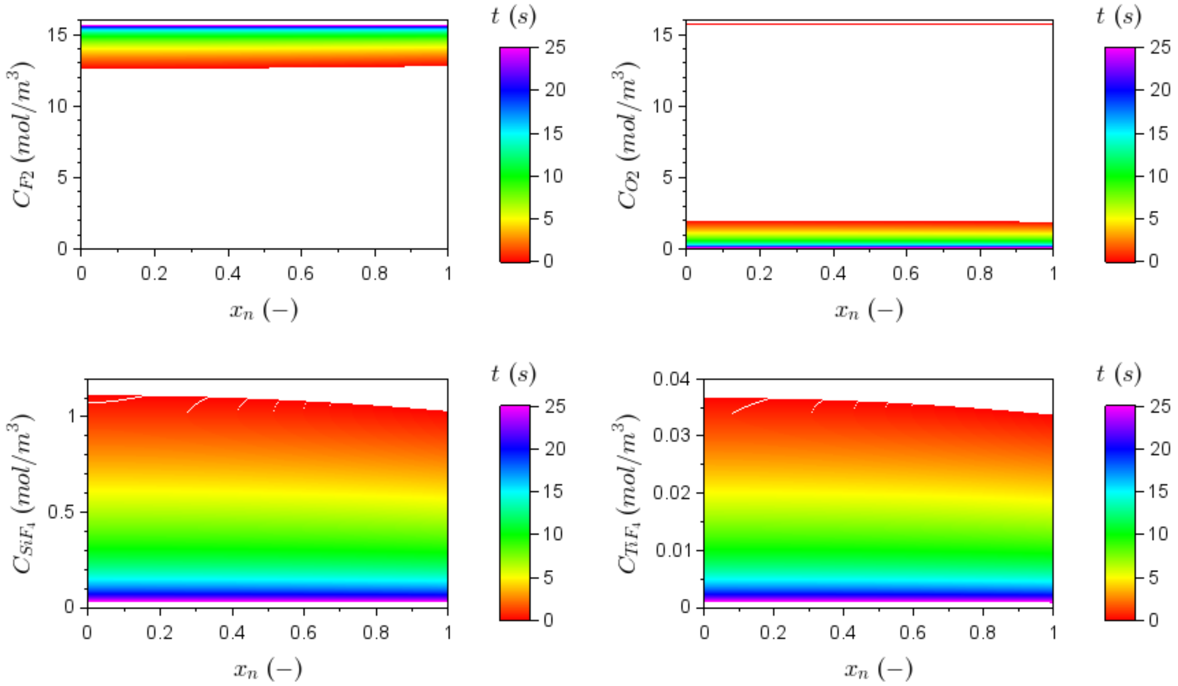

C 54: Effect of reaction rate constant = 0.01 (m3/mol.s) on gas concentrations through the particle.

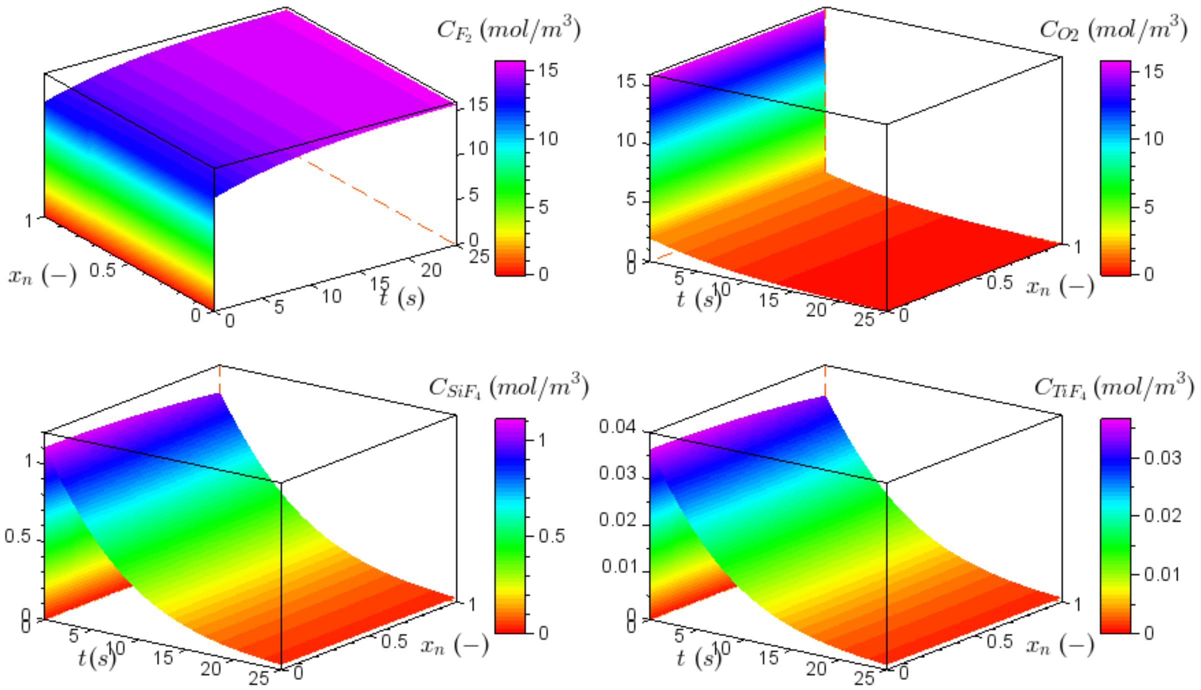

C 55: Surface graphs showing the effect of reaction rate constant = 0.01 (m3/mol.s) on gas concentrations.

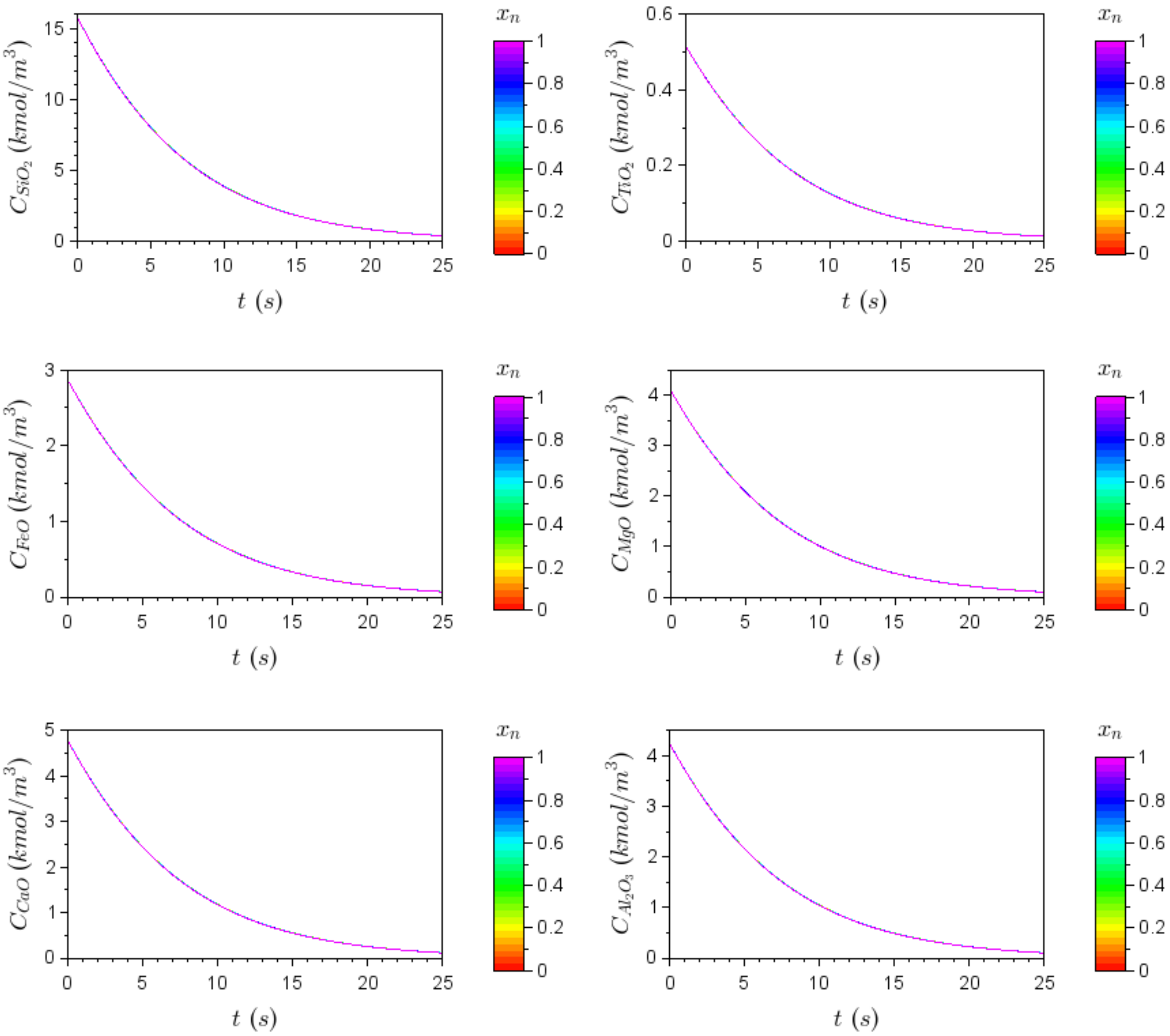

C 56: Effect of reaction rate constant = 0.01 (m3/mol.s) on solid reactant concentrations over time.

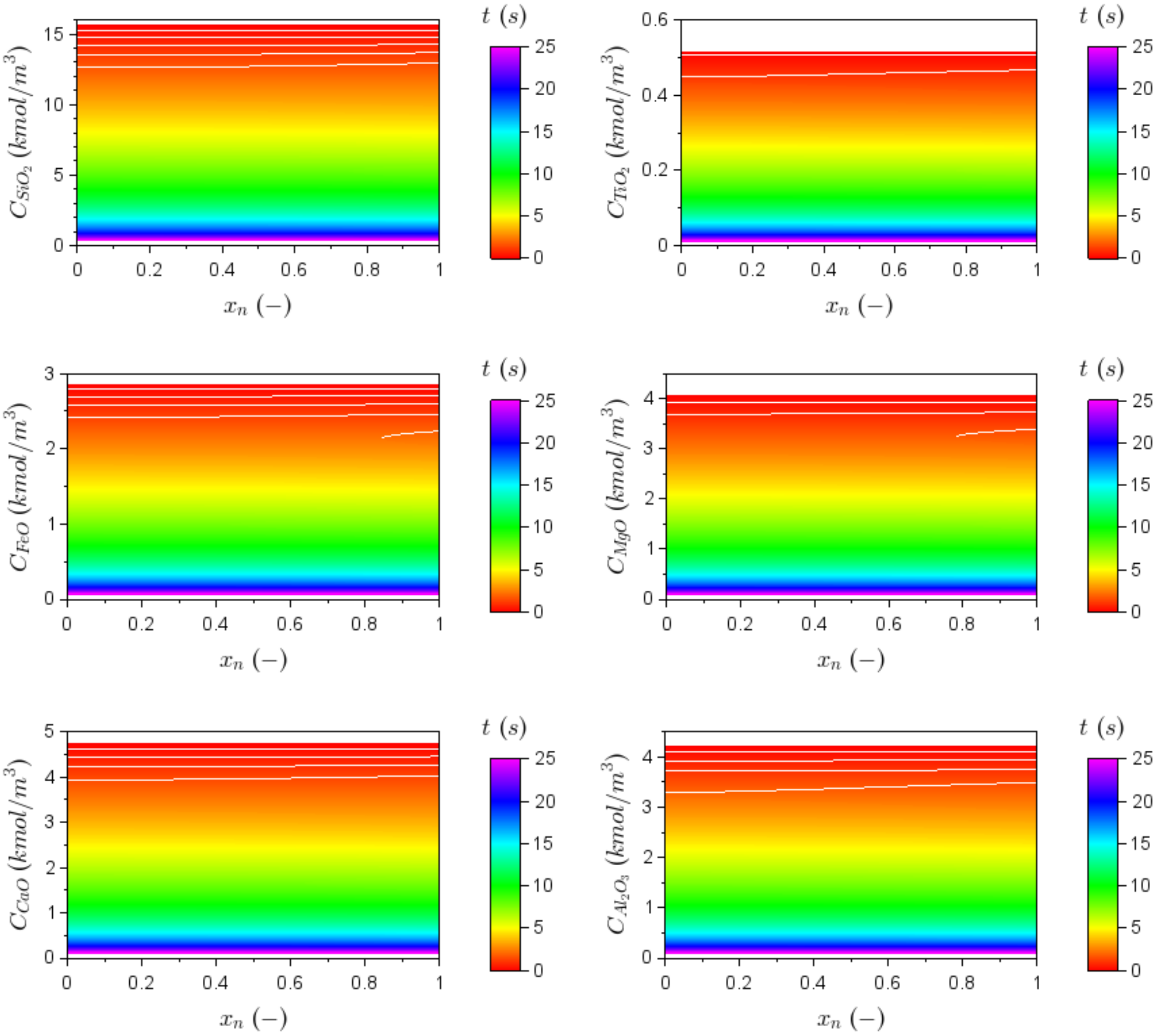

C 57: Effect of reaction rate constant = 0.01 (m3/mol.s) on solid reactant concentrations through the particle.

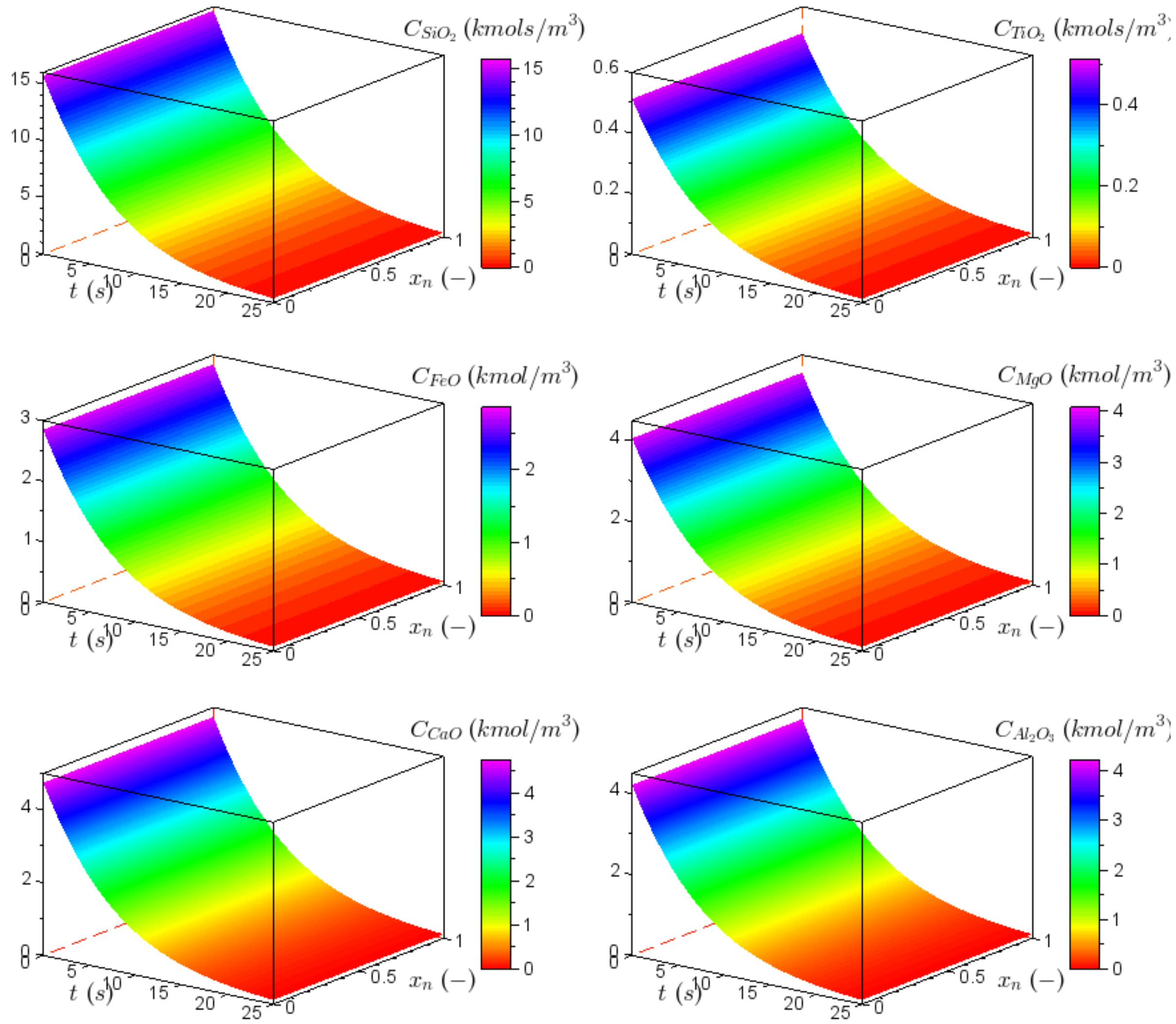

C 58: Surface graphs showing the effect of reaction rate constant = 0.01 (m3/mol.s) on solid reactants concentrations.

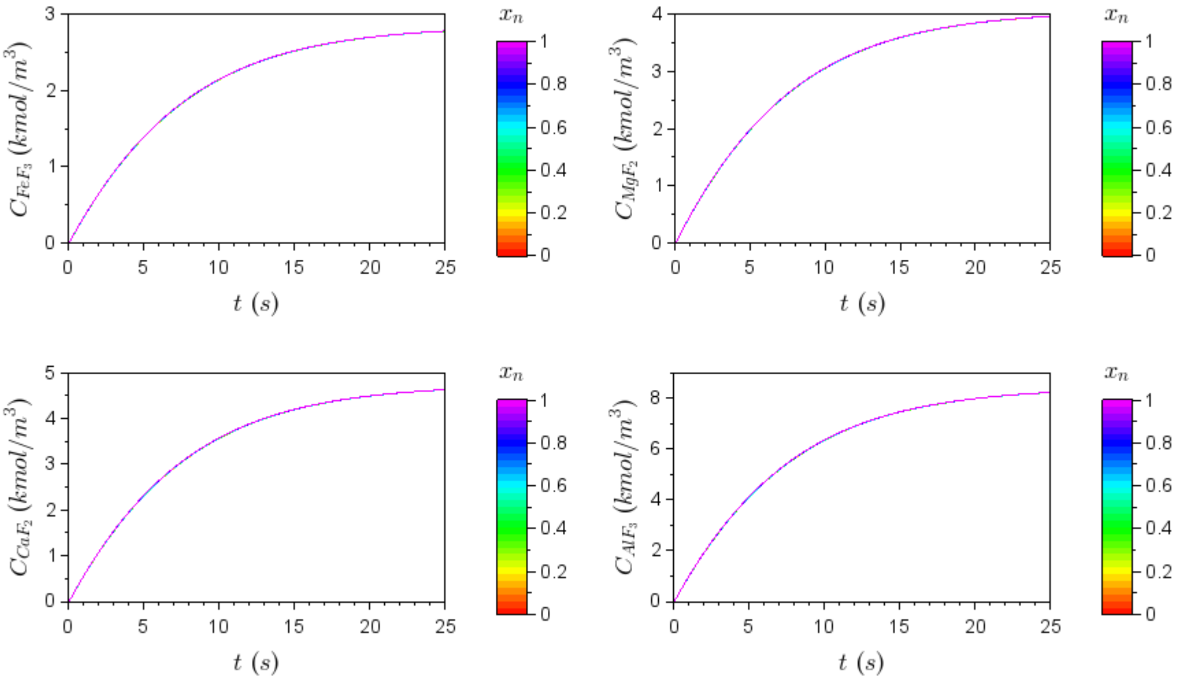

C 59: Effect of reaction rate constant = 0.01 (m3/mol.s) on solid products concentrations over time.

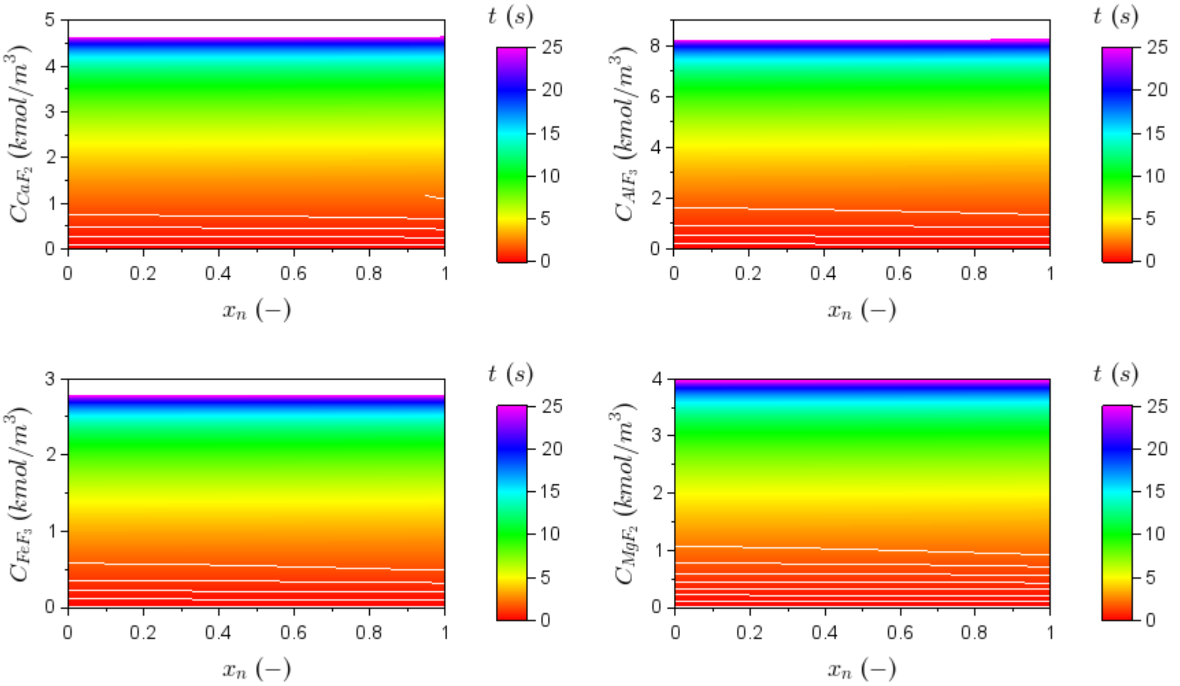

C 60: Effect of reaction rate constant = 0.01 (m3/mol.s) on solid products concentrations through the particle.

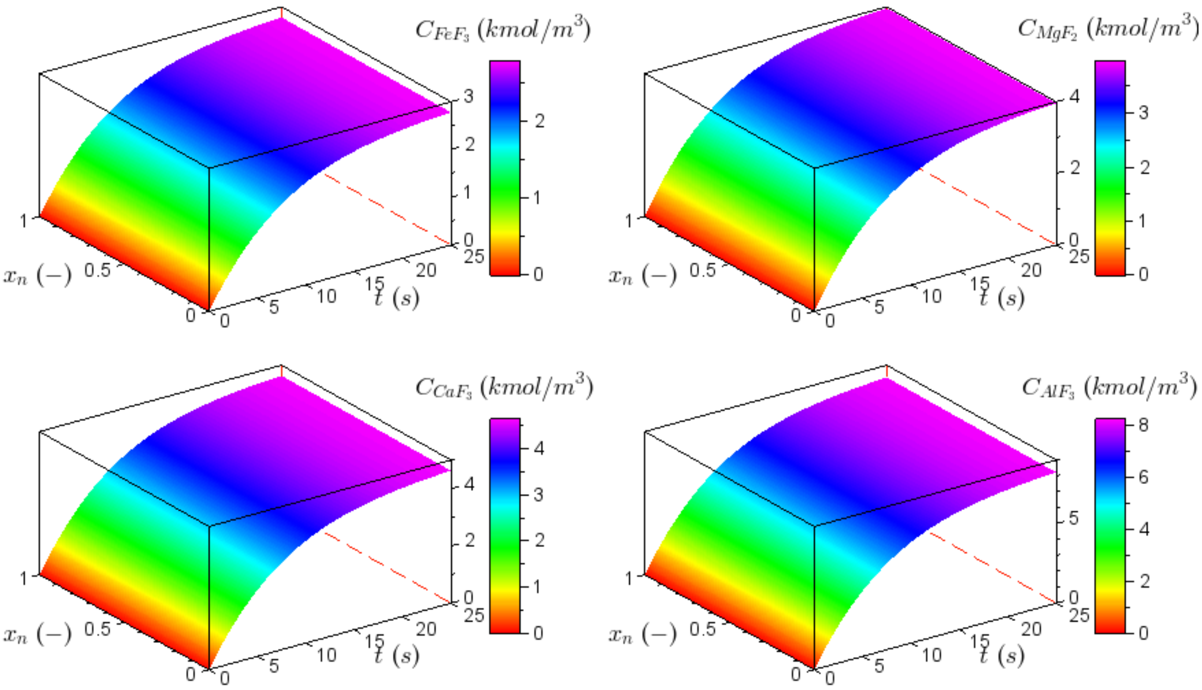

C 61: Surface graphs showing the effect of reaction rate constant = 0.01 (m3/mol.s) on solid products concentrations.

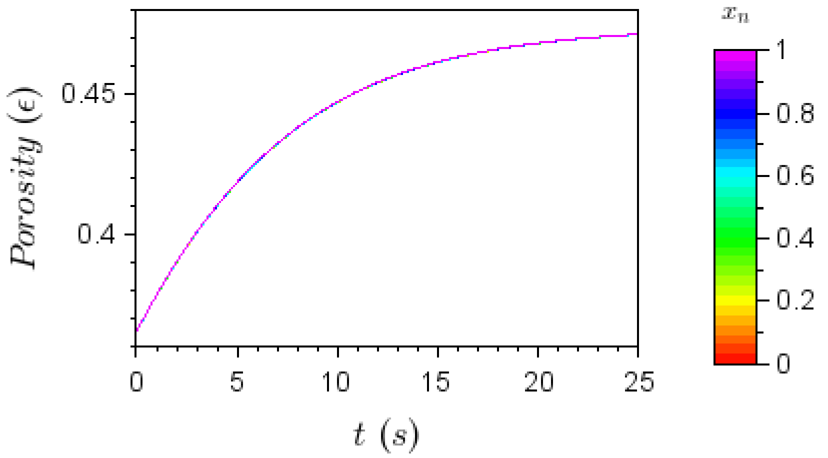

C 62: Effect of reaction rate constant = 0.01 (m3/mol.s) on porosity over time.

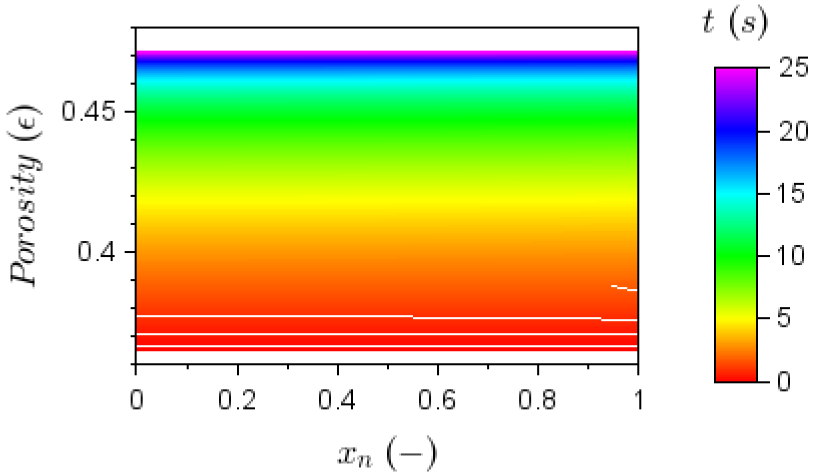

C 63: Effect of reaction rate constant = 0.01 (m3/mol.s) on porosity through the particle.

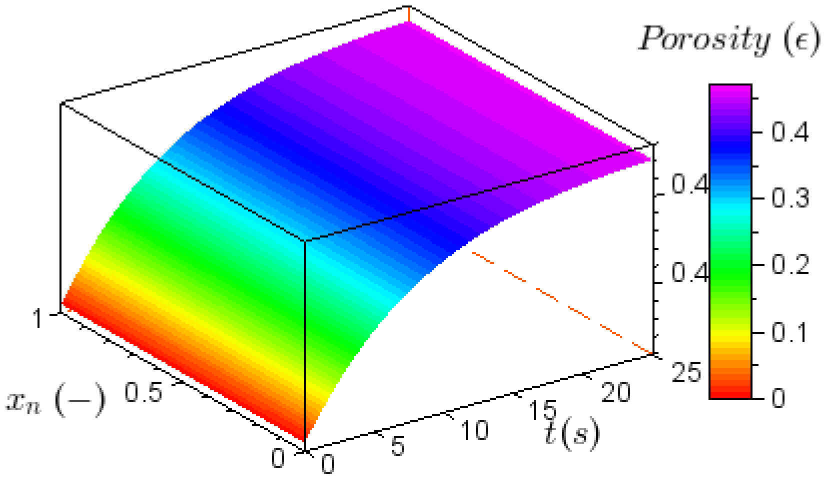

C 64: Surface graph showing the effect of reaction rate constant = 0.01 (m3/mol.s) on porosity.

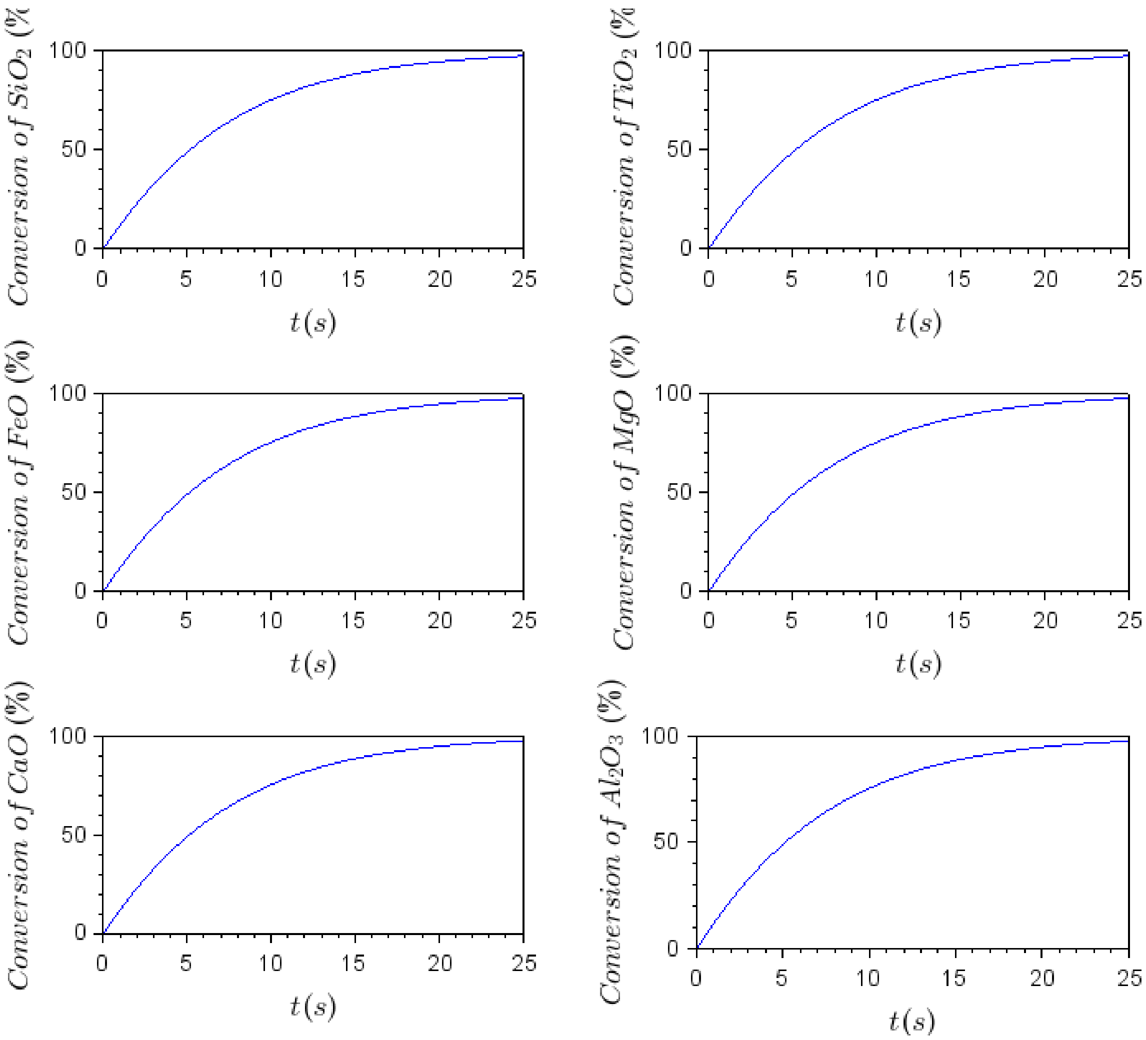

C 65: Effect of reaction rate constant = 0.01 (m3/mol.s) conversion over time.

Reaction rate constant variation - $k_j = 0.1\ 1/s$

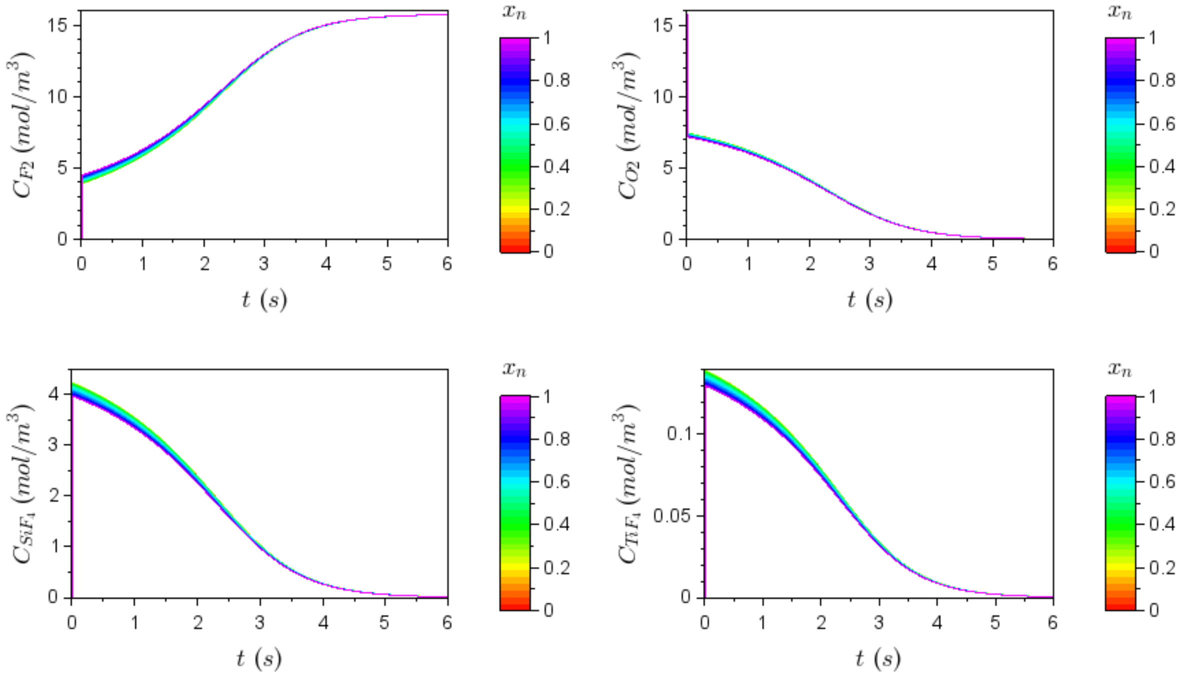

C 66: Effect of reaction rate constant = 0.1 (m3/mol.s) on gas concentrations over time.

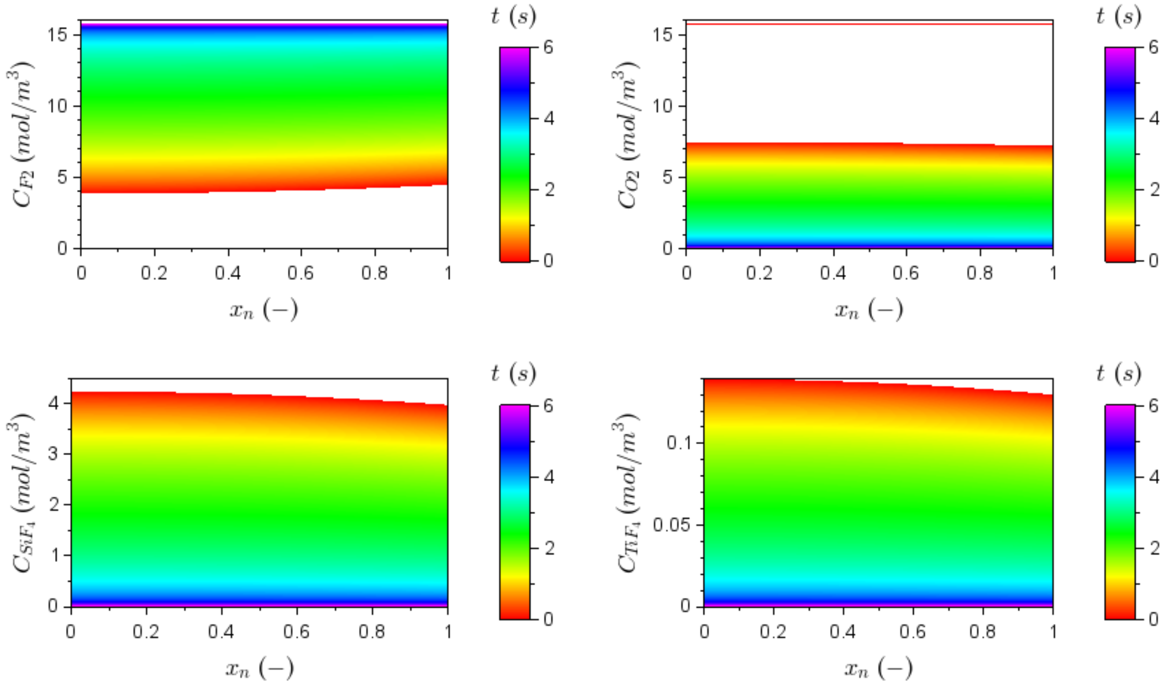

C 67: Effect of reaction rate constant = 0.1 (m3/mol.s) on gas concentrations through the particle.

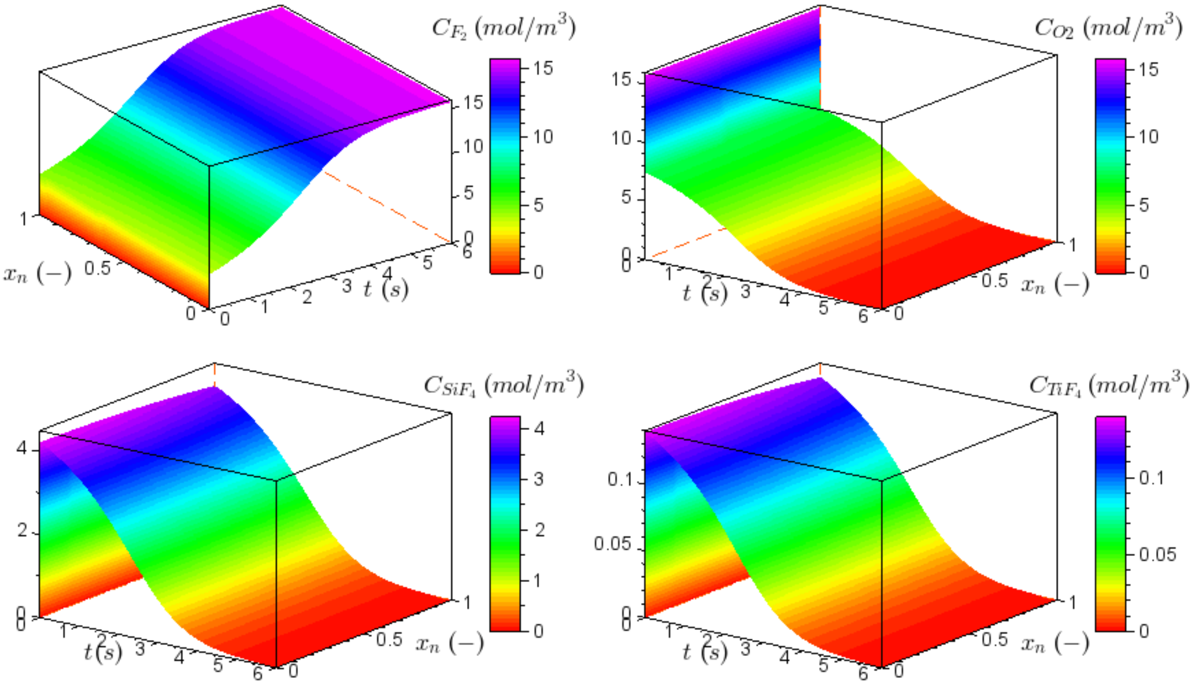

C 68: Surface graphs showing the effect of reaction rate constant = 0.1 (m3/mol.s) on gas concentrations.

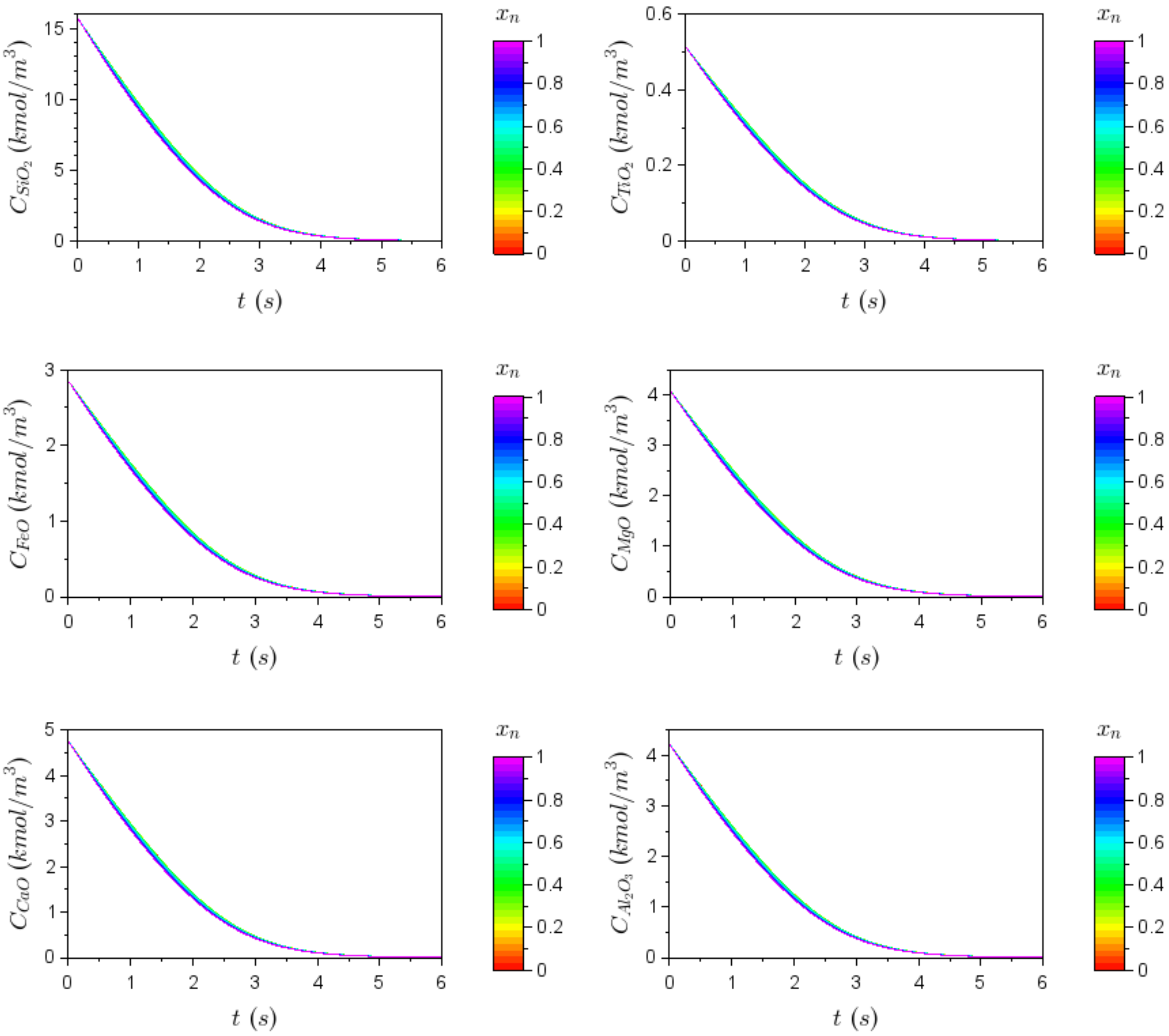

C 69: Effect of reaction rate constant = 0.1 (m3/mol.s) on solid reactant concentrations over time.

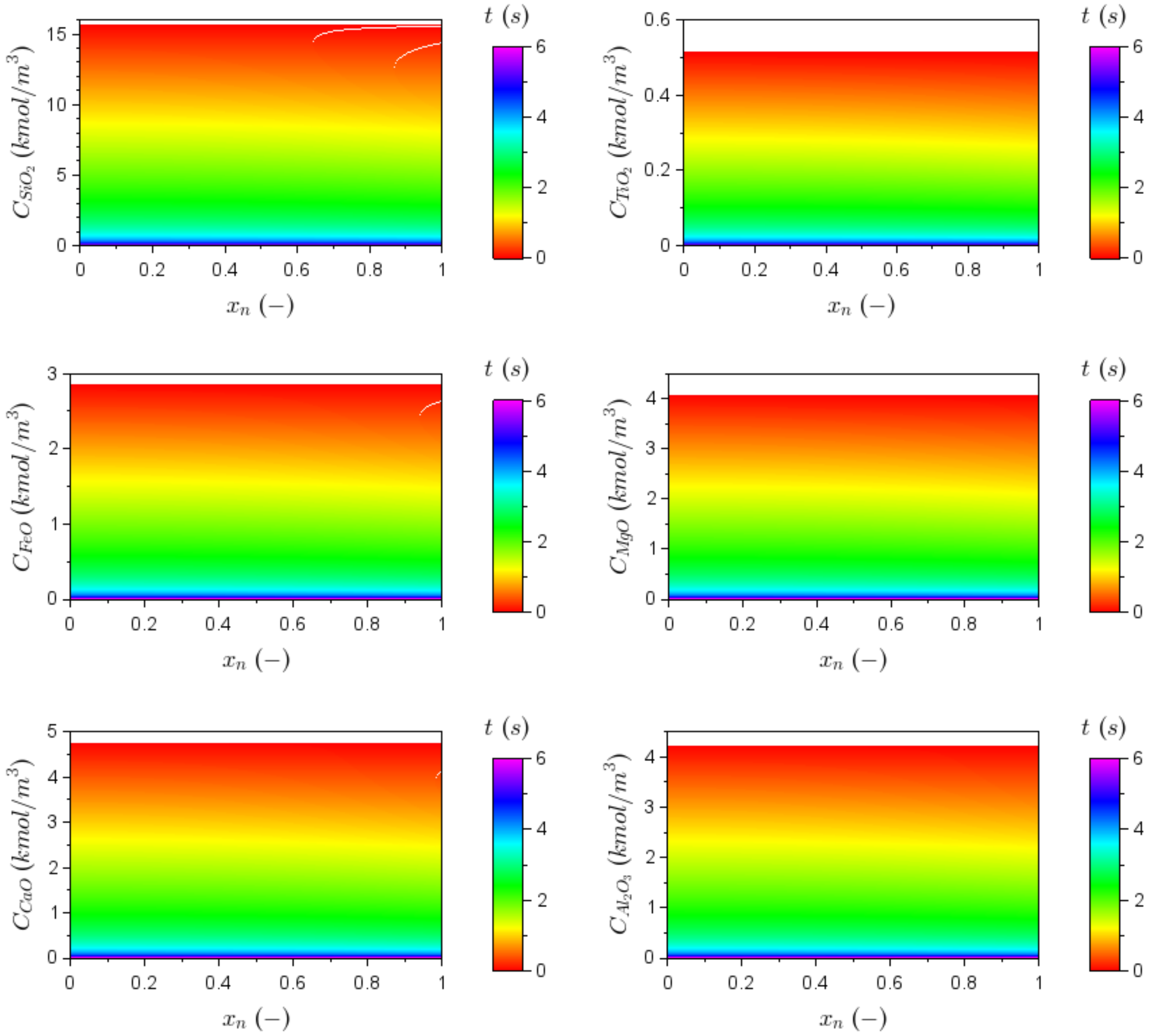

C 70: Effect of reaction rate constant = 0.1 (m3/mol.s) on solid reactant concentrations through the particle.

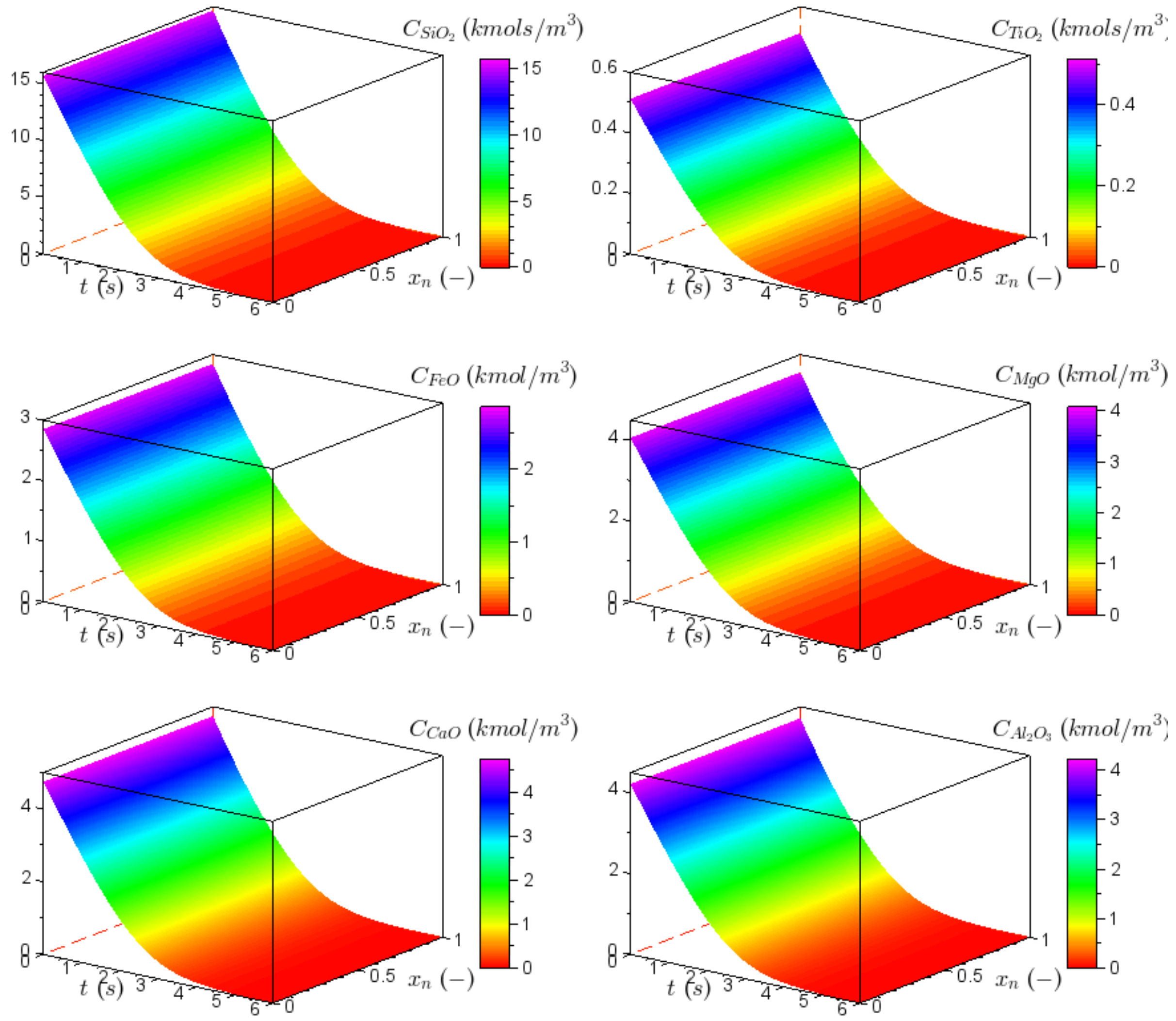

C 71: Surface graphs showing the effect of reaction rate constant = 0.1 (m3/mol.s) on solid reactants concentrations.

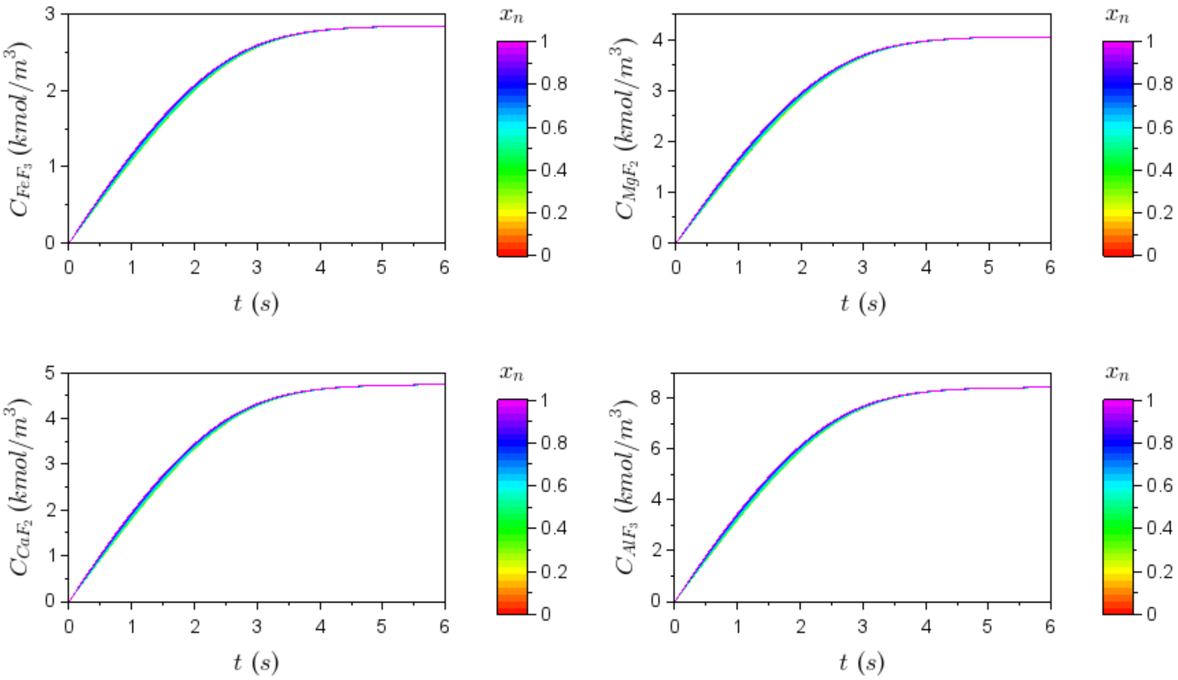

C 72: Effect of reaction rate constant = 0.1 (m3/mol.s) on solid products concentrations over time.

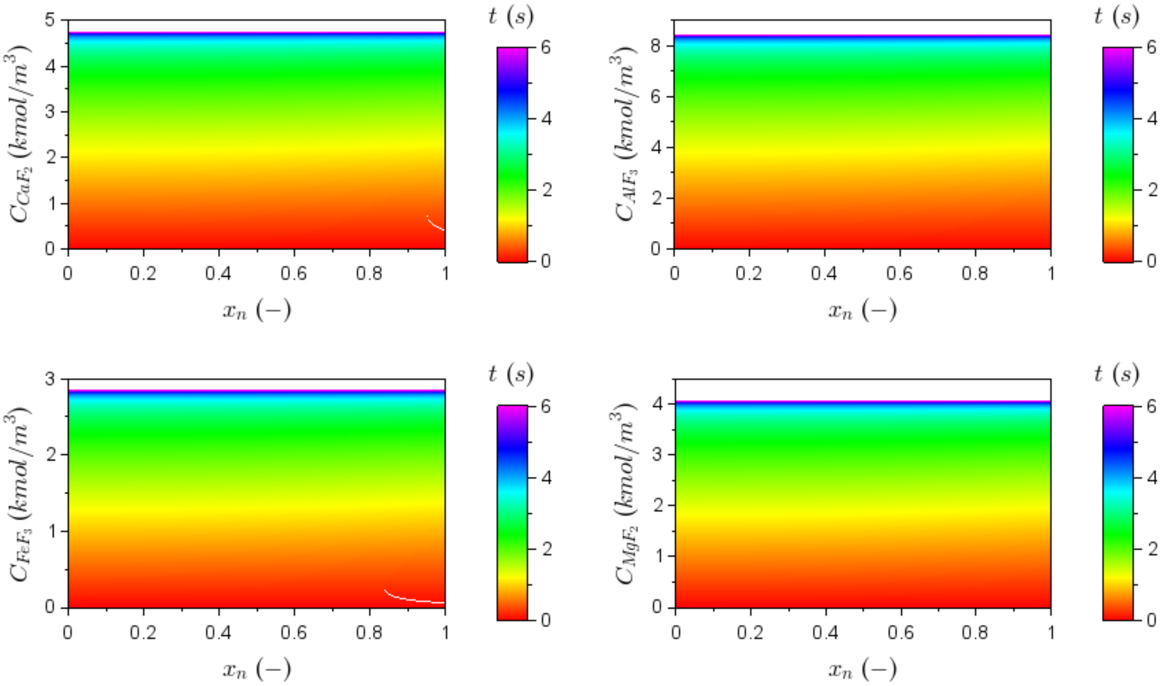

C 73: Effect of reaction rate constant = 0.1 (m3/mol.s) on solid products concentrations through the particle.

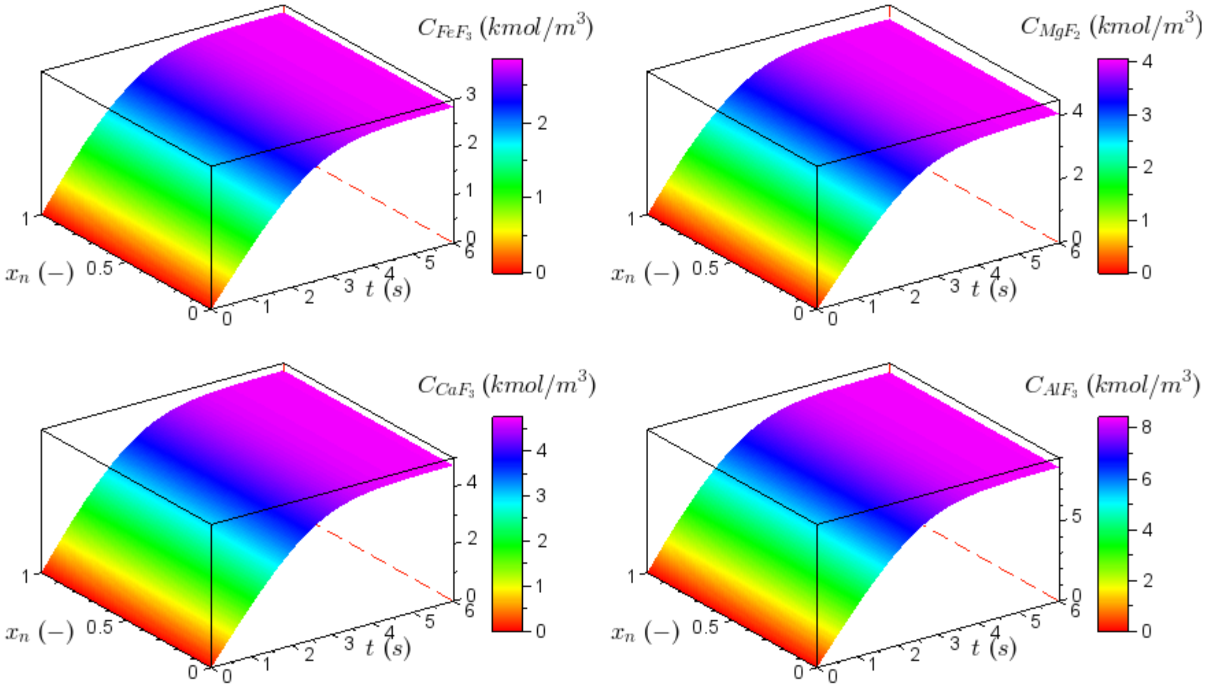

C 74: Surface graphs showing the effect of reaction rate constant = 0.1 (m3/mol.s) on solid products concentrations.

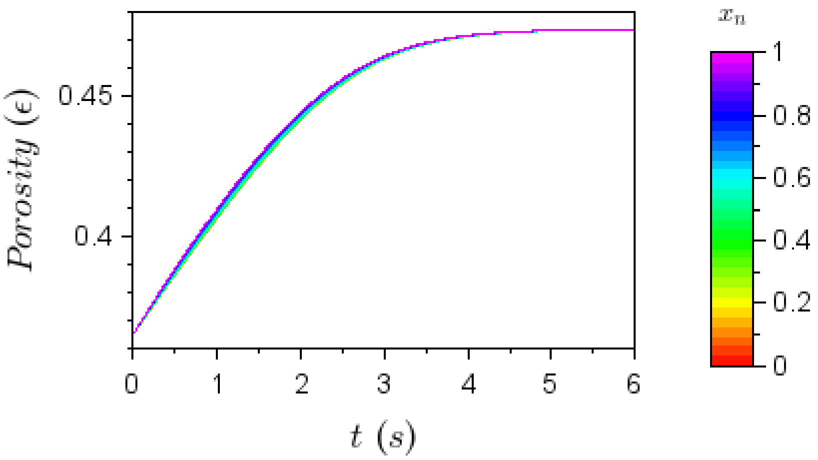

C 75: Effect of reaction rate constant = 0.1 (m3/mol.s) on porosity over time.

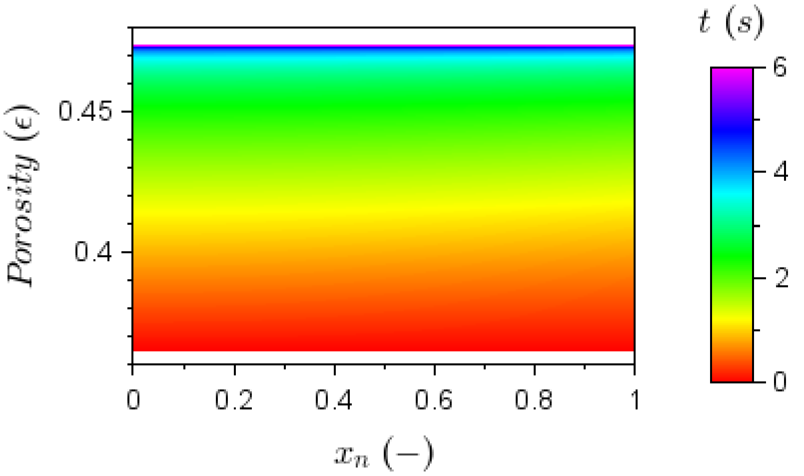

C 76: Effect of reaction rate constant = 0.1 (m3/mol.s) on porosity through the particle.

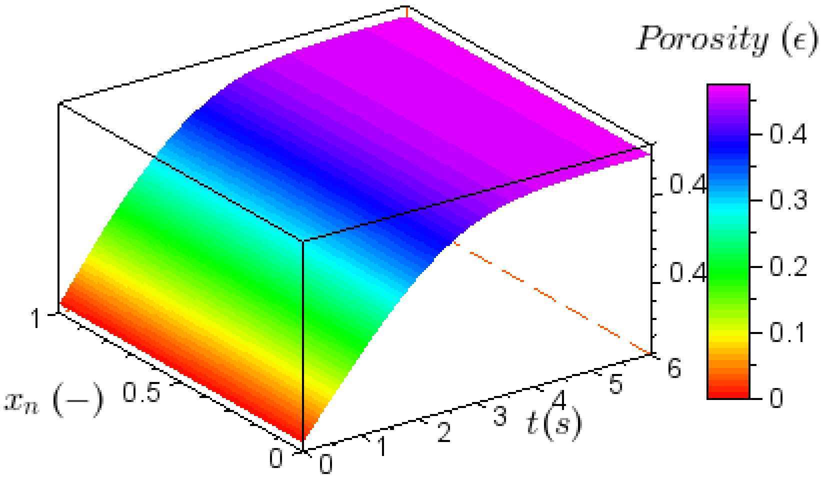

C 77: Surface graph showing the effect of reaction rate constant = 0.1 (m3/mol.s) on porosity.

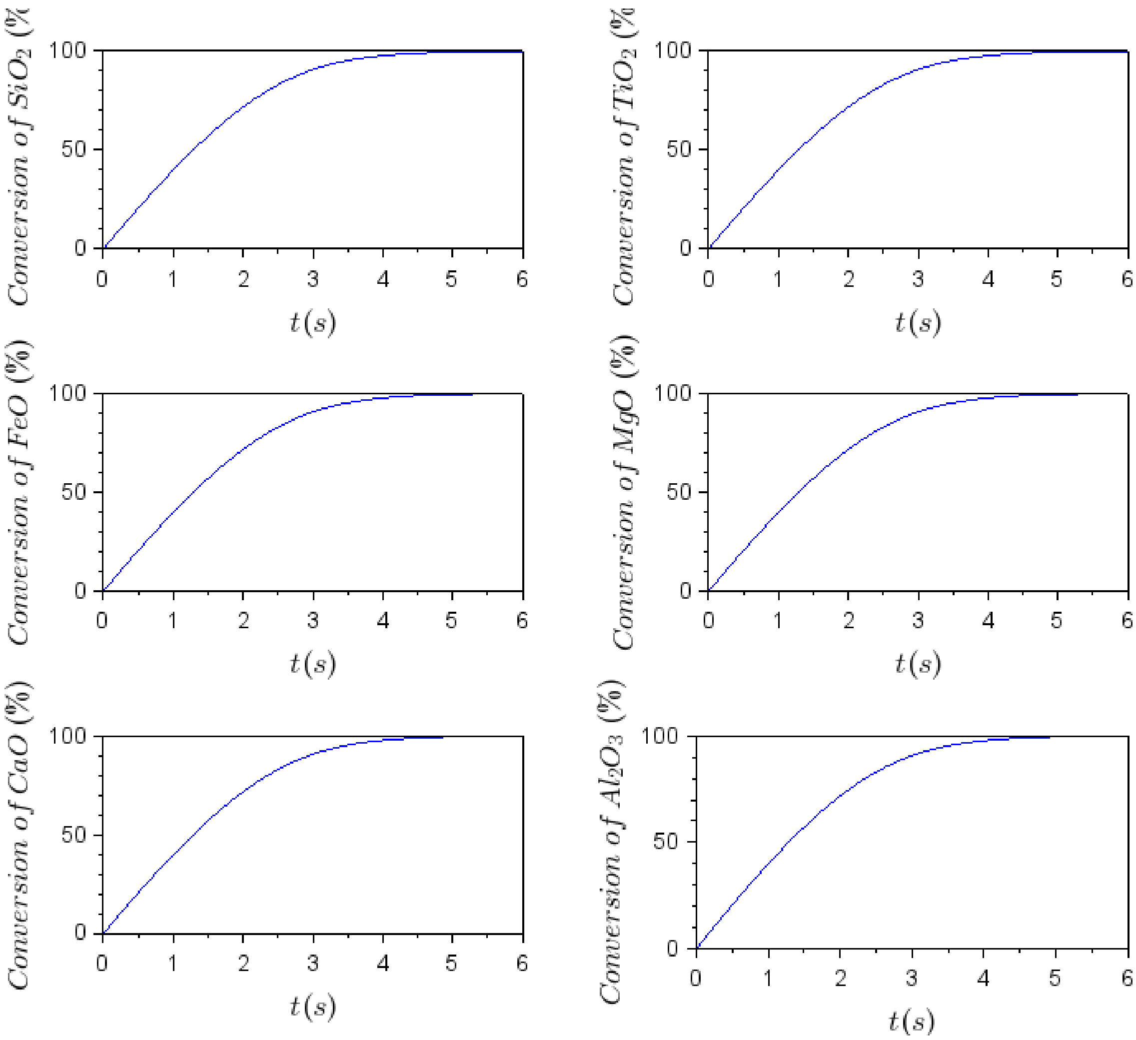

C 78: Effect of reaction rate constant = 0.1 (m3/mol.s) conversion over time.

Reaction rate constant variation - $k_j = 10\ 1/s$

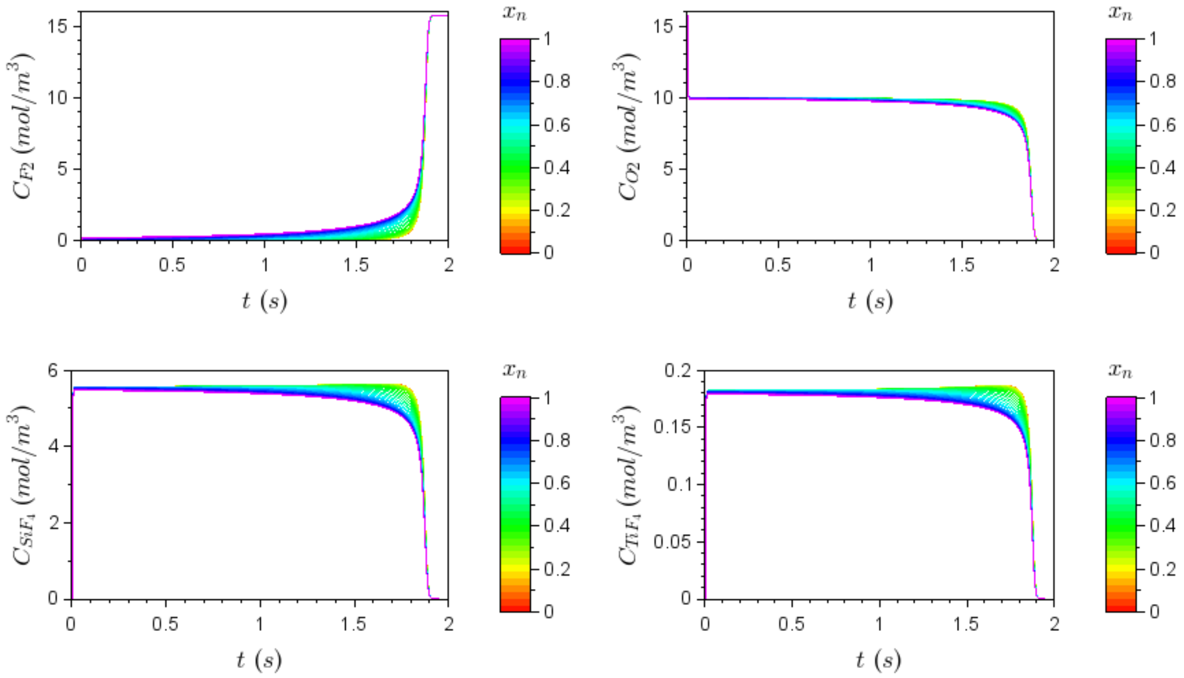

C 79: Effect of reaction rate constant = 10 (m3/mol.s) on gas concentrations over time.

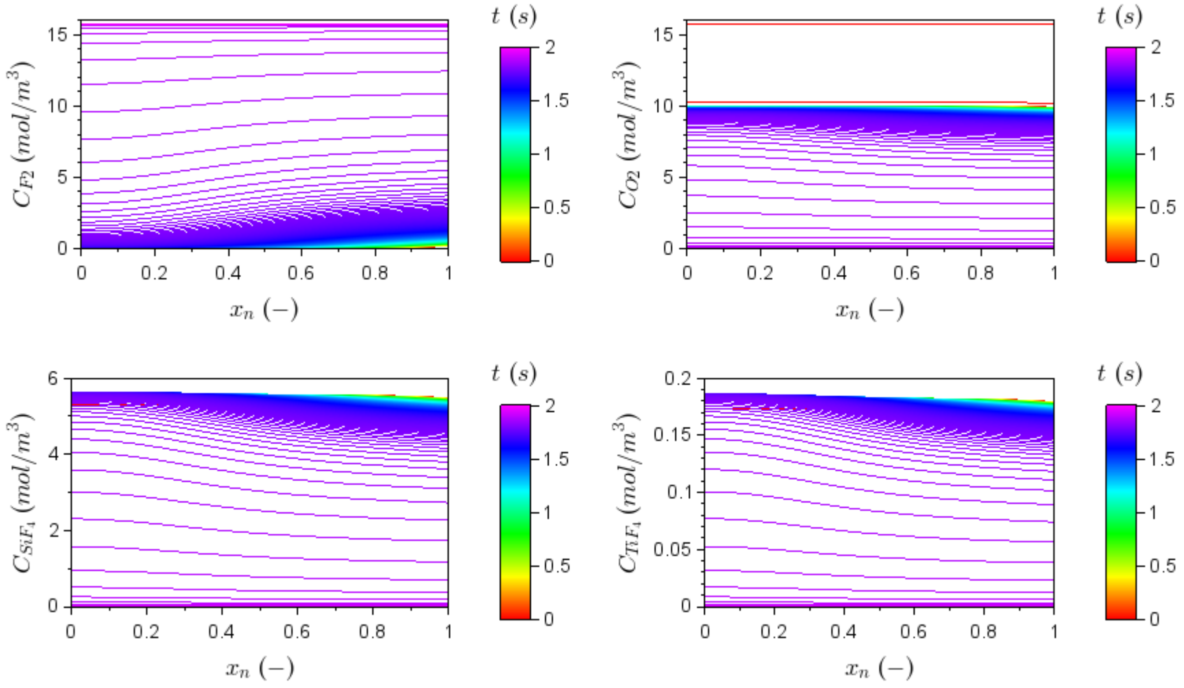

C 80: Effect of reaction rate constant = 10 (m3/mol.s) on gas concentrations through the particle.

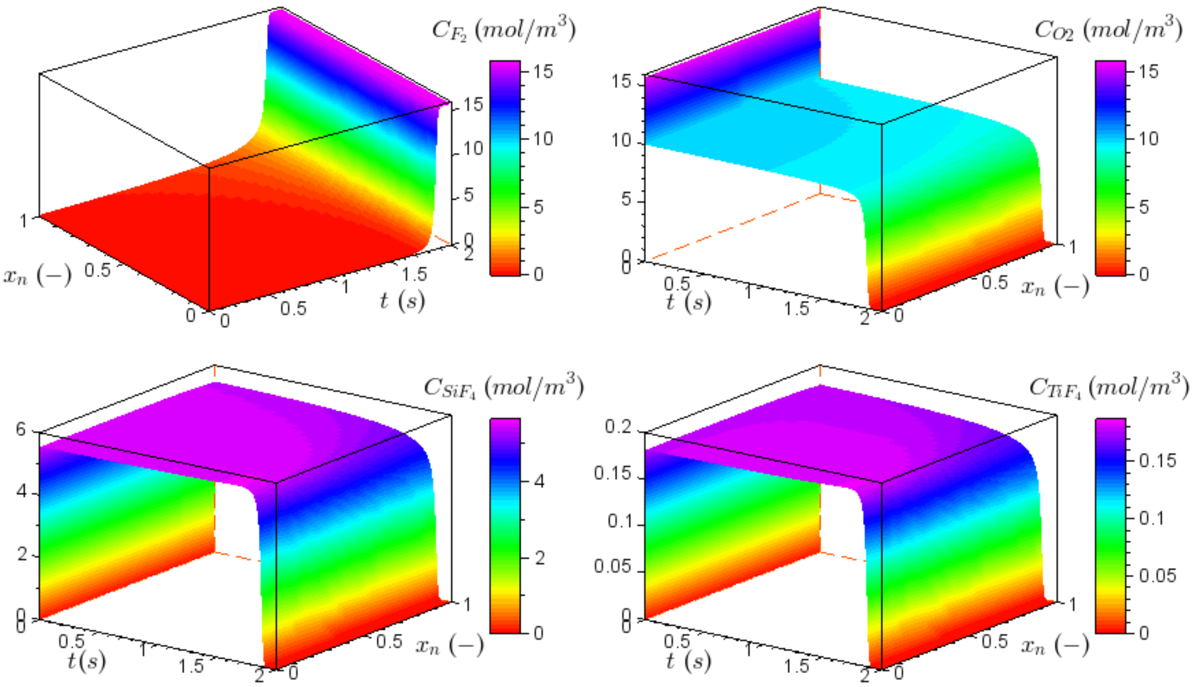

C 81: Surface graphs showing the effect of reaction rate constant = 10 (m3/mol.s) on gas concentrations.

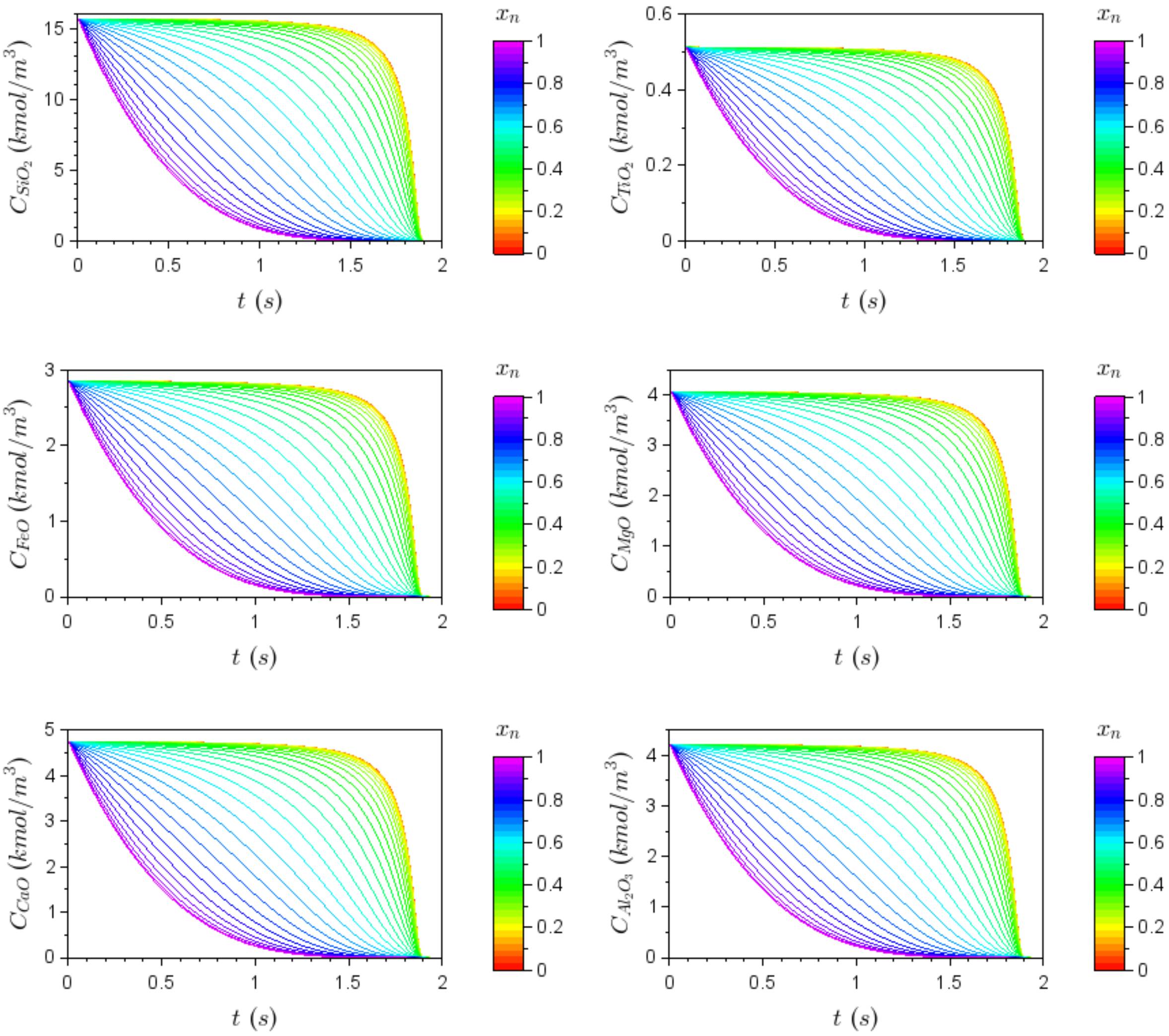

C 82: Effect of reaction rate constant = 10 (m3/mol.s) on solid reactant concentrations over time.

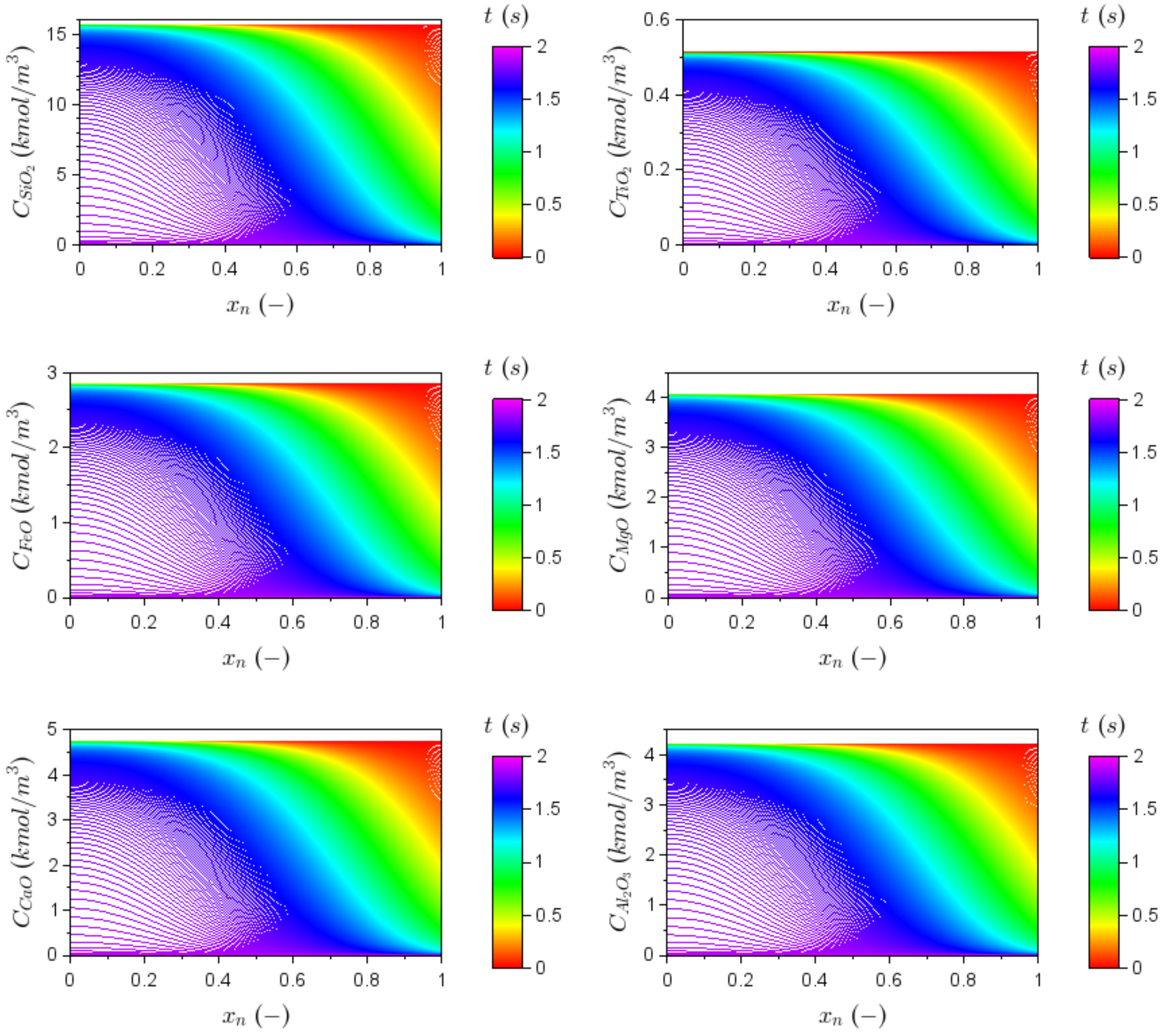

C 83: Effect of reaction rate constant = 10 (m3/mol.s) on solid reactant concentrations through the particle.

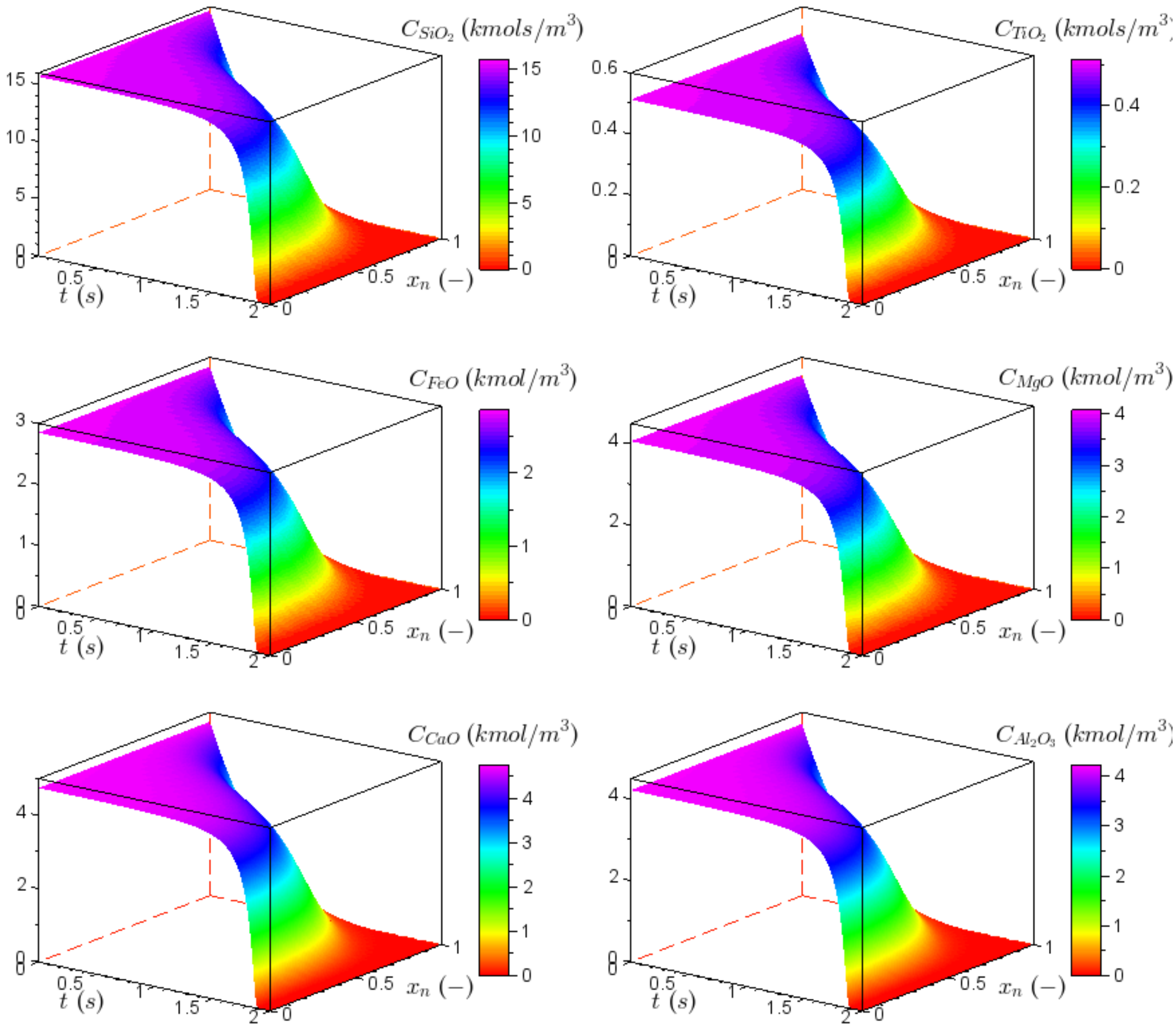

C 84: Surface graphs showing the effect of reaction rate constant = 10 (m3/mol.s) on solid reactants concentrations.

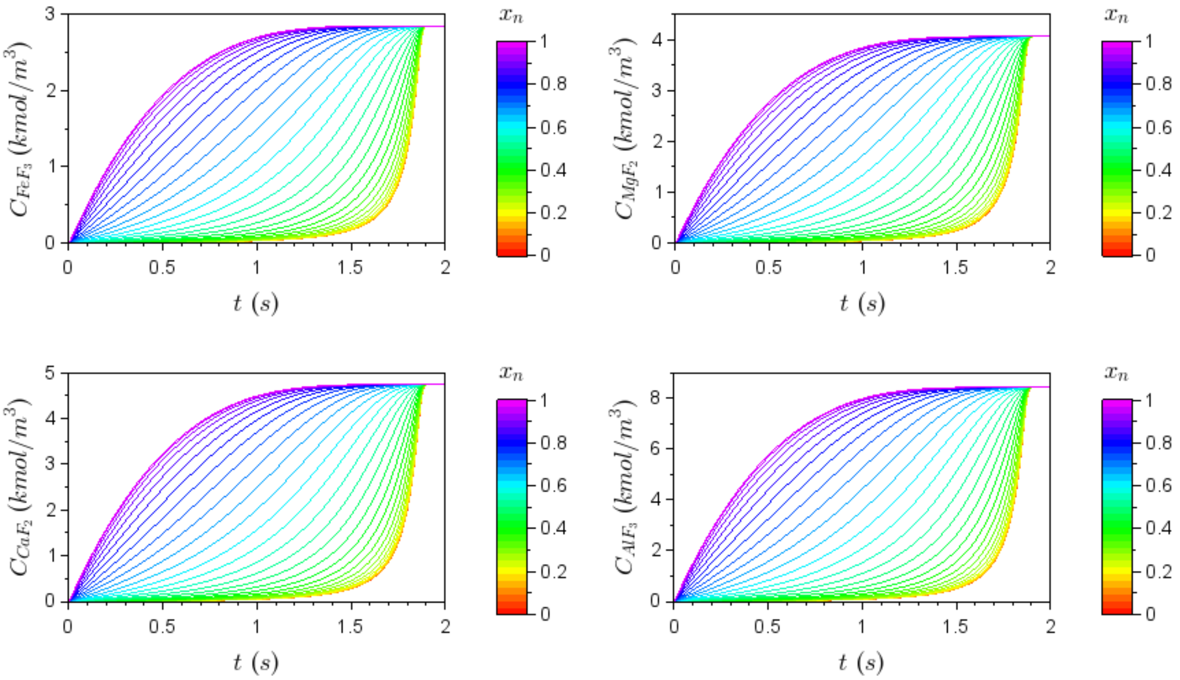

C 85: Effect of reaction rate constant = 10 (m3/mol.s) on solid products concentrations over time.

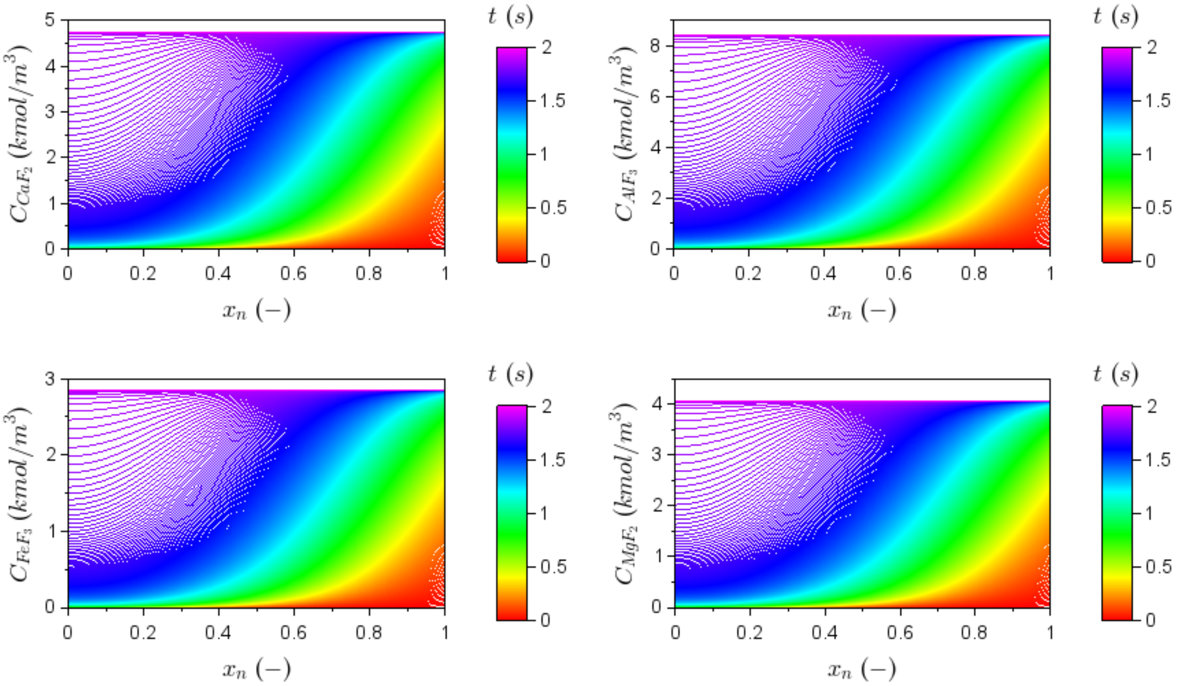

C 86: Effect of reaction rate constant = 10 (m3/mol.s) on solid products concentrations through the particle.

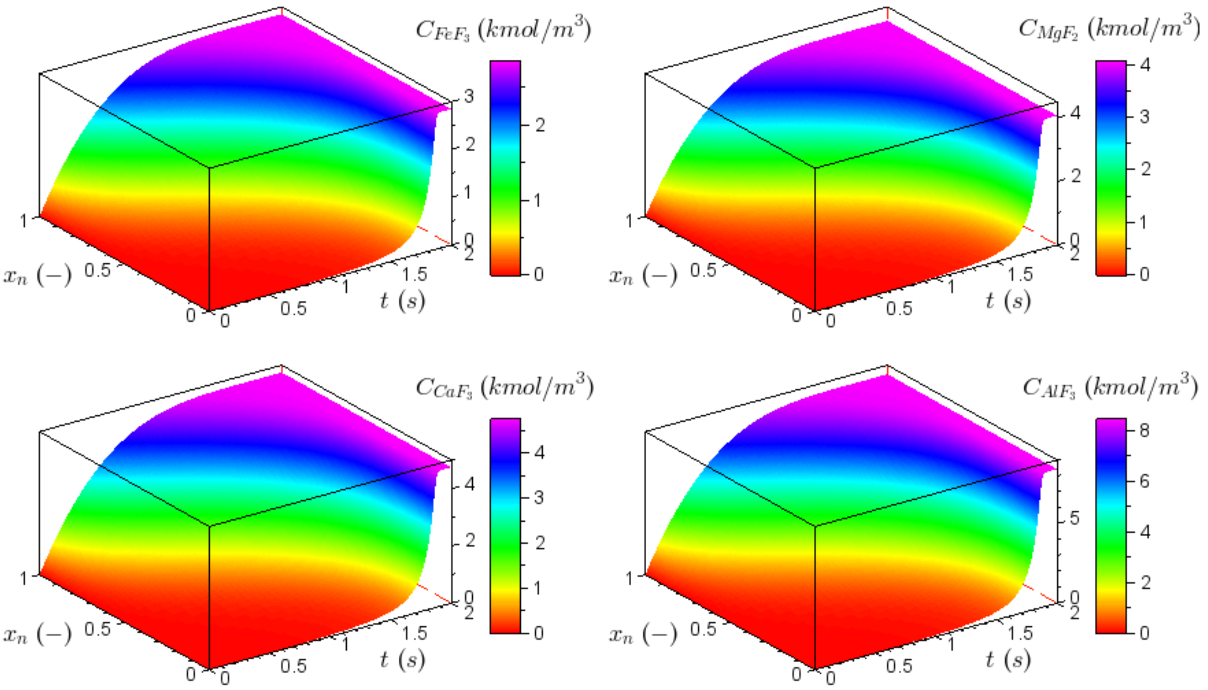

C 87: Surface graphs showing the effect of reaction rate constant = 10 (m3/mol.s) on solid products concentrations.

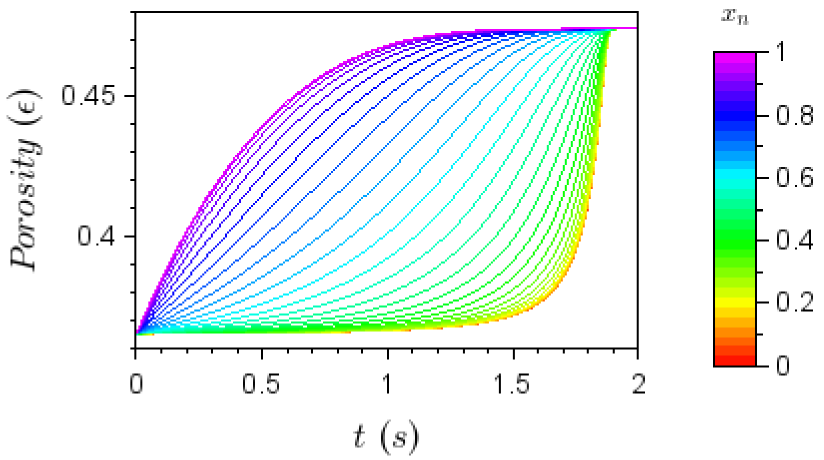

C 88: Effect of reaction rate constant = 10 (m3/mol.s) on porosity over time.

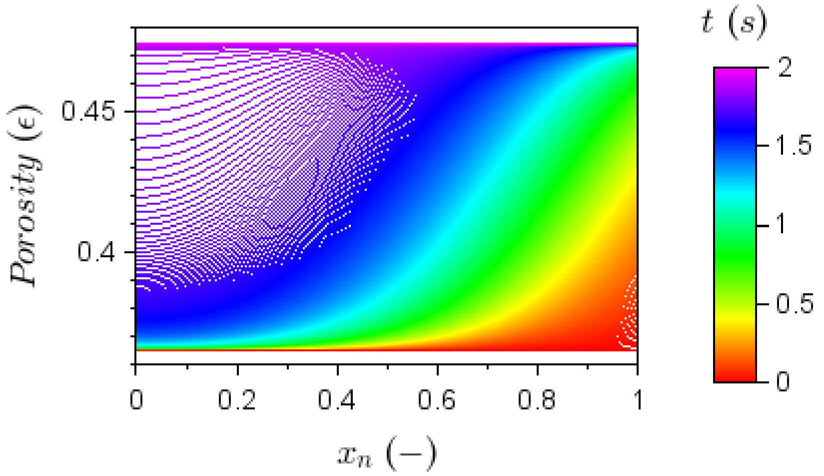

C 89: Effect of reaction rate constant = 10 (m3/mol.s) on porosity through the particle.

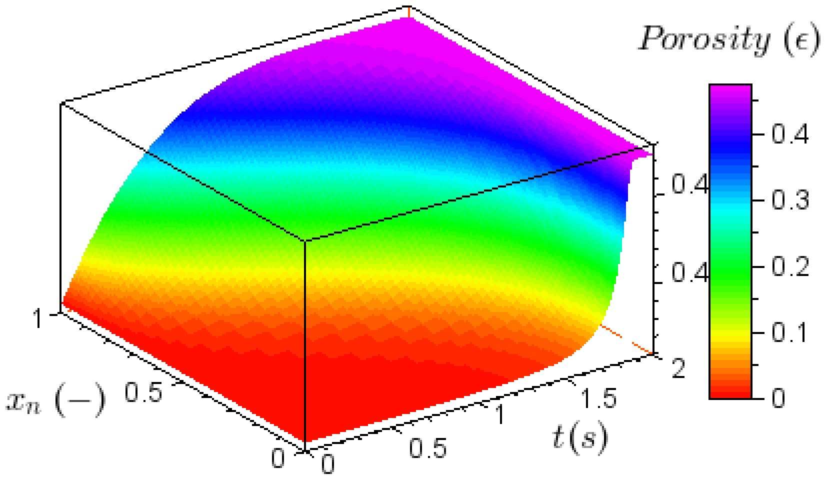

C 90: Surface graph showing the effect of reaction rate constant = 10 (m3/mol.s) on porosity.

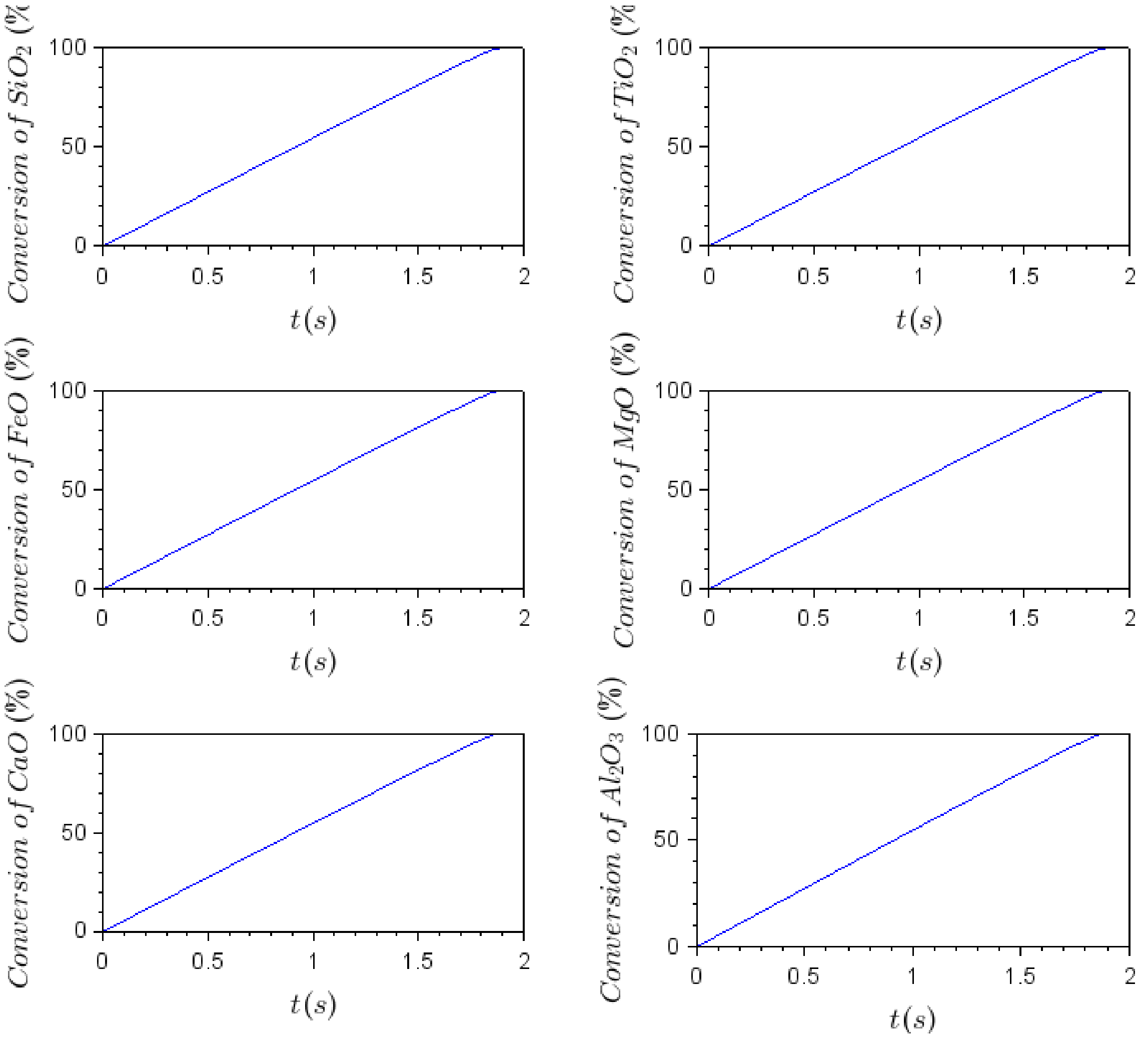

C 91: Effect of reaction rate constant = 10 (m3/mol.s) conversion over time.

Reaction rate constant variation - $k_j = 100\ 1/s$

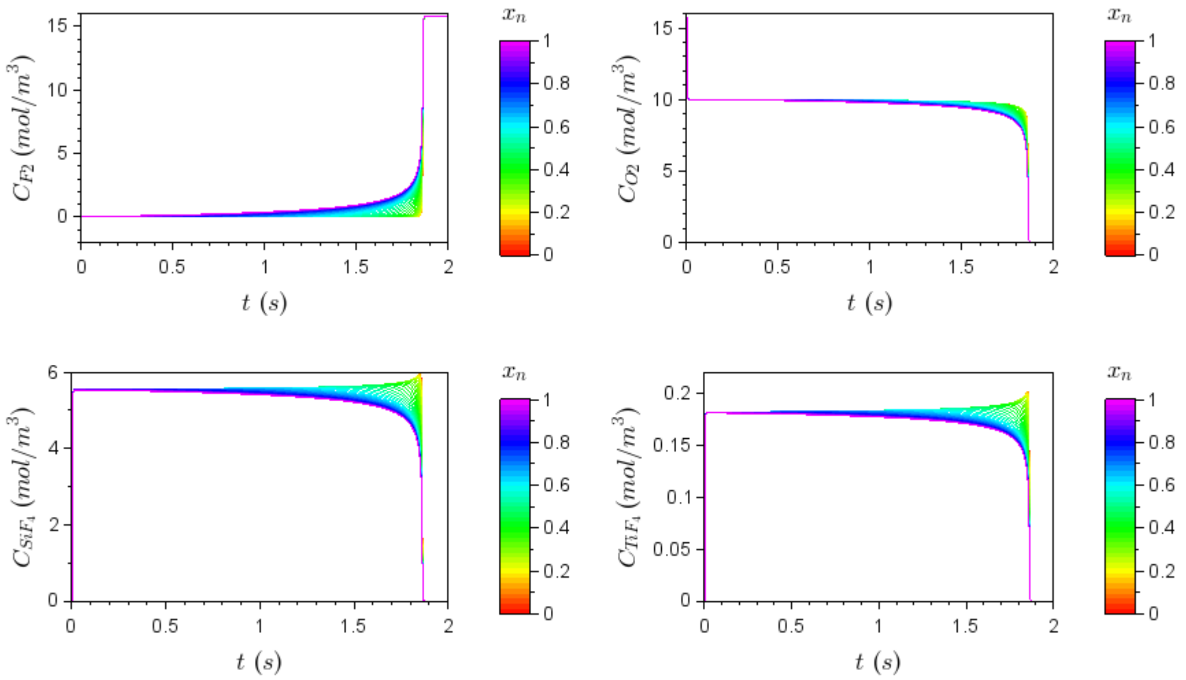

C 92: Effect of reaction rate constant = 100 (m3/mol.s) on gas concentrations over time.

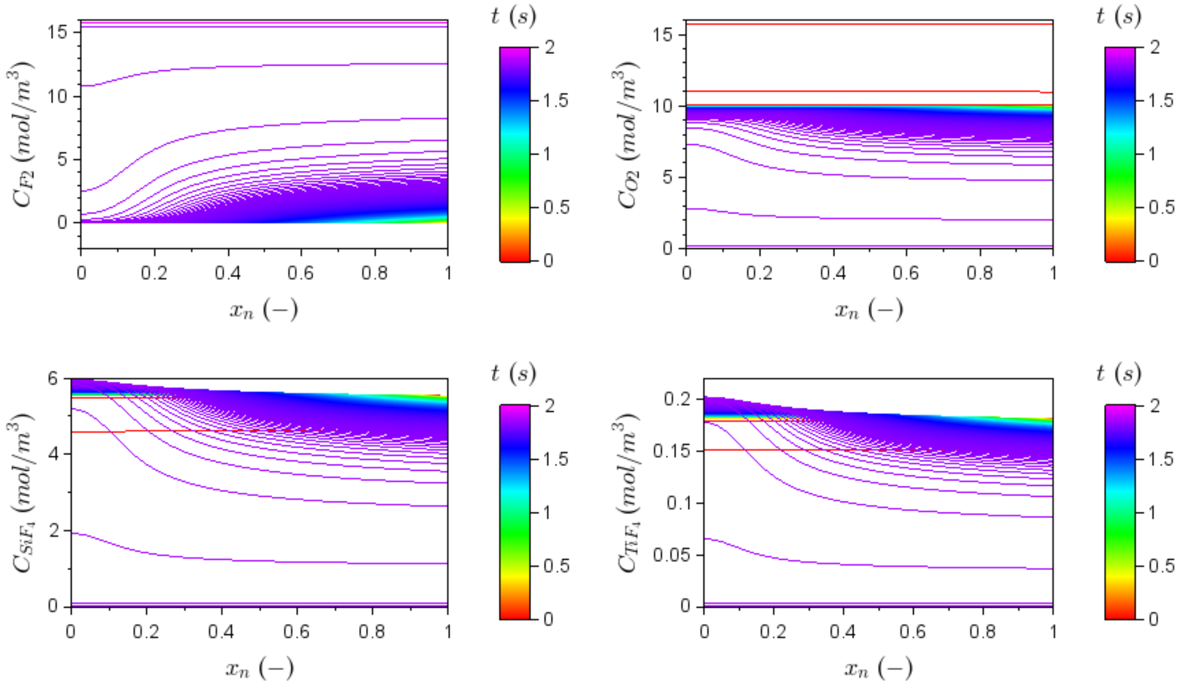

C 93: Effect of reaction rate constant = 100 (m3/mol.s) on gas concentrations through the particle.

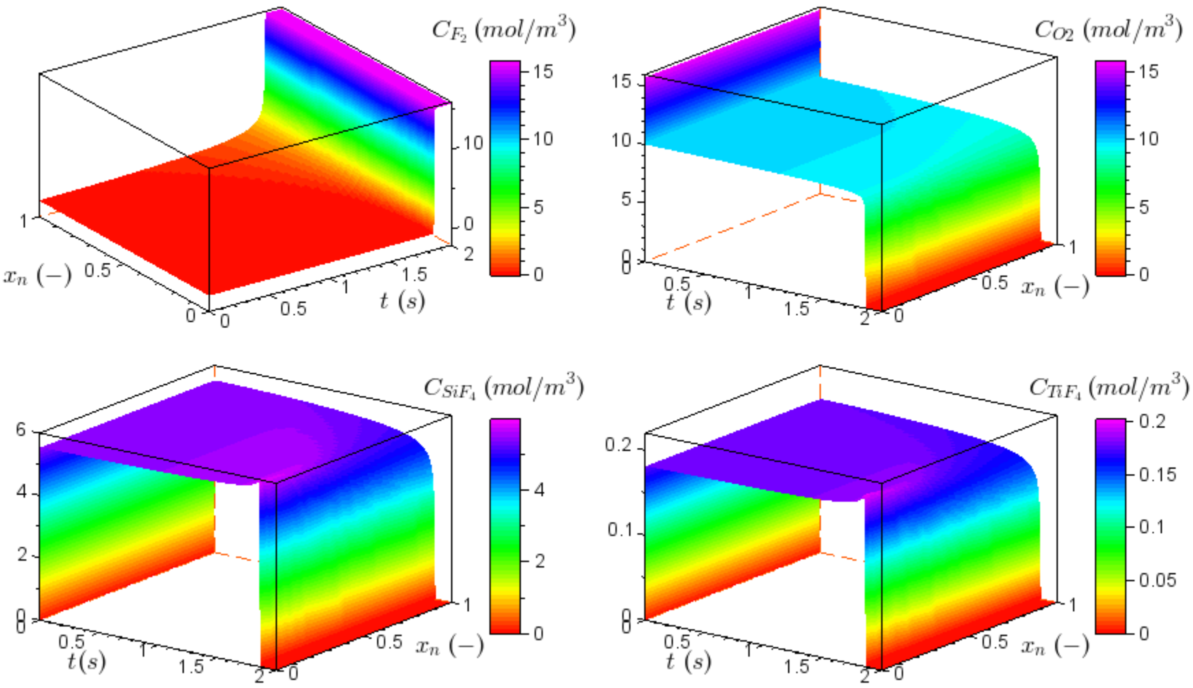

C 94: Surface graphs showing the effect of reaction rate constant = 100 (m3/mol.s) on gas concentrations.

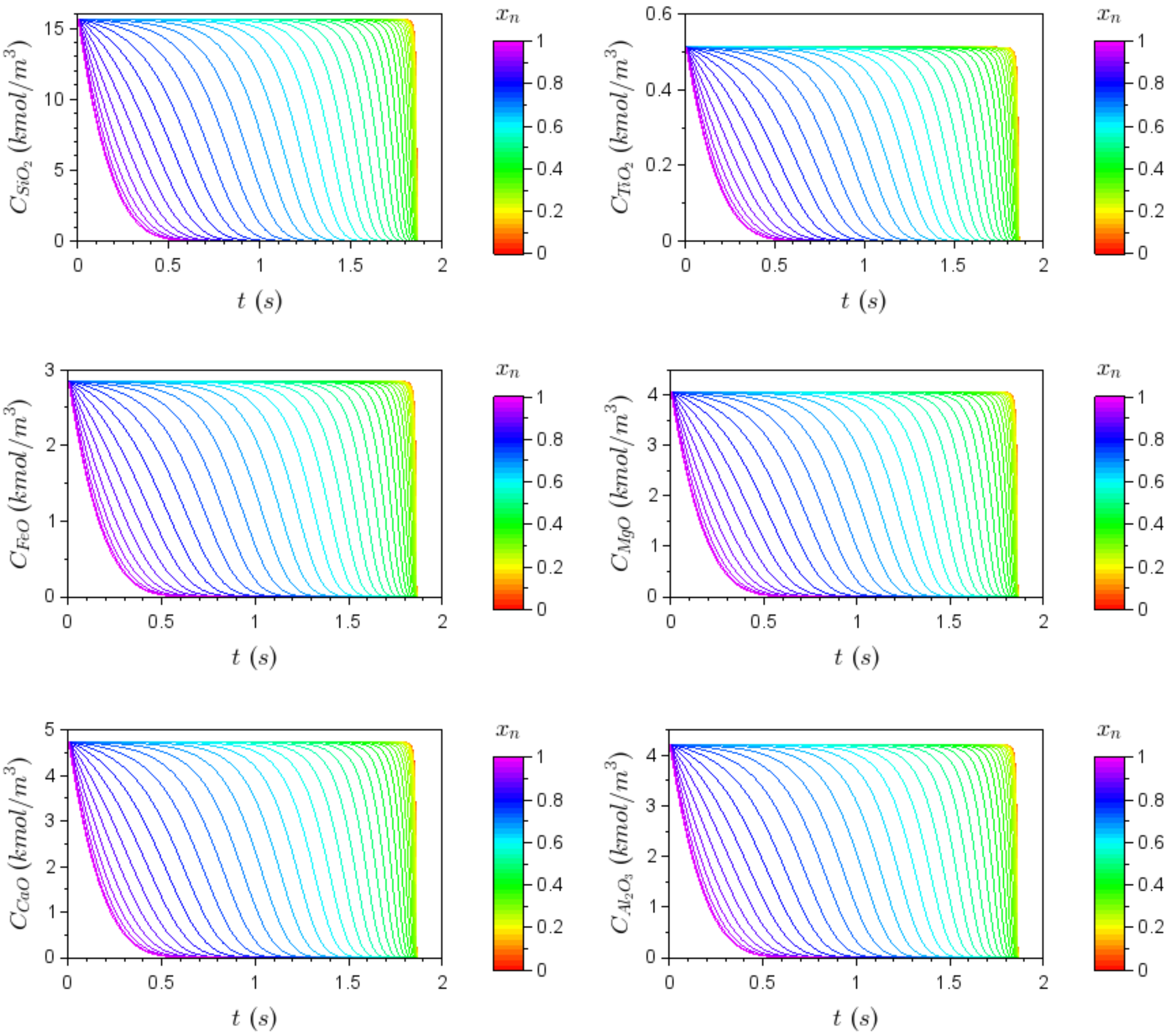

C 95: Effect of reaction rate constant = 100 (m3/mol.s) on solid reactant concentrations over time.

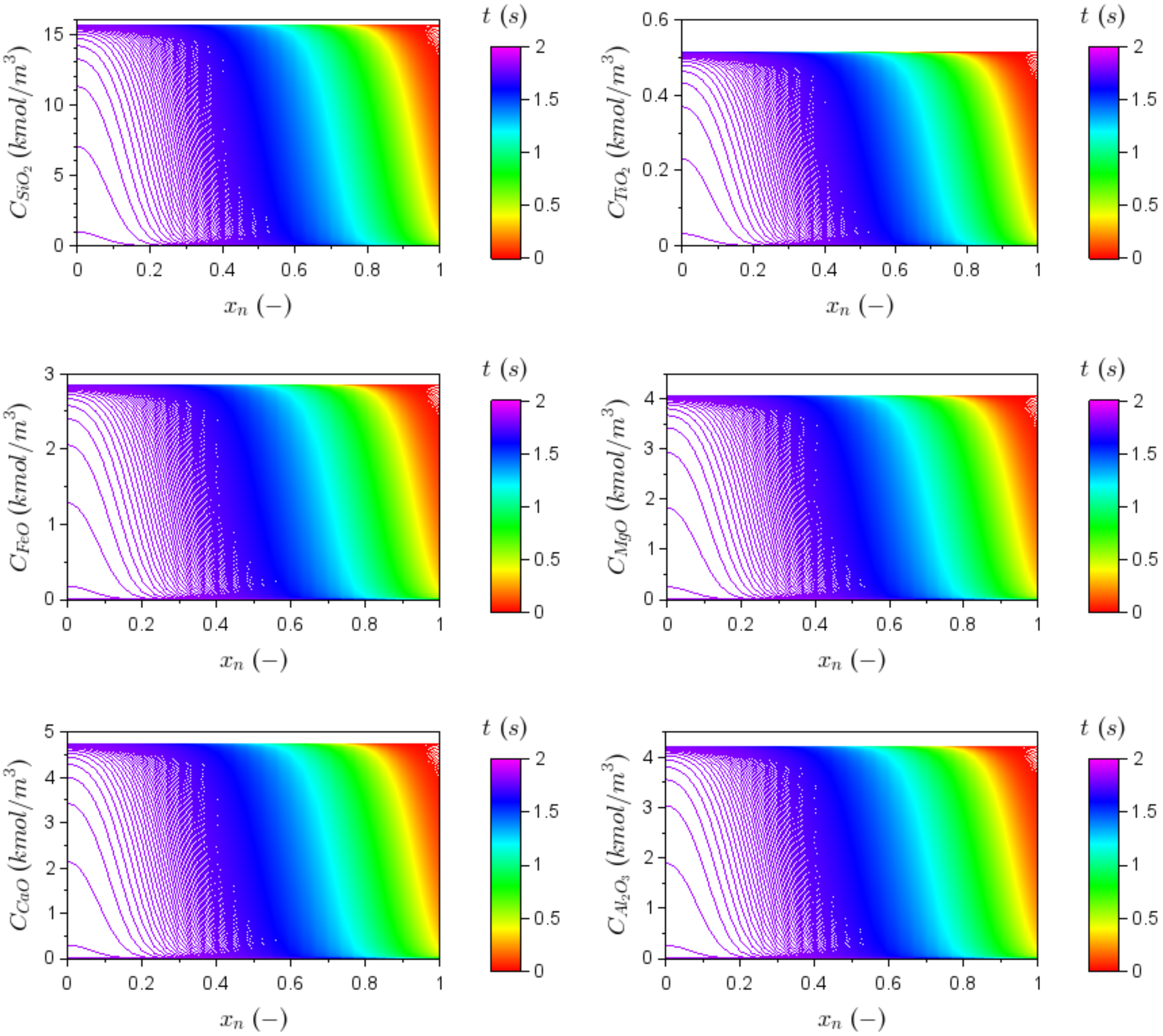

C 96: Effect of reaction rate constant = 100 (m3/mol.s) on solid reactant concentrations through the particle.

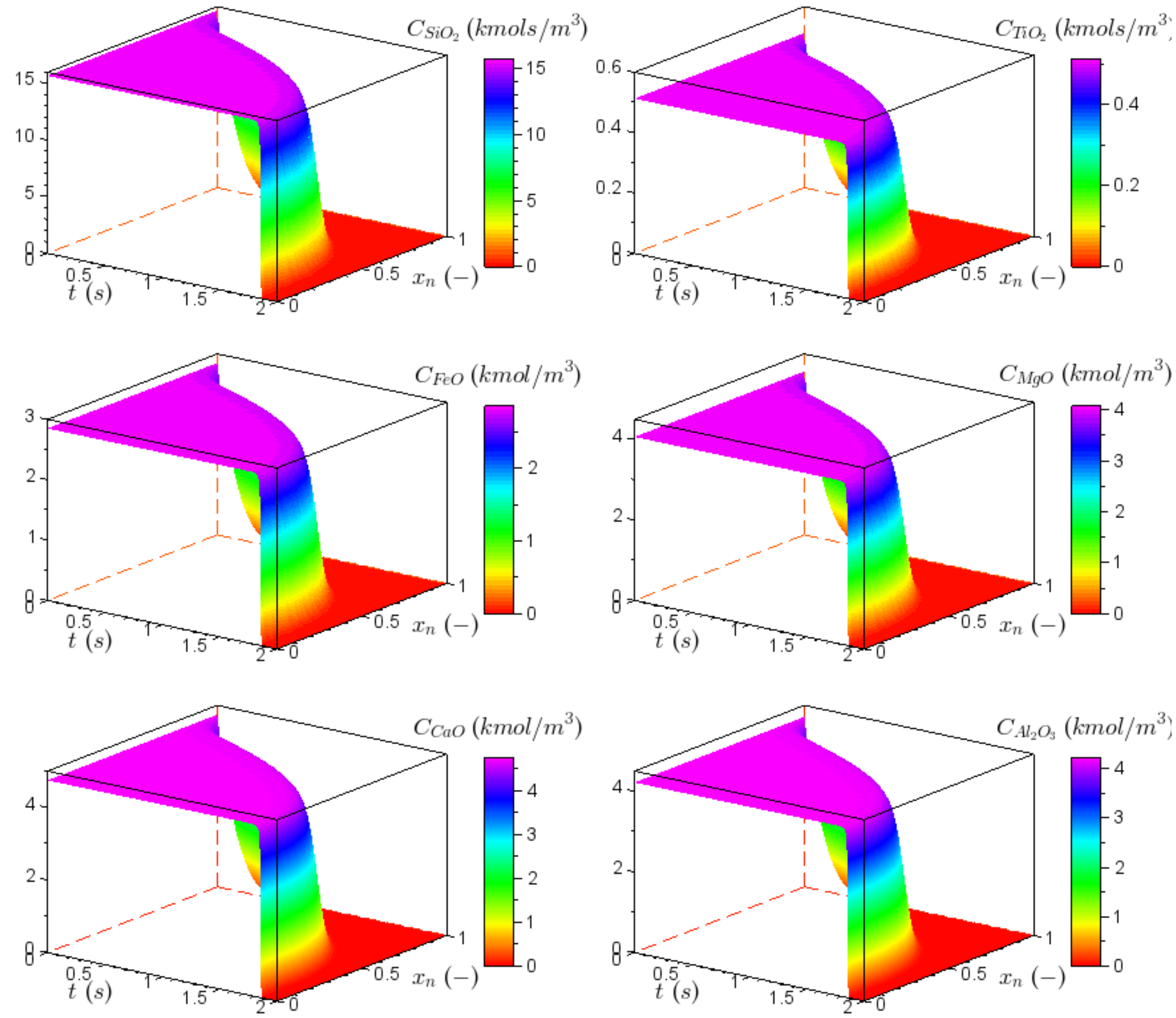

C 97: Surface graphs showing the effect of reaction rate constant = 100 (m3/mol.s) on solid reactants concentrations.

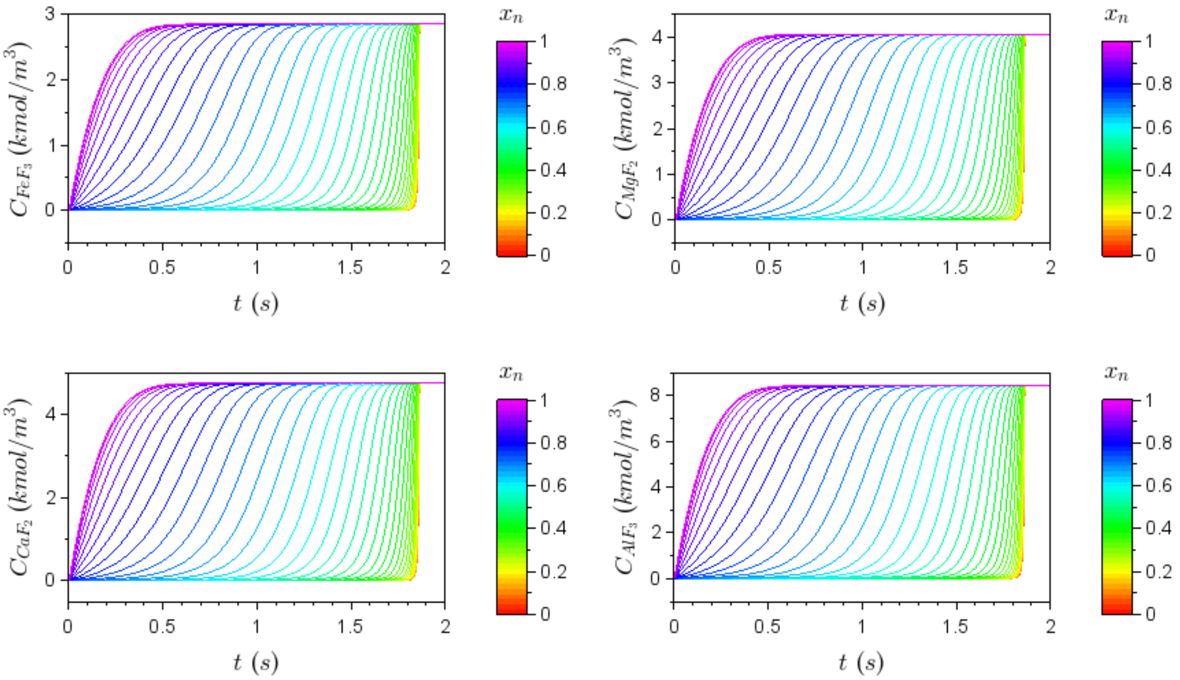

C 98: Effect of reaction rate constant = 100 (m3/mol.s) on solid products concentrations over time.

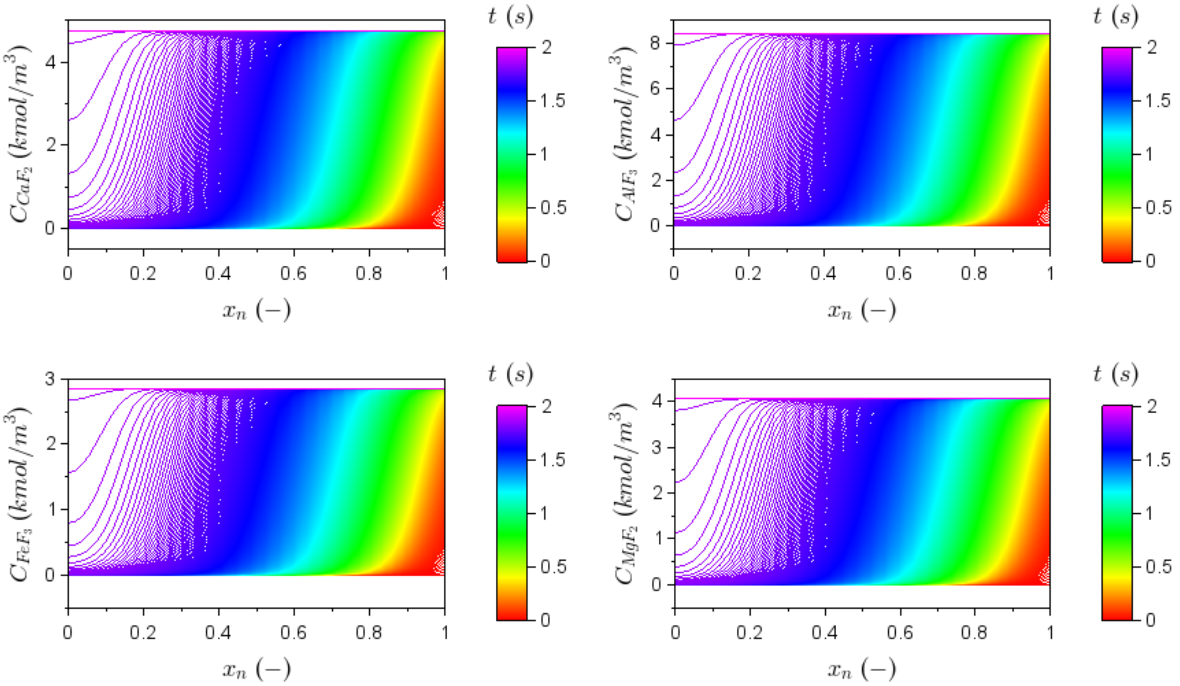

C 99: Effect of reaction rate constant = 100 (m3/mol.s) on solid products concentrations through the particle.

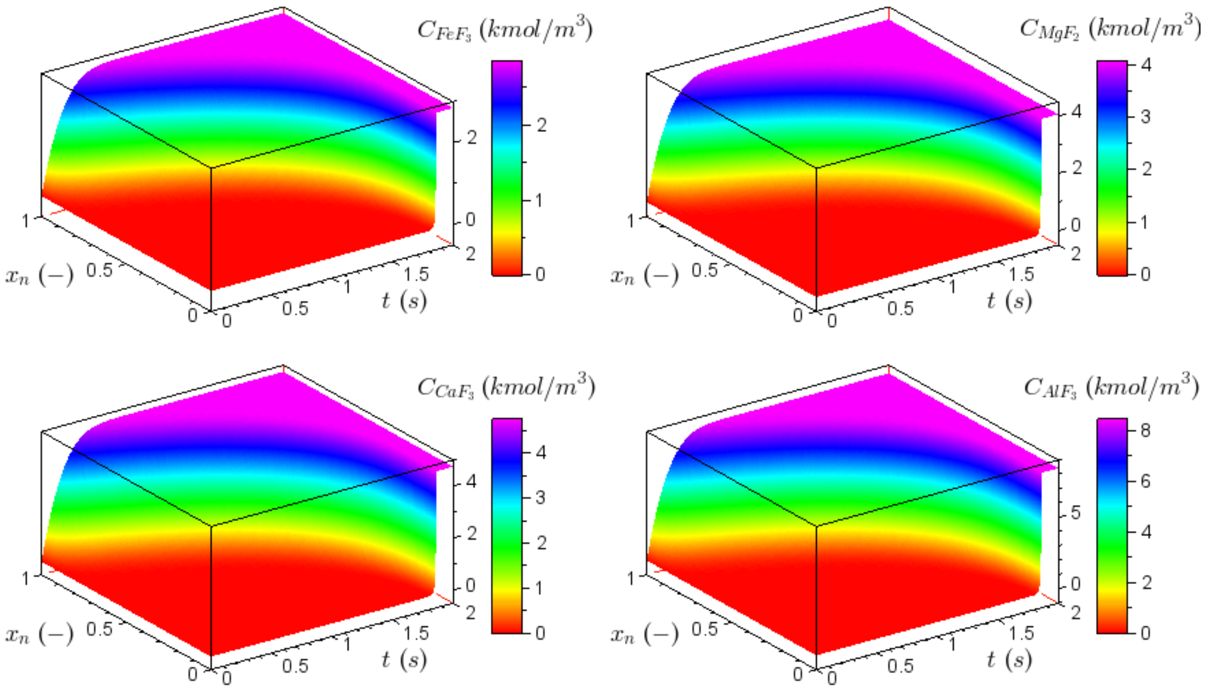

C 100: Surface graphs showing the effect of reaction rate constant = 100 (m3/mol.s) on solid products concentrations.

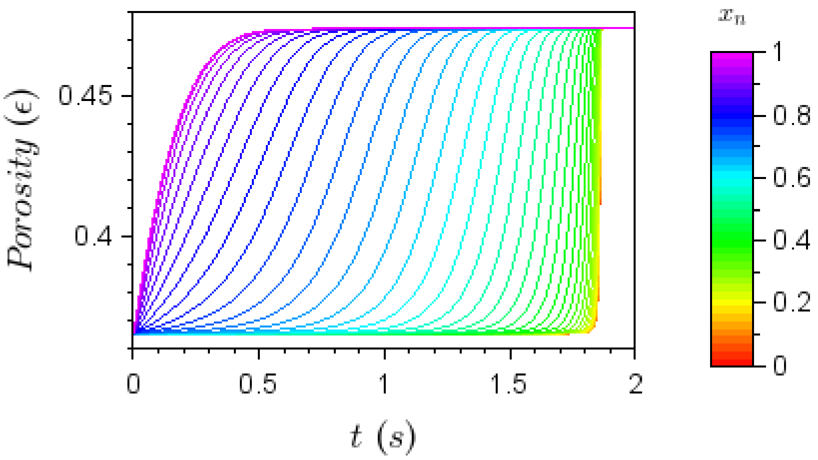

C 101: Effect of reaction rate constant = 100 (m3/mol.s) on porosity over time.

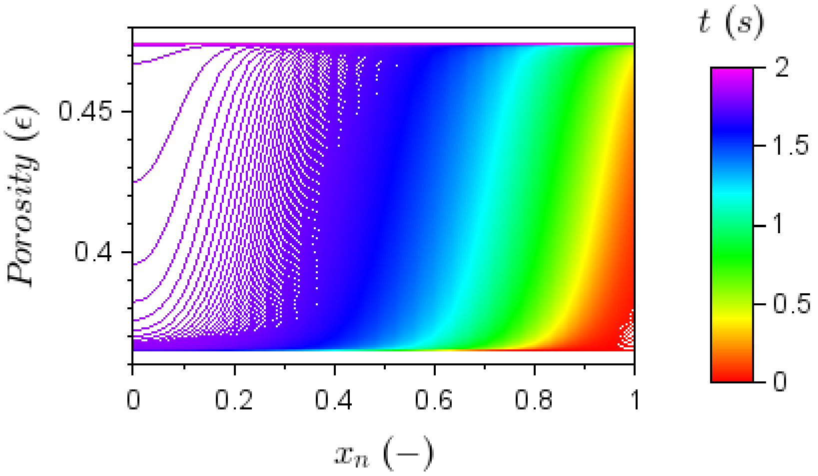

C 102: Effect of reaction rate constant = 100 (m3/mol.s) on porosity through the particle.

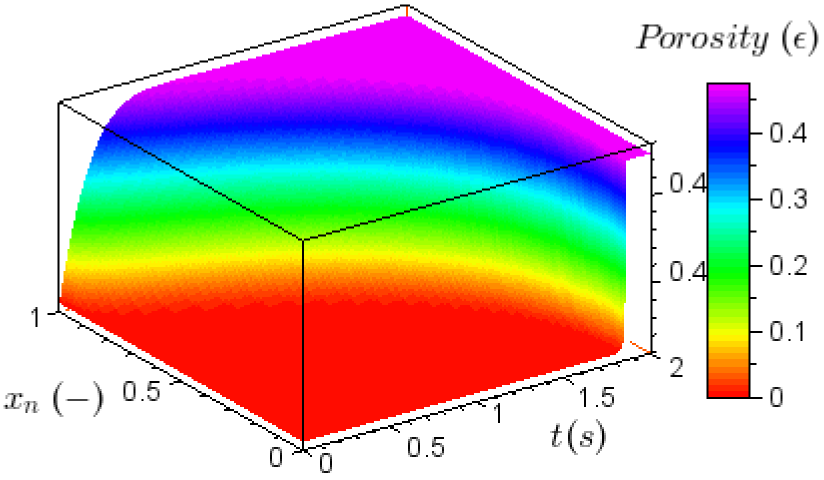

C 103: Surface graph showing the effect of reaction rate constant = 100 (m3/mol.s) on porosity.

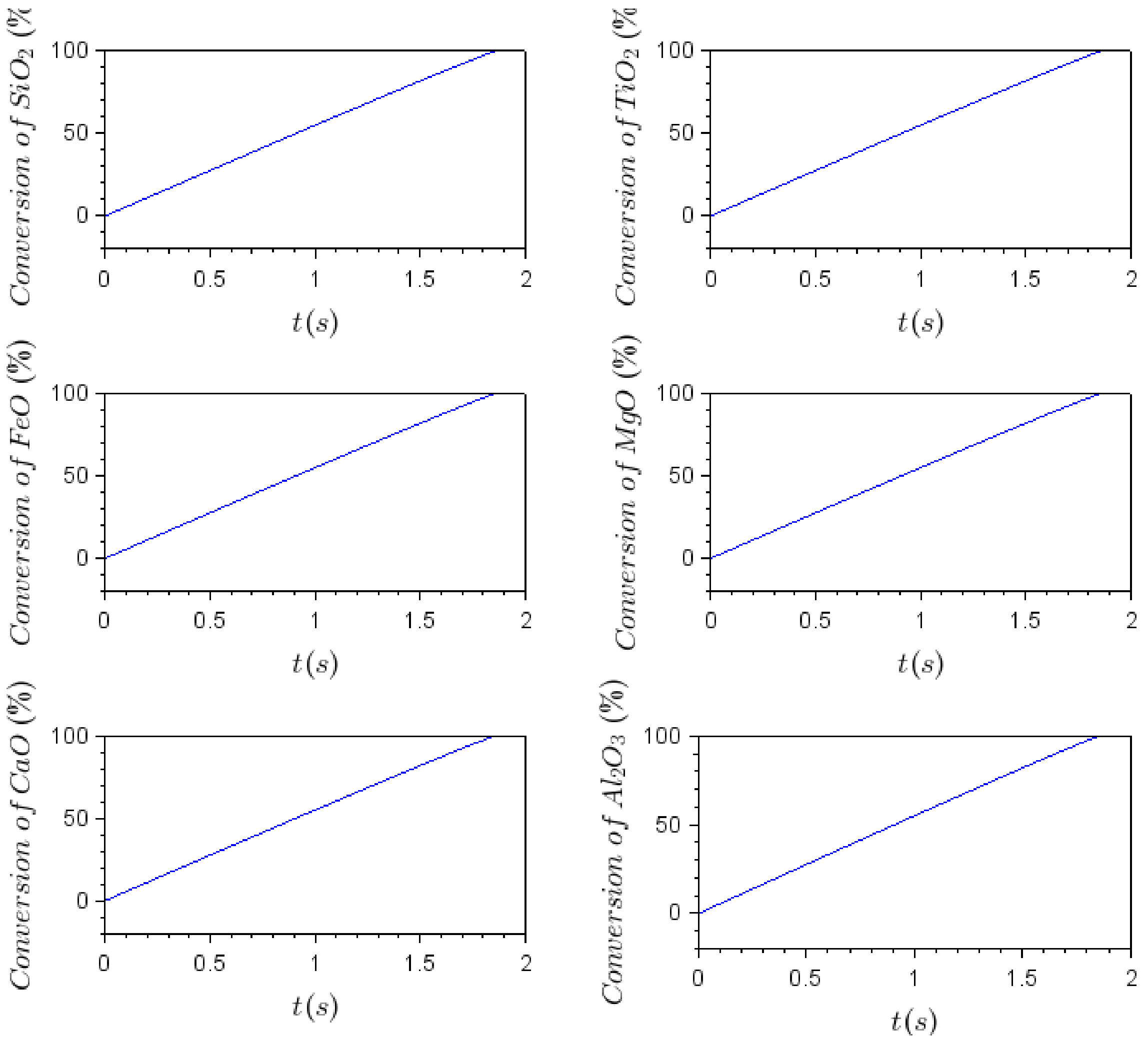

C 104: Effect of reaction rate constant = 100 (m3/mol.s) conversion over time.

Particle size variation - $R_p = 0.35\ \mu m$

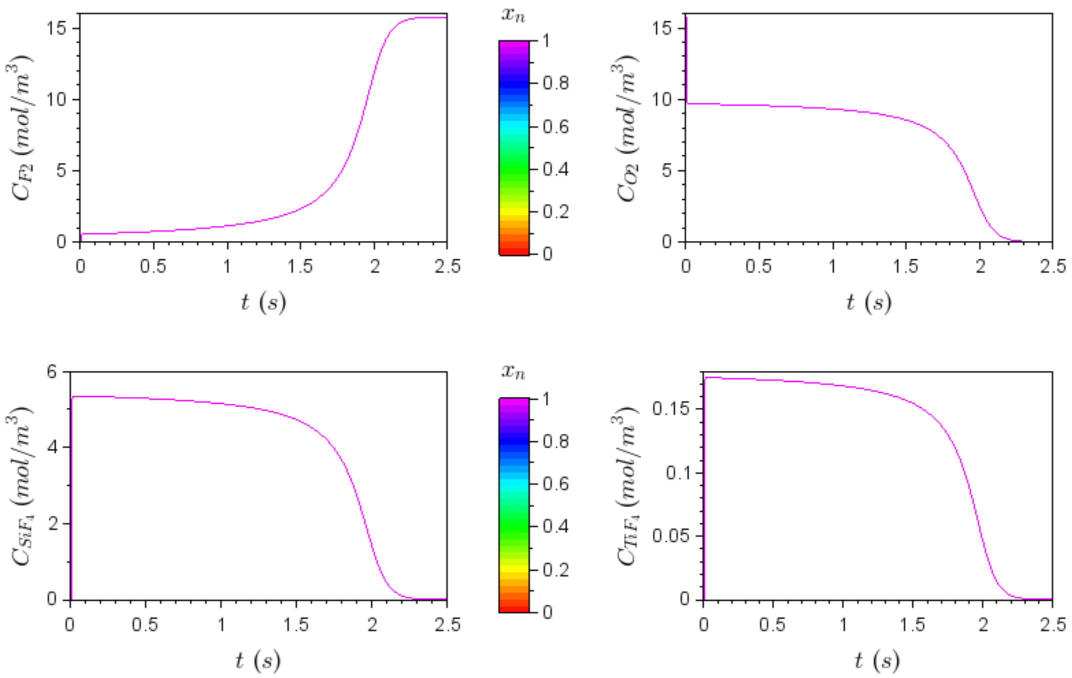

C 105: Effect of particle size = 35x10^{-7} m on gas concentrations over time.

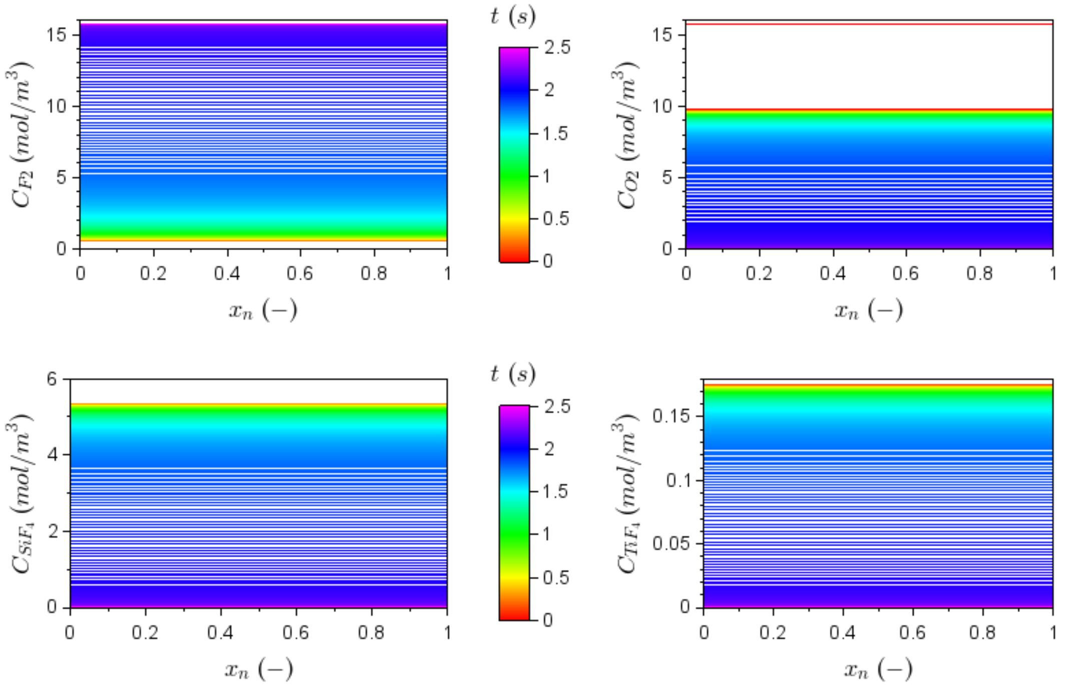

C 106: Effect of particle size = 35x10^{-7} m on gas concentrations through the particle.

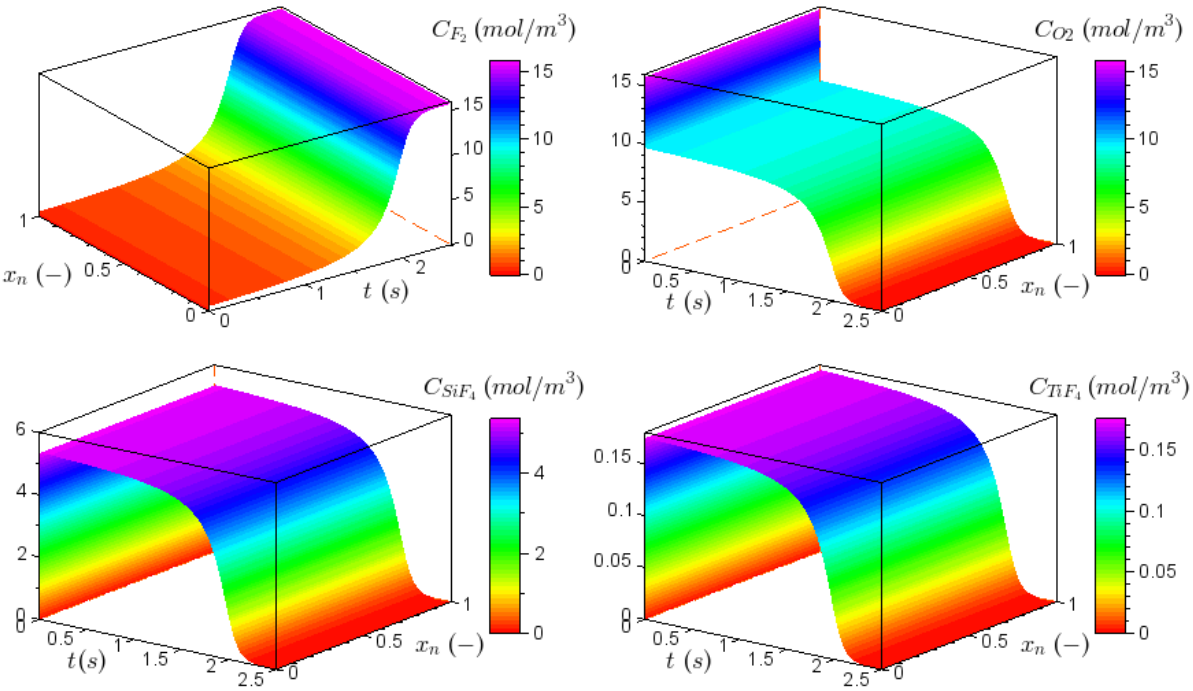

C 107: Surface graphs showing the effect of particle size = 35x10^{-7} m on gas concentrations.

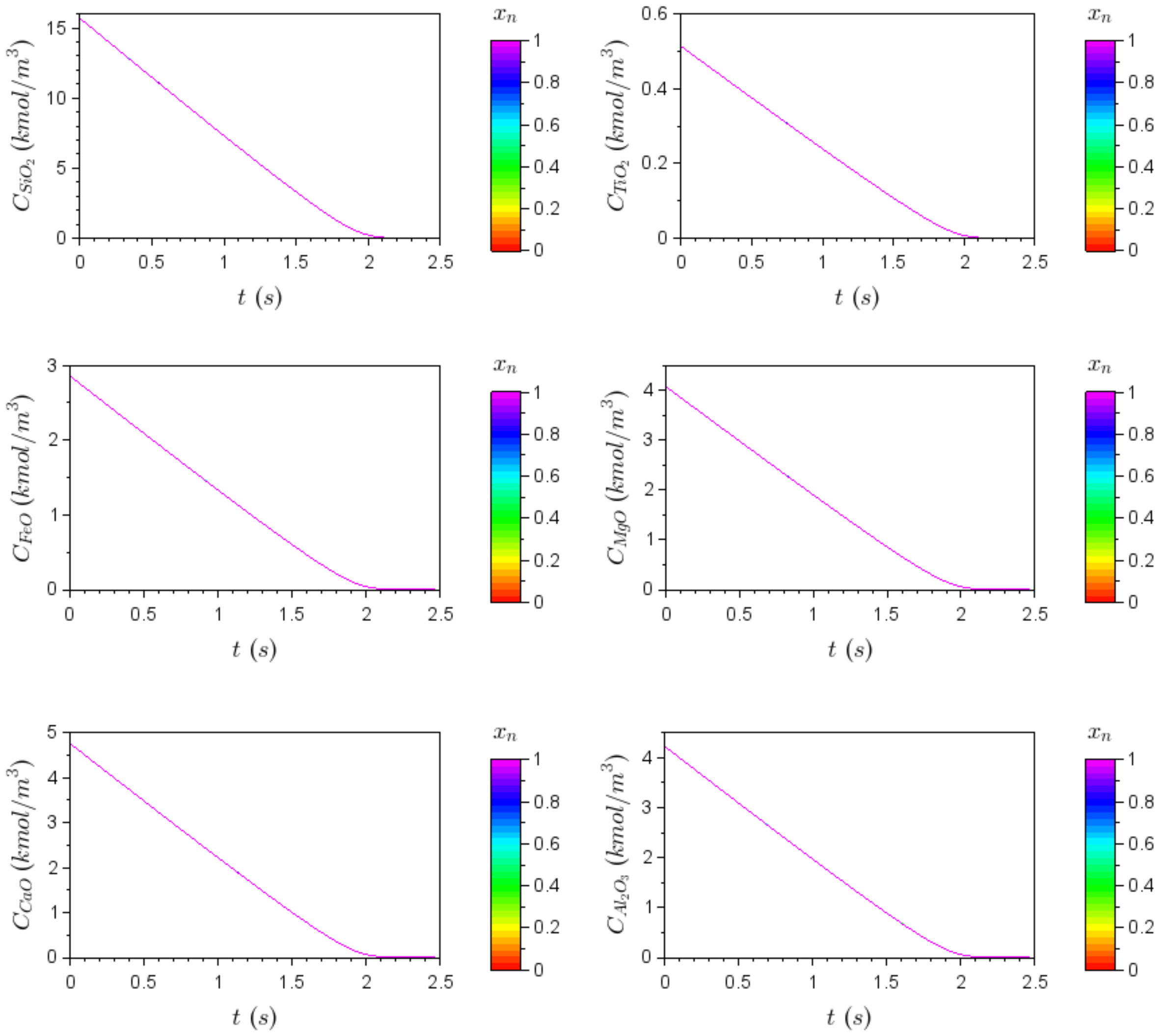

C 108: Effect of particle size = 35x10^{-7} m on solid reactants concentrations over time.

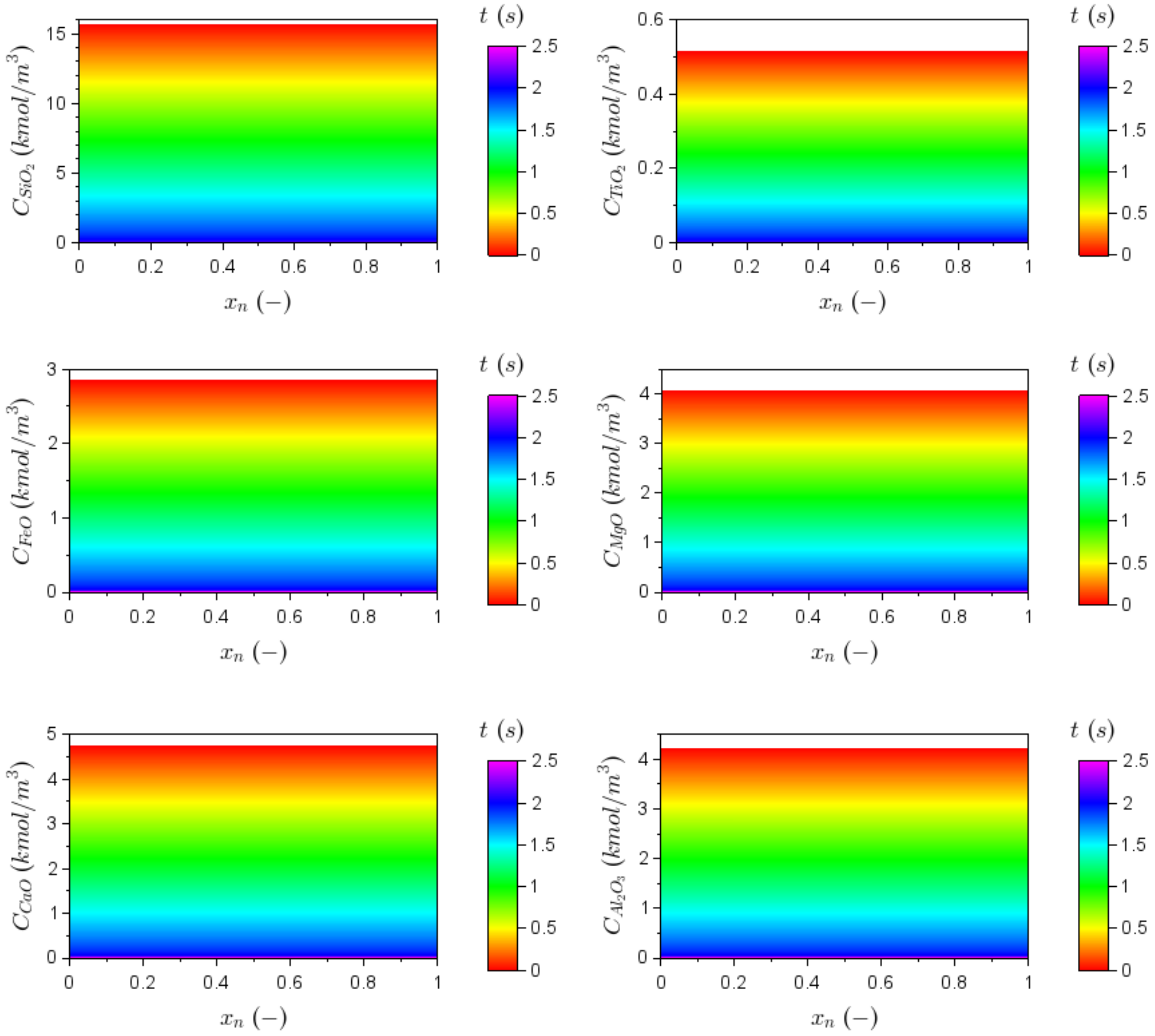

C 109: Effect of particle size = 35x10^{-7} m on solid reactants concentrations through the particle.

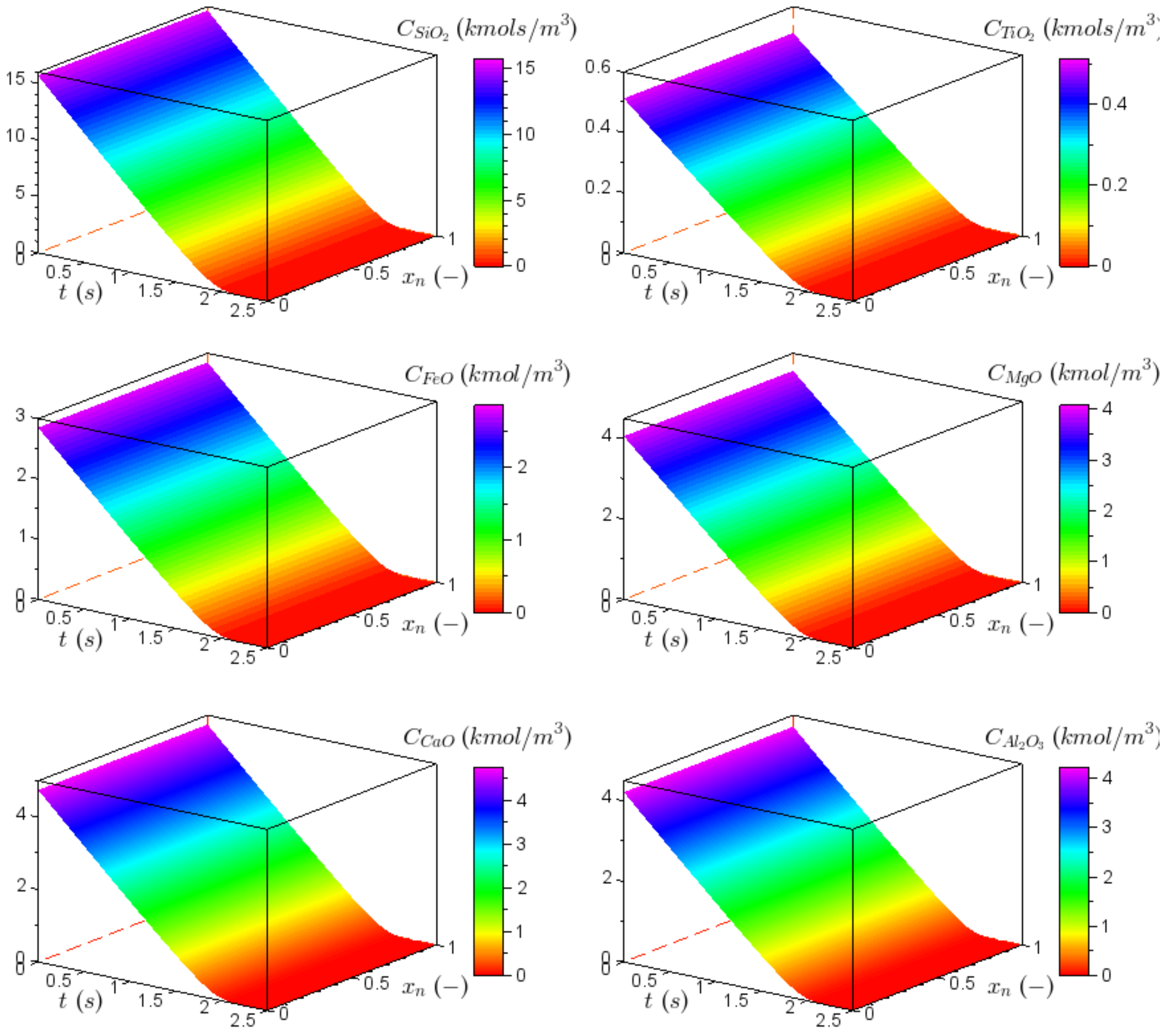

C 110: Surface graphs showing the effect of particle size = 35x10^{-7} m on solid reactants concentrations.

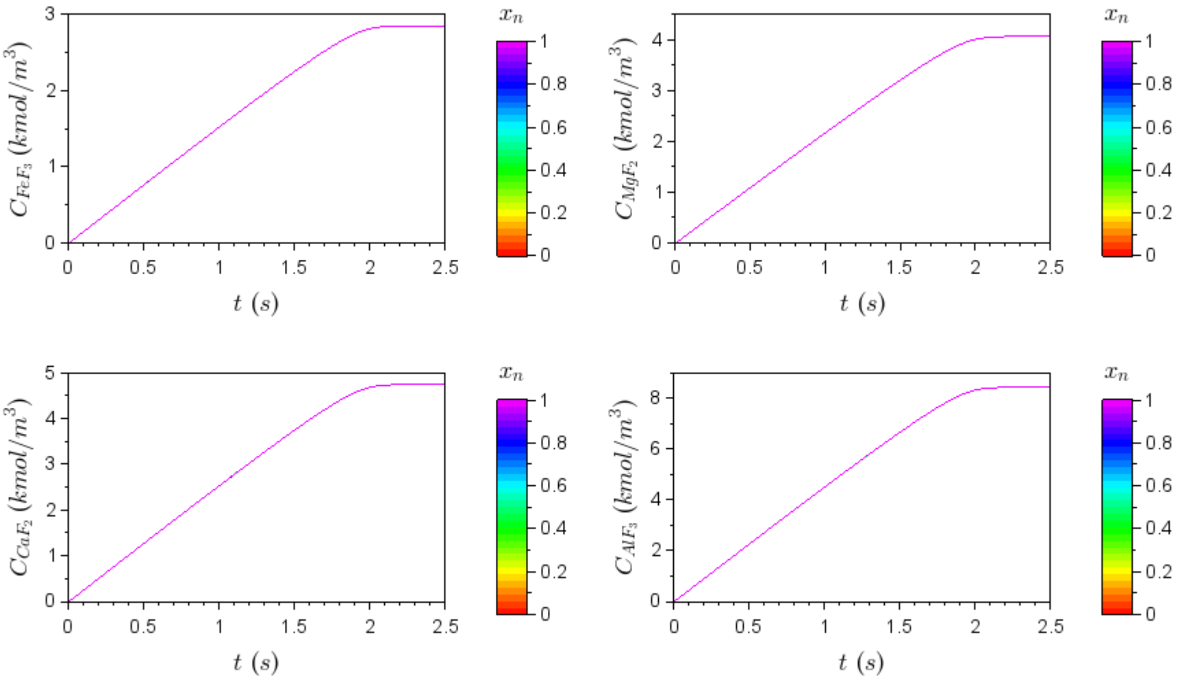

C 111: Effect of particle size = 35x10^{-7} m on solid products concentrations over time.

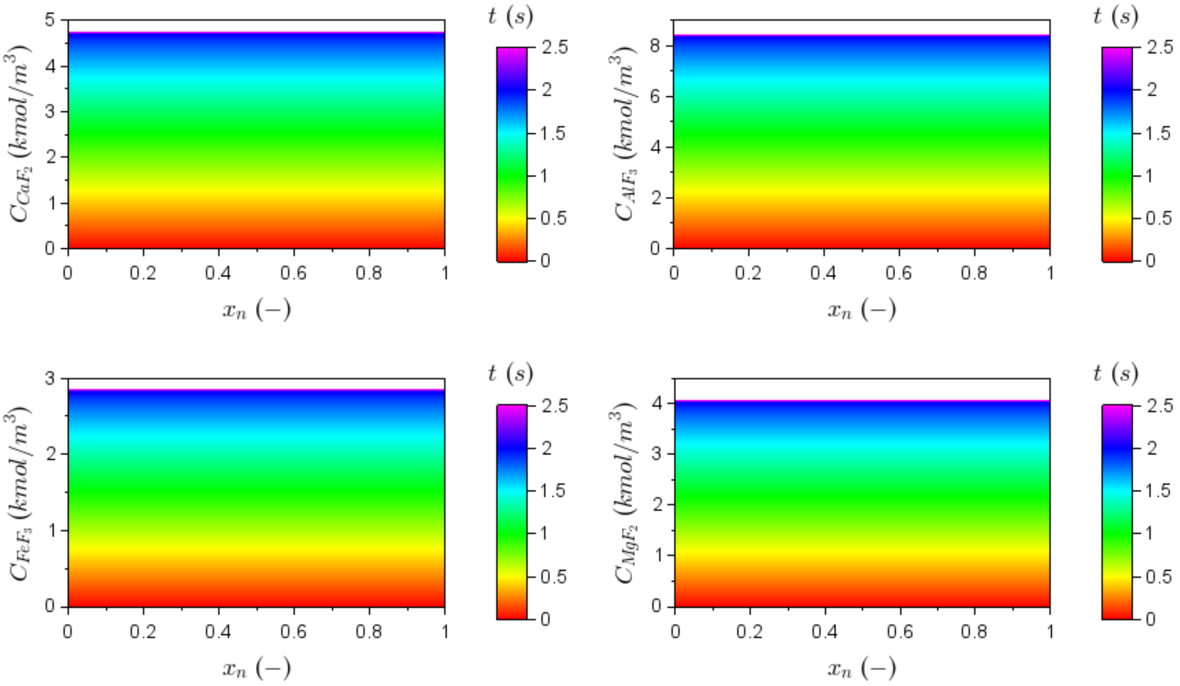

C 112: Effect of particle size = 35x10^{-7} m on solid products concentrations through the particle.

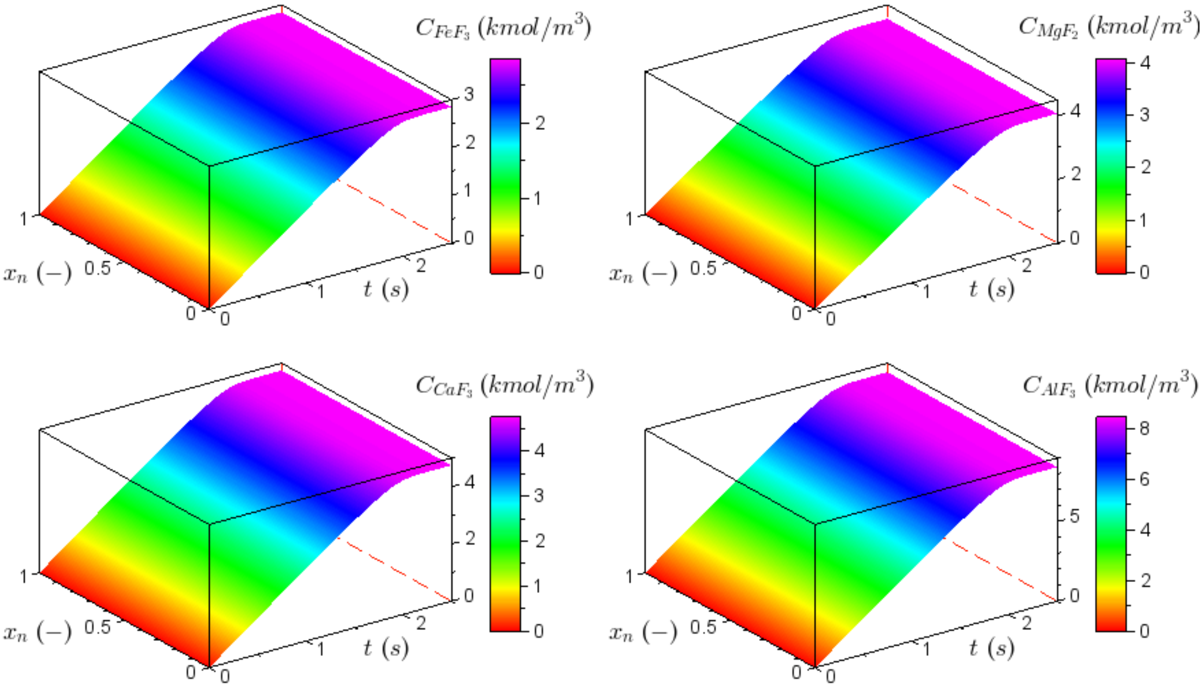

C 113: Surface graphs showing the effect of particle size = 35x10^{-7} m on solid products concentrations.

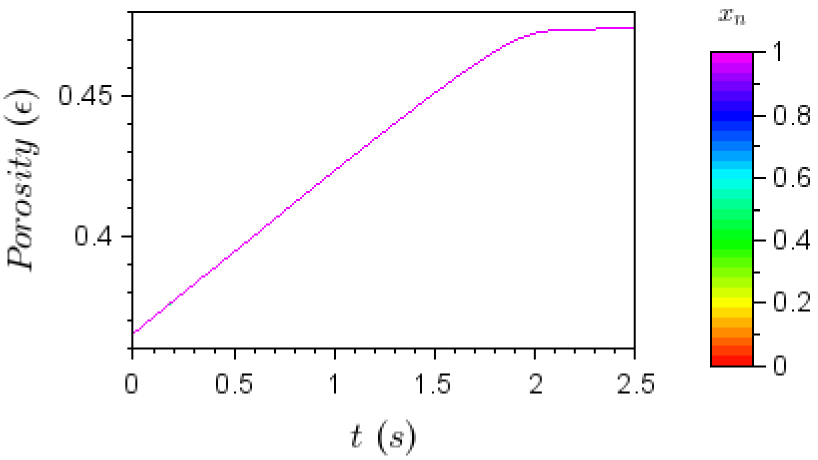

C 114: Effect of particle size = 35x10^{-7} m on porosity over time.

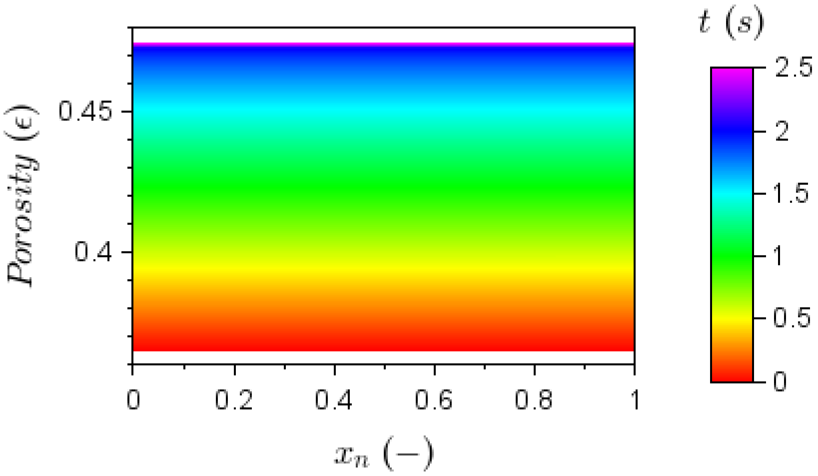

C 115: Effect of particle size = 35x10^{-7} m on porosity through the particle.

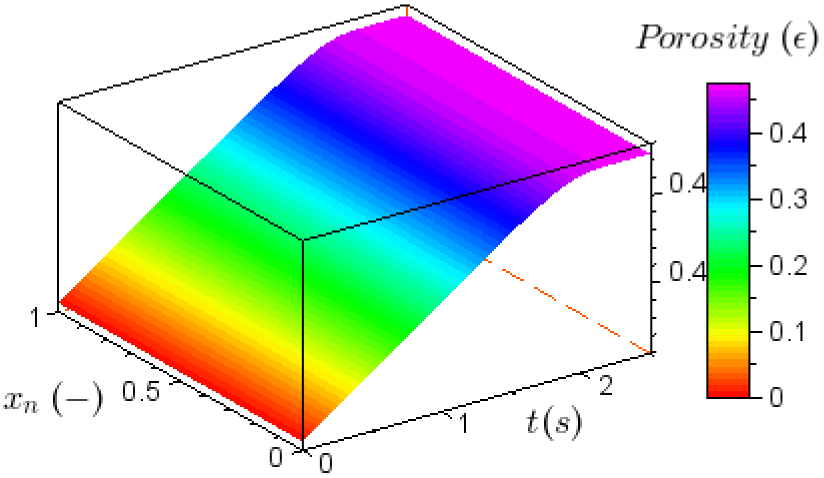

C 116: Surface graphs showing the effect of particle size = 35x10-7 m on porosity.

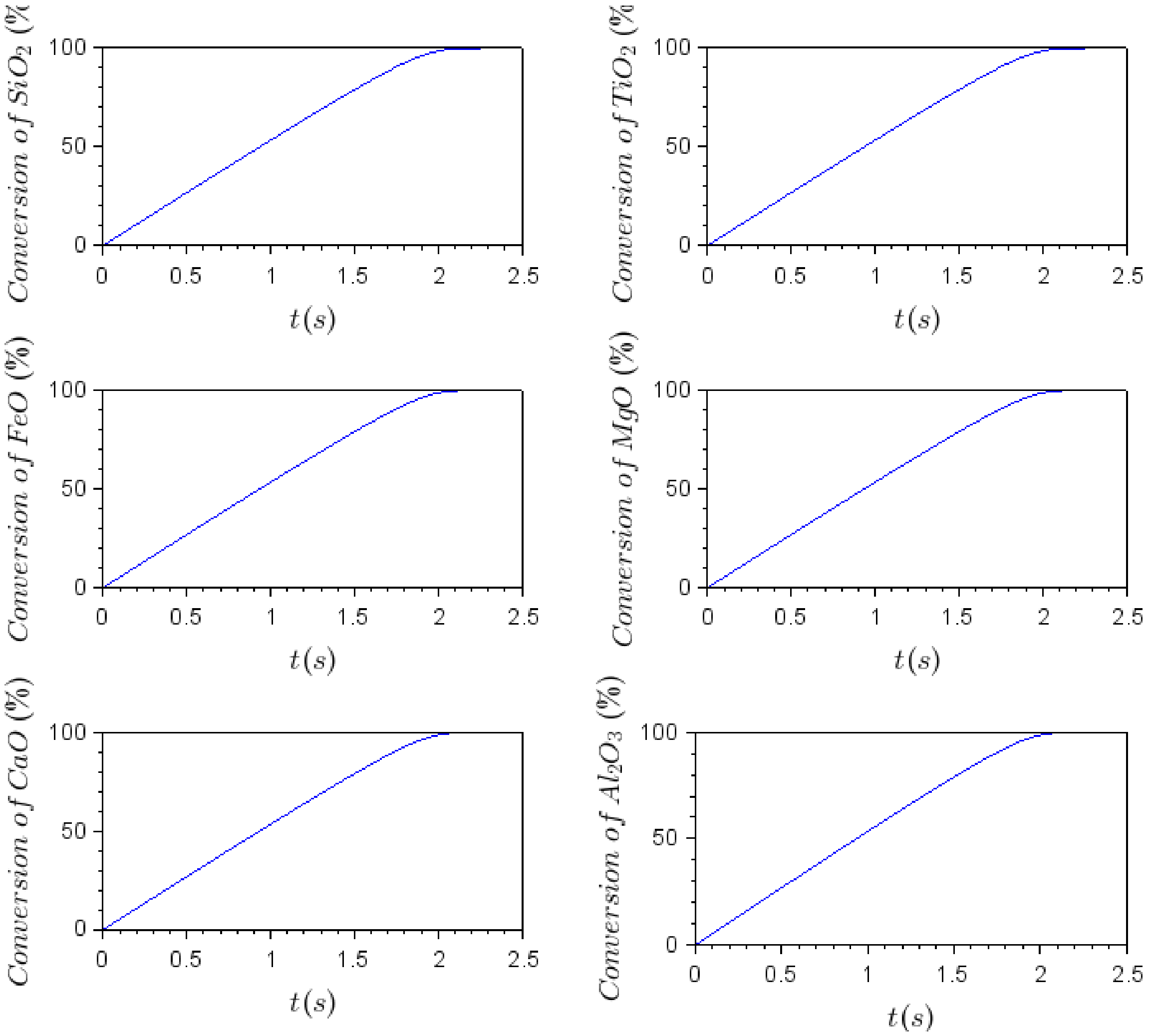

C 117: Effect of particle size = 35x10^{-7} m on conversion over time.

Particle size variation - $R_p = 3.5\ \mu m$

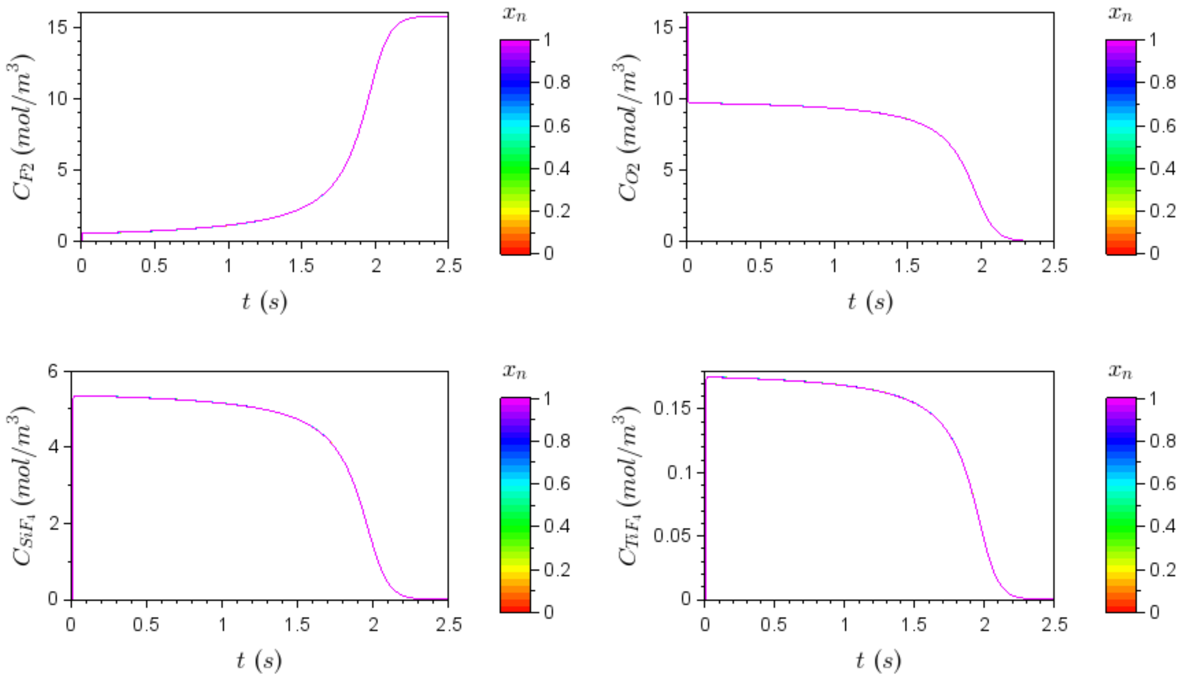

C 118: Effect of particle size = 35x10^{-6} m on gas concentrations over time.

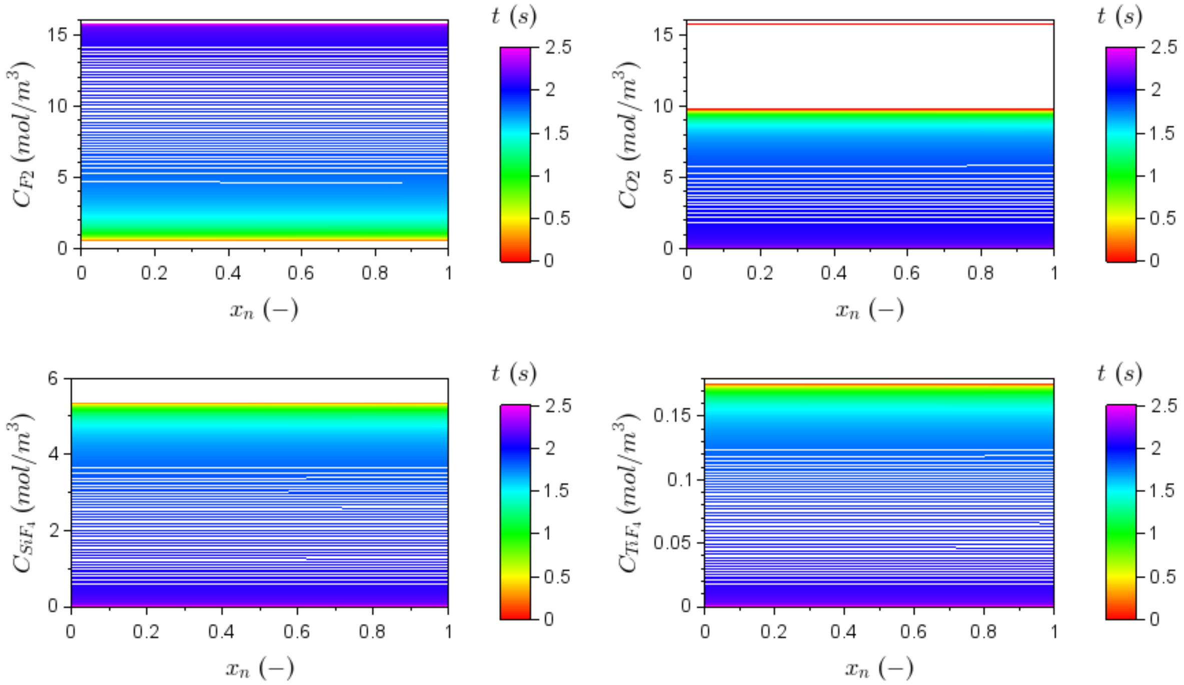

C 119: Effect of particle size = 35x10^{-6} m on gas concentrations through the particle.

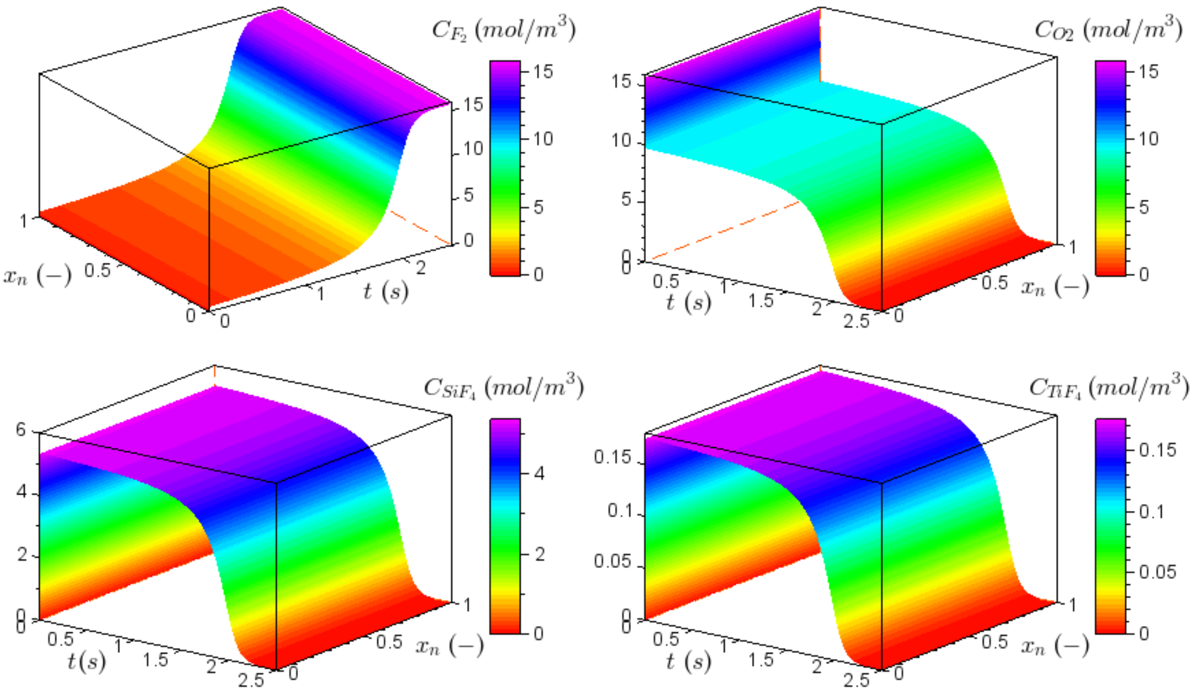

C 120: Surface graphs showing the effect of particle size = 35x10^{-6} m on gas concentrations.

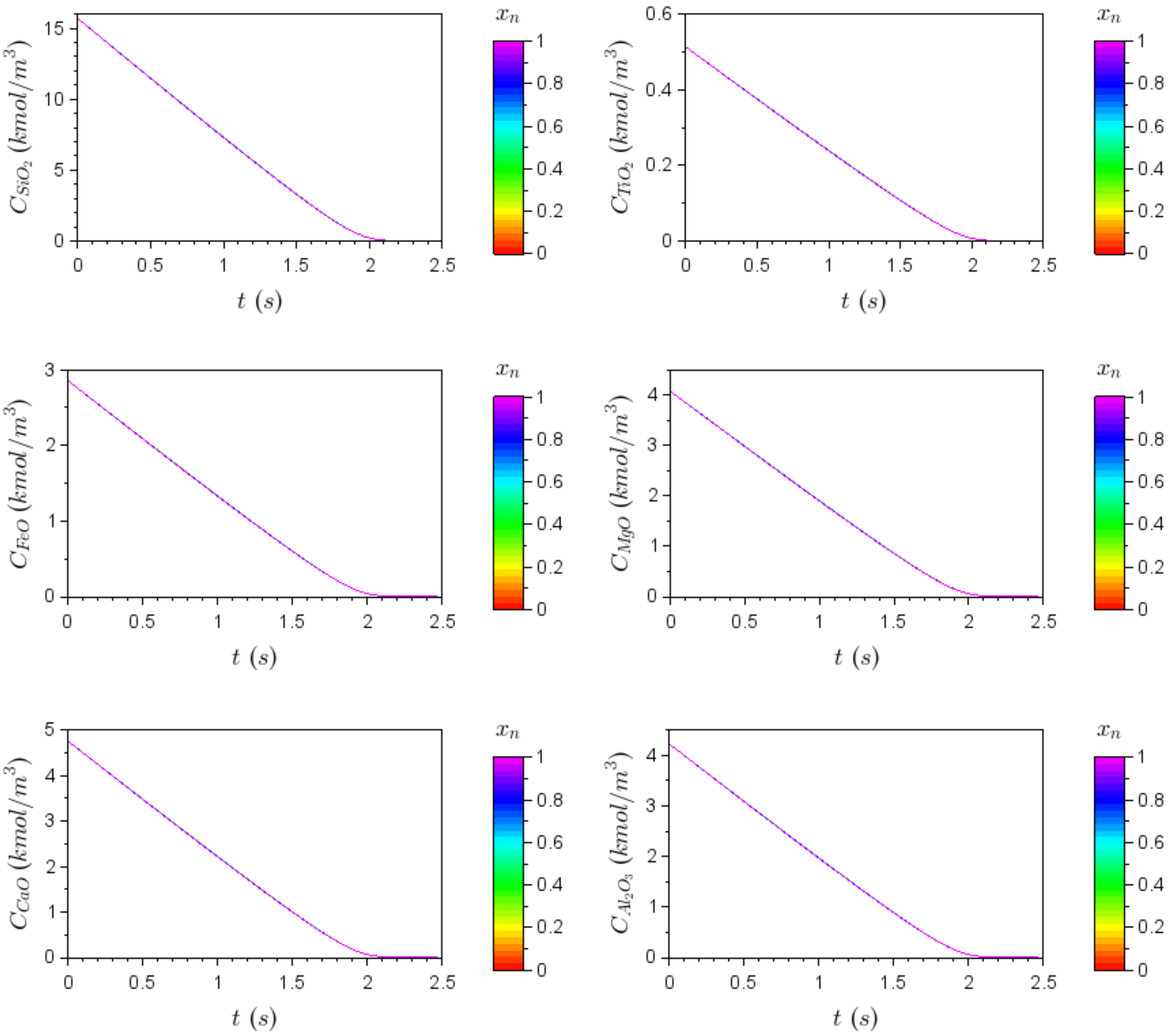

C 121: Effect of particle size = 35x10^{-6} m on solid reactants concentrations over time.

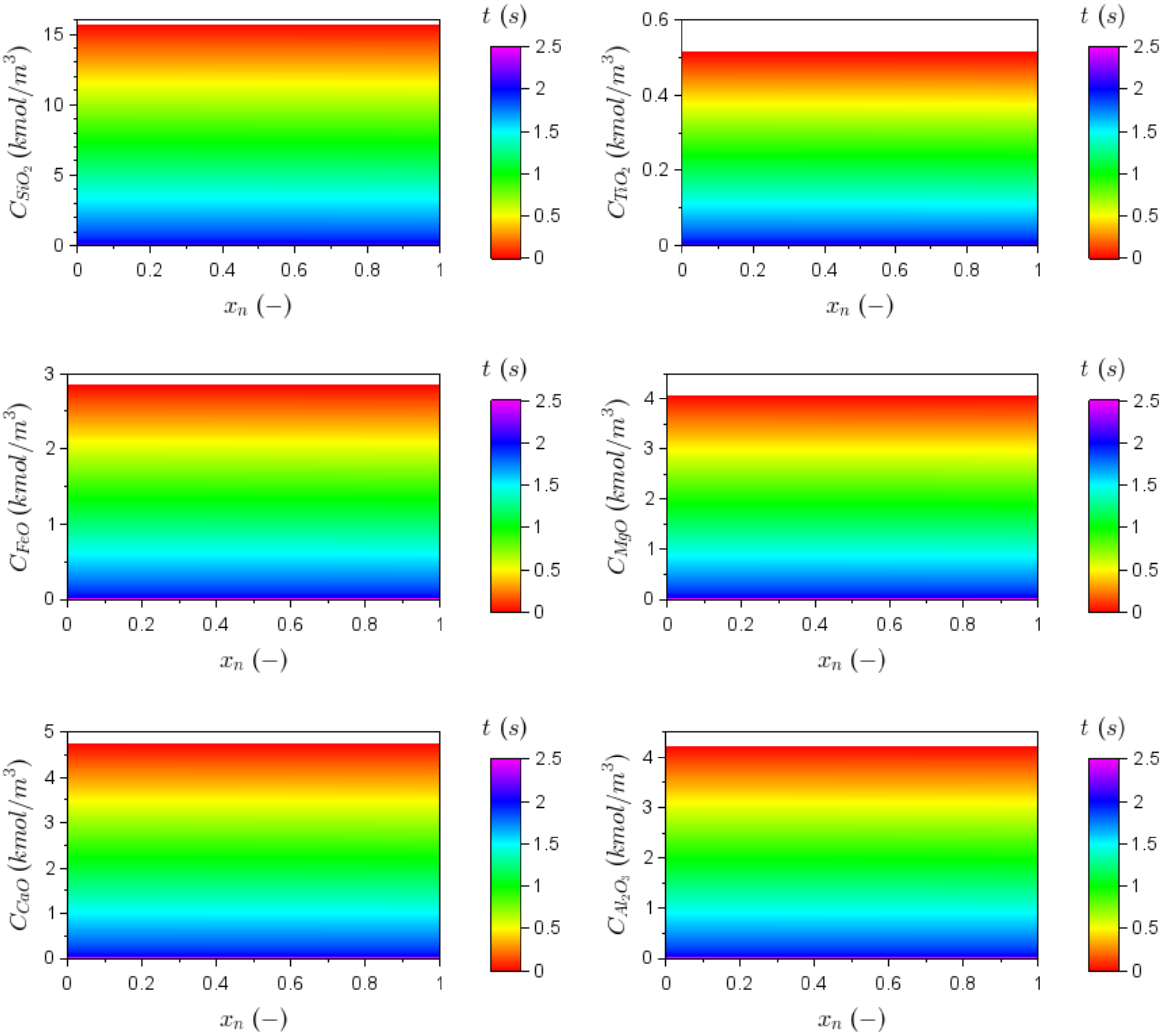

C 122: Effect of particle size = $35x10^{-6}$ m on solid reactants concentrations through the particle.

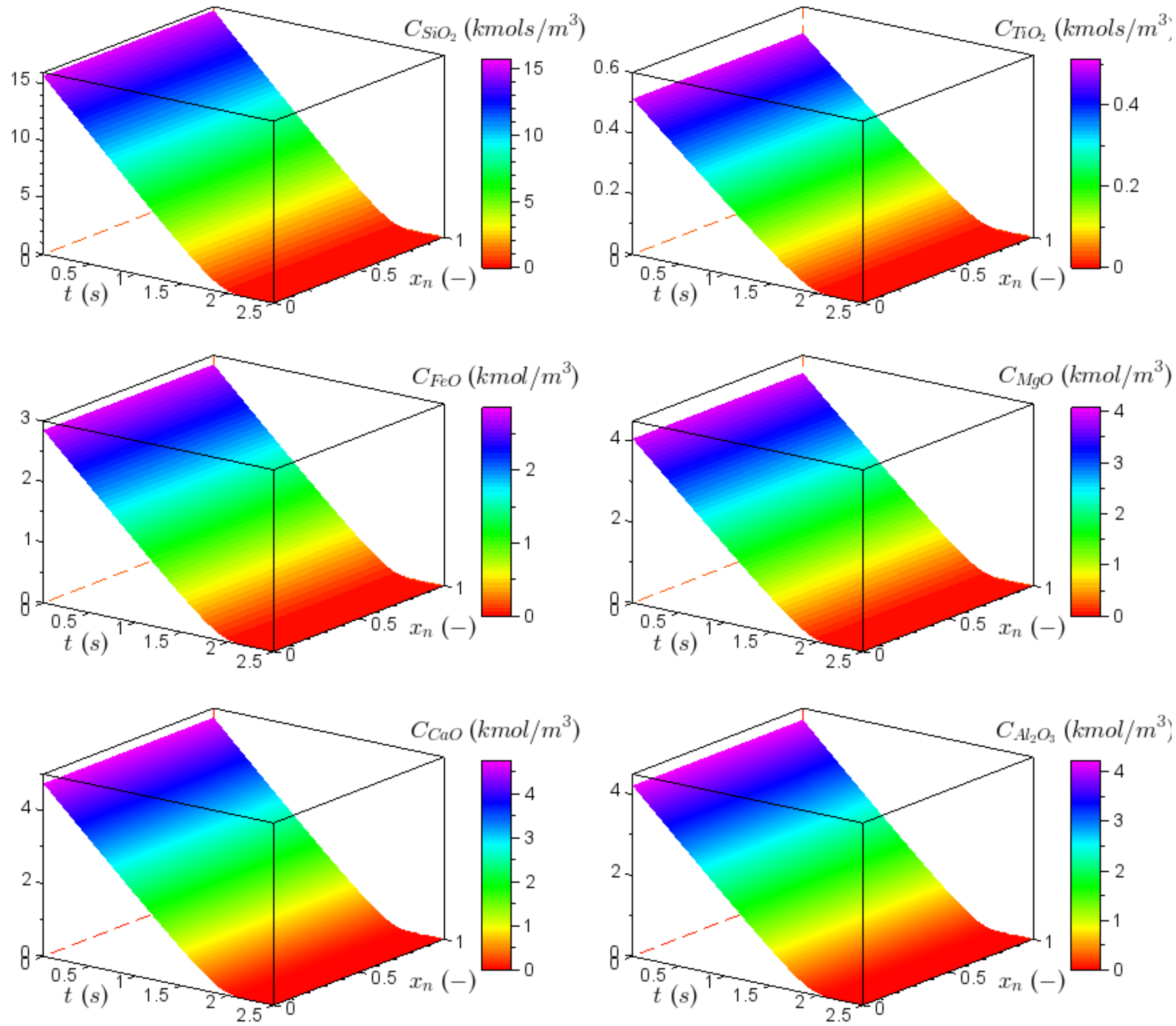

C 123: Surface graphs showing the effect of particle size = 35x10^{-6} m on solid reactants concentrations.

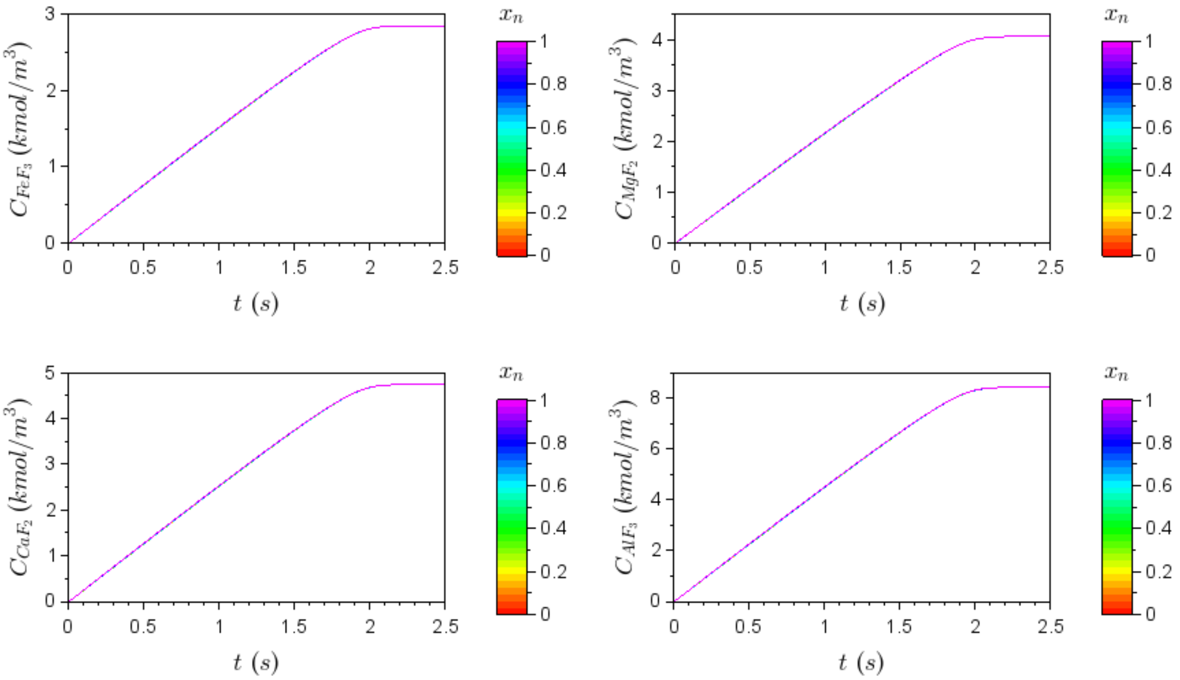

C 124: Effect of particle size = 35x10^{-6} m on solid products concentrations over time.

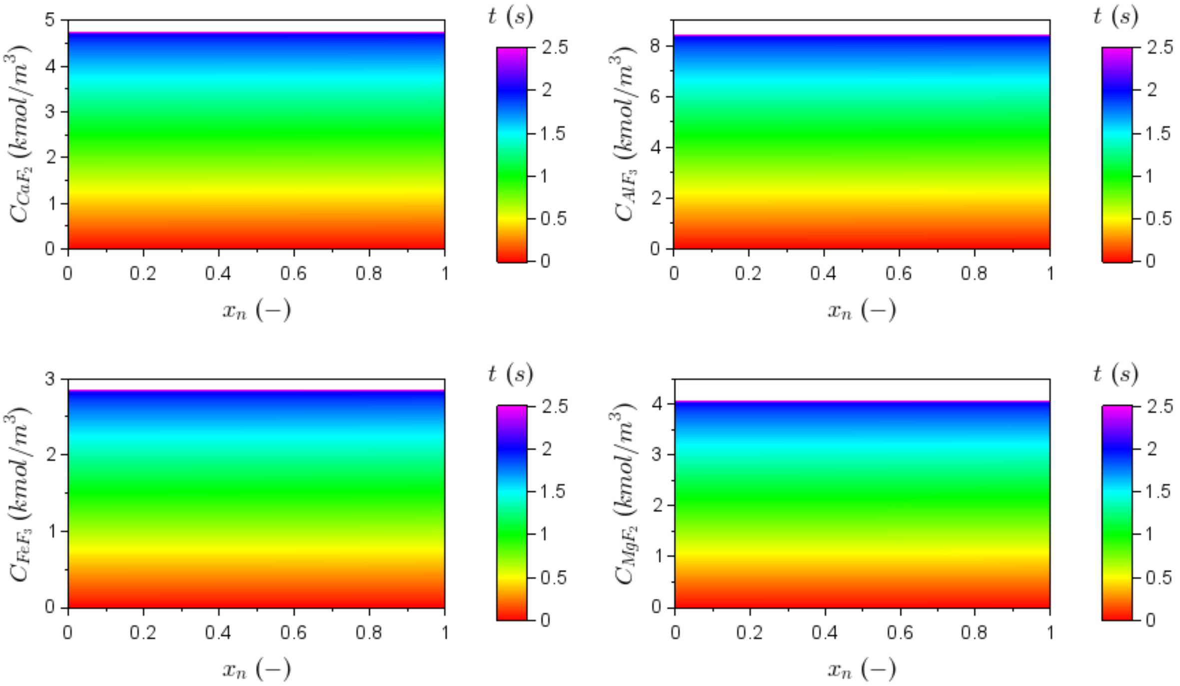

C 125: Effect of particle size = 35x10^{-6} m on solid products concentrations through the particle.

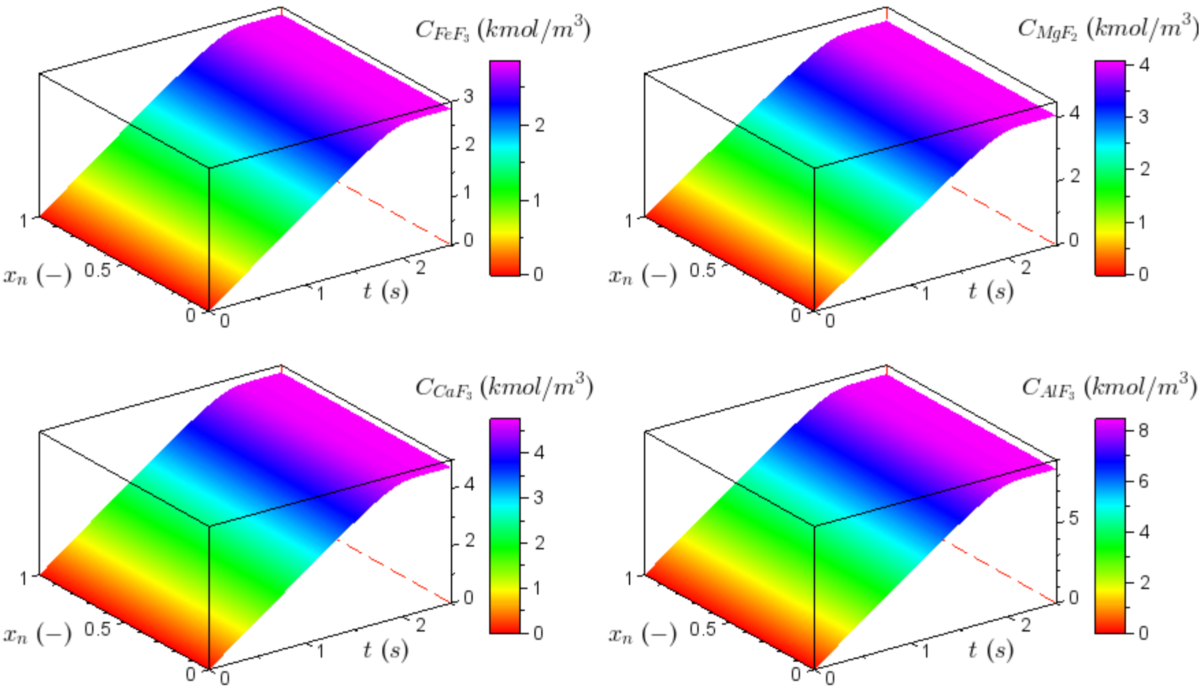

C 126: Surface graphs showing the effect of particle size = 35x10^{-6} m on solid products concentrations.

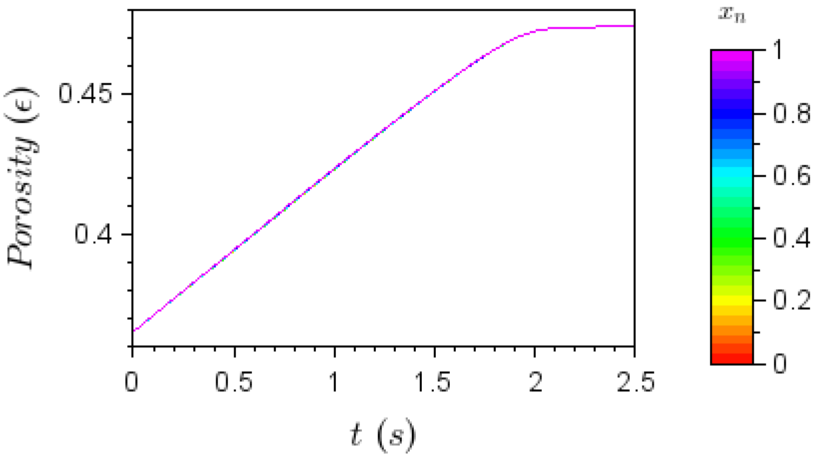

C 127: Effect of particle size = 35x10^{-6} m on porosity over time.

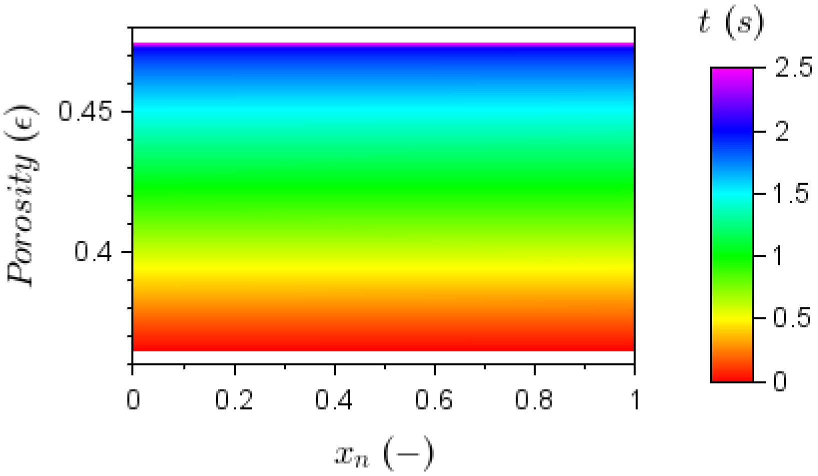

C 128: Effect of particle size = 35x10^{-6} m on porosity through the particle.

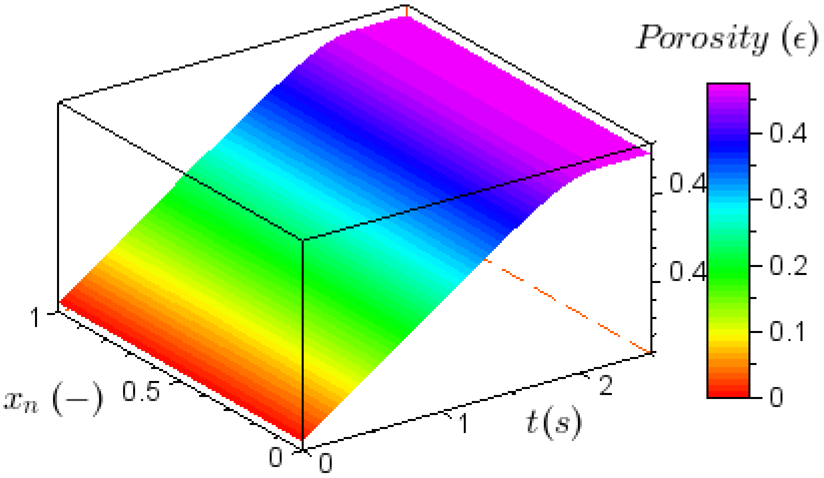

C 129: Surface graphs showing the effect of particle size = 35x10^{-6} m on porosity.

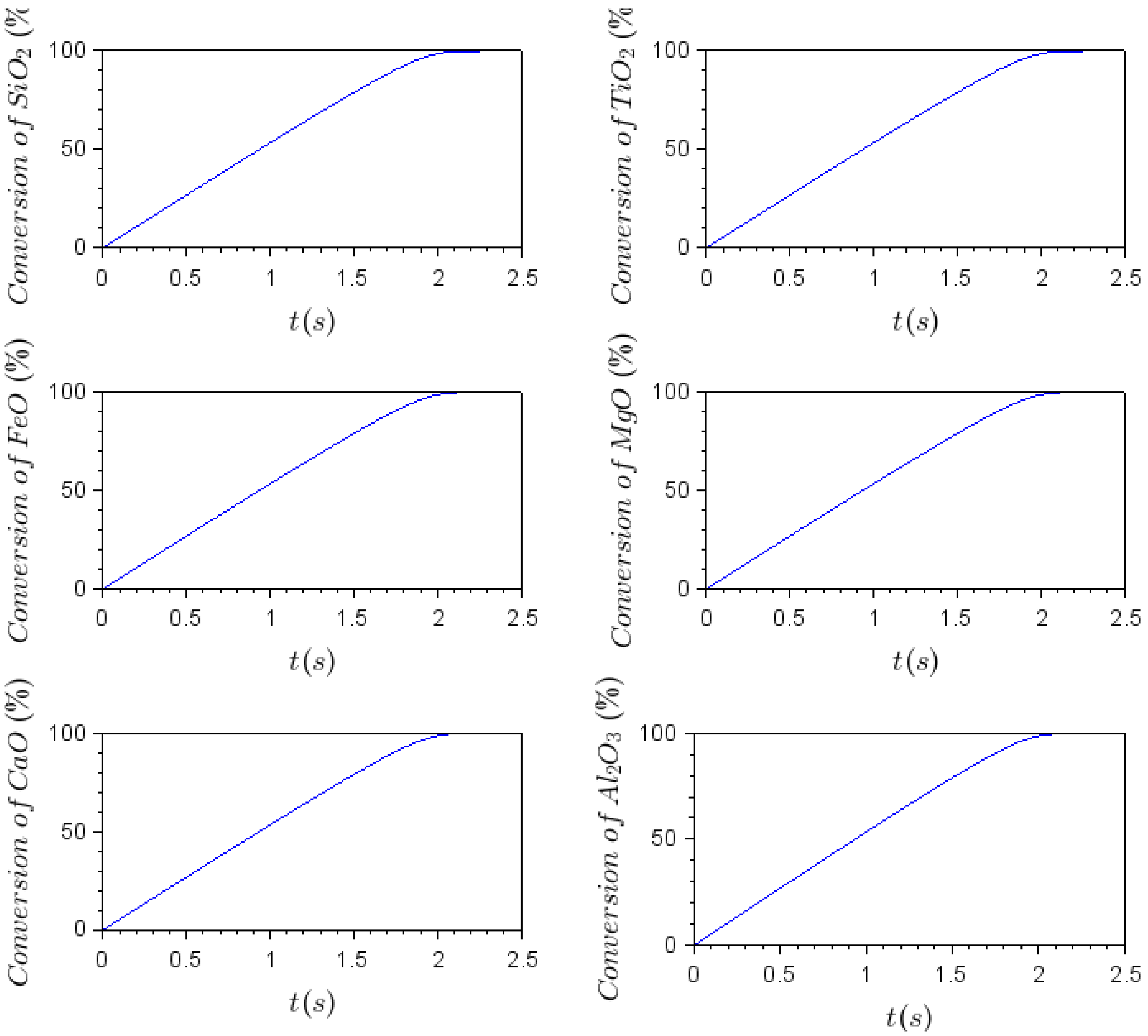

C 130: Effect of particle size = 35x10^{-6} m on conversion over time.

Particle size variation - $R_p = 35\ \mu m$

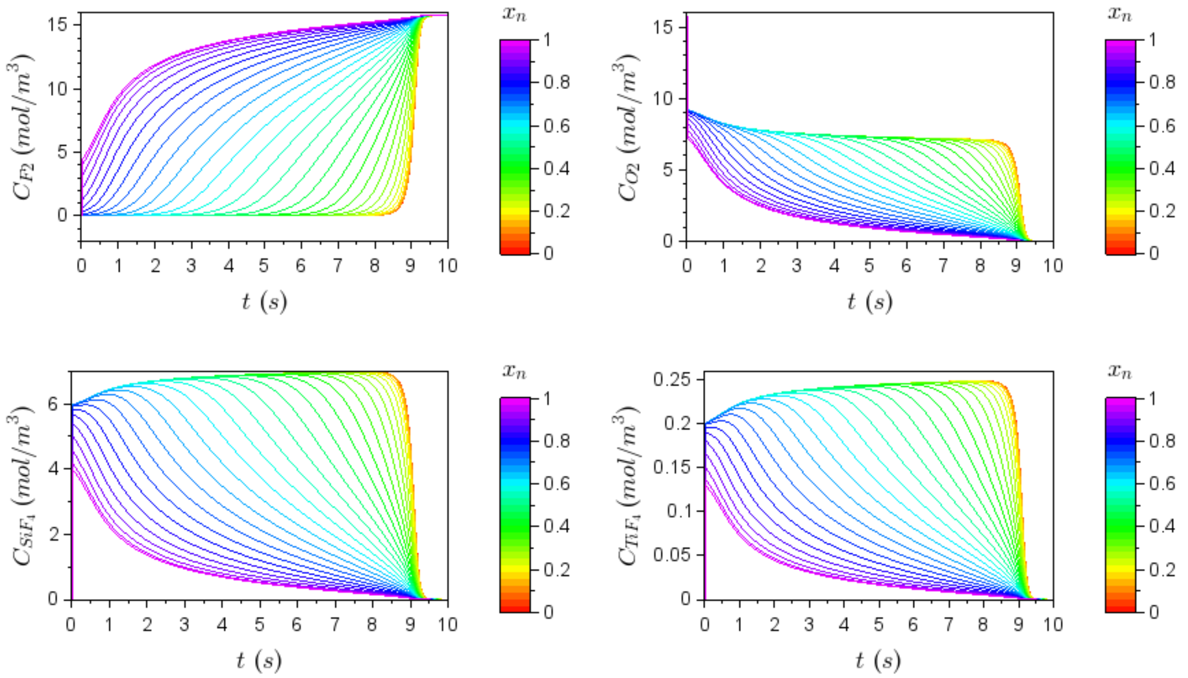

C 131: Effect of particle size = $35x10^{-4}$ m on gas concentrations over time.

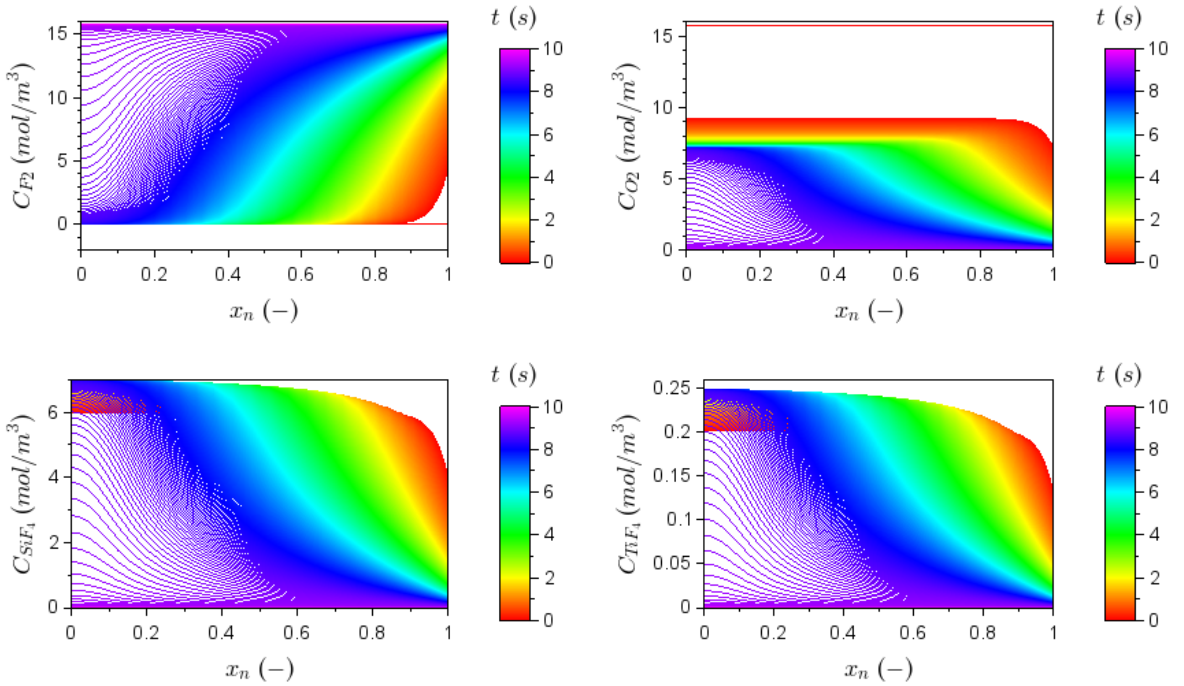

C 132: Effect of particle size = $35x10^{-4}$ m on gas concentrations through the particle.

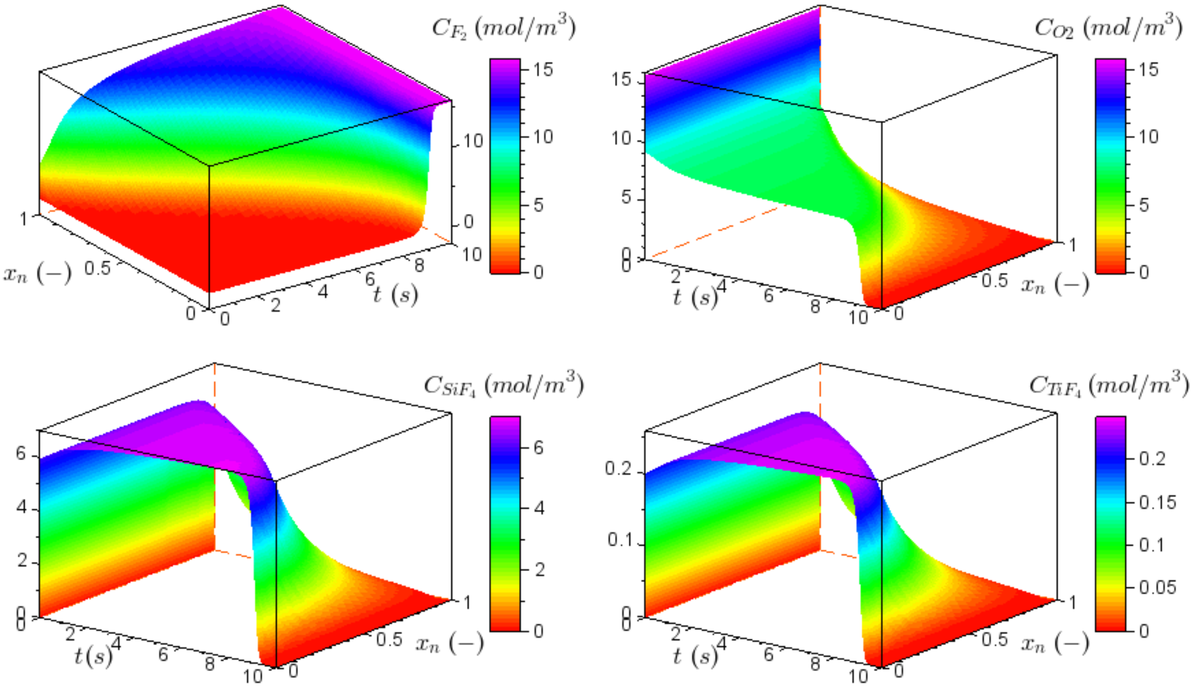

C 133: Surface graphs showing the effect of particle size = 35x10^{-4} m on gas concentrations.

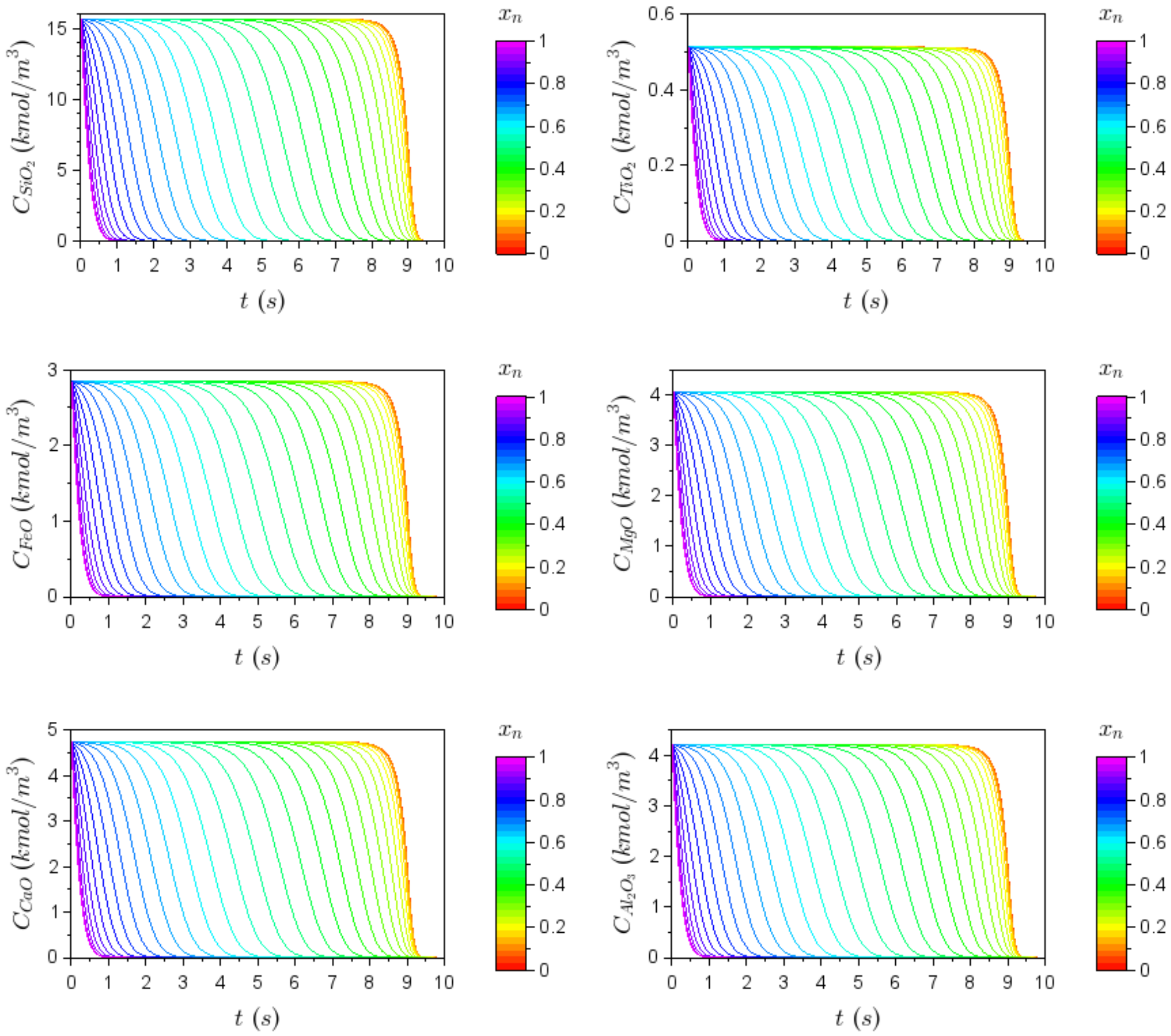

C 134: Effect of particle size = 35x10^{-4} m on solid reactants concentrations over time.

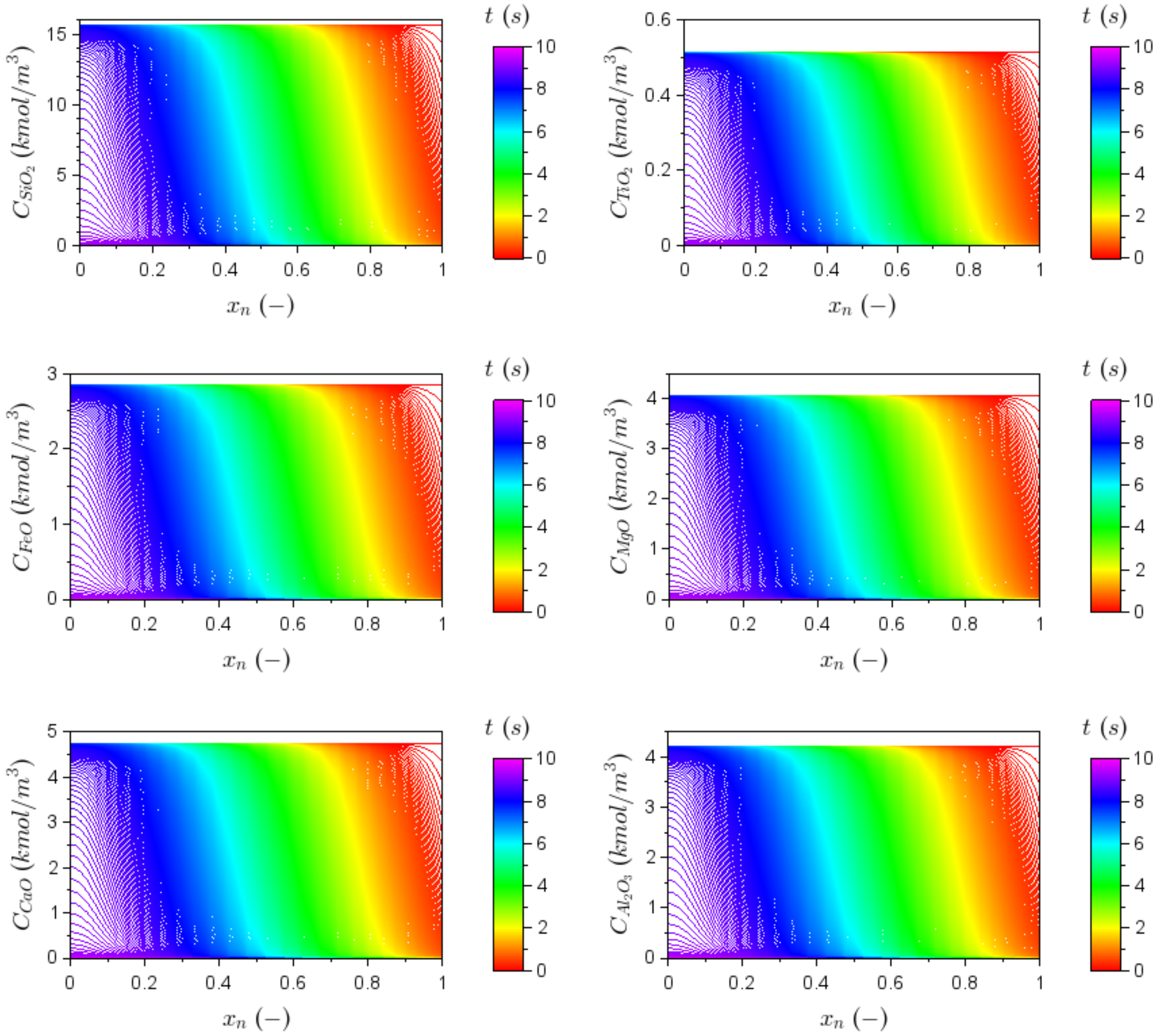

C 135: Effect of particle size = $35x10^{-4}$ m on solid reactants concentrations through the particle.

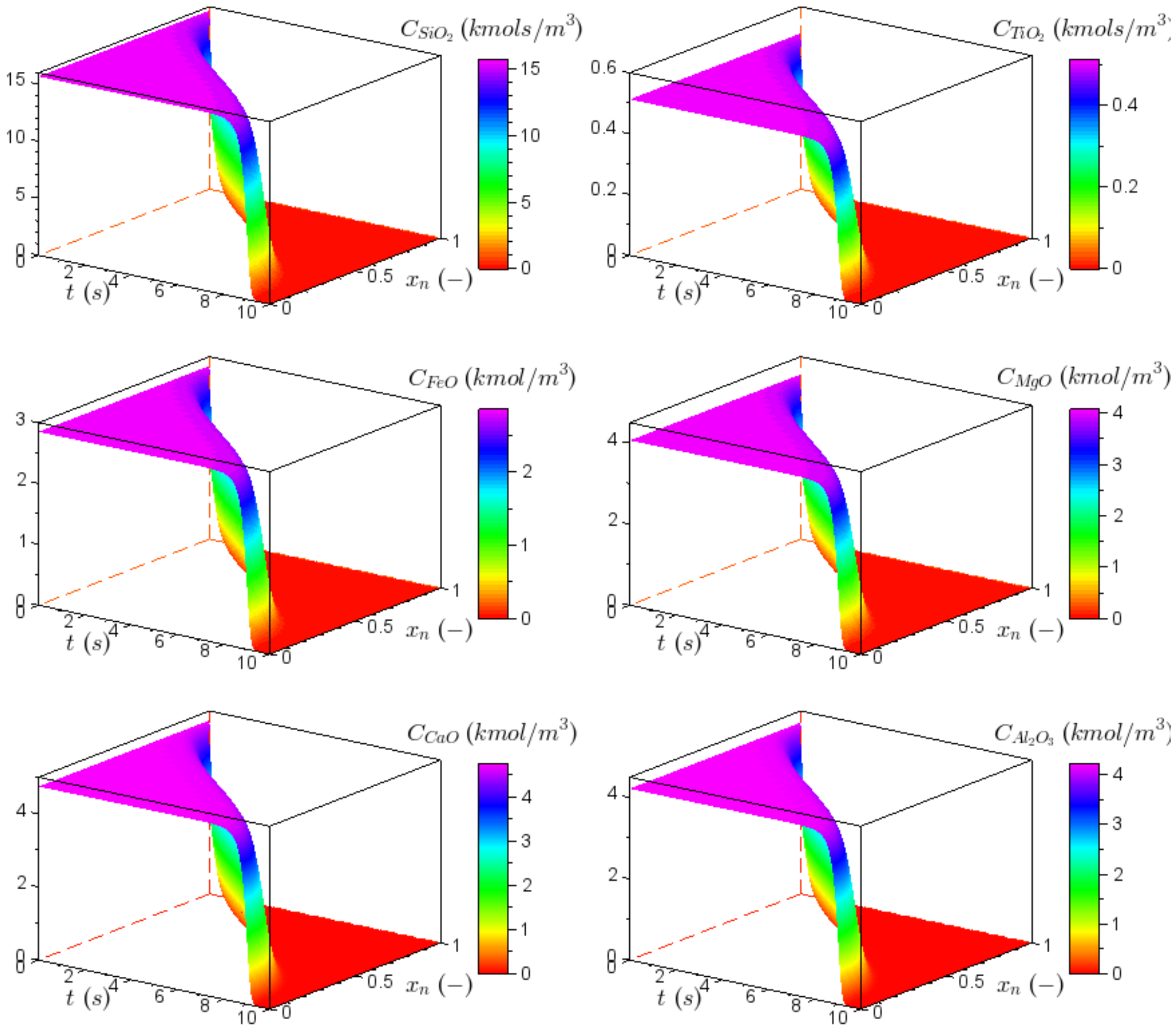

C 136: Surface graphs showing the effect of particle size = $35x10^{-4}$ m on solid reactants concentrations.

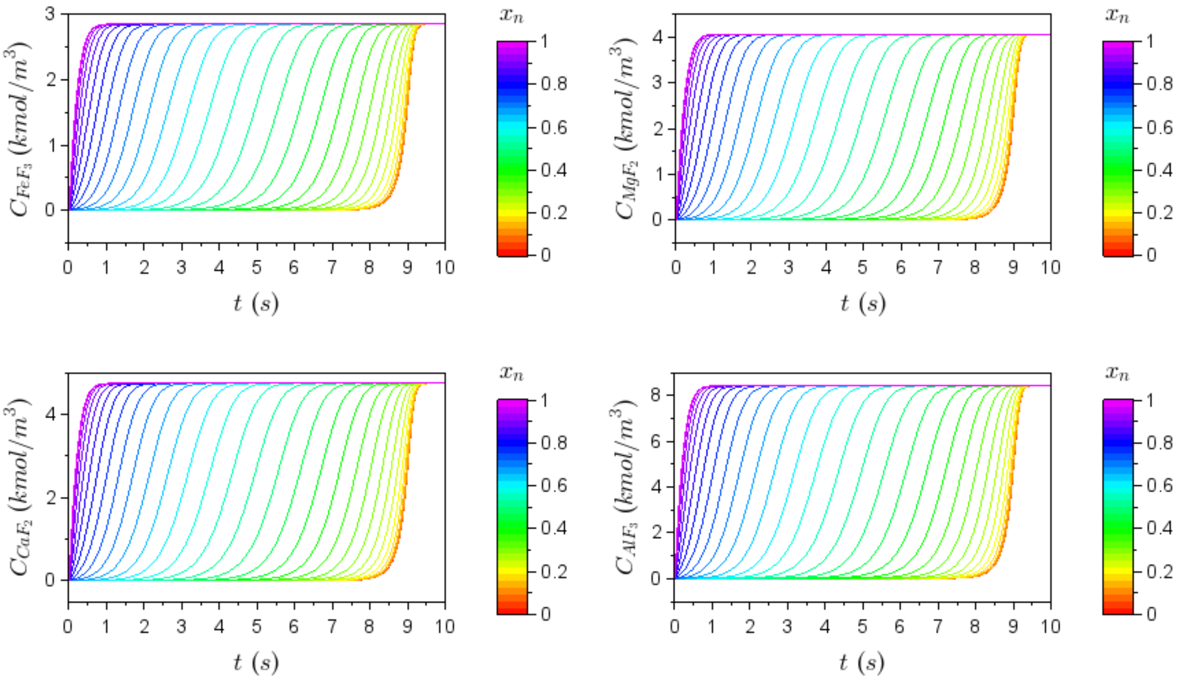

C 137: Effect of particle size = 35x10^{-4} m on solid products concentrations over time.

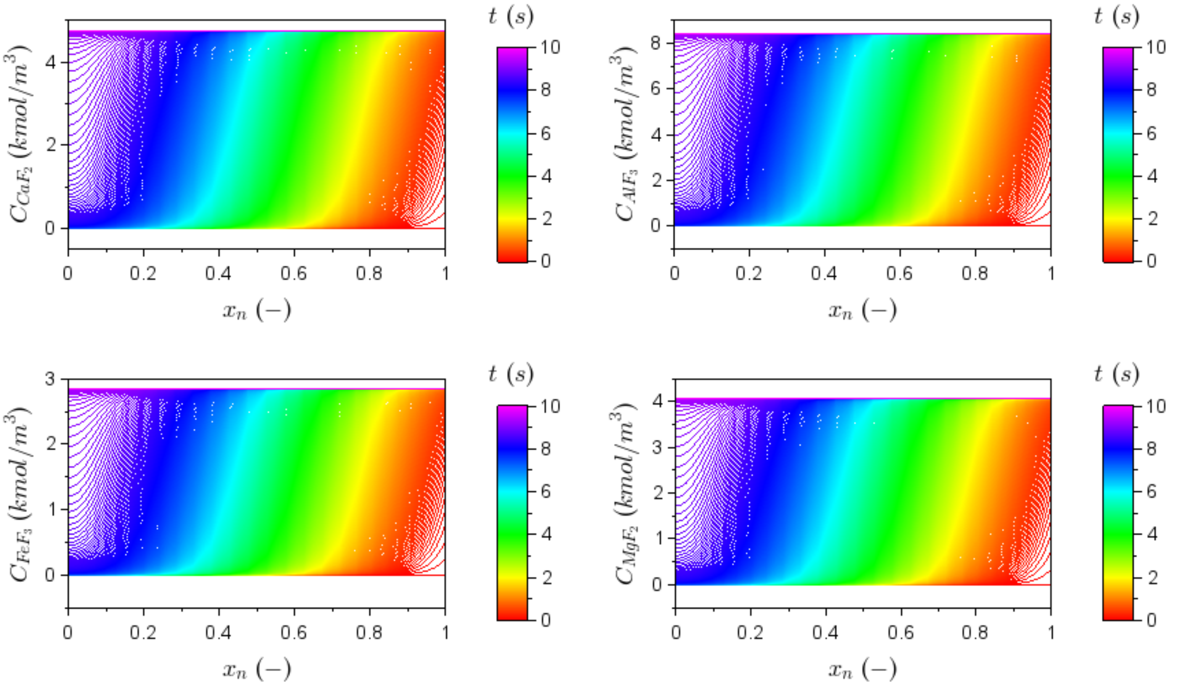

C 138: Effect of particle size = 35x10^{-4} m on solid products concentrations through the particle.

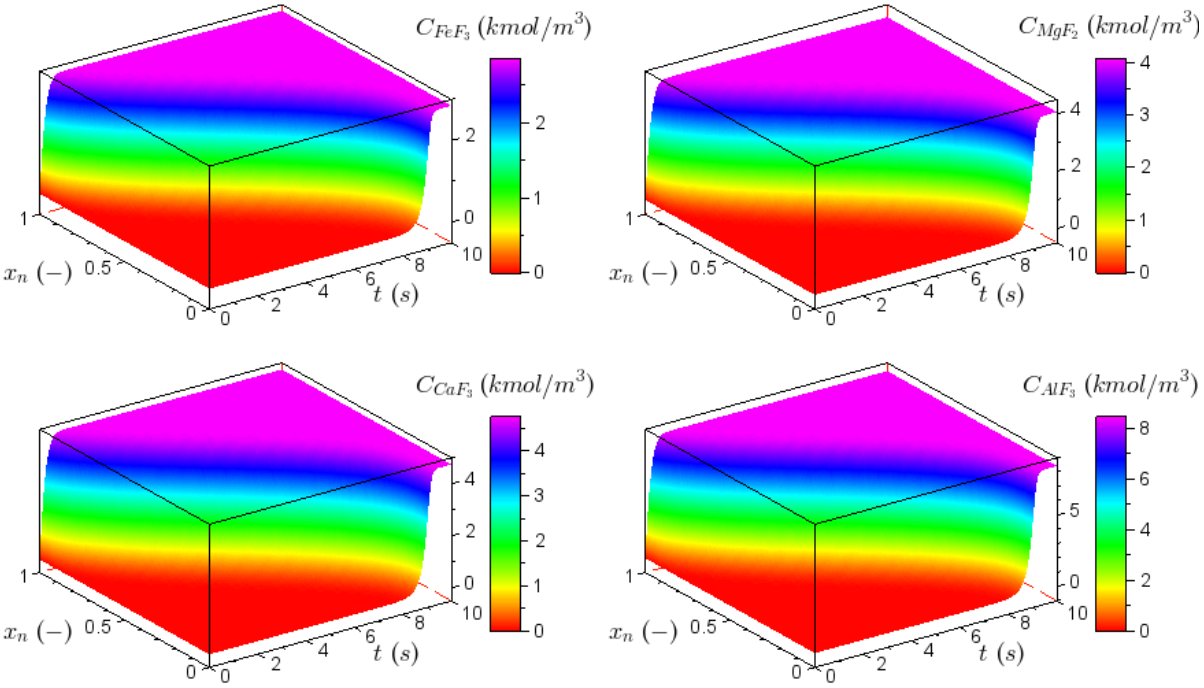

C 139: Surface graphs showing the effect of particle size = 35x10^{-4} m on solid products concentrations.

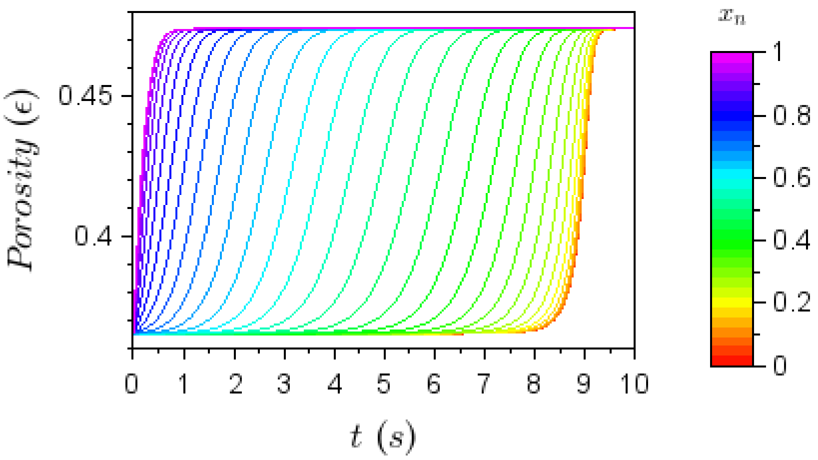

C 140: Effect of particle size = 35x10^{-4} m on porosity over time.

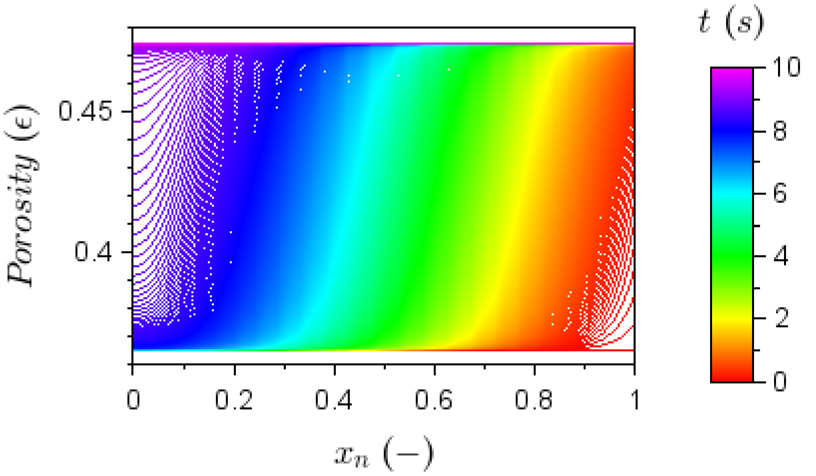

C 141: Effect of particle size = 35x10^{-4} m on porosity through the particle.

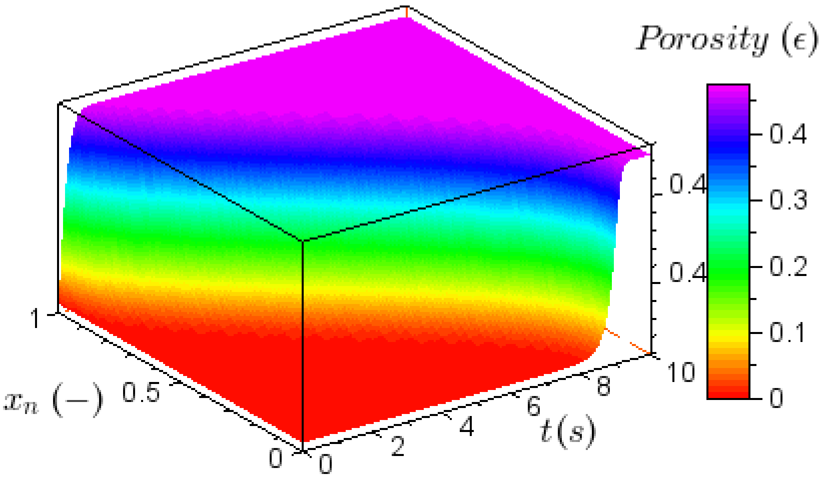

C 142: Surface graphs showing the effect of particle size = 35x10^{-4} m on porosity.

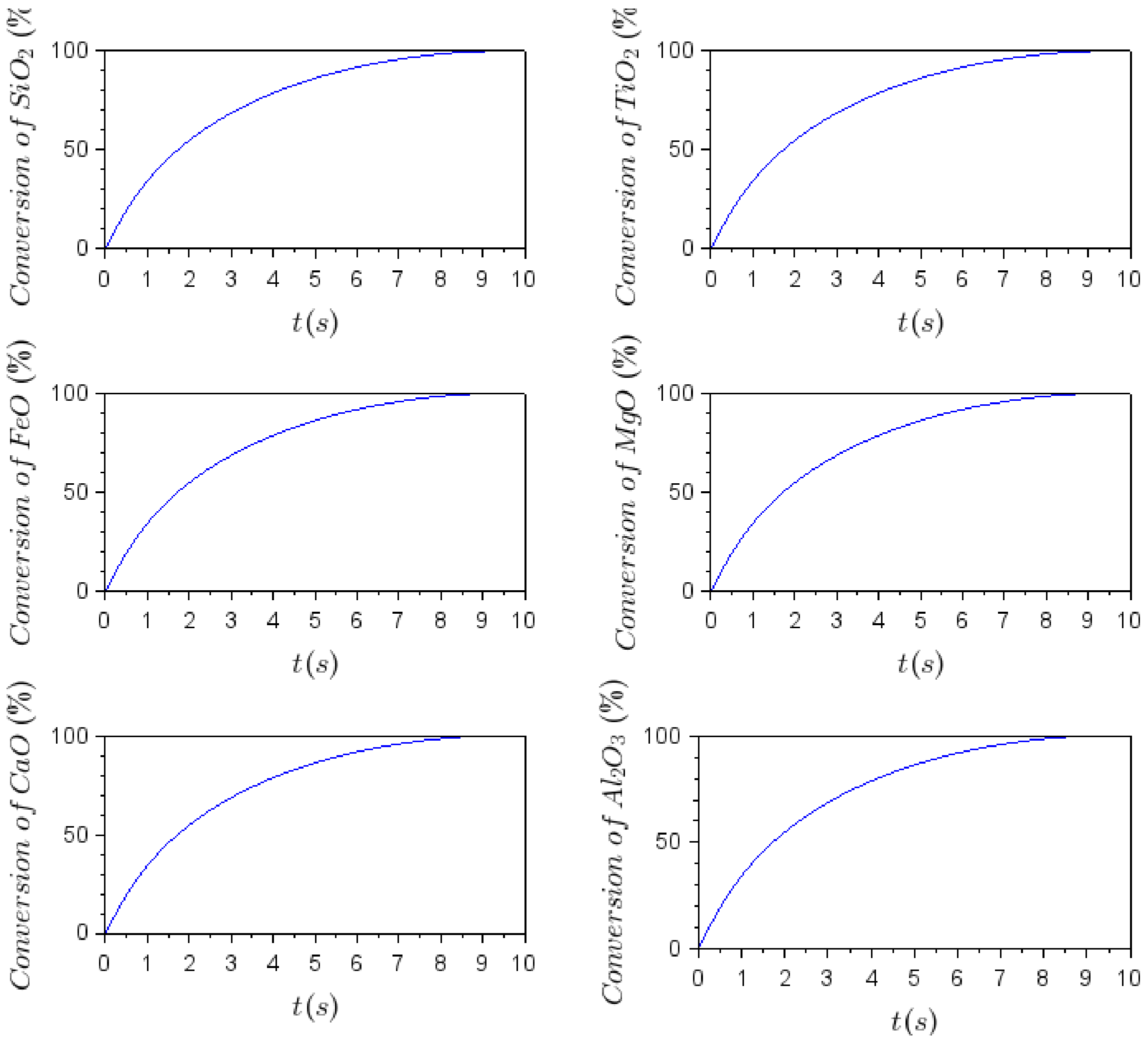

C 143: Effect of particle size = 35x10^{-4} m on conversion over time.

Particle size variation - $R_p = 70\ \mu m$

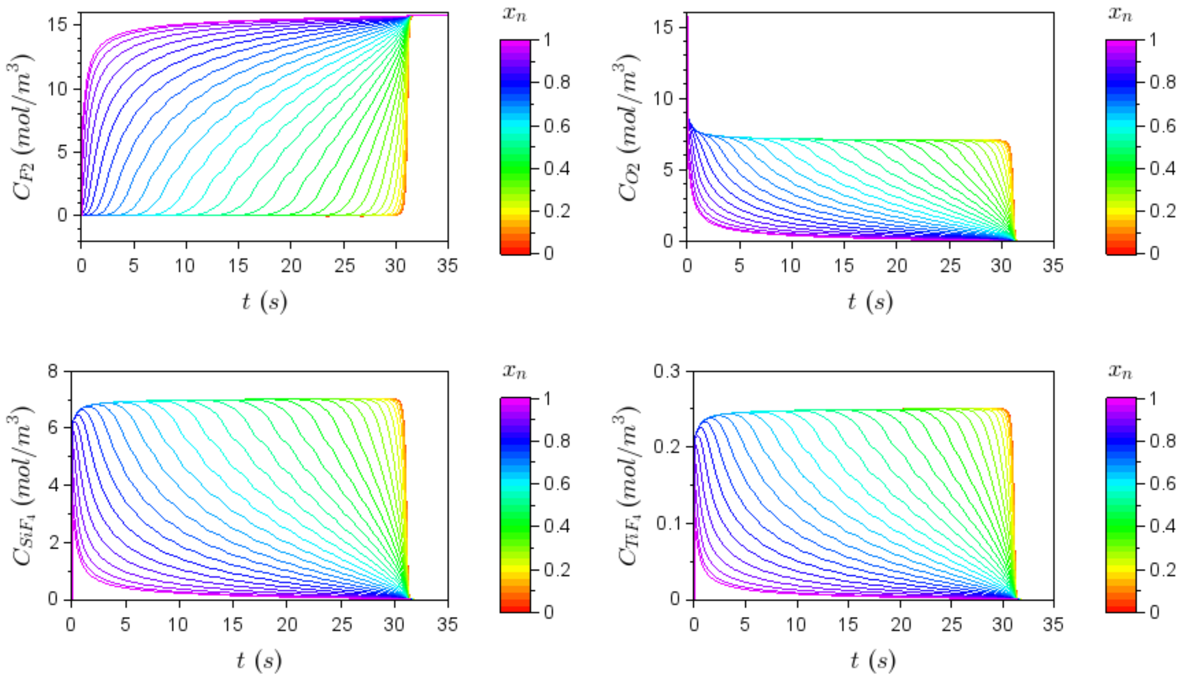

C 144: Effect of particle size = 70x10^{-4} m on gas concentrations over time.

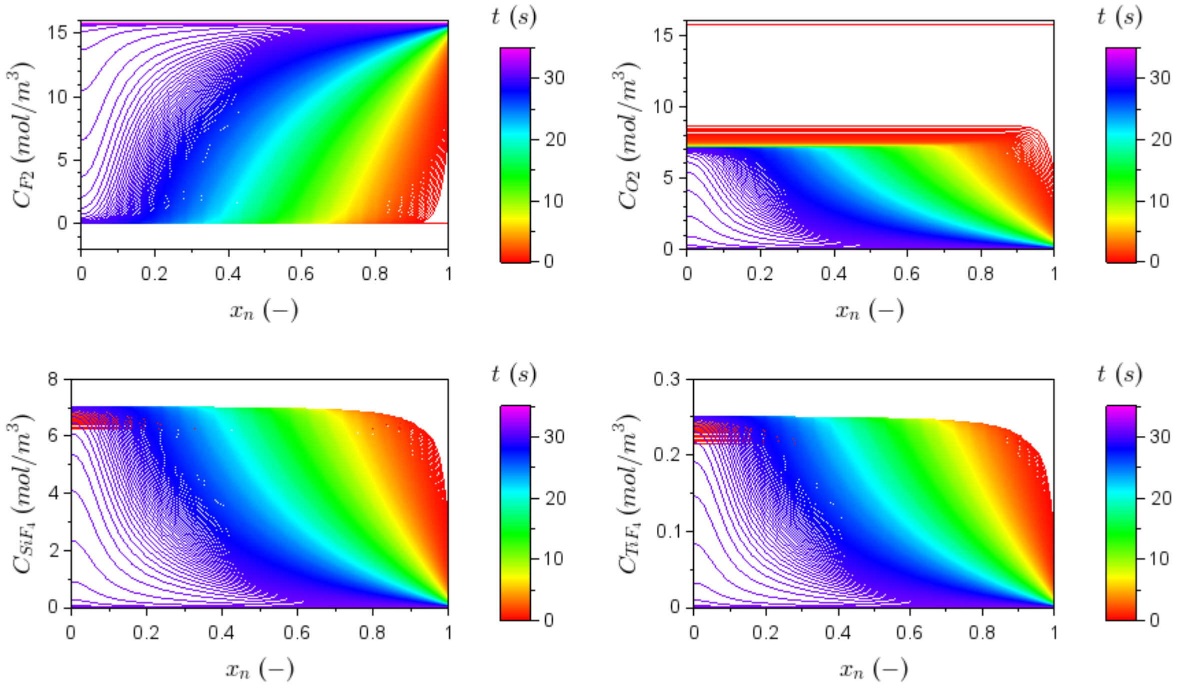

C 145: Effect of particle size = 70x10^{-4} m on gas concentrations through the particle.

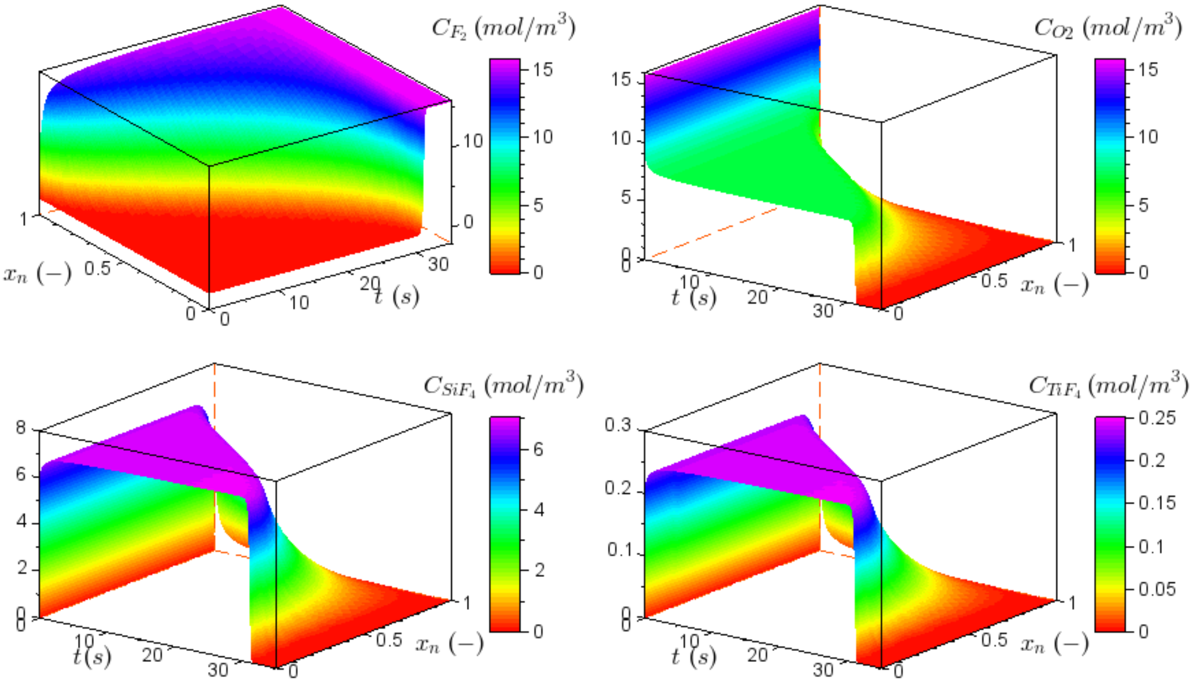

C 146: Surface graphs showing the effect of particle size = $70x10^{-4}$ m on gas concentrations.

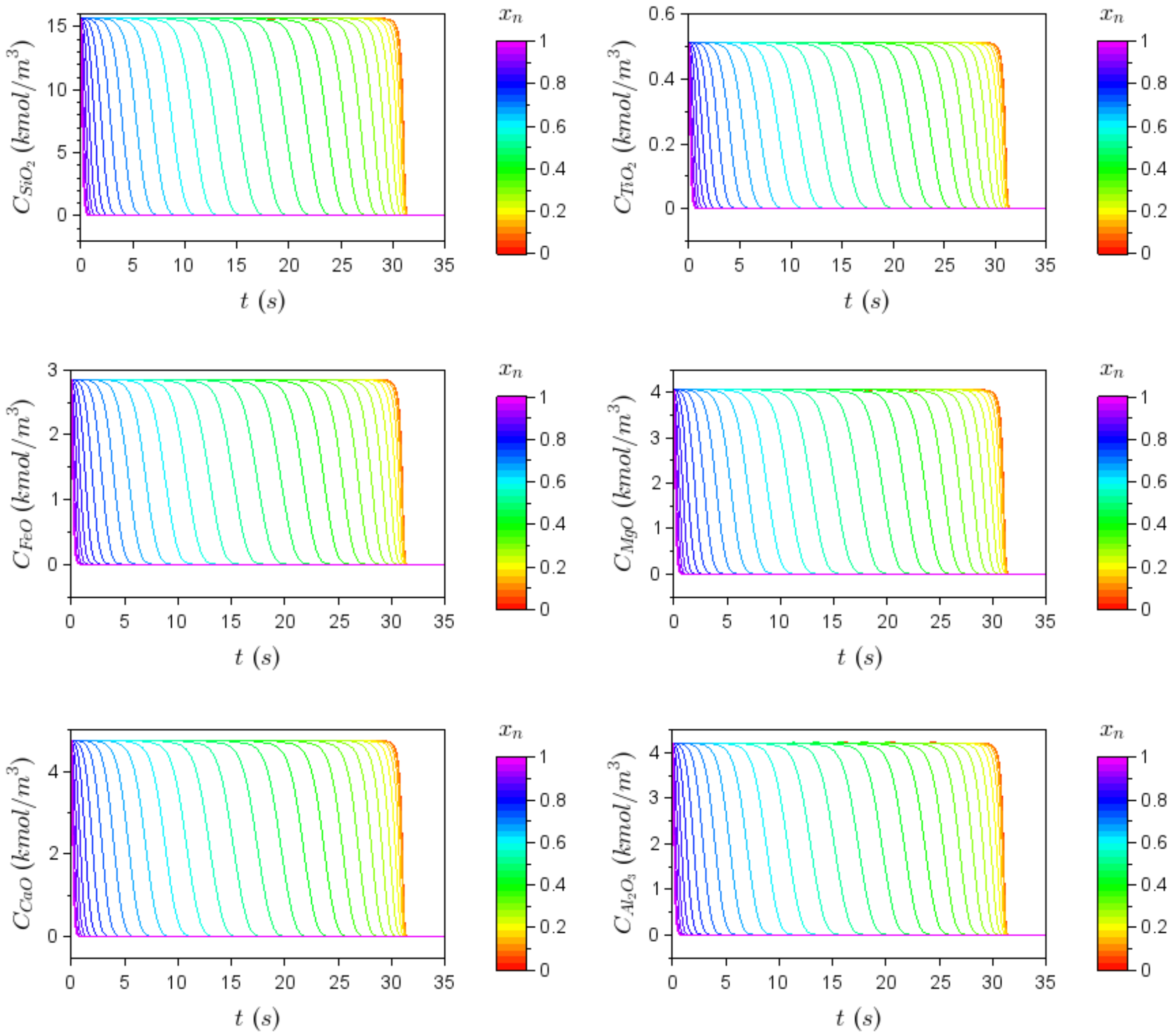

C 147: Effect of particle size = 70x10^{-4} m on solid reactants concentrations over time.

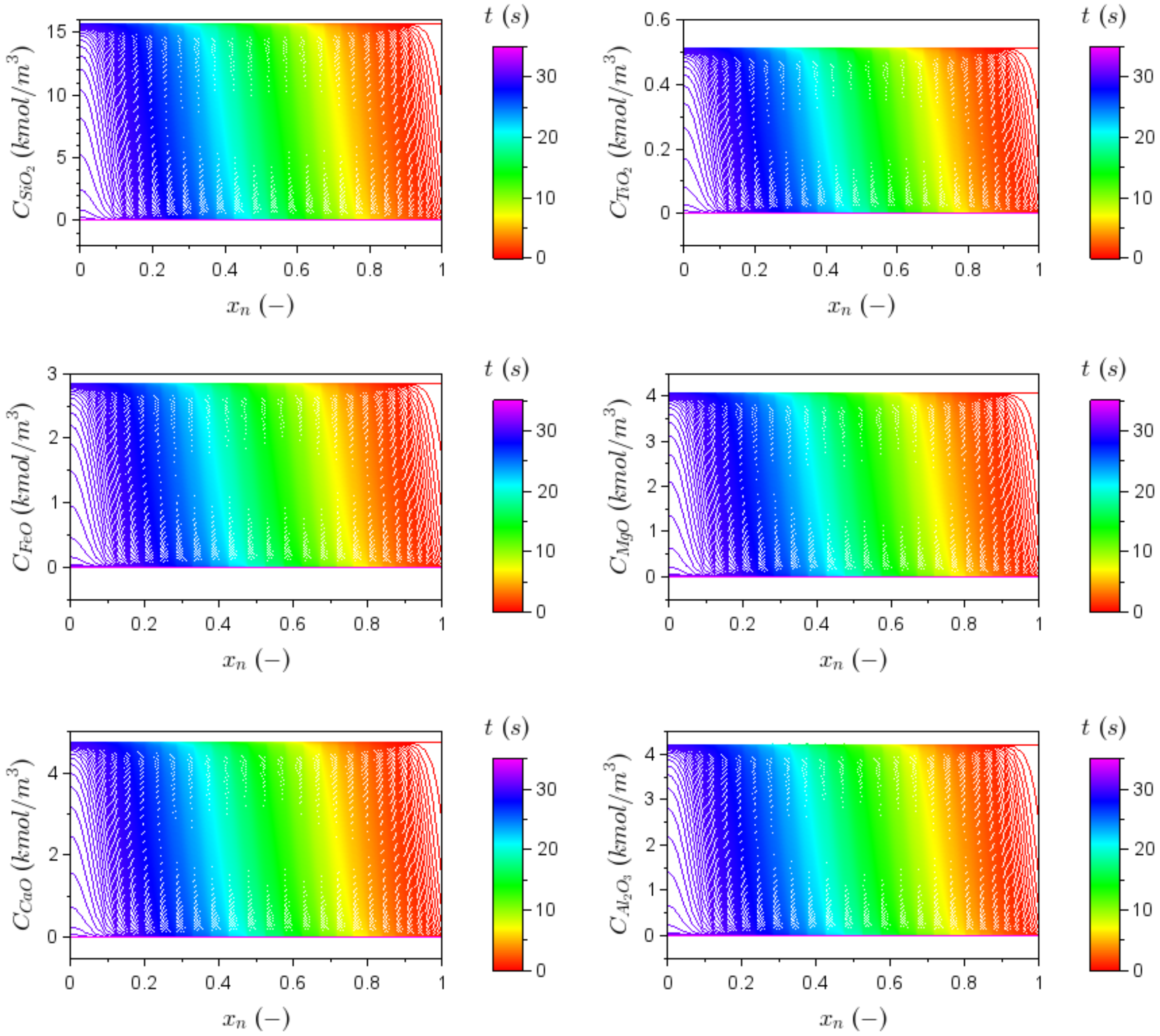

C 148: Effect of particle size = 70x10^{-4} m on solid reactants concentrations through the particle.

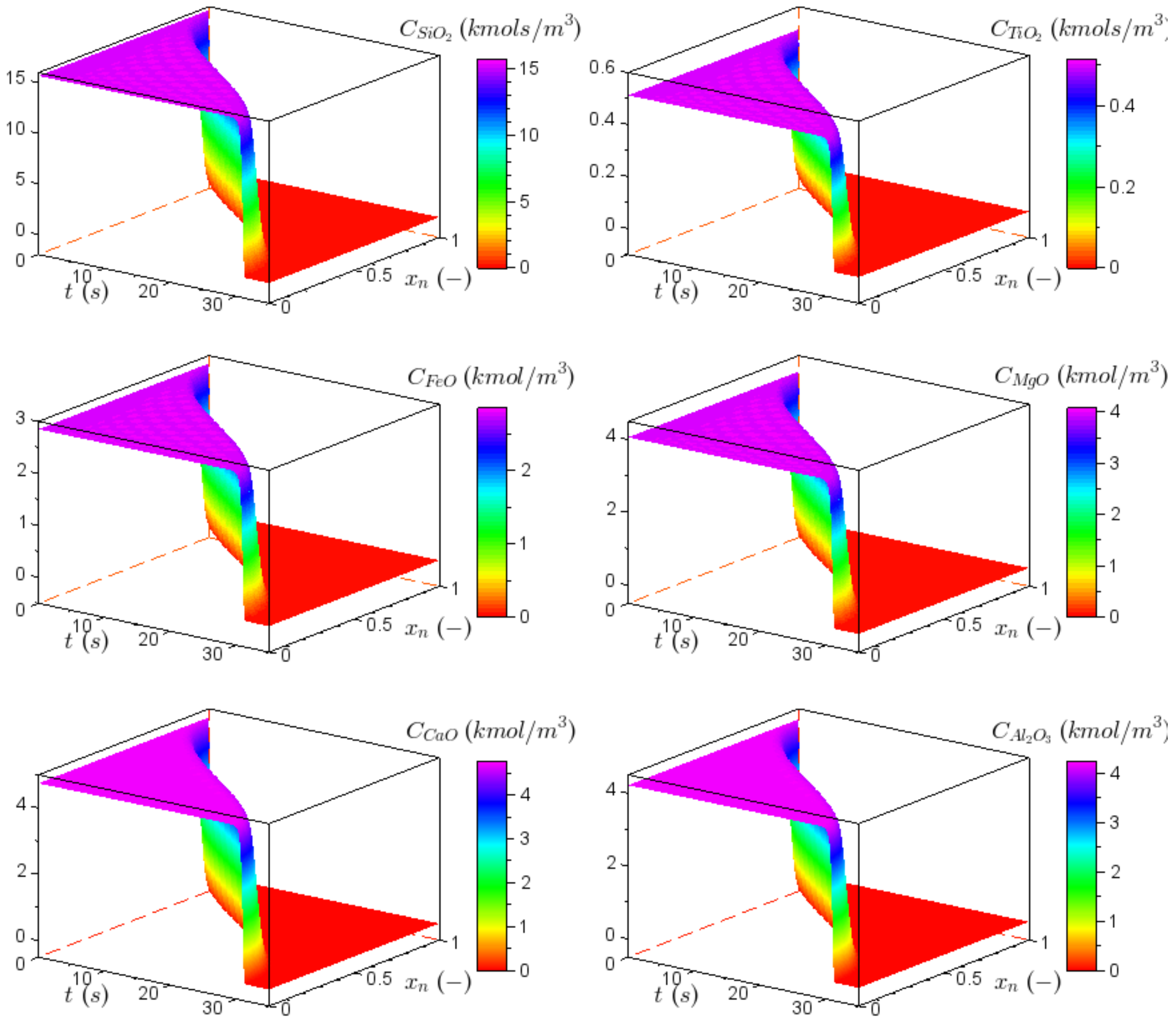

C 149: Surface graphs showing the effect of particle size = 70x10^{-4} m on solid reactants concentrations.

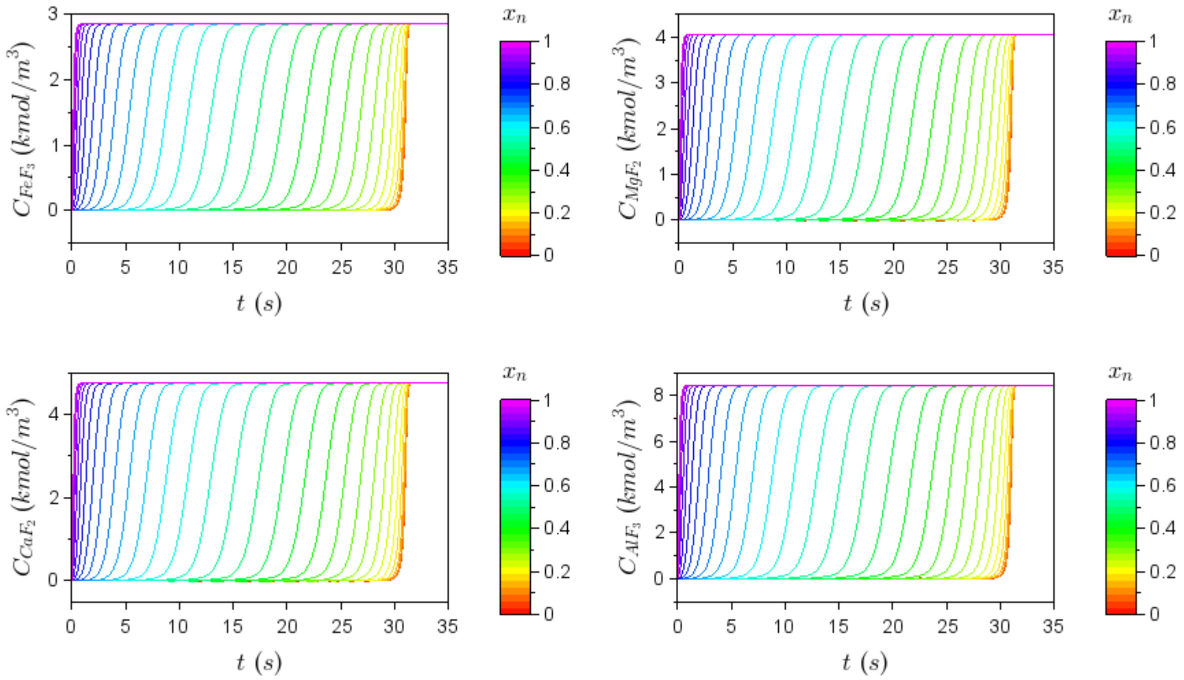

C 150: Effect of particle size = 70x10^{-4} m on solid products concentrations over time.

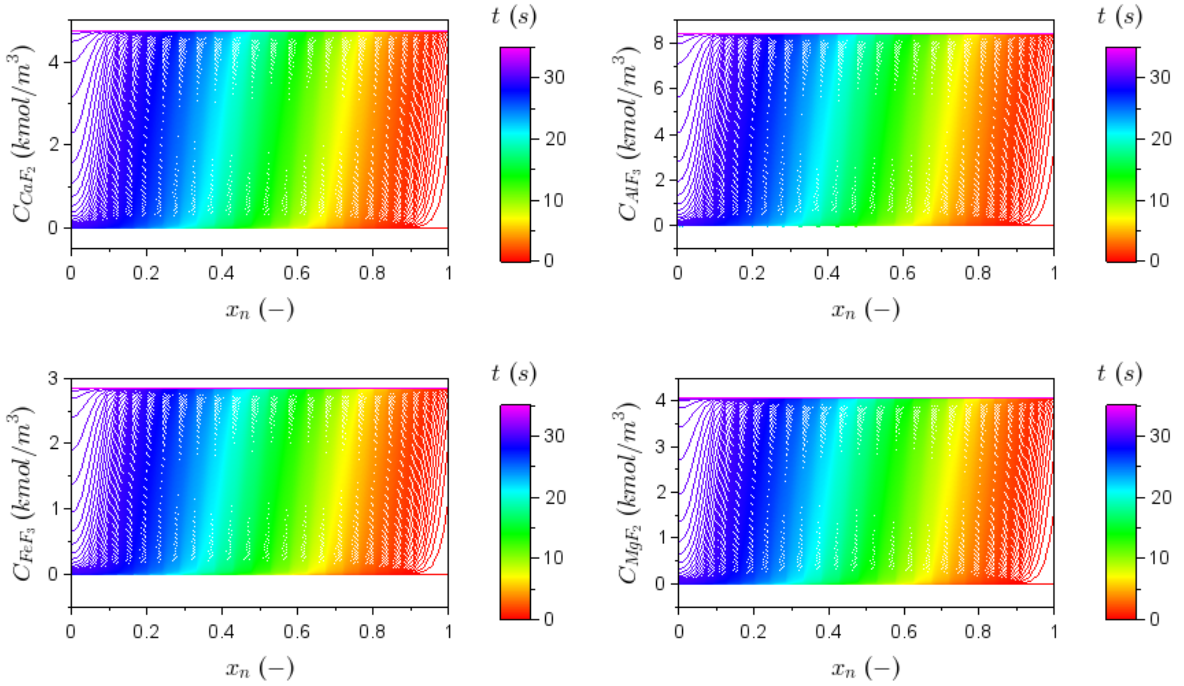

C 151: Effect of particle size = 70x10^{-4} m on solid products concentrations through the particle.

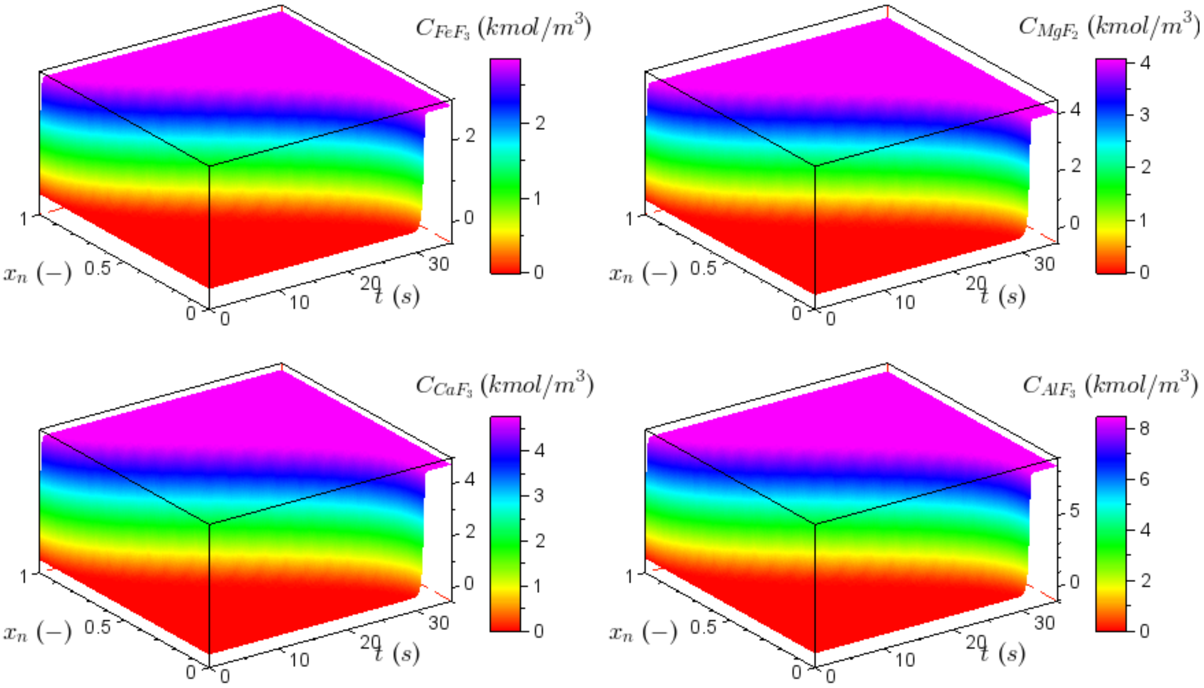

C 152: Surface graphs showing the effect of particle size = 70x10^{-4} m on solid products concentrations.

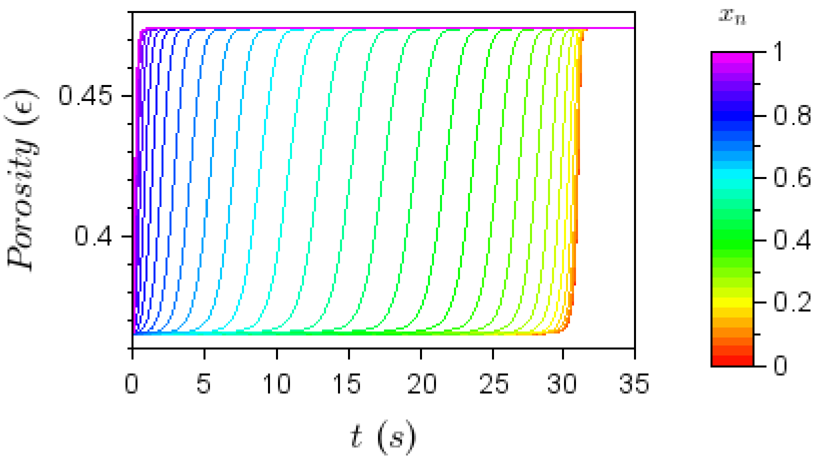

C 153: Effect of particle size = 70x10^{-4} m on porosity over time.

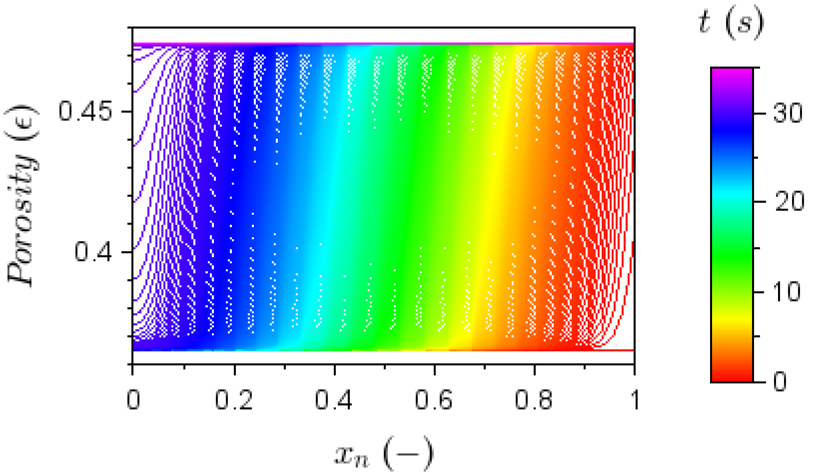

C 154: Effect of particle size = 70x10^{-4} m on porosity through the particle.

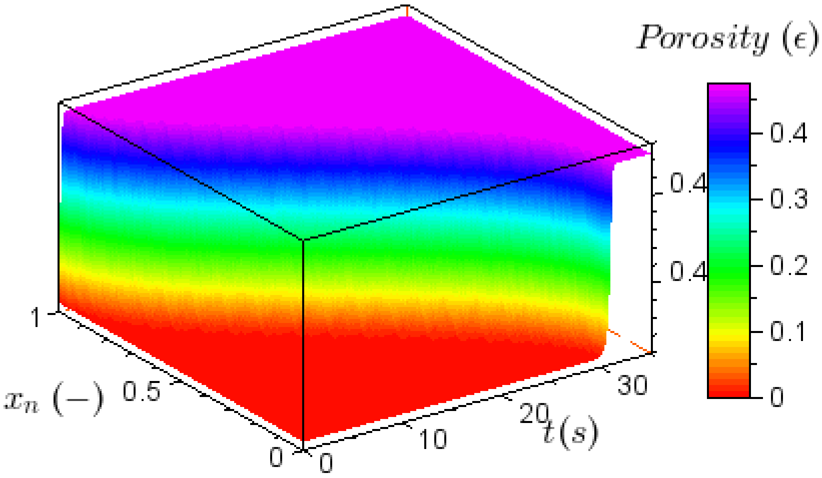

C 155: Surface graphs showing the effect of particle size = 70x10^{-4} m on porosity.

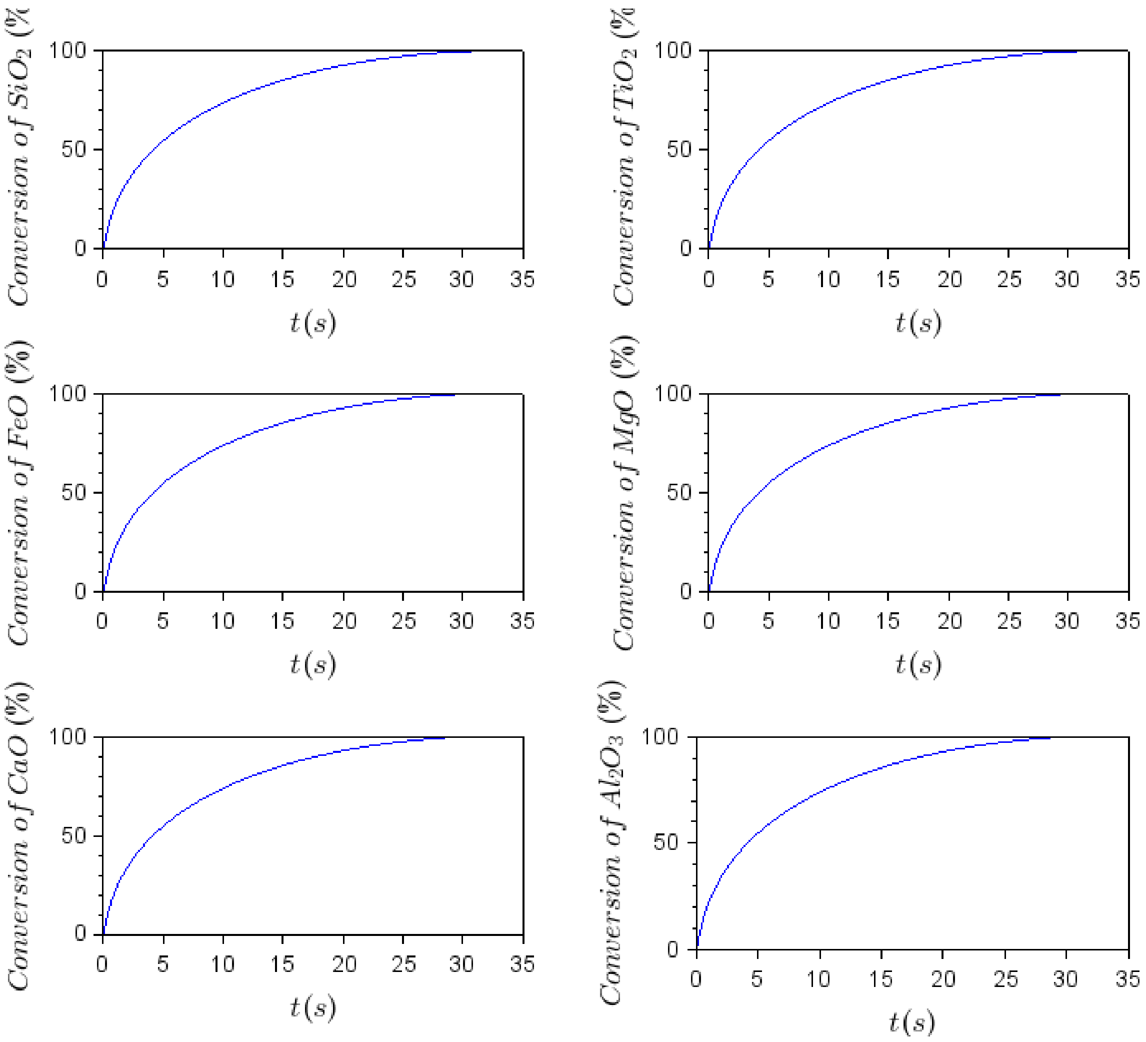

C 156: Effect of particle size = 70x10^{-4} m on conversion over time.

Appendix D – Scilab Code

```
clear;clc()
//---------------------------------------------------------------------------
//simulation of a multi-species reaction of F2 with lunar Regolith
//in a semi-batch fluidised bed reaction system
//---------------------------------------------------------------------------

//collocation constants=====================================================
//load collocation libraries
exec("C:\Users\riddh\OneDrive\Documents\Mphil Thesis\Code\Collocation scripts\colloc.sci",-1)
exec("C:\Users\riddh\OneDrive\Documents\Mphil Thesis\Code\Collocation scripts\dfopr.sci",-1)
exec("C:\Users\riddh\OneDrive\Documents\Mphil Thesis\Code\Collocation scripts\intrp.sci",-1)
exec("C:\Users\riddh\OneDrive\Documents\Mphil Thesis\Code\Collocation scripts\jcobi.sci",-1)
exec("C:\Users\riddh\OneDrive\Documents\Mphil Thesis\Code\Collocation scripts\radau.sci",-1)
//exec("..\Collocation\colloc.sci",-1)
//exec("..\Collocation\dfopr.sci",-1)
//exec("..\Collocation\intrp.sci",-1)
//exec("..\Collocation\jcobi.sci",-1)
//exec("..\Collocation\radau.sci",-1)
//set collocation constants
n=30 //internal collocation points, adjustable depending on profile steepness
n0=1 //include boundary at x=0
n1=1 //include boundary at x=1 (n+2)
al=0 //jacobi polynomial
be=0 //jacobi polynomial
s=2 //spherical geometry
sx=0 //no symmetry
BCincl=%T //include BCs in integration
[An,Bn,wn,xn,dif1]=colloc(n,n0,n1,al,be,s,sx,BCincl)

//Regolith reactor and solid particle ========================================
// Aim: to determine the exit concentration of a semi-batch CSTR reactor
//      which reacts regolith particles with flourine gas to produce gas and
//      solid species, which will be further seperated into constituents, downstream.
// Reaction system is defined as 6 simultaneous reduction reactions. The reaction
// rate is linked to the porosity of the particle
//      SiO2   + 2F2    ->  SiF4  + O2
//      TiO2   + 2F2    ->  TiF4  + O2
//      FeO    + 3/2F2  ->  FeF3  + 0.5O2
//      MgO    + F2     ->  MgF2  + 0.5O2
//      CaO    + F2     ->  CaF2  + 0.5O2
//      Al2O3 + 3F2     ->  2AlF3 + 3/2O2
// yi=[F2,O2,SiF4,TiF4] Gas Species
// ys0=[SiO2, TiO2, FeO, MgO, CaO, Al2O3, FeF3, MgF2, CaF2, AlF3]// Solid species

//====System assumptions====================================================
//  1. Assume no gas-solid surface mass transfer limitations
//  2. The particle holds its shape, the solids are converted into solid
//      metal flourides
//  3. the reaction is 1st order in the gas phase, and 1st order in the solid phase.
//  4. Inner BC condition dC/dx=0
//  5. The exit concentration from the particle is equal to the exit concentration
//      of the reactor because of assumption 1.
//  6. Assume Vp (volume of the particle) and it is constant
//  7. Porosity changes with solid composition
//  8. Perfectly homogeneous mixture of all solids, fluidised bed assumption

//System constants==========================================================
//work in mol/s and mol/m3 units
Rgas=1*0.022414/273.15   //atm, m3, gmol, K
Vr=1                  // Volume of the reactor (m3)
P=1                   // atm
T0=500+273.15         // K constant isothermal reaction, reference temperature
T=T0;                 // reaction temperature
```

```
e0=0.365              // initial porosity estimate
M0=1e6                // assume a basis of solids g (1 tonne of solid)
Q0=10000               // Initial flowrate in m3/s
Ct=P/(Rgas*T0)         // Total gas concentration that stays constant mol/m3
alpha=1000             // time constant for the input step function, Q(t)

//elements
Si=28.085;O=16;Ti=47.867;Fe=55.845;     //elemental molecular weights
Mg=24.305;Ca=40.078;Al=26.982;F=19      //elemental molecular weights

//gas phase species------------------------------------------------------------
names_g=["F_2","O_2","SiF_4","TiF_4"]'  //text
names_gas="$mathsf{"+names_g+"}$"  //latex
Mwtg=[F*2,O*2,Si+F*4,Ti+F*4]'  // molecular weights (g/mol) for gases
yi0=[0,1,0,0]'       //initial composition in the gas phase, pure O2
yi0=yi0/sum(yi0)
nga=length(yi0)     //number of gas species
Cgf=[1, 0, 0, 0]'*Ct  //gas feed composition, pure F2
printf("initial gas composition of the system\n")
printf("name       mol/m3 \n")
printf("%-7s%10.4f\n",names_g,Cgf)

//solid phase species----------------------------------------------------------
names_s=["SiO_2","TiO_2","FeO","MgO","CaO","Al_2O_3","FeF_3","MgF_2","CaF_2","AlF_3"]'
names_solids="$\mathsf{"+names_s+"}$"  //latex
Mwts=[Si+O*2,Ti+O*2,Fe+O,Mg+O,Ca+O,..
      Al*2+O*3,Fe+F*3,Mg+F*2,Ca+F*2,Al+F*3]'  //Molecular weights (g/mol) solids
rhom=[2.65, 4.23, 5.74, 3.58, 3.34, 3.95, 3.87,..
      3.15, 3.18, 2.88]'*1e6  //density of solid species (g/m3)
ym0=[0.46, 0.02, 0.1, 0.08, 0.13, 0.21, 0, 0, 0, 0]'  //initial composition of solid
ym0=ym0/sum(ym0)  //make sure its normalised
ns=length(ym0)   //number of solid species
printf("\nsolid mass fraction\n")
printf("name       weight%% \n")
printf("%-7s%10.6f\n",names_s,ym0)

//particle properties----------------------------------------------------------
Vs=(M0*sum(ym0./rhom))/(1-e0) // volume of solid
Rp=70*(1e-6)/2   // particle radius (m), diameter=70um
Vp=4/3*%pi*Rp^3  //volume of particle
Np=Vs/Vp  //number of particles
printf("\nparticle properties\n")
printf("Volume of solid \t%e\n",Vs)
printf("Particle radius \t%e\n",Rp)
printf("Volme of particle \t%e\n",Vp)
printf("number of particles \t%e\n",Np)

//Knudsen Diffusivity in the particle------------------------------------------
//$Dk=4850*d_{pore}*(T/Mwt)^{0.5}$ where T[K],dpore(cm),Mwt(kg/kmol),Dk(cm2/s)
Tk=T0
dp=1000*1e-8*(1)  //cm, 1000 angstrom (1A=1e-8cm) pore (100 x bigger than a nanopore)
//So the pore diameter actually gets bigger as the reaction proceeds, we need to
//account for that by using the change of porosity like this
//assume that the pores are cylinders, so, Vpore,t = e*Vp = %pi/4*dp^2*R*N
//R is the particle radius, Vp is the particle volume, N number of particles
//re-arrange for dp such : dp(t) = sqrt(4*e(t)*Vp/(R*N*%pi)
//applying between t=0 and t where Vp, R, N are constants
// dp(t)=dp(0)*sqrt(e(t)/e(0))
D=4850*dp*sqrt(Tk./Mwtg)*1e-4  //m2/s
printf("\nKnudsen diffusion coeffients\n")
printf("name\t\tDk(m2/s) \n")
printf("%-7s\t\t%11.3e\n",names_g,D)
DD=(ones(n+2,1)*D')/(Rp^2)  //repeating D/Rp^2, species across, n+2 nodes down
printf("\ndiffusion time constants\n")
printf("name\t\tDk/R^2(/s) \n")
printf("%-7s\t\t%10.4f\n",names_g,DD(1,:)')

//reaction stoichiometric matrices---------------------------------------------
//gas stoich matrix
```

```
nug=[-2 -2 -3/2 -1 -1 -3
    1 1 1/2 1/2 1/2 3/2
    1 0 0 0 0 0
    0 1 0 0 0 0]
//solids stoich matrix
nus=[-1 0 0 0 0 0
     0 -1 0 0 0 0
     0 0 -1 0 0 0
     0 0 0 -1 0 0
     0 0 0 0 -1 0
     0 0 0 0 0 -1
     0 0 1 0 0 0
     0 0 0 1 0 0
     0 0 0 0 1 0
     0 0 0 0 0 2]

//reaction rate term: $ri=k_iC_{F_2}C_{s,i}$------------------------------------
//Calculating reaction rate constant
k1=1;k2=1;k3=1;k4=1;k5=1;k6=1
Ea=50000;  //J/mol, activation energy
K=ones(n+2,1)*[k1 k2 k3 k4 k5 k6]*1*exp(-Ea/8.314*(1/T-1/T0))     // repeating matrix of K
printf("\nreaction rate constants\n")
printf("K(%1i)\t%f\n",(1:6)',K(1,:)')

//initial conditions-------------------------------------------------------------
//must have species across the row and collocation down the column
Cg0=ones(n+2,1)*yi0'*Ct  //gas phase
Cs0=ones(n+2,1)*((M0*ym0')./(Mwts'*Vs)) //solid phase
ne=1  // defines length porosity, one value
e00=e0*ones(n+2,1)  //initial repeating n+2 rows
Ci0=[Cg0 Cs0 e00]  //initial starting vector for DAE solver
dCi0=zeros(n+2,(nga+ns+ne)) //initial starting gradient for DAE solver

//dimensionless constants-------------------------------------------------------
tauR=Vr/Q0  //reactor time constant
tauS=Vs/(Q0*Cgf(1))  //solid time constant
//$\phi=\sqrt{\dfrac{(kC_s)}{(D/R^2)}}$
n_s=1:6  //reacting solids
n_g=1  //reacting gas
KCs=K.*Cs0(:,n_s)
thiele=sqrt(KCs(1,:)'./DD(1,1))  //only reactants needed
printf("\ntime constants for system\n")
printf("tauR=Vr/Q0=%f [s]\n",tauR)
printf("tauS=Vs/(Q0*Cgf(1))=%f [s]\n",tauS)
printf("initial Thiele modulus = sqrt(k*Cs*R^2/D)),\nworst case, Cs gets smaller with time\n")
printf("%s\t\tD(%s)\n","names","Thiele(F2)")
printf("%s\t\t%f\n",names_s,thiele)
//only apply to solid reactions with F2
//some notes on the thiele ranges and collocation
//  1.  thiele <0.1 no diffusion limitations on the reaction,
//      flat profiles, few collocation points needed, <=5
//  2.  thiele >100 strong diffusion limitations on the reaction,
//      very steep profiles, many collocation points needed, max 50
//  3.  0.1<thiele<100, varying diffusion limitations,
//      around 15 - 25 collocation points
//choose even numbers, as the symmetric BC, dC/dr=0 requires even powers in x

//the model equations===============================================================
//function terms that are constants
//the 2/x^2 term, constant across, varies down with collocation
x=[1;(2)./xn(2:n+1);0]
X=repmat(x,[1,4]) //same shape as Cgi
wx2=3*xn.^2.*wn  //gaussian integration coefficient, 3*wn*xn^2 in Rave=sum(wx2*Rg)
mrho=(Mwts./rhom)  //solid phase Mwt/density
//printf("wx2=",wx2)
ones_nga=ones(1,nga)

//reactor functions-------------------------------------------------------------
function [f, ires]=reactor(t, Ci, dCi)
```

```
    Ci=matrix(Ci,n+2,(nga+ns+ne)) //convert vector Ci into a matrix[1:n+2,nga+ns+ne]
    Cg=Ci(:,1:nga)                //Gas concentrations
    Cs=Ci(:,nga+1:ns+nga)         //Solid concentrations
    e=Ci(:,(ns+nga)+1)            //porosity
    dCi=matrix(dCi,2+n,(nga+ns+ne)) //convert dCi into a matrix[1:n+2,nga+ns+ne]
    dCg=dCi(:,1:nga)              //Gas concentrations
    dCs=dCi(:,nga+1:ns+nga)       //Solid concentrations
    de=dCi(:,(ns+nga)+1)          //porosity
    rj=K.*(Cg(:,1)*ones(1,6)).*(Cs(:,1:6)) //reaction rates at every collocation
                                  //point and for every reaction
    //reaction rates
    Rg=rj*nug'  //gas phase species reaction rate
    Rs=rj*nus'  //solid phase species reaction rates
    Rave=Rg'*wx2   //gas phase average reaction rates
    //flow rates
    Qt=Q0*(1-exp(-alpha*t^2))  //volume feed rate, step up function
    Q=Qt+(1/Ct)*sum(Rave)*Vs  //exit gas rate
    //gas phase particle balances, includes wrong boundary points
    ett=e*ones_nga
    dett=de*ones_nga
    f1=(DD.*((ett.*(Bn*Cg))+((ett.*X).*(An*Cg))+((An*ett).*(An*Cg))))..
      +Rg-(ett.*dCg)-(Cg.*(dett))
    //correction for boundary points
    f1(1,:)=An(1,:)*Cg  //central boundary, replace first row, n=1
//    $CSTR=(Q_t*C_{gf})-(Q*C_{g(n+2,:)})+(R_{ave}*V_p)'-(V_r*dC_{g(n+2,:)})$ //
    f1(n+2,:)=(Qt*Cgf')-(Q*Cg(n+2,:))+(Rave*Vs)'-(Vr*dCg(n+2,:))  //CSTR balance
                                          //replaces last row, n+2
    f2=Rs-dCs  //solids balance
    f3=e-(1-(Cs*mrho)) //porosity e equations
    f=[matrix(f1,nga*(n+2),1);matrix(f2,ns*(n+2),1);f3] //convert f to vector
                                          //the same shape as Ci
    ires=0
endfunction
function f=surfx(t, Ca)
    //this is a dummy function, it does nothing, but you need ng=0 and
    //then nn=0 on output
endfunction
ng=0

//DAE solver====================================================================
//initial values in vector form
Ci0=matrix(Ci0,(nga+ns+ne)*(n+2),1)
dCi0=matrix(dCi0,(nga+ns+ne)*(n+2),1)
atol=1e-6
rtol=1e-6
t=linspace(0,1,400)'  //linear time steps
nt=length(t)
alpha=3/(t($)/1000)^2  //target at first 0.1% of the time window
                   // is 1-exp(-3)=1-exp(-alpha*t(2)^2)
tic()
[y,nn]=dasrt([Ci0,dCi0],t(1),t,atol,rtol,reactor,ng,surfx)
disp("runtime="+string(toc()))
y=y'

//Extracting the data
tt=y(:,1)  // time matrix, seconds
Cg=y(:,2:(nga*(n+2))+1)  //gases blocks: (n+2) columns, n time rows
Cs=y(:,(nga*(n+2))+2:((ns+nga)*(n+2))+1)  //solids blocks: (n+2) columns, n time rows
e=y(:,(ns+nga)*(n+2)+2:(nga+ns+ne)*(n+2)+1)  //porosity block: (n+2) column vs t rows
Qt=Q0*(1-exp(-alpha*t^2))// this is the feed, you need Q, the exit flow rate to get
// the mass flow rate of products.
//get rj, get Rg, get Rave, get Q
//K: ones(length(t),1)*matrix(K,1,length(K))  The K matrix
//cols=collocation points, rows=time
//C(F2)*Cs: for each reaction at each collocation point for all time
//((ones(1,6).*.Cg(:,1:n+2))).*Cs(:,1:(n+2)*6)
rj=(ones(length(t),1)*matrix(K,1,length(K))).*((ones(1,6).*.Cg(:,1:n+2))).*Cs(:,1:(n+2)*6)

for i=1:nt
```

```
    Cgg=matrix(Cg(i,:),n+2,nga)
    Css=matrix(Cs(i,:),n+2,ns)
    rj=K.*(Cgg(:,1)*ones(1,6)).*(Css(:,1:6))
    Rg=rj*nug'  //gas phase species reaction rate
    Rs=rj*nus'  //solid phase species reaction rates
    Rave=Rg'*wx2   //gas phase average reaction rates
    //flow rates
    Qtt=Q0*(1-exp(-alpha*t(i)^2))  //volume feed rate, step up function
    Q(i)=Qtt+(1/Ct)*sum(Rave)*Vs  //exit gas rate
end

//=======conversion calculations=============
//solids $X_i=1-(C_{i,ave}/C_{i,0 ave})$
XSiO2=(1-((Cs(:,1:n+2)*wx2)/Cs0(1,1)))*100
XTiO2=(1-((Cs(:,(n+2)+1:(n+2)*2)*wx2)/Cs0(1,2)))*100
XFeO=(1-((Cs(:,2*(n+2)+1:(n+2)*3)*wx2)/Cs0(1,3)))*100
XMgO=(1-((Cs(:,3*(n+2)+1:(n+2)*4)*wx2)/Cs0(1,4)))*100
XCaO=(1-((Cs(:,4*(n+2)+1:(n+2)*5)*wx2)/Cs0(1,5)))*100
XAl2O3=(1-((Cs(:,5*(n+2)+1:(n+2)*6)*wx2)/Cs0(1,6)))*100

printf("\n\n")
//======================================================================================
===
//plotting the data
//======================================================================================
===

//------------------------------------
//2D plots, C vs t at each x-position
//------------------------------------
posix=string(int(xn*1000)/1000)
cmap=rainbowcolormap(n+2)//plotting colloc points
fig=scf(1);
clf
printf("%s\n","figure "+string(gcf().figure_id))
drawlater()
fig.figure_size = [900 650]
fig.children.font_size = 4
fig.color_map=cmap
logflag="nnn"
subplot(2,2,1)
    plot(logflag,tt,Cg(:,1:n+2),"color",cmap)
    xlabel("$t \;(s)$",'fontsize',4)
    ylabel("$C_F_2 \;(mol/m^3)$",'fontsize',4)
    gca().tight_limits = ["off","off","off"]
    gca.font_size = 3
    colorbar(0,1,[1 n+2])
    gce().title.text="$x_n$"
    gce().font_size=3
    gce().title.font_size=4
subplot(2,2,2)
    plot(logflag,tt,Cg(:,(n+2)+1:(n+2)*2),"color",cmap)
    xlabel("$t \;(s)$",'fontsize',4)
    ylabel("$C_O_2 \;(mol/m^3)$",'fontsize',4)
    gca().tight_limits = ["off","off","off"]
    gca.font_size = 3
    colorbar(0,1,[1 n+2])
    gce().title.text="$x_n$"
    gce().font_size=3
    gce().title.font_size=4
subplot(2,2,3)
    plot(logflag,tt,Cg(:,2*(n+2)+1:(n+2)*3),"color",cmap)
    xlabel("$t \;(s)$",'fontsize',4)
    ylabel("$C_{SiF_4 }\;(mol/m^3)$",'fontsize',4)
    gca().tight_limits = ["off","off","off"]
    gca.font_size = 3
    colorbar(0,1,[1 n+2])
    gce().title.text="$x_n$"
    gce().font_size=3
```

```
    gce().title.font_size=4
subplot(2,2,4)
    plot(logflag,tt,Cg(:,3*(n+2)+1:(n+2)*4),"color",cmap)
    xlabel("$t \;(s)$",'fontsize',4)
    ylabel("$C_{TiF_4} \;(mol/m^3)$",'fontsize',4)
    gca().tight_limits = ["off","off","off"]
    gca.font_size = 3
    colorbar(0,1,[1 n+2])
    gce().title.text="$x_n$"
    gce().font_size=3
    gce().title.font_size=4
drawnow()
xs2png(gcf().figure_id,"C:\Users\riddh\OneDrive\Desktop\plots v1.0\"+string(gcf().figure_id)+" Gas concentrations vs t.png");

fig=scf(2);
clf
printf("%s\n","figure "+string(gcf().figure_id))
drawlater()
fig.figure_size = [900 650]
fig.children.font_size = 4
fig.color_map=cmap
logflag="nnn"
subplot(2,2,1)
    plot(logflag,tt,Cs(:,1:n+2)/1000,"color",cmap)
    xlabel("$t \;(s)$",'fontsize',4)
    ylabel("$C_{SiO_2} \;(kmol/m^3)$",'fontsize',4)
    gca().tight_limits = ["off","off","off"]
    gca.font_size = 3
    colorbar(0,1,[1 n+2])
    gce().title.text="$x_n$"
    gce().font_size=3
    gce().title.font_size=4
subplot(2,2,2)
    plot(logflag,tt,Cs(:,(n+2)+1:(n+2)*2)/1000,"color",cmap)
    xlabel("$t \;(s)$",'fontsize',4)
    ylabel("$C_{TiO_2} \;(kmol/m^3)$",'fontsize',4)
    gca().tight_limits = ["off","off","off"]
    gca.font_size = 3
    colorbar(0,1,[1 n+2])
    gce().title.text="$x_n$"
    gce().font_size=3
    gce().title.font_size=4
subplot(2,2,3),
    plot(logflag,tt,Cs(:,2*(n+2)+1:(n+2)*3)/1000,"color",cmap)
    xlabel("$t \;(s)$",'fontsize',4)
    ylabel("$C_{FeO} \;(kmol/m^3)$",'fontsize',4)
    gca().tight_limits = ["off","off","off"]
    gca.font_size = 3
    colorbar(0,1,[1 n+2])
    gce().title.text="$x_n$"
    gce().font_size=3
    gce().title.font_size=4
subplot(2,2,4)
    plot(logflag,tt,Cs(:,3*(n+2)+1:(n+2)*4)/1000,"color",cmap)
    xlabel("$t \;(s)$",'fontsize',4)
    ylabel("$C_{MgO} \;(kmol/m^3)$",'fontsize',4)
    gca().tight_limits = ["off","off","off"]
    gca.font_size = 3
    colorbar(0,1,[1 n+2])
    gce().title.text="$x_n$"
    gce().font_size=3
    gce().title.font_size=4
drawnow()
xs2png(gcf().figure_id,"C:\Users\riddh\OneDrive\Desktop\plots v1.0\"+string(gcf().figure_id)+" solid concentrations vs t
a.png")

fig=scf(3)
clf
printf("%s\n","figure "+string(gcf().figure_id))
```

```
drawlater()
fig.figure_size = [900 650/1.67]
fig.children.font_size = 4
fig.color_map=cmap
logflag="nnn"
subplot(1,2,1)
    plot(logflag,tt,Cs(:,4*(n+2)+1:(n+2)*5)/1000,"color",cmap)
    xlabel("$t \;(s)$",'fontsize',4)
    ylabel("$C_{CaO} \;(kmol/m^3)$",'fontsize',4)
    gca().tight_limits = ["off","off","off"]
    gca.font_size = 3
    colorbar(0,1,[1 n+2])
    gce().title.text="$x_n$"
    gce().font_size=3
    gce().title.font_size=4
subplot(1,2,2)
    plot(logflag,tt,Cs(:,5*(n+2)+1:(n+2)*6)/1000,"color",cmap)
    xlabel("$t \;(s)$",'fontsize',4)
    ylabel("$C_{Al_2O_3} \;(kmol/m^3)$",'fontsize',4)
    gca().tight_limits = ["off","off","off"]
    gca.font_size = 3
    colorbar(0,1,[1 n+2])
    gce().title.text="$x_n$"
    gce().font_size=3
    gce().title.font_size=4
drawnow()
xs2png(gcf().figure_id,"C:\Users\riddh\OneDrive\Desktop\plots v1.0\"+string(gcf().figure_id)+" solid concentrations vs t b.png")

fig=scf(4)
clf
printf("%s\n","figure "+string(gcf().figure_id))
drawlater()
fig.figure_size = [900 650]
fig.children.font_size = 4
fig.color_map=cmap
logflag="nnn"
subplot(2,2,1)
    plot(logflag,tt,Cs(:,6*(n+2)+1:(n+2)*7)/1000,"color",cmap)
    xlabel("$t \; (s)$",'fontsize',4)
    ylabel("$C_{FeF_3} \;(kmol/m^3)$",'fontsize',4)
    gca().tight_limits = ["off","off","off"]
    gca.font_size = 3
    colorbar(0,1,[1 n+2])
    gce().title.text="$x_n$"
    gce().font_size=3
    gce().title.font_size=4
subplot(2,2,2)
    plot(logflag,tt,Cs(:,7*(n+2)+1:(n+2)*8)/1000,"color",cmap)
    xlabel("$t \;(s)$",'fontsize',4)
    ylabel("$C_{MgF_2} \;(kmol/m^3)$",'fontsize',4)
    gca().tight_limits = ["off","off","off"]
    gca.font_size = 3
    colorbar(0,1,[1 n+2])
    gce().title.text="$x_n$"
    gce().font_size=3
    gce().title.font_size=4
subplot(2,2,3)
    plot(logflag,tt,Cs(:,8*(n+2)+1:(n+2)*9)/1000,"color",cmap)
    xlabel("$t \;(s)$",'fontsize',4)
    ylabel("$C_{CaF_2} \;(kmol/m^3)$",'fontsize',4)
    gca().tight_limits = ["off","off","off"]
    gca.font_size = 3
    colorbar(0,1,[1 n+2])
    gce().title.text="$x_n$"
    gce().font_size=3
    gce().title.font_size=4
subplot(2,2,4)
    plot(logflag,tt,Cs(:,9*(n+2)+1:(n+2)*10)/1000,"color",cmap)
```

```
    xlabel("$t \;(s)$",'fontsize',4)
    ylabel("$C_{AlF_3} \;(kmol/m^3)$",'fontsize',4)
    gca().tight_limits = ["off","off","off"]
    gca.font_size = 3
    colorbar(0,1,[1 n+2])
    gce().title.text="$x_n$"
    gce().font_size=3
    gce().title.font_size=4
drawnow()
xs2png(gcf().figure_id,"C:\Users\riddh\OneDrive\Desktop\plots v1.0\"+string(gcf().figure_id)+" solid concentrations vs t
c.png")

// porosity over time
fig=scf(5);
clf
printf("%s\n","figure "+string(gcf().figure_id))
fig.figure_size = [450 650/1.67]
fig.children.font_size = 3
fig.color_map=cmap
logflag="nnn"
plot(logflag,tt,e,"color",cmap)
xlabel("$t \;(s)$",'fontsize',4)
ylabel("$Porosity \;(\epsilon)$",'fontsize',4)
gca().tight_limits = ["off","off","off"]
colorbar(0,1,[1 n+2])
gce().title.text="$x_n$"
gce().font_size=3
gce().title.font_size=3
xs2png(gcf().figure_id,"C:\Users\riddh\OneDrive\Desktop\plots v1.0\"+string(gcf().figure_id)+" porosity vs t.png")

//2D plots, C vs x at each t-point
fig=scf(6);
clf
printf("%s\n","figure "+string(gcf().figure_id))
drawlater()
fig.figure_size = [900 650]
cmap=rainbowcolormap(nt)//plotting time points
fig.color_map = cmap;
logflag="nnn"
subplot(2,2,1)
    plot(logflag,xn,Cg(:,1:n+2)',"color",cmap)
    xlabel("$x_n\;(-) $",'fontsize',4)
    ylabel("$C_F_2 \;(mol/m^3)$",'fontsize',4)
    gca().tight_limits = ["off","off","off"]
    gca.font_size = 3
    colorbar(0,t($),[1 nt])
    gce().title.text="$t\;(s)$"
    gce().font_size=3
    gce().title.font_size=4
subplot(2,2,2)
    plot(logflag,xn,Cg(:,(n+2)+1:(n+2)*2)',"color",cmap)
    xlabel("$x_n\;(-)$",'fontsize',4)
    ylabel("$C_O_2 \;(mol/m^3)$",'fontsize',4)
    gca().tight_limits = ["off","off","off"]
    gca.font_size = 3
    colorbar(0,t($),[1 nt])
    gce().title.text="$t\;(s)$"
    gce().font_size=3
    gce().title.font_size=4
subplot(2,2,3)
    plot(logflag,xn,Cg(:,2*(n+2)+1:(n+2)*3)',"color",cmap)
    xlabel("$x_n\;(-)$",'fontsize',4)
    ylabel("$C_{SiF_4} \;(mol/m^3)$",'fontsize',4)
    gca().tight_limits = ["off","off","off"]
    gca.font_size = 3
    colorbar(0,t($),[1 nt])
    gce().title.text="$t\;(s)$"
    gce().font_size=3
    gce().title.font_size=4
```

```
subplot(2,2,4)
    plot(logflag,xn,Cg(:,3*(n+2)+1:(n+2)*4)',"color",cmap)
    xlabel("$x_n\;(-)$",'fontsize',4)
    ylabel("$C_{TiF_4} \;(mol/m^3)$",'fontsize',4)
    gca().tight_limits = ["off","off","off"]
    gca.font_size = 3
    colorbar(0,t($),[1 nt])
    gce().title.text="$t\;(s)$"
    gce().font_size=3
    gce().title.font_size=4
drawnow()
xs2png(gcf().figure_id,"C:\Users\riddh\OneDrive\Desktop\plots v1.0\"+string(gcf().figure_id)+" Gas concentrations vs x.png")

fig=scf(7);
clf
printf("%s\n","figure "+string(gcf().figure_id))
drawlater()
cmap=rainbowcolormap(nt)//plotting time points
fig.figure_size = [900 650]
fig.color_map = cmap;
logflag="nnn"
subplot(2,2,1)
    plot(logflag,xn,Cs(:,1:n+2)'/1000,"color",cmap)
    xlabel("$x_n\;(-)$",'fontsize',4)
    ylabel("$C_{SiO_2} \;(kmol/m^3)$",'fontsize',4)
    gca().tight_limits = ["off","off","off"]
    gca.font_size = 3
    colorbar(0,t($),[1 nt])
    gce().title.text="$t\;(s)$"
    gce().font_size=3
    gce().title.font_size=4
subplot(2,2,2)
    plot(logflag,xn,Cs(:,(n+2)+1:(n+2)*2)'/1000,"color",cmap)
    xlabel("$x_n\;(-)$",'fontsize',4)
    ylabel("$C_{TiO_2} \;(kmol/m^3)$",'fontsize',4)
    gca().tight_limits = ["off","off","off"]
    gca.font_size = 3
    colorbar(0,t($),[1 nt])
    gce().title.text="$t\;(s)$"
    gce().font_size=3
    gce().title.font_size=4
subplot(2,2,3),
    plot(logflag,xn,Cs(:,2*(n+2)+1:(n+2)*3)'/1000,"color",cmap)
    xlabel("$x_n\;(-)$",'fontsize',4)
    ylabel("$C_{FeO} \;(kmol/m^3)$",'fontsize',4)
    gca().tight_limits = ["off","off","off"]
    gca.font_size = 3
    colorbar(0,t($),[1 nt])
    gce().title.text="$t\;(s)$"
    gce().font_size=3
    gce().title.font_size=4
subplot(2,2,4)
    plot(logflag,xn,Cs(:,3*(n+2)+1:(n+2)*4)'/1000,"color",cmap)
    xlabel("$x_n\;(-)$",'fontsize',4)
    ylabel("$C_{MgO} \;(kmol/m^3)$",'fontsize',4)
    gca().tight_limits = ["off","off","off"]
    gca.font_size = 3
    colorbar(0,t($),[1 nt])
    gce().title.text="$t\;(s)$"
    gce().font_size=3
    gce().title.font_size=4
drawnow()
xs2png(gcf().figure_id,"C:\Users\riddh\OneDrive\Desktop\plots v1.0\"+string(gcf().figure_id)+" solid concentrations vs x
a.png")

fig=scf(8);clf
printf("%s\n","figure "+string(gcf().figure_id))
drawlater()
cmap=rainbowcolormap(nt)//plotting time points
```

```
fig.figure_size = [900 650/1.67]
fig.color_map = cmap;
logflag="nnn"
subplot(1,2,1)
    plot(logflag,xn,Cs(:,4*(n+2)+1:(n+2)*5)'/1000,"color",cmap)
    xlabel("$x_n\;(-)$",'fontsize',4)
    ylabel("$C_{CaO}\; (kmol/m^3)$",'fontsize',4)
    gca().tight_limits = ["off","off","off"]
    gca.font_size = 3
    colorbar(0,t($),[1 nt])
    gce().title.text="$t\;(s)$"
    gce().font_size=3
    gce().title.font_size=4
subplot(1,2,2)
    plot(logflag,xn,Cs(:,5*(n+2)+1:(n+2)*6)'/1000,"color",cmap)
    xlabel("$x_n\;(-)$",'fontsize',4)
    ylabel("$C_{Al_2O_3} \;(kmol/m^3)$",'fontsize',4)
    gca().tight_limits = ["off","off","off"]
    gca.font_size = 3
    colorbar(0,t($),[1 nt])
    gce().title.text="$t\;(s)$"
    gce().font_size=3
    gce().title.font_size=4
drawnow()
xs2png(gcf().figure_id,"C:\Users\riddh\OneDrive\Desktop\plots v1.0\"+string(gcf().figure_id)+" solid concentrations vs x
b.png")

fig=scf(9);
clf
printf("%s\n","figure "+string(gcf().figure_id))
drawlater()
cmap=rainbowcolormap(nt)//plotting time points
fig.figure_size = [900 650]
fig.color_map = cmap;
logflag="nnn"
subplot(2,2,1)
    plot(logflag,xn,Cs(:,8*(n+2)+1:(n+2)*9)'/1000,"color",cmap)
    xlabel("$x_n\;(-)$",'fontsize',4)
    ylabel("$C_{CaF_2} \;(kmol/m^3)$",'fontsize',4)
    gca().tight_limits = ["off","off","off"]
    gca.font_size = 3
    colorbar(0,t($),[1 nt])
    gce().title.text="$t\;(s)$"
    gce().font_size=3
    gce().title.font_size=4
subplot(2,2,2)
    plot(logflag,xn,Cs(:,9*(n+2)+1:(n+2)*10)'/1000,"color",cmap)
    xlabel("$x_n\;(-)$",'fontsize',4)
    ylabel("$C_{AlF_3} \;(kmol/m^3)$",'fontsize',4)
    gca().tight_limits = ["off","off","off"]
    gca.font_size = 3
    colorbar(0,t($),[1 nt])
    gce().title.text="$t\;(s)$"
    gce().font_size=3
    gce().title.font_size=4
subplot(2,2,3)
    plot(logflag,xn,Cs(:,6*(n+2)+1:(n+2)*7)'/1000,"color",cmap)
    xlabel("$x_n\;(-)$",'fontsize',4)
    ylabel("$C_{FeF_3} \;(kmol/m^3)$",'fontsize',4)
    gca().tight_limits = ["off","off","off"]
    gca.font_size = 3
    colorbar(0,t($),[1 nt])
    gce().title.text="$t\;(s)$"
    gce().font_size=3
    gce().title.font_size=4
subplot(2,2,4)
    plot(logflag,xn,Cs(:,7*(n+2)+1:(n+2)*8)'/1000,"color",cmap)
    xlabel("$x_n\;(-)$",'fontsize',4)
    ylabel("$C_{MgF_2} \;(kmol/m^3)$",'fontsize',4)
```

```
    gca().tight_limits = ["off","off","off"]
    gca.font_size = 3
    colorbar(0,t($),[1 nt])
    gce().title.text="$t\;(s)$"
    gce().font_size=3
    gce().title.font_size=4
drawnow()
xs2png(gcf().figure_id,"C:\Users\riddh\OneDrive\Desktop\plots v1.0\"+string(gcf().figure_id)+" solid concentrations vs x c.png")

// porosity over position

fig=scf(10);clf
printf("%s\n","figure "+string(gcf().figure_id))
fig.figure_size = [450 650/1.67]
fig.color_map=cmap
logflag="nnn"
plot(logflag,xn,e',"color",cmap)
xlabel("$x_n\;(-)$",'fontsize',4)
ylabel("$Porosity \;(\epsilon)$",'fontsize',4)
gca().tight_limits = ["off","off","off"]
gca().font_size=3
colorbar(0,t($),[1 nt])
gce().title.text="$t\;(s)$"
gce().font_size=3
gce().title.font_size=4
xs2png(gcf().figure_id,"C:\Users\riddh\OneDrive\Desktop\plots v1.0\"+string(gcf().figure_id)+" porosity vs xn.png")

//--------------------------------------------------------------------------------
//3D surface plots, C vs xn at every t
//--------------------------------------------------------------------------------
ttx=tt*ones(1,n+2)  //defining the time vector to correct shape
xxn=(xn*ones(1,length(tt)))'  //defining the position vector to correct shape

fig=scf(11);clf
printf("%s\n","figure "+string(gcf().figure_id))
drawlater()
fig.figure_size = [900 650]
fig.children.font_size = 4
gcf().color_map=rainbowcolormap(50)
subplot(2,2,1)
    surf(ttx,xxn,Cg(:,1:n+2))
    gca().children.color_mode=-2
    gca().children.color_flag=3
    ylabel("$x_n\;(-)$",'fontsize',4)
    xlabel("$t\; (s)$",'fontsize',4)
    zlabel("",'fontsize',4)
    gca().tight_limits = ["off","off","off"]
    gca().z_label.font_angle=-90
    gca().font_size=3
    gca.margins =  [0.1,0.1,0.05,0.1]
    colorbar(0,max(Cg(:,1:n+2)),[1 nt])
    gce().title.text="$C_{F_2} \;(mol/m^3)$"
    gce().font_size=3
    gce().title.font_size=4
subplot(2,2,2)
    surf(ttx,xxn,Cg(:,(n+2)+1:(n+2)*2))
    gca().children.color_mode=-2
    gca().children.color_flag=3
    xlabel("$t\;(s)$",'fontsize',4)
    ylabel("$x_n\;(-)$",'fontsize',4)
    zlabel("",'fontsize',4)
    gca().tight_limits = ["off","off","off"]
    gca().z_label.font_angle=-90
    gca().font_size=3
    gca.rotation_angles = [65.75,-53.5]
    gca.margins = [0.1,0.1,0.05,0.1]
    colorbar(0,max(Cg(:,(n+2)+1:(n+2)*2)),[1 nt])
    gce().title.text="$C_O_2 \;(mol/m^3)$"
```

```
    gce().font_size=3
    gce().title.font_size=4
subplot(2,2,3)
    surf(ttx,xxn,Cg(:,2*(n+2)+1:(n+2)*3))
    gca().children.color_mode=-2
    gca().children.color_flag=3
    xlabel("$t(s)$",'fontsize',4)
    ylabel("$x_n\;(-)$",'fontsize',4)
    zlabel("",'fontsize',4)
    gca().tight_limits = ["off","off","off"]
    gca().z_label.font_angle=-90
    gca().font_size=3
    gca.rotation_angles = [65.75,-53.5]
    gca.margins = [0.1,0.1,0.05,0.1]
    colorbar(0,max(Cg(:,2*(n+2)+1:(n+2)*3)),[1 nt])
    gce().title.text="$C_{SiF_4} \;(mol/m^3)$"
    gce().font_size=3
    gce().title.font_size=4
subplot(2,2,4)
    surf(ttx,xxn,Cg(:,3*(n+2)+1:(n+2)*4))
    gca().children.color_mode=-2
    gca().children.color_flag=3
    xlabel("$t\;(s)$",'fontsize',4)
    ylabel("$x_n\;(-)$",'fontsize',4)
    zlabel("",'fontsize',4)
    gca().tight_limits = ["off","off","off"]
    gca().z_label.font_angle=-90
    gca().font_size=3
    gca.rotation_angles = [65.75,-53.5]
    gca.margins = [0.1,0.1,0.05,0.1]
    colorbar(0,max(Cg(:,3*(n+2)+1:(n+2)*4)),[1 nt])
    gce().title.text="$C_{TiF_4}\; (mol/m^3)$"
    gce().font_size=3
    gce().title.font_size=4
drawnow()
xs2png(gcf().figure_id,"C:\Users\riddh\OneDrive\Desktop\plots v1.0\"+string(gcf().figure_id)+" gas surf plot.png")

fig=scf(12);
clf
printf("%s\n","figure "+string(gcf().figure_id))
drawlater()
fig.figure_size = [900 650]
fig.children.font_size = 4
gcf().color_map=rainbowcolormap(50)
subplot(2,2,1)
    surf(ttx,xxn,Cs(:,1:n+2)/1000)
    gca().children.color_mode=-2
    gca().children.color_flag=3
    ylabel("$x_n\;(-)$",'fontsize',4)
    xlabel("$t \;(s)$",'fontsize',4)
    zlabel("",'fontsize',4)
    gca().tight_limits = ["off","off","off"]
    gca().z_label.font_angle=-90
    gca().font_size=3
    gca.rotation_angles = [65.75,-53.5]
    gca.margins = [0.1,0.1,0.05,0.1]
    colorbar(0,max(Cs(:,1:n+2)/1000),[1 nt])
    gce().title.text="$C_{SiO_2} \;(kmols/m^3)$"
    gce().font_size=3
    gce().title.font_size=4
subplot(2,2,2)
    surf(ttx,xxn,Cs(:,(n+2)+1:(n+2)*2)/1000)
    gca().children.color_mode=-2
    gca().children.color_flag=3
    ylabel("$x_n\;(-)$",'fontsize',4)
    xlabel("$t \;(s)$",'fontsize',4)
    zlabel("",'fontsize',4)
    gca().tight_limits = ["off","off","off"]
    gca().z_label.font_angle=-90
```

```
    gca().font_size=3
    gca.rotation_angles = [65.75,-53.5]
    gca.margins = [0.1,0.1,0.05,0.1]
    colorbar(0,max(Cs(:,(n+2)+1:(n+2)*2)/1000),[1 nt])
    gce().title.text="$C_{TiO_2} \;(kmols/m^3)$"
    gce().font_size=3
    gce().title.font_size=4
subplot(2,2,3)
    surf(ttx,xxn,Cs(:,2*(n+2)+1:(n+2)*3)/1000)
    gca().children.color_mode=-2
    gca().children.color_flag=3
    ylabel("$x_n\;(-)$",'fontsize',4)
    xlabel("$t\; (s)$",'fontsize',4)
    zlabel("",'fontsize',4)
    gca().tight_limits = ["off","off","off"]
    gca().z_label.font_angle=-90
    gca().font_size=3
    gca.rotation_angles = [65.75,-53.5]
    gca.margins = [0.1,0.1,0.05,0.1]
    colorbar(0,max(Cs(:,2*(n+2)+1:(n+2)*3)/1000),[1 nt])
    gce().title.text="$C_{FeO} \;(kmol/m^3)$"
    gce().font_size=3
    gce().title.font_size=4
subplot(2,2,4)
    surf(ttx,xxn,Cs(:,3*(n+2)+1:(n+2)*4)/1000)
    gca().children.color_mode=-2
    gca().children.color_flag=3
    ylabel("$x_n\;(-)$",'fontsize',4)
    xlabel("$t \;(s)$",'fontsize',4)
    zlabel("",'fontsize',4)
    gca().tight_limits = ["off","off","off"]
    gca().z_label.font_angle=-90
    gca().font_size=3
    gca.rotation_angles = [65.75,-53.5]
    gca.margins = [0.1,0.1,0.05,0.1]
    colorbar(0,max(Cs(:,3*(n+2)+1:(n+2)*4)/1000),[1 nt])
    gce().title.text="$C_{MgO}\; (kmol/m^3)$"
    gce().font_size=3
    gce().title.font_size=4
drawnow()
xs2png(gcf().figure_id,"C:\Users\riddh\OneDrive\Desktop\plots v1.0\"+string(gcf().figure_id)+" solid surf plot a.png")

fig=scf(13);
clf
printf("%s\n","figure "+string(gcf().figure_id))
drawlater()
fig.figure_size = [900 650/1.67]
fig.children.font_size = 4
gcf().color_map=rainbowcolormap(150)
subplot(1,2,1)
    surf(ttx,xxn,Cs(:,4*(n+2)+1:(n+2)*5)/1000)
    gca().children.color_mode=-2
    gca().children.color_flag=3
    ylabel("$x_n\;(-)$",'fontsize',4)
    xlabel("$t \;(s)$",'fontsize',4)
    zlabel("",'fontsize',4)
    gca().tight_limits = ["off","off","off"]
    gca().z_label.font_angle=-90
    gca().font_size=3
    gca.rotation_angles = [65.75,-53.5]
    gca.margins = [0.1,0.1,0.05,0.1]
    colorbar(0,max(Cs(:,4*(n+2)+1:(n+2)*5)/1000),[1 nt])
    gce().title.text="$C_{CaO}\; (kmol/m^3)$"
    gce().font_size=3
    gce().title.font_size=4
subplot(1,2,2)
    surf(ttx,xxn,Cs(:,5*(n+2)+1:(n+2)*6)/1000)
    gca().children.color_mode=-2
    gca().children.color_flag=3
```

```
    ylabel("$x_n\;(-)$",'fontsize',4)
    xlabel("$t \;(s)$",'fontsize',4)
    zlabel("",'fontsize',4)
    gca().tight_limits = ["off","off","off"]
    gca().z_label.font_angle=-90
    gca().font_size=3
    gca.rotation_angles = [65.75,-53.5]
    gca.margins = [0.1,0.1,0.05,0.1]
    colorbar(0,max(Cs(:,5*(n+2)+1:(n+2)*6)/1000),[1 nt])
    gce().title.text="$C_{Al_2O_3} \;(kmol/m^3)$"
    gce().font_size=3
    gce().title.font_size=4
drawnow()
xs2png(gcf().figure_id,"C:\Users\riddh\OneDrive\Desktop\plots v1.0\"+string(gcf().figure_id)+" solid surf plot b.png")

fig=scf(14);
clf
printf("%s\n","figure "+string(gcf().figure_id))
drawlater()
fig.figure_size = [900 650]
fig.children.font_size = 4
gcf().color_map=rainbowcolormap(150)
subplot(2,2,1)
    surf(ttx,xxn,Cs(:,6*(n+2)+1:(n+2)*7)/1000)
    gca().children.color_mode=-2
    gca().children.color_flag=3
    ylabel("$x_n\;(-)$",'fontsize',4)
    xlabel("$t \;(s)$",'fontsize',4)
    zlabel("",'fontsize',4)
    gca().tight_limits = ["off","off","off"]
    gca().z_label.font_angle=-90
    gca().font_size=3
    gca.margins = [0.1,0.1,0.05,0.1]
    colorbar(0,max(Cs(:,6*(n+2)+1:(n+2)*7)/1000),[1 nt])
    gce().title.text="$C_{FeF_3}\; (kmol/m^3)$"
    gce().font_size=3
    gce().title.font_size=4
subplot(2,2,2)
    surf(ttx,xxn,Cs(:,7*(n+2)+1:(n+2)*8)/1000)
    gca().children.color_mode=-2
    gca().children.color_flag=3
    ylabel("$x_n\;(-)$",'fontsize',4)
    xlabel("$t \;(s)$",'fontsize',4)
    zlabel("",'fontsize',4)
    gca().tight_limits = ["off","off","off"]
    gca().z_label.font_angle=-90
    gca().font_size=3
    gca.margins = [0.1,0.1,0.05,0.1]
    colorbar(0,max(Cs(:,7*(n+2)+1:(n+2)*8)/1000),[1 nt])
    gce().title.text="$C_{MgF_2} \;(kmol/m^3)$"
    gce().font_size=3
    gce().title.font_size=4
subplot(2,2,3)
    surf(ttx,xxn,Cs(:,8*(n+2)+1:(n+2)*9)/1000)
    gca().children.color_mode=-2
    gca().children.color_flag=3
    ylabel("$x_n\;(-)$",'fontsize',4)
    xlabel("$t \;(s)$",'fontsize',4)
    zlabel("",'fontsize',4)
    gca().tight_limits = ["off","off","off"]
    gca().z_label.font_angle=-90
    gca().font_size=3
    gca.margins = [0.1,0.1,0.05,0.1]
    colorbar(0,max(Cs(:,8*(n+2)+1:(n+2)*9)/1000),[1 nt])
    gce().title.text="$C_{CaF_3} \;(kmol/m^3)$"
    gce().font_size=3
    gce().title.font_size=4
subplot(2,2,4)
    surf(ttx,xxn,Cs(:,9*(n+2)+1:(n+2)*10)/1000)
```

```
    gca().children.color_mode=-2
    gca().children.color_flag=3
    ylabel("$x_n\;(-)$",'fontsize',4)
    xlabel("$t \;(s)$",'fontsize',4)
    zlabel("",'fontsize',4)
    gca().tight_limits = ["off","off","off"]
    gca().z_label.font_angle=-90
    gca().font_size=3
    gca.margins = [0.1,0.1,0.05,0.1]
    colorbar(0,max(Cs(:,9*(n+2)+1:(n+2)*10)/1000),[1 nt])
    gce().title.text="$C_{AlF_3} \;(kmol/m^3)$"
    gce().font_size=3
    gce().title.font_size=4
drawnow()
xs2png(gcf().figure_id,"C:\Users\riddh\OneDrive\Desktop\plots v1.0\"+string(gcf().figure_id)+" solid surf plot c.png")

fig=scf(15);
clf
printf("%s\n","figure "+string(gcf().figure_id))
drawlater()
fig.figure_size = [450 650/1.67]
fig.children.font_size = 4
gcf().color_map=rainbowcolormap(50)
surf(ttx,xxn,e)
gca().children.color_mode=-2
gca().children.color_flag=3
ylabel("$x_n\;(-)$",'fontsize',4)
xlabel("$t (s)$",'fontsize',4)
zlabel("",'fontsize',4)
gca().z_label.font_angle=-90
gca().tight_limits = ["off","off","off"]
gca().font_size=3
//gca.rotation_angles = [65.75,-53.5]
gca.margins = [0.1,0.1,0.05,0.1]
colorbar(0,max(e),[1 nt])
gce().title.text="$Porosity\;(\epsilon)$"
gce().font_size=3
gce().title.font_size=4
drawnow()
xs2png(gcf().figure_id,"C:\Users\riddh\OneDrive\Desktop\plots v1.0\"+string(gcf().figure_id)+" porosity vs t vs x surf.png")

//---------------------------------------------------------------------------
//conversion plots
//---------------------------------------------------------------------------
//the solids are not moving and thus conversion can be used here
fig=scf(16);
clf
printf("%s\n","figure "+string(gcf().figure_id))
drawlater()
fig.figure_size = [750 750]
fig.children.font_size = 4
logflag="nnn"
subplot(3,2,1)
    plot(logflag,tt,XSiO2,"color","-red")
    xlabel("$t (s)$",'fontsize',4)
    ylabel("$Conversion\; of \;SiO_2\;(\%)$",'fontsize',4)
    gca().tight_limits = ["off","off","off"]
    gca.font_size = 3
subplot(3,2,2)
    plot(logflag,tt,XTiO2,"color","-red")
    xlabel("$t (s)$",'fontsize',4)
    ylabel("$Conversion\; of \;TiO_2 \;(\%)$",'fontsize',4)
    gca().tight_limits = ["off","off","off"]
    gca.font_size = 3
subplot(3,2,3)
    plot(logflag,tt,XFeO,"color","-red")
    xlabel("$t (s)$",'fontsize',4)
    ylabel("$Conversion\; of \;FeO\; (\%)$",'fontsize',4)
    gca().tight_limits = ["off","off","off"]
```

```
    gca.font_size = 3
subplot(3,2,4)
    plot(logflag,tt,XMgO,"color","-red")
    xlabel("$t (s)$",'fontsize',4)
    ylabel("$Conversion\; of \;MgO\; (\%)$",'fontsize',4)
    gca().tight_limits = ["off","off","off"]
    gca.font_size = 3
subplot(3,2,5)
    plot(logflag,tt,XCaO,"color","-red")
    xlabel("$t (s)$",'fontsize',4)
    ylabel("$Conversion\; of \;CaO\; (\%)$",'fontsize',4)
    gca().tight_limits = ["off","off","off"]
    gca.font_size = 3
subplot(3,2,6)
    plot(logflag,tt,XAl2O3,"color","-red")
    xlabel("$t (s)$",'fontsize',4)
    ylabel("$Conversion\; of \;Al_2O_3\; (\%)$",'fontsize',4)
    gca().tight_limits = ["off","off","off"]
    gca.font_size = 3
drawnow()
xs2png(gcf().figure_id,"C:\Users\riddh\OneDrive\Desktop\plots v1.0\"+string(gcf().figure_id)+" solid conversion vs t.png")
```